

UNIVERSITY OF KWAZULU-NATAL
COLLEGE OF AGRICULTURE, ENGINEERING AND SCIENCE

**DESIGN OF A NOVEL HYDROKINETIC TURBINE FOR
OCEAN CURRENT POWER GENERATION**


Kumaresan Cunden

**Dissertation submitted in fulfilment of the academic requirements for the
degree of Master of Science in Mechanical Engineering**

Supervisor: Dr Freddie L. Inambao

October 2014

“As the candidate’s Supervisor I agree/~~do not agree~~ to the submission of this dissertation”.
The supervisor must sign all copies after deleting which is not applicable.

Dr Freddie L. Inambao 

NAME OF SUPERVISOR SIGNATURE

COLLEGE OF AGRICULTURE, ENGINEERING AND SCIENCE

DECLARATION 1 - PLAGIARISM

I, Kumaresan Cunden, declare that:

1. The research reported in this dissertation, except where otherwise indicated, is my original research.
2. This dissertation has not been submitted for any degree or examination at any other university.
3. This dissertation does not contain other persons' data, pictures, graphs or other information, unless specifically acknowledged as being sourced from other persons.
4. This dissertation does not contain other persons' writing, unless specifically acknowledged as being sourced from other researchers. Where other written sources have been quoted, then:
 - a. Their words have been re-written but the general information attributed to them has been referenced.
 - b. Where their exact words have been used, then their writing has been placed in italics and inside quotation marks, and referenced.
5. This dissertation does not contain text, graphics or tables copied and pasted from the Internet, unless specifically acknowledged, and the source being detailed in the dissertation and in the References sections.

Signed



.....

COLLEGE OF AGRICULTURE, ENGINEERING AND SCIENCE

DECLARATION 2 - PUBLICATIONS

DETAILS OF CONTRIBUTION TO PUBLICATIONS that form part and/or include research presented in this dissertation (include publications in preparation, submitted, in press and published and give details of the contributions of each author to the experimental work and writing of each publication).

Publication 1: F. L. Inambao and K. Cunden, “Design and numerical simulation of a small scale helical cross-flow turbine,” in *Proceedings of 13th Botswana Institution of Engineers Biennial Conference*, [CD Rom], 15 to 18 October, 2013, Gaborone, Botswana, pp. 23-32.

Publication 2: K. Cunden and F. Inambao, “Numerical simulation of a vertical axis cross-flow helical hydrokinetic turbine,” in *Proceedings of First Eskom Power Plant Engineering Institute Student Conference* Eskom Academy of Learning, 5 & 6, May 2014.

ACKNOWLEDGEMENTS

The last two years of my life has allowed me to open my eyes to the depths of engineering. I have gained so much knowledge beyond what I would have expected. I dedicate this dissertation to my parents for all their time, patience, understanding and hard work to overcome the challenges which we have faced as a family throughout my life. Thank you for the infinite love, guidance and motivation – it has been my source of energy.

To my lecturer, supervisor and someone who I regard as my second father, Dr Freddie L. Inambao: I thank you for all the guidance, support and motivation to strive for nothing but perfection in life. You have shown me what it is and how to be an excellent engineer as well as imparting an unimaginable amount of knowledge and leadership skills to me. Спасибо, я желаю вам долгую и процветающее будущее.

To my fellow postgraduate colleagues, thank you for all the assistance with my work and multiple favours when I really required them. I appreciate the time you have taken to help me in my times of need. To the many lecturers who have assisted and guided me during the duration of my studies, I thank you. You have opened my mind to a world I would never have dreamt of otherwise.

To whoever is about to read this dissertation, I leave you with words from one of my role models:

“The scientists of today think deeply instead of clearly. One must be sane to think clearly, but one can think deeply and be quite insane.” — Nikola Tesla

ABSTRACT

In a world with a growing need for energy, but also a growing need to decrease dependence on fossil fuel energy production, new methods of energy generation are required. The energy which exists in flowing rivers, ocean currents and various other artificial water channels is considered a viable option for a source of renewable power. Water energy harnessing systems are referred to as Hydrokinetic conversion systems. These types of systems are still in the infant stages of development as the main focus of renewable energy in recent years has been solar and wind energy harvesting.

Research into ocean currents focusing on the Agulhas Current was conducted to be used as a basis for a Subsea Hydrokinetic system to be implemented off the coast of South Africa. The results obtained from Eskom's Acoustic Doppler Current Profiler (ADCP) readings depict that the Agulhas current is a more than adequate source of renewable energy. The readings indicate that the Agulhas current varies from 0.3 m/s to 1.2 m/s throughout the year.

A proposed Vertical-Axis Hydrokinetic turbine was designed to harness power from the Agulhas current. The design focuses on the selection of blade profile to exploit the lift force which is a result of the interaction with the flow medium. The blade's helical structure is based on the relationship with the initial attack angle of the blade at a 0° azimuthal position based on the mathematical formulae derived by Gorlov. The study compares a toe-out angle which is not modelled by Gorlov. It was assumed that the turbine's efficiency would be increased as long as the toe-out angle is within a specified range.

Analytical and Computational Fluid Dynamic (CFD) simulations have been conducted on the designed hydrokinetic turbine. The analytical simulations implement double multiple stream tube models which have been used for predecessors of the vertical axis helical turbine. The analytical model was performed in QBlade which is software that implements the double multiple streamtube theory. The CFD model was conducted within Star CCM+TM which included complex vortex interaction and interference with the turbine.

Results obtained from the analytical model show that the turbine with a toe-out blade pitch had a slightly lower performance coefficient than the turbine with no blade pitch within the range of 1° to 2° . The results from the CFD simulations and the analytical modelling were in good agreement. The results obtained for the performance of the turbine for toe-out blade

pitch from the analytical and CFD modelling were 50% and 52%, respectively. The results are in line with that of simulations and testing of similar type turbines conducted by previous researchers. Comparisons from the effect of toe-out angle on the turbine's performance proved that the turbine does not experience an increase in efficiency; however, the torque fluctuations decreased for increasing blade pitch. The toe out angle reduced the amount of torque fluctuations on the turbine rotor which provides fewer fluctuations to the coupled generator.

Keywords: Agulhas Current, Hydrodynamic, Vertical Axis, Numerical Modelling, CFD

TABLE OF CONTENTS

Declaration 1 - Plagiarism	II
Declaration 2 - Publications.....	III
Acknowledgements.....	IV
Abstract.....	V
Table Of Contents	VII
List of Figures	XI
List of Tables	XV
Nomenclature.....	XVI
Acronyms and Abbreviations	XX
Chapter 1 Introduction.....	1
1.1 Background.....	1
1.2 Research Questions.....	1
1.3 Aims and Objectives of the Study	2
1.4 Layout of the Dissertation.....	3
1.5 Scope of the Study	5
1.6 Contribution of the Study to the body of Knowledge.....	5
1.7 Publications.....	6
1.7.1 Conference Proceedings.....	6
Chapter 2 Literature Review.....	7
2.1 Ocean Currents.....	7
2.2 The Agulhas Current.....	11
2.3 Marine Current Turbines.....	14
2.4 Ducted Turbines.....	18
2.5 Marine Current Turbines with Blade Variation.....	21
2.6 Dynamic Stall and Vortex Structures	22
Chapter 3 Types of Ocean Energy.....	25
3.1 Wave Energy.....	25
3.2 Ocean Thermal Energy Converters (OTEC).....	28

3.3	Tidal Energy.....	30
3.3.1	Types of Tidal Energy	32
3.3.2	Tidal Barrages.....	32
3.4	Marine Current Turbines.....	34
Chapter 4	Ocean Energy Technologies	37
4.1	Wave Energy Technologies	37
4.1.1	Oscillating Wave Column (OWC).....	37
4.1.2	The Pelamis.....	38
4.1.3	The Wave Dragon.....	39
4.1.4	The Archimedes Wave Swing	40
4.2	Ocean Thermal Energy Converter (OTEC) Technologies.....	41
4.2.1	The Closed OTEC Cycle	41
4.2.2	The Open OTEC Cycle.....	42
4.2.3	Hybrid OTEC Cycle	42
4.3	Tidal Barrage Technologies.....	43
4.3.1	La Rance, France	43
4.3.2	Annapolis Tidal Generation, Bay of Fundy, Canada.....	44
4.3.3	Kislaya Guba Power Facility, Russia.....	44
4.3.4	Jangxia Creek, East China Sea.....	45
4.4	Types of Tidal Current Turbines.....	46
4.4.1	Delta Stream Turbine	46
4.4.2	Evopod Tidal Turbine	47
4.4.3	Lunar Energy Tidal Turbine	47
4.4.4	Free Flow Turbine.....	48
4.4.5	Neptune Tidal Stream Device.....	49
4.4.6	Nereus and Solon Tidal Turbines	50
4.4.7	SeaGen	51
Chapter 5	Analysis of the Agulhas Current.....	52
5.1	Agulhas Current Potential Site Locations.....	53
5.1.1	Port Edward	53
5.1.2	Cape Morgan.....	56
5.1.3	East London	61

5.2	Site Selection	66
5.3	Estimated Energy Yield	67
Chapter 6	Design of Turbine system	71
6.1	Selection of Turbine.....	71
6.1.1	Drag Based Turbines.....	71
6.1.2	Lift Based Turbines.....	72
6.1.3	Hybrid Turbines	75
6.2	Hydrodynamics of the Cross-Flow Turbine	77
6.3	Turbine Performance Parameters.....	83
6.4	Helical Turbine design parameters	85
6.4.1	Hydrofoil Profile.....	85
6.4.2	Blade Wrap	89
6.4.3	Turbine Aspect Ratio	90
6.4.4	Number of Blades	91
6.4.5	Blade Geometry	92
6.4.6	Central Shaft Design.....	94
6.4.7	Turbine Strut Design.....	95
6.4.8	Turbine Blade Attachment.....	96
6.5	Shrouding Device.....	97
6.5.1	Selection of Shroud.....	98
6.5.2	Channel Flow Theory	100
Chapter 7	Modelling of Vertical Axis turbine.....	105
7.1	The Blade Element Theory	105
7.2	Momentum Modelling	107
7.3	Vortex Modelling.....	111
7.3.1	Added Mass Effects	111
7.3.2	Circulatory Effects	112
7.3.3	Dynamic Stall.....	114
7.3.4	Shed Vortex Structure.....	115
7.4	Numerical Analysis of Turbine.....	119
7.4.1	Numerical Model	119
7.4.2	Computational Fluid Dynamic Model	129

Chapter 8	Results and Discussions	136
8.1	Helical Turbine – No Pitch Angle	136
8.2	Helical Turbine – Addition of Pitch Angle.....	144
8.3	Helical Turbine – Addition of Channel	146
Chapter 9	Conclusions and Recommendations	150
9.1	Conclusions.....	150
9.2	Recommendations.....	152
References.....		153
Appendix A – Naca 0024 Coefficients of Lift and Drag		160
Appendix B – Numerical formulation for the tubrine Hydrodynamics.....		169

List of Figures

Figure 2-1: Thermohaline Current	8
Figure 2-2: Trade Winds	9
Figure 2-3: Surface Ocean Currents	10
Figure 2-4: Agulhas Current	12
Figure 2-5: Conceptual portrayal of Agulhas sources	13
Figure 3-1: Formation of waves.....	26
Figure 3-2: Areas of high kinetic wave energy.....	27
Figure 3-3: Kinetic and Potential energy of waves.....	27
Figure 3-4: Latitude band of Ocean Thermal Concentration.....	29
Figure 3-5: Forces which produce tides.....	31
Figure 4-1: Oscillating wave column.....	38
Figure 4-2 The Pelamis.....	38
Figure 4-3 The Wave Dragon process of operation.....	39
Figure 4-4: The Archimedes Wave Swing.....	40
Figure 4-5: Closed OTEC Cycle.....	41
Figure 4-6: Open OTEC Cycle	42
Figure 4-7: La Rance Tidal barrage Power Facility in France.....	43
Figure 4-8: Annapolis tidal power facility.....	44
Figure 4-9: Delta Stream Turbine	46
Figure 4-10: Evopod Tidal Turbine	47
Figure 4-11: Lunar Energy Tidal Turbine	48
Figure 4-12: Free Flow Turbine.....	49
Figure 4-13: Neptune Tidal Stream Device	50
Figure 4-14: Above the Nereus Turbine and below the Solon Turbine.....	51
Figure 5-1: ADCP measurement, Port Edward 60 m	53
Figure 5-2: ADCP measurement, Port Edward 30 m	54

Figure 5-3: Frequency Distribution, Port Edward 60 m	55
Figure 5-4: Frequency Distribution, Port Edward 30 m	55
Figure 5-5: Polar Plots - (a) 60 m Depth; (b) 30 m Depth.....	56
Figure 5-6: ADCP measurement, Cape Morgan 80 m.....	57
Figure 5-7: ADCP measurement, Cape Morgan 83 m.....	57
Figure 5-8: ADCP measurement, Cape Morgan 85 m.....	58
Figure 5-9: Frequency Distribution, Cape Morgan 80 m	59
Figure 5-10: Frequency Distribution, Cape Morgan 83 m	59
Figure 5-11: Frequency Distribution, Cape Morgan 85 m	60
Figure 5-12: Average Velocity Vs. Average Depth for Cape Morgan	60
Figure 5-13: Polar Plots - (a) 80 m Depth; (b) 85 m Depth.....	61
Figure 5-14: ADCP measurement, East London 87 m	62
Figure 5-15: ADCP measurement, East London 87 m	62
Figure 5-16: ADCP measurement, East London 94 m	63
Figure 5-17: Frequency Distribution, East London 87 m.....	63
Figure 5-18: Frequency Distribution, East London 87 m.....	64
Figure 5-19: Frequency Distribution, East London 94 m.....	64
Figure 5-20: Average Velocity Vs. Average Depth for East London.....	65
Figure 5-21: Polar Plots - (a) 87 m Depth; (b) 94 m Depth.....	65
Figure 5-22: Theoretical power available	68
Figure 5-23: Energy density for various current speeds	70
Figure 6-1: Savonius turbine.....	72
Figure 6-2: (a) Darrieus troposkein turbine, (b) Darrieus straight bladed turbine.....	73
Figure 6-3: Vector diagram of turbine	74
Figure 6-4: Gorlov helical turbine	75
Figure 6-5: Hybrid turbine tested in water.....	76
Figure 6-6: Velocity triangle for cross flow turbine	78

Figure 6-7: Angle of attack Vs. Azimuthal Angle	80
Figure 6-8: Upstream and downstream of turbine	80
Figure 6-9: Blade Reynolds number for one full blade revolution	81
Figure 6-10: Coefficient of lift for superior cambered blade profiles	87
Figure 6-11: Coefficient of lift Vs. Angle of attack.....	88
Figure 6-12: Cl/Cd for NACA 0024	89
Figure 6-13: Blade wrap ratio Vs. Helical pitch angle	91
Figure 6-14: Mathematical layout of helical turbine	92
Figure 6-15: Angle of attack for 0° blade pitch	93
Figure 6-16: Blade pitch toe-out angle of 7.5°	94
Figure 6-17: Designed Turbine	97
Figure 6-18: Non-Dimensional Schematic	99
Figure 6-19: Power available in the flow vs. Power from channel.....	101
Figure 6-20: Velocity Profile for the Channel	104
Figure 7-1: Normal and Tangent coefficients	107
Figure 7-2: Simple actuator disc model	107
Figure 7-3: Pressure and velocity change across turbine.....	108
Figure 7-4: Momentum models	110
Figure 7-5: Cascade momentum model	111
Figure 7-6: Wake comparison at 0.5s and 4s time steps.....	112
Figure 7-7: Shed vortices from hydrofoil profile.....	116
Figure 7-8 Formation of nascent vortex.....	116
Figure 7-9: Relationship of induced vortex strength to vortex core	117
Figure 7-10: Formation of counter clockwise shed vortex	118
Figure 7-11: Expansion of actuator disc theory	120
Figure 7-12: Multiple Actuator Disc Theory	122
Figure 7-13: Flow Diagram of Program Logic	128

Figure 7-14: Turbine and Flow Region	130
Figure 7-15: Prism Layer, CD-Adapco	131
Figure 7-16: Threshold Mesh of Flow Field and Tubrine	132
Figure 7-17: Volumetric Control of Mesh.....	132
Figure 7-18: Discretization of Flow Field & Turbine.....	133
Figure 8-1: Discretization of Turbine	137
Figure 8-2: Effects of Flow Curvature.....	138
Figure 8-3: Force Coefficient on a Single Blade	139
Figure 8-4: Torque Coefficient Plot for a Single Blade.....	140
Figure 8-5: Combined force distribution on each blade and resultant torque coefficients on rotor.....	140
Figure 8-6: Cp for Turbine at 1 m/s.....	141
Figure 8-7: Resultant Torque Loading on Turbine Central Shaft.....	142
Figure 8-8: Polar plot of single blade torque and power coefficient – TSR 1.85	143
Figure 8-9: Cp for various blade pitch angles.....	144
Figure 8-10: Polar plot of blade torque for various blade pitch angles	145
Figure 8-11: Torque Coefficient for various blade pitch angles.....	146
Figure 8-12: Cp for various flow speeds.....	147
Figure 8-13: Cp Vs. Blade Pitch for Normal & Increased Flow	148
Figure 8-14: Cp - Comparison of Blade Pitch with Normal & Increased Flow	149

LIST OF TABLES

Table 1: Reynolds Numbers for increasing flow velocity	136
Table 2: NACA 0024 Coefficients of Lift & Drag for Reynolds Number 50 000	160
Table 4: NACA 0024 Coefficients of Lift & Drag for Reynolds Number 100 000	160
Table 5: NACA 0024 Coefficients of Lift & Drag for Reynolds Number 150 000	160
Table 6: NACA 0024 Coefficients of Lift & Drag for Reynolds Number 200 000	164
Table 7: NACA 0024 Coefficients of Lift & Drag for Reynolds Number 250 000	164
Table 8: NACA 0024 Coefficients of Lift & Drag for Reynolds Number 300 000	164

NOMENCLATURE

Roman Symbols

A	Cross-sectional area of the flow (m^2)
A_c	Turbine cross-sectional swept area (m^2)
A_{Ch}	Cross-Sectional area of the channel (m^2)
c	Chord length of airfoil profile (m)
C_p	Seawater specific enthalpy (J/kg K)
c_s	Scale parameter (m/s)
D	Diameter of the turbine (m)
D	Drag force on profile centre of pressure (N)
F_N	Normal Force (N)
F_T	Tangential Force (N)
H	Turbine height (m)
H_s	Significant wave height (m)
L	Linear crest length (m)
L	Lift force on profile centre of pressure (N)
P	Hydrodynamic power (W)
P_{MAX}	Maximum Power which can be extracted by the channel (W)
P_{wave}	Power within the wave (kW)
ΔP	Pressure Difference (Pa)
Q	Volumetric flow rate (m^3/s)
Q_{avg}	Average torque on turbine (Nm)
Q_i	Instantaneous torque on a single turbine blade (Nm)
r	Distance from the vortex centre outside the vortex core (m)
R	Radius of the turbine (m)

T	Absolute temperature of OTEC warm seawater (K)
ΔT	OTEC seawater temperature difference between surface and 1000 m depth ($^{\circ}\text{C}$)
T_z	Mean zero crossing wave period (s)
T	Torque (Nm)
T_{avg}	Average Torque (Nm)
T_i	Instantaneous Torque on a single blade (Nm)
$Time_{Step}$	Time Step for the solution (s)
u_i	Induced velocity – Upwind (m/s)
u_i'	Induced velocity – Downwind (m/s)
U_{Bound}	Induced bound vortex velocity (m/s)
U_0	Asymptotic flow velocity (m/s)
U_{Rel}	Relative velocity due to vortex interference (m/s)
U_{Tip}	Blade tip speed (m/s)
$U_{Trailing}$	Induced velocity from trailing vortex (m/s)
U_{∞}	Free stream velocity (m/s)
V	Velocity of flow (m/s)
V_{rmc}	Root mean squared velocity of fluid (m/s)
w	Relative velocity – Upwind (m/s)
w'	Relative velocity – Downwind (m/s)
w_{cw}	OTEC equivalent deep seawater vertical velocity (m/s)
W_v^i	Induced velocity from shed vortex (m/s)

Greek Symbols

α	Angle of Attack ($^{\circ}$)
$\dot{\alpha}$	Rate of change of angle of attack ($^{\circ}/\text{s}$)
α	Attack Angle – Upwind ($^{\circ}$)

α'	Attack Angle – Downwind (°)
γ_s	Vortex strength (m/s)
ω	Rotational Speed (rad/s)
δ	Helix angle (°)
ρ	Density of fluid (Kg/m ³)
θ	Azimuthal Angle (°)

Non Dimensional Symbols

a	Interference / Induction factor – Upwind (-)
a'	Interference / Induction factor – Downwind (-)
B	Number of Blades (-)
C_D	Coefficient of Drag (-)
C_L	Coefficient of Lift (-)
C_n	Normal Coefficient (-)
C_{power}	Power coefficient of the turbine (-)
$C_{P,Max}$	Maximum power coefficient for free flow (-)
C_Q	Coefficient of torque (-)
C_t	Tangential Coefficient (-)
C_{Thrust}	Thrust coefficient (-)
ε	Blockage Ratio (-)
ε_{tg}	Combined OTEC turbo-generator efficiency (-)
γ	Ratio of OTEC surface seawater flow rate and OTEC deep seawater flow rate (-)
λ	Tip Speed Ratio (-)
σ	Solidity Ratio (-)
k_{waves}	Constant for waves (-)
k_p	Pitch rate parameter (-)

k_s	Shape factor (-)
N_θ	Number of streamtube (-)

ACRONYMS AND ABBREVIATIONS

ADCP	Acoustic Doppler Current Profiler
AoA	Angle of Attack
AWS	Archimedes Wave Swing
CAD	Computer Aided Design
CFD	Computational Fluid Dynamics
DVM	Discrete Vortex Method
EMEC	European Marine Energy Centre
GHG	Greenhouse Gases
OTEC	Ocean Thermal Energy Conversion/Converters
OWC	Oscillating Wave Column
PMG	Permanent Magnet Generator
Rel	Relative
RMS	Root Mean Square
TSR	Tip Speed Ratio
VAWT	Vertical Axis Wind Turbine

CHAPTER 1 INTRODUCTION

1.1 Background

The world is undergoing a positive shift from fossil fuels to renewable energy solutions. This is mainly due to the depletion of fossil fuels and an increase in greenhouse gas (GHG) emissions. These emissions directly affect the climate and in recent years the climate change has been evident. The growing concern in the world is how much the severe increase in climate change will directly affect the worlds increasing population.

In South Africa energy is predominately produced from coal fired power stations. This means that the carbon foot print of South Africa is relatively high on a continental scale. The reliance on coal fired power stations is due to South Africa's vast coal deposits which make the cost of energy production cheaper as coal does not need to be imported. However, coal is a finite resource supply which is one of the factors affecting recent power outages. For South Africa to move forward and meet world regulations of reduction in carbon footprint, "greener" energy solutions need to be obtained.

The research conducted in this dissertation highlights the energy which can be extracted by the Agulhas current by means of a hydrokinetic turbine system. A system was developed consisting of a vertical axis turbine which is to be situated along the most suitable area of the KwaZulu-Natal coast which experiences peak current flow on an assumed regular basis. The turbine design was based on the Darrieus straight blade and the Gorlov helical turbine concept. The turbine has been modified to operate at its maximum efficiency. The turbine was designed to extract a maximum power from the marine current in which it is situated. The findings from this study can be used to design and implement a multi turbine configuration system to be situated at an appropriate location offshore to extract power and supply the country with additional energy. This would cut down the carbon emissions of the country and help support the grid by reducing the current strain on the national grid at locations which the system is feeding into.

1.2 Research Questions

The need for renewable, cleaner energy sources is of high priority in the world today, in light of the global situation regarding global warming and the nuclear disaster in Japan, 2011. The

main focus for alternative sources of energy presently are predominately solar and wind energy technologies but there also exists a vast potential source of renewable energy within the oceans of the world. One of the challenges facing the ocean energy network of the world is developing a suitable turbine to extract enough energy from the ocean without disturbing the natural cycle of the oceanic site.

Harvesting energy from the ocean's currents can provide a relatively sustainable source of clean energy and be of immense benefit to the South African economy. The Agulhas current is one of the southern hemispheres strongest oceanic currents. The Agulhas current is known to reverse its flow periodically throughout a given year so adequate research into the stability of the current flow needs to be conducted, [1].

Knowing the theoretical predicted potential of the current flow, one needs to determine the amount of energy which may be extracted from the flow without disrupting the natural environment and wildlife and how much of this extracted energy may be converted to useful electrical energy.

As the turbine is exploiting the flow conditions of a natural resource, and understanding the law of conservation of mass and energy, there is a need to know how the extraction of energy would affect the surrounding natural environment. The effect on the sea life and ecosystem needs to be considered and possible solutions to reduce the environmental impact need to be ready for implementation.

The research questions of the research study are:

1. What is the estimated amount of available power within the renewable resource?
2. Can the proposed turbine device be utilised to extract energy from the current resource?
3. What are the limiting parameters of the turbine system which affect power production?
4. Would the implementation of a channelling device have a positive influence on the turbine's energy extraction?

1.3 Aims and Objectives of the Study

Using the ocean currents as an alternative energy source poses various difficulties. The main challenges which arise with using oceanic currents are the direction of the current over an

annual period, the speed of the current and the location of where a turbine would be best suited to extract the most amount of energy from the flow without adversely affecting the natural resource.

There are already a vast number of technologies which are currently being implemented in various locations all over the world. The use of a Gorlov cross-flow turbine in the Agulhas current is most suitable because the current tends to reverse its flow direction a full 180° periodically during the year. This reversal is due to the multiple eddies which develop as the current retroflects from the bottom of the Eastern Cape to complete the circulation of the current back to the Indian Ocean.

A vertical axis cross-flow turbine will be of value as the turbine does not depend on the direction of incoming flow as do standard horizontal axis turbines but rather is dependent on the speed of the incoming flow.

The aim of this study was to design a suitable cross-flow turbine which is based on the Gorlov Helical turbine but with added blade pitch to increase the turbine efficiency and to prove that the proposed turbine is capable of supplying energy from the flow. A ducting system is required to increase the flow which is fed into the turbine to further increase performance so as to extract the most energy possible from the natural resource without affecting the natural flow.

The research objectives which are in accordance with the aims set out for the study are as follows:

1. Research in greater detail the design and performance of the Gorlov helical turbine.
2. Research and implement methods to optimise the performance and efficiency of the turbine.
3. Design a prototype hydrokinetic turbine to extract energy from a simulated average current speed based on the Agulhas current.
4. Validation of theoretical research by means of various analytical and numerical simulation methods of a small scale prototype of the hydrokinetic system.

1.4 Layout of the Dissertation

The dissertation is set out to achieve the aims and objectives which are accomplished in 10 chapters. Each of the individual chapter's contents are summarized below.

Chapter 1 presents the background to the study which outlines the need for more sustainable energy solutions and explains the potential energy which exists in the Agulhas current. Within this chapter are the research questions which need to be met followed closely by the aims and objectives of the study, the layout of dissertation, the scope of the study, original contribution of the study to the renewable energy field, in particular the ocean energy division, and relevant contributing publications.

Chapter 2 is the literature review which covers the previous work which has been conducted in the same or similar field of study. This review consists of conference proceedings, journal articles and other dissertations on a masters and doctoral level.

Chapter 3 outlines the various forms of ocean energies which are currently being exploited internationally. Each form of ocean energy is explained briefly allowing the reader to understand the method of energy capture and conversion.

Chapter 4 describes the various ocean energy technologies which are currently being used in accordance with the different forms of ocean energy.

Chapter 5 provides an analysis of the Agulhas current according to data which was recorded by Eskom and made public in August 2013. This data served as a benchmark in determining the potential kinetic energy of the Agulhas current's average speed and direction values.

Chapter 6 expands on the design of the hydrokinetic cross-flow turbine. The parameters which are associated with this type of turbine are further discussed within this chapter. The mathematical modelling and design of the turbine blades, blade profiles and the turbine as a whole is expanded on in the latter part of the chapter. The shrouding and the design of the shrouding system which is to be used are examined in this chapter.

Chapter 7 describes the hydrodynamics of the cross-flow turbine and covers how the turbine interacts with the fluid medium and what vector forces are exerted on the turbine as it moves through the fluid. The complex interaction between the fluid and the turbine are described within this chapter. The various methods of numerical modelling are explained and the complex vortex formation is also further examined in this chapter. The different types of numerical simulations which were conducted on the turbine, the turbine shroud and the combined system are also covered in this chapter.

Chapter 8 provides a detailed analysis of the results obtained from the testing, CFD and analytical models which were implemented, conducted in QBlade. These results were also compared with each other to obtain validity of the two simulations.

Chapter 9 summarises and concludes the dissertation based on the results and observations that were obtained from Chapter 8. This chapter also includes recommendations for future work which may be of benefit based on the research conducted within this dissertation.

Chapter 10 highlights some of the future work which should be researched and conducted with the aid of this dissertation to further develop the turbine and increase efficiency.

1.5 Scope of the Study

The research conducted in the study is focused on the design and evaluation of a hydrokinetic cross-flow turbine system to be implemented so as to extract energy from a natural resource (the Agulhas current) and convert it into useful electrical energy to be supplied to the shore.

This research study outlines the analysis of a renewable resource and estimated power prediction based on the available amount of power within the flow, selection of hydrodynamic hydrofoil profiles, blade profile design and suitable shrouding selection to increase flow into the turbine. The design was subjected to computer aided fluid dynamic analysis and numerical modelling conducted within a numerical solver.

1.6 Contribution of the Study to the body of Knowledge

The concept of a hydrokinetic turbine used to extract energy from free flowing water sources such as rivers and streams is a relatively old technology, but the concept of using the same or similar modified turbines to be used in an oceanic environment to extract the energy from ocean currents is still in the “infant” phase. The use of a vertical axis turbine as a hydrokinetic sea turbine is less common than that of the now conventional horizontal axis hydrokinetic turbine.

This dissertation contributes to the scientific knowledge of the design of a vertical axis hydrokinetic turbine; analytical and numerical simulation models were compared for validation of the simulations.

1.7 Publications

1.7.1 Conference Proceedings

The following conference papers have been produced from the research which is presented within the following dissertation. The papers were presented at one international conference and one national conference.

Publication 1: F. L. Inambao and K. Cunden, “Design and numerical simulation of a small scale helical cross-flow turbine,” in *Proceedings of 13th Botswana Institution of Engineers Biennial Conference*, [CD Rom], 15 to 18 October, 2013, Gaborone, Botswana, pp. 23-32.

Publication 2: K. Cunden and F. Inambao, “Numerical simulation of a vertical axis cross-flow helical hydrokinetic turbine,” in *Proceedings of First Eskom Power Plant Engineering Institute Student Conference* Eskom Academy of Learning, 5 & 6, May 2014.

CHAPTER 2 LITERATURE REVIEW

The global need for alternative forms of energy production has increased in the last decade. Large amounts of energy exist within the ocean which can be extracted by various methods. Although ocean current turbines are relatively higher in cost than that of wind, the power from the ocean is more predictable and stable. Hydrokinetic or marine current turbines provide a useful means of extracting energy from natural flowing fluid resources. The advantages lie within the cross flow turbines which generate power despite the direction of the flowing medium. The following section is a literature review of the ocean currents, the Agulhas current and hydrokinetic cross-flow turbines and ocean current turbines.

2.1 Ocean Currents

Ocean currents of the world serve a major role in climate change and seasonal migration of marine life. The world consists of 71% of ocean and hence a large part of solar irradiation is absorbed by the ocean. Due to the solar irradiation absorption the ocean has a high heat capacity. The stored heat is redistributed to the atmosphere as the ocean circulates the world. The global circulation of large masses of water and energy in the form of temperature is transported by the Thermohaline circulation. The energy which is stored in the absorbed radiation is of such high importance, it influences the planets' climates around the world, Toggweiler and Key [1].

Two major types of currents exist in the world's oceans, namely, surface currents and deep sea currents. These two distinct forms of current circulate the oceans water masses. Surface currents are found in the upper 400 m of the ocean and are caused by wind and surface friction phenomena and salinity gradient migration during the Thermohaline cycle. Deep sea currents are formed due to the density gradient changes which stems from the salinity exchange of deep, dense salt water with the upper, less dense salt water. The Thermohaline circulations (Figure 2-1) can be viewed as deep sea currents.

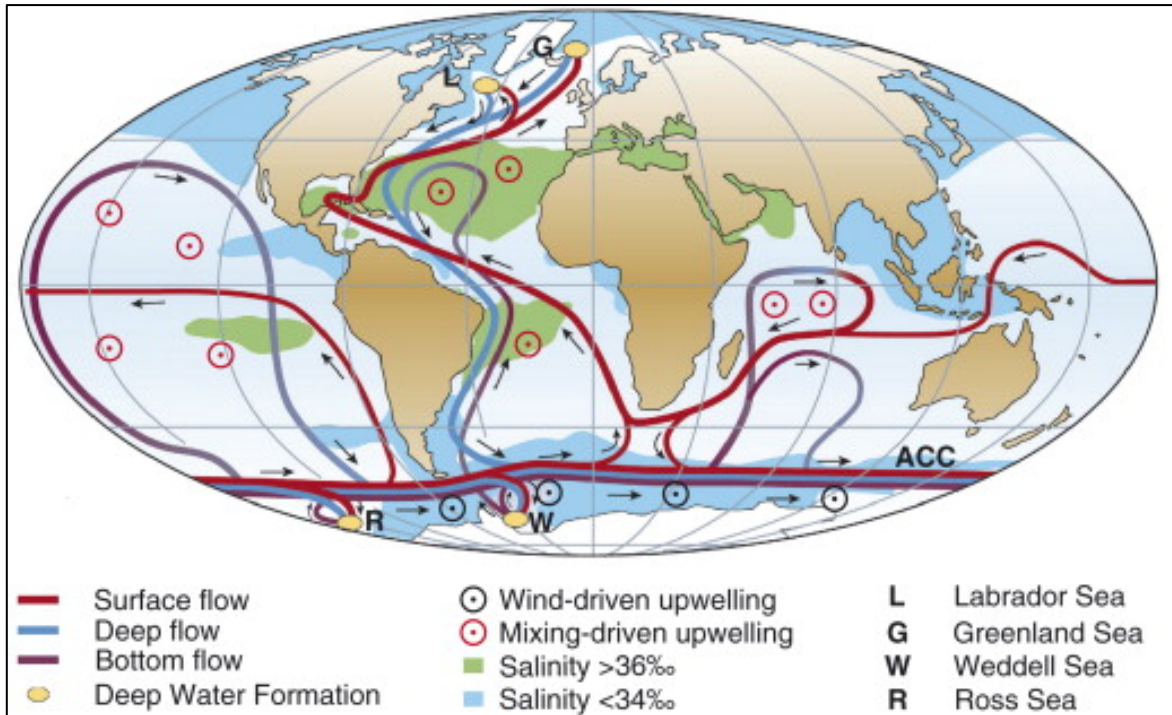


Figure 2-1: Thermohaline Current [2]

The Thermohaline circulation is named such because it is responsible for the heating, cooling, freshening and salinification of the ocean waters which produces regional density differences. Radiocarbon measurements show that the Thermohaline circulation turns all of the oceans deep sea water in an estimated 600 year cycle. The Thermohaline circulation is of importance to the Earth’s climate change as the circulation is responsible in transporting roughly 10^{15} W of heat pole ward which can be translated into about a quarter of the world’s ocean/atmospheric circulation, Toggweiler and Key [1]. The Thermohaline circulation consists of two phases which are warming and cooling which are directly related to the upwelling and downwelling of the circulation process respectively.

The differences in densities are taken as a function of temperature and the salinity of the ocean waters at different depths. The warmer water forms a layer on top of the colder water due to the difference in densities in respect to the salinity of each layer which is termed “Stable Stratification”. The mixing of warm water coming from the tropics and subtropics with cooler water coming from the Polar Regions, at key areas on the planet, create the Thermohaline current. As the warm water mixes with the cooler waters from the poles the upper layer tends to sink and become denser and the cooler water rises and becomes less dense due to the exchange of salinity between the two layers of water masses, Toggweiler and Key [1]. The upwelling phase is when the cooler water is now circulated to the surface

regions. This helps bring nutrients from the deeper water to the surface which marine life feed on, Moreno, et al. [3].

The ocean currents are formed primarily by the sun's radiation into the Earth's atmosphere and the temperature difference between the equator zone and the poles. Due to the higher temperature of the equator region compared to that of the planet's polar regions, a wind-current is formed from the equator to the North and South poles respectively. The origins of the Trade Winds arise from the dense cold air which tends to migrate to regions of lower density such as the equator due to the warmer air. Another factor which contributes to the formation of wind is the Coriolis Effect which describes the wind trajectory. The wind does not follow a rectilinear trajectory due to the rotational motion of the planet. Figure 2-2 depicts how the wind moves in spiral formations, which are in opposing direction in the Northern hemisphere compared to the Southern hemisphere. The wind in the Northern hemisphere spirals in a clockwise rotation and in the Southern hemisphere in an anti-clockwise rotation. These wind spirals affect the surface water and currents of the oceans to a depth of 400 m. Tidal forces also play a role in the formation of the ocean currents. The gravitational interaction of the moon with the Earth causes the tides to rise and subside. This movement of the tides adds to the motion of the ocean currents, Anyi and Kirke [4].

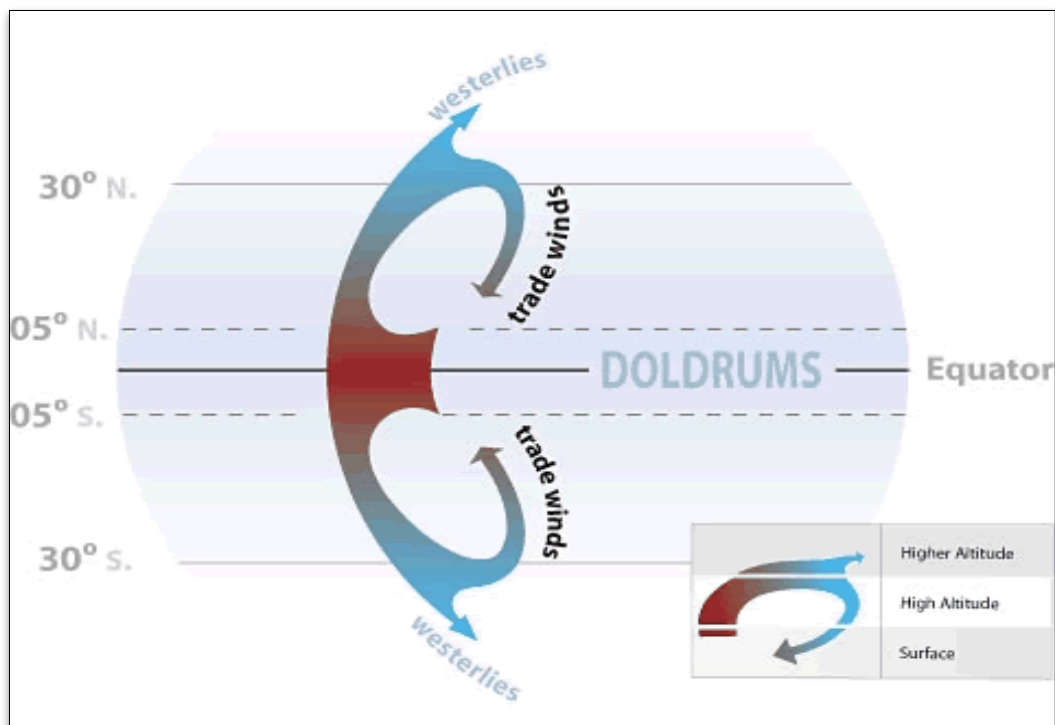


Figure 2-2: Trade Winds [4]

Figure 2-3 shows that the surface and subsurface currents produce closed loops which occur around the world transporting warm and cold water which stem from the deeper Thermohaline currents. The surface currents, being a subsystem of the Thermohaline circulation, significantly impact the weather conditions of land masses which they flow proximate to. This is due to the surface temperature of the currents which dissipate energy to the surrounding atmosphere. These currents are also used by marine life to migrate from one destination to another, be it for breeding purposes or to move over a large distance. The closed looped surface currents are directly linked to the thermohaline circulation as they assist with the mixing of the warm surface waters with the deeper waters.

The depletion of the ozone and annual increase in temperature in the polar regions can be contributed to the excess consumption of the planets fossil fuels to meet the rise in power demand of the world's growing population. Due to this, cleaner power generation technologies need to be developed to meet the rising demands in power without adversely affecting the planet. In terms of energy, the ocean currents can be viewed as a constant source of free, clean energy. As the flow of water of the currents provide an almost steady supply of linear motion, turbines can be used to convert the linear motion from the current into rotational motion. This rotational motion of the turbine can be used to generate electricity by means of a generator.

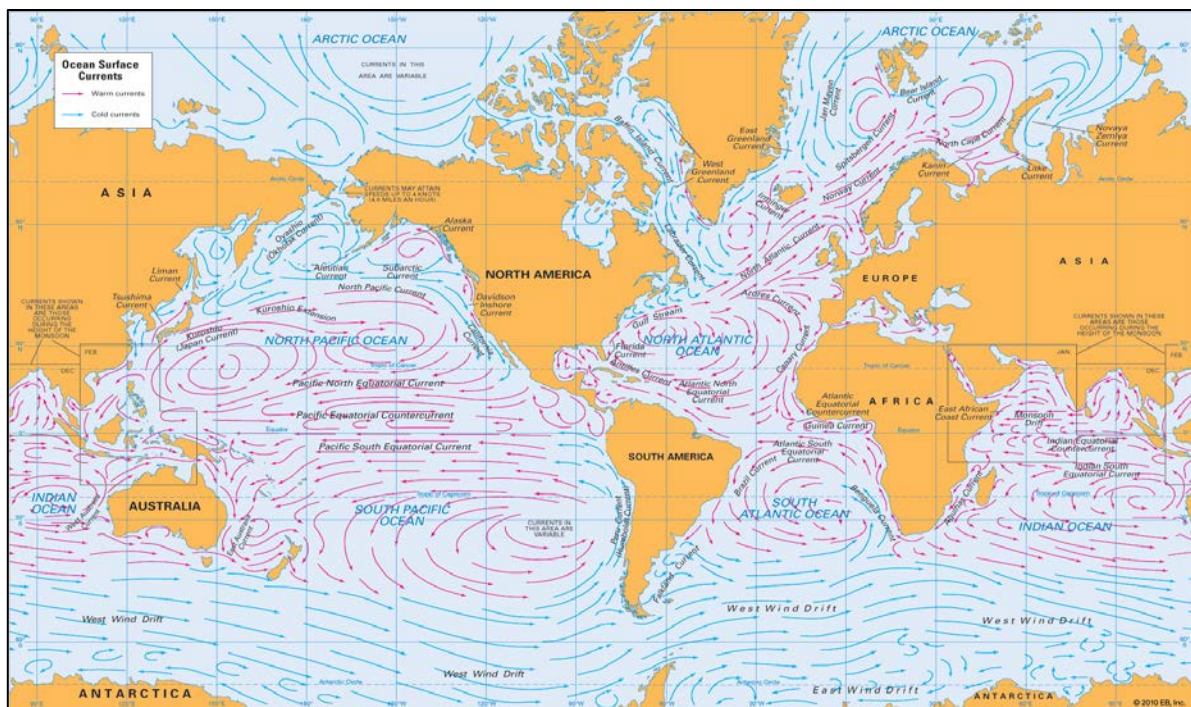


Figure 2-3: Surface Ocean Currents, [5]

2.2 The Agulhas Current

The Agulhas current was one of the first currents in the ocean to receive a great amount of scientific attention. The current was described in detail as early as 1766 by Major James Rennell who was a prominent British geographer in that period. This was followed by a wide range of Dutch and European mariners during the 1800's. The scientific scrutiny was purely motivated by nautical concerns as the Agulhas current was one of the main currents used for European vessels to travel to India and other regions which lie to the East. The Second World War was the reason why the investigations of German scientists and mariners stopped. During the past few decades the Agulhas current has been of concern but this was for different reasons, Lutjeharms and Ansorge [6].

It has been shown that the greater Agulhas current system (Figure 2-4) has a significant impact on the climate change and variability of the Southern African subcontinent. It also has been known that the current plays a key role in the exchange of water between ocean basins and thus has a key role in the oceans circulation system which directly influences global climate change, as mentioned in Section 2.1. This renewed interest in the current has sparked great scientific expeditions, research cruises, the deployment and placement of current meter moorings, satellite investigations and theoretical modelling of the flow of the current. All of these investigations have led to an increase in knowledge of the Agulhas current, Lutjeharms and Ansorge [6].

The Agulhas current forms a Western boundary circulation system in the South Indian Ocean. The Agulhas current source is interrupted however, by the island of Madagascar. Figure 2-4 shows how the island splits the source of the Agulhas which forms two minor western boundary currents, the East Madagascar current and the Mozambique drift. There exists some leakage from the Mozambique Channel of the East Madagascar current into the Agulhas current but it can be seen that most of the Agulhas current's water is sourced from the subgyre of the South Indian Ocean (Figure 2-5).

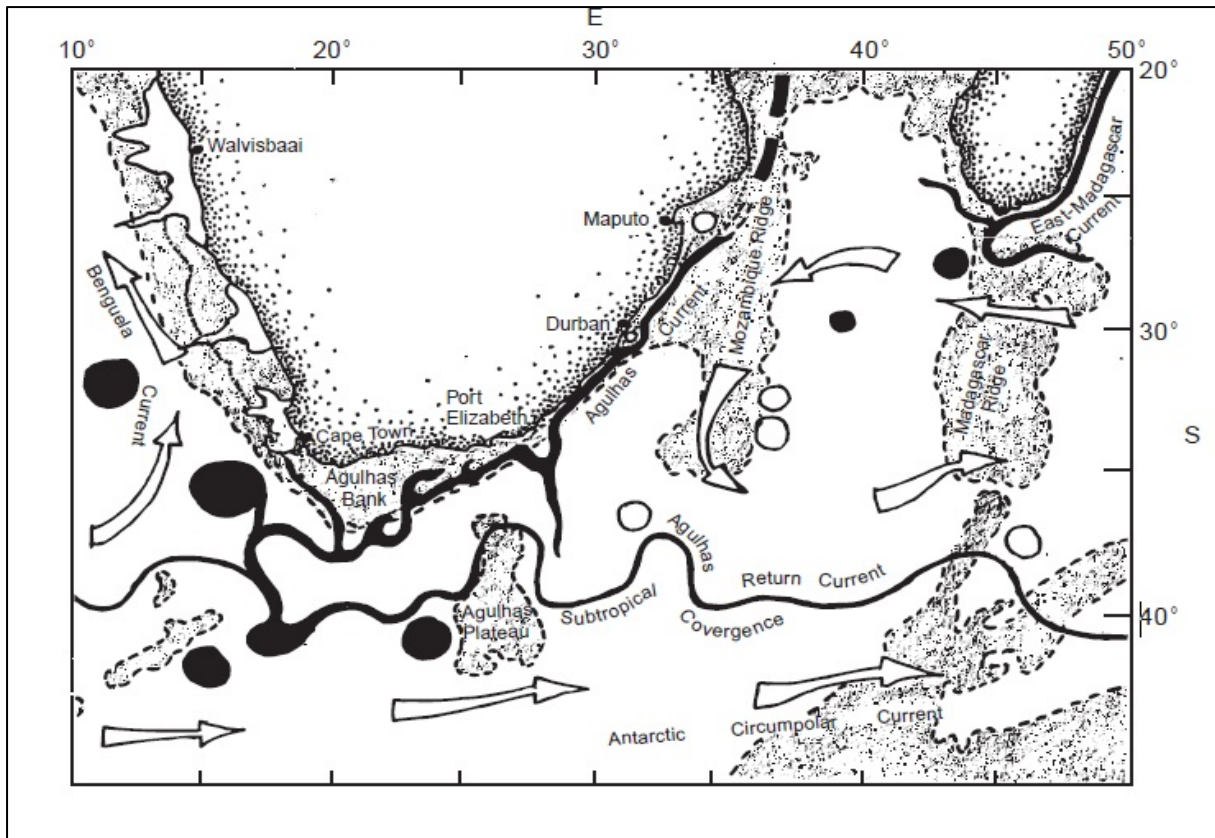


Figure 2-4: Agulhas Current [6]

The Agulhas current proper forms along the western coast of Southern Africa. This current is a warm water surface current which consists of two distinct parts being the Northern Agulhas and the Southern Agulhas. The Northern Agulhas current is seen to be the more steady current starting from the Mozambique Ridge and ending near Port Elizabeth. The Southern Agulhas current flows along a wide shelf expanse of the Agulhas Bank and flows widely in relation to the steady Northern current. The Agulhas current retroflects in a tight loop like formation and flows eastward and forms the Agulhas return current. This retroflexion loop is unstable and at arbitrary intervals can split off from the return current and form Agulhas rings or eddy structures which may have a life span of a few months. The retroflexion eddies which stem from the south of the country are sometimes also referred to as Natal Pulses. The Agulhas return current flows back into the South Indian Ocean along the subtropical convergence and is recirculated to the larger current which it is linked to, Lutjeharms and Anson [6].

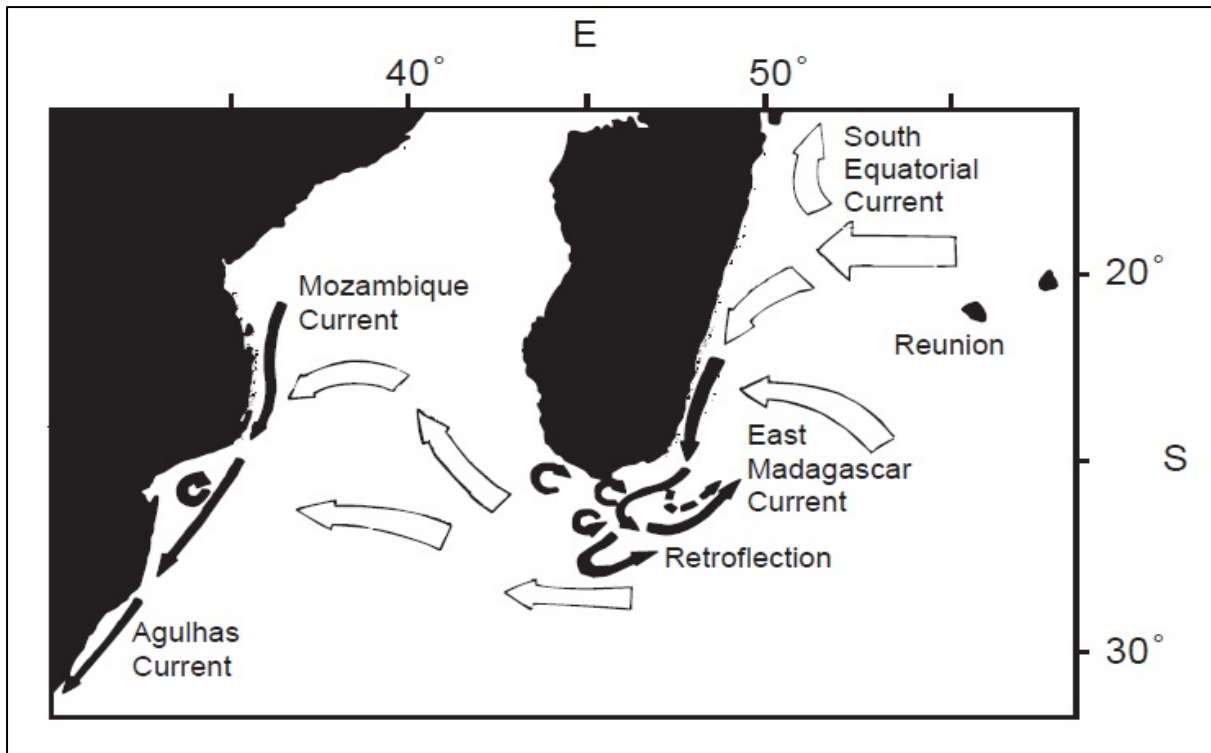


Figure 2-5: Conceptual portrayal of Agulhas sources [6]

The Agulhas current transport flows towards the South Pole and delivers the warm water from the equator to the cooler Benguela current. There also exists an under current system which hugs the continental slope on which the Agulhas flows. The undercurrent, which lies below the zero velocity isotach, transports water from the South Pole towards the equator, Lutjeharms and Ansorge [6].

The Northern Agulhas current is the more steady current due to it flowing on the steep continental shelf. The current does reverse its direction seasonally but at low speeds and normally lasts for about a week. The core of the current goes as far as 15 km to either side of the flow. At Durban the core of the current lies 20 km offshore and can be as deep as 2500 m. This shows how the surface current of the Agulhas can directly affect the Thermohaline current which exist in deeper waters. The total volume flux of the current is estimated to be 73 Sv (1 Sievert or 1 Sv translates to $1 \times 10^6 \text{ m}^3/\text{s}$) and this value is said to increase by 6 Sv for every 100 km downstream in the Northern Agulhas current, Lutjeharms and Ansorge [6]. The Northern Current is more stable south of Durban near Port Edward as results from current moorings demonstrate, Bryden, et al. [7].

2.3 Marine Current Turbines

Alam and Iqbal [8] developed a hybrid vertical axis turbine which incorporates both a drag style turbine and a lift style turbine. The design includes a coupling of a double step Savonius turbine (based on drag) and a Darrieus turbine (based on lift). The Darrieus turbine was placed on top of the Savonius turbine. This hybrid configuration vertical axis turbine outputted better self-starting characteristics than the Darrieus turbine on its own due to the addition of the Savonius turbine. The design was tested in three parts. The hybrid design was tested first then the Savonius and Darrieus turbine was tested separately in variable current speeds. The results from the testing showed mechanical power extracted to be 0.405 W for a designed 1 m/s flow. This result was low and was stated to be as a result of drag from the radial support arms and bearing friction. The turbine was not tested above 1 m/s due to unexpected vibration. The researchers concluded that the expected performance of the turbine was not achieved due to the drag of the radial arms of the Darrieus turbine section and the mechanical losses of the system. The second prototype was improved by replacing the radial arms with a more aerodynamic profile. The cut in speed of the hybrid turbine was about 0.3 m/s which indicated good self-starting qualities. The study recommends that the proper radius ratio of the turbines and positioning of the turbines need to be done in order to increase the turbine overall performance and further explains that this design can also be implemented for wind applications.

Khan, et al. [9] performed a numerical analysis on a hydrokinetic energy conversion system which was coupled with a multi pole permanent magnet generator via Matlab simulation and testing. The study focuses on electromechanical dynamics of the system. The system which is being analysed consists of a NECI rotor, a gearbox, a permanent magnet generator, power electronics for conversion of power and a simulated resistive load. Analysis of the tests data show that the turbine starts to rotate when the speed of the fluid is between 1.75 m/s and 1.85 m/s. The study shows that the start-up of the generator can be difficult due to the gearbox torque requirements and cogging torque of the generator. These are extra loads which the rotor has to overcome at start-up before energy may be extracted. The study developed suitable mathematical models which can be used to represent the system as the models correlated positively with the experimental data taken from the prototype. Khan, et al. explain that further research into the start-up characteristics of the system needs to be done. Improvement of the rotor frame and further understanding of ducting systems need to be

investigated further. Khan et al. concluded that the mathematical formulations and the MATLAB models have proven to be successful as the results from models matched the experimental results. They further state that these models can be refined and adjusted for other hydrokinetic systems.

Akimoto, et al. [10] conducted a conceptual study of a floating axis water current turbine to be implemented for low cost energy harvesting. The concept is based on the floating axis wind turbine which was proposed in previous research. The concept turbine which is being analysed has a helical profile which was first studied and later patented by Gorlov [11]. This was adopted as the helical profile turbine operates at low head and does not require dam construction which reduces the cost of the power plant. The concept turbine does not have a fixed angle of tilt but rather the tilt angle varies as the current speed varies making sure not to go beyond a tilt threshold and not reduce performance of the turbine. This concept is applicable to small scale use and large tidal and ocean current uses. The sample design analysed in the study was rated at 2 MW twin turbine configuration. The turbine design showed good economic potential.

Ikoma, et al. [12] researched the validation of computational fluid dynamic (CFD) models on a three bladed Darrieus water turbine with numerical calculations and experimental test data. The research focused on the hydrodynamic forces which act on the turbine fixed blades at various attack angles and the characteristics of the torque on the blades. These areas of interest are discussed with experimental CFD models. Ikoma, et al. [12] concluded that the computational analysis was validated by comparison with the experimental test results. The research also includes optimization of the torque performance of the turbine by controlling the attaching angle of the blades if the attack angles do not change. The control theory was done by using the blade element and momentum theory.

Yang and Lawn [13] conducted a study on the Hunter turbine. This type of turbine is a drag style turbine which is based on a similar concept to the Savonius turbine. The difference with the Hunter turbine is that the blades of the turbine are not fixed but pivot about the drum which they are connected to. Flow simulations were conducted on the turbine to determine and understand the behaviour of the blades at different drum positions. A two-dimensional CFD analysis was conducted to obtain detailed information about the flow field surrounding the turbine. This analysis included pressure and velocity contours and pressure distribution along the surface of the pivoting blades. The flow coefficient is the relationship between the

turbine blade's material density to the flow density. The study uses the flow coefficient to understand the performance of the turbine. Yang and Lawn [13] concluded that the blade opening and closing process was independent of the flow coefficient and the blades open and closing process begins at 90° and ends at 120° . For the greatest efficiency of converting the kinetic energy flow into rotation movement, the optimum flow coefficient for the Hunter turbine was found by CFD simulation to be between 0.44 – 0.47. Yang and Lawn [13] further incorporate a polynomial function to be used with the CFD simulation data to calculate the net forces acting on the turbine blades.

Zhang, et al. [14] conducted a study on the hydrodynamic characteristics of a vertical axis Darrieus turbine. The study combines experimental and numerical simulations. These models are used to test the turbine's kinematics and dynamics under simulated flow conditions. Using the results from the study performance upgrades to the turbine can be implemented. Zhang, et al. validate the CFD simulation results with the corresponding fluid dynamic governing equations and concluded that this type of turbine has good self-starting capabilities. Performance of the turbine power and structural integrity can be improved by adjusting the range of the limit angle. The researchers further explain that optimizing the attack angles of the turbine blades contributes to increasing the performance of the turbine along with decreasing the vortex formed by the rotating blades.

Niblick [15] conducted an analytical, computational and experimental analysis of a Gorlov based helical turbine for the generation of micro-power. Niblick's dissertation includes the feasibility of using micro-scale tidal generation to power autonomous oceanographic instrumentation and emphasises turbine design and performance. The components of the system are reviewed and include the turbine, gearbox, control system, convertor and battery storage bank. Niblick also developed a steady state model for a tidal resource with a peak current velocity of 1.5 m/s. The testing includes performance characteristics, freewheel stall, static torque as a function of the turbine blade azimuthal angle and performance degradation and inclination angles up to 10° and stream wise wake velocity profiles. The study also shows how the turbine efficiency increased with an increase in the flume velocity. Modelling of the free-vortex characteristics of the flow was performed and modified to simulate the helical turbine performance. The model and analytical results were compared to the experimental results for an array of strut designs and inflow velocities. Niblick concluded that the model results were validated by comparison to the experimental data but deviates under certain

conditions and also recommends further study of secondary effects for high chord-to-radius ratio turbines.

Niblick's research also laid out how to power the helical turbine and researched various generators which are currently employed by wind generators and other water generator systems. He found that the best suited generator for this type of turbine configuration is a permanent magnet generator as it can be used as a direct drive generator and does not require a gearbox or lose power due to brushes. Niblick [15] made this selection of generator as the turbine required a low start up torque and operating speeds was able to operate at maximum efficiencies at low rotational speeds. He demonstrates that there are two types of permanent magnet generators which are the radial flux and axial flux permanent magnet generators. The radial flux DC generators are the most common used generator which originates from the automotive world but if spacing requirements are little then a more desirable generator would be the axial flux generator. This is because due to the axial path of the flux more poles may be accommodated by the generator resulting in the generator being able to operate at low rotational speeds.

Biadgo, et al. [16] recognised that most of the studies which were conducted on vertical axis wind turbines (VAWTs) were based on the prediction of efficiency of the device. The research was focused on the progress and developments of aerodynamic models for studying VAWTs with an emphasis on a streamtube model approach. The study investigates a straight bladed Darrieus turbine by numerical and analytical methods using a Naca 0012 blade profile. The numerical CFD analysis is based on a two-dimensional unsteady flow around the VAWT model by solving the respective Navier-Stokes equations. Comparison of the double multiple streamtube model used for analytical analysis and numerical models was performed to validate the mathematical approach used. The results from both the models show negative performance for lower tip speed ratios. Biadgo, et al. concluded that the negative performance at lower tip speeds was due to the inability of the Naca profile to self-start.

Camporeale and Magi [17] researched a proposed mathematical model for simulating a marine current turbine. They isolated a potential site in Italy called the Strait of Messina which could be used to harness the flow resource. They have considered a vertical axis marine current turbine based on the Voith-Schneider system which utilises oscillating blades about a pivot axis. The research presents a preliminary theoretical investigation of the turbine performance that may be employed to harness marine current energy sources. The study was

conducted by means of applying a simple momentum model which is based on the “single-disk single-streamtube” approach. The results from the study were compared with experimental measurements and were found to be in adequate agreement with the experimental. This proved that by applying the simple approach taken by the researchers, an adequate prediction of turbine performance can be accomplished by means of mathematical modelling.

Goundar and Ahmed [18] recognised that the Pacific Island Countries have a large potential for renewable energy to cater for the region’s energy demand needs. The researchers recognised that Fiji has a large amount of marine current streams which are available to be exploited by suitable marine current turbines. They concluded that a horizontal axis marine current turbine would be adequate to generate electricity from the available streams. In order to complete the design, Gounder and Ahmed conducted a resource assessment of the region’s waters and found a suitable site named Gun-barrel passage. At the site which was identified they deployed and read data from an acoustic current doppler profiler (ADCP). The researchers found, from the data, that a turbine with a diameter between 5 and 8 m would be suitable for energy extraction at this particular site and based their turbine design on this.

2.4 Ducted Turbines

Kirke [19] performed tests on ducted and bare helical and straight blade profile Darrieus hydrokinetic turbines. The vertical axis hydrokinetic turbines are advantageous in some ways compared to axial turbines but they also have disadvantages. Some of the drawbacks include issues such as the inability to self-start under load conditions, low efficiency and vibration. This however can be reduced by means of variable blade pitch for the straight blade Darrieus turbine which increases starting torque and turbine efficiency, ducting of the turbines which increases the power output substantially and helical profile blades which produce a smooth torque compared to the Darrieus straight blade design. Testing of the turbines were conducted in Australia and Canada by mounting each configuration separately on a barrage and toed in still water. The water speeds ranged from less than 1 m/s to 5 m/s. Kirke concluded that the diffuser increased the power factor by a factor of 3 compared to the turbine without a diffuser but this was not reflected with all the turbine designs and the cost effectiveness of a diffuser system was doubtful. A fish screen was also implemented applied to the turbine configuration without a diffuser. The screen reduced the flow area and thus efficiency of the turbine. The study also showed that marine life was not harmed by the hydrokinetic turbine and the

ecosystem surrounding or further downstream from the turbine was not affected, which is normally the case with hydropower stations. Kirke's study recommends that further investigations into variable pitch turbines without a diffuser and fish screens need to be conducted.

Davis [20] summarises work which has been conducted in the field of vertical axis water turbines, identifies potential hydro-energy harvesting sites, areas of design for the Davis turbine, project development and financing for the project. The Davis turbine is based on the Darrieus turbine and hence is a lift type water turbine. The turbine is housed in a concrete frame which serves as a ducting system. In the study, Davis proposes to use a tidal fence to harness the maximum amount of power from the resource. A tidal fence has a rectangular cross section which can hold multiple turbines. With the turbines placed above each other, one main rotating shaft can be used to couple all the turbines. The shaft is fixed on the top and bottom of the fence as well as the top and bottom of the turbines to eliminate vibration. The tidal fence also serves as a duct to increase the flow of the tidal resource. For the field testing a variable speed generator was used as the tidal resource flow was not constant.

Research conducted by Ponta and Jacovkis [21] was based on trends which can lead to feasible marine current power generation for the future and introduces a more technological solution to help emerging projects reach that goal. The paper focuses on floating marine current technology and power generating systems and introduces conceptual innovations to improve technical and economic measures of the technology. Ponta and Jacovkis researched the effects of a diffuser augmented design with a hydrokinetic turbine. The diffuser would increase the velocity of flow entering the turbine which thus increases the amount of energy which may be extracted. The results show that a ducted system would increase the output power of a typical marine current turbine compared to a non-ducted system. The idea of a ducted system would be highly beneficial to the vertical axis helical turbine being discussed in this report.

Ponta and Shankar Dutt [22] conducted a theoretical and practical study on a channelling device to aid a floating water current turbine system. This system would increase the power output of the turbine due to the increase of flow velocity through the turbine. The main advantages of a floating channel aided system were the reduction in need of fixed civil works which could be highly detrimental to the environment, ease of transportation and relocation of the device and predicted low cost system with a long life time which reduces the cost on

frequent maintenance. This does not however mean that the system should not be carefully monitored. The study further models the channel being used for the system as an open channel and analyses the Froude number as a function of velocity in the neighbourhood of the rotor. The results show that for the selected channel device the Froude number does not reach critical flow conditions and the Froude number remains below one in the position where the rotor would be situated. This is needed so as to decrease the effects of wave turbulence on the existing vortices which are created by the turbine.

Luquet, et al. [23] studied a new marine current turbine design which incorporated a ducted rotor. The study which was conducted on couples of water turbines fixed on a rotating arm free to rotate about a vertical axis fixed on the seafloor. This meant that the turbine could have an asymmetric design and be fully optimised as well. Another unique aspect of the project was to incorporate a ducting mechanism which allowed for the increase in flow velocity which enters the turbine. To validate the study the analysis required calculation and experimentation of the device. The turbine output via the incorporated ducting mechanism was modelled using Reynolds Average Navier-Stokes calculations to understand the impact of the incoming flow rates to the turbine. From the ducting it was found, by the researchers, that the flow velocity reached 1.4 m/s entering the turbine. A scaled model was constructed for both the horizontal axis turbine and two ducting mechanisms. A specific test setup was developed to simulate flow conditions for the constructed model turbine. The numerical simulation was validated from the experiments which were conducted. Optimisation to the system was done and the final results lead to the turbine obtaining a performance coefficient of 0.75.

Giles, et al. [24] present research which was conducted on a preliminary experimental investigation which examined the potential of increasing flow by means of a foundation based flow acceleration system to marine current turbines. The structures would provide multiple benefits including increased turbine power output, foundation foot print and scour protection to the device. The experiments on such a system were conducted in two phases, first being a series of tests which were caused by a ramp foundation without the turbine and second with the addition of a commercial marine current turbine with a gravity based ramp foundation. The first phase of experiments were scaled on a shallow tidal flow site and the results proved evidence that the system could provide power benefits of 12 to 25% depending

on the ramp size and flow depth. The researchers formulated an optimum ramp size based on the vertical velocity profiles for energy extraction.

2.5 Marine Current Turbines with Blade Variation

Yang and Shu [25] conducted a study on the optimization of hydrofoils which are used for a helical vertical axis turbine for increased performance. The optimization was achieved by means of traditional generic algorithms and a hierarchical computational model. Yang and Shu used a Bezier curve to parameterize the marine current hydrofoil and numerical analysis was conducted to evaluate performance of the turbine. The lift to drag ratio is discussed in detail in the study. Performance and computational tests were conducted to compare the optimised hydrofoil to that of other competitive hydrofoils. The experimental results verify that the optimised hydrofoil is more suited for marine current turbines and also is of benefit to turbine efficiency and can be seen as a positive prospective hydrofoil for the vertical axis helical turbine.

Shino, et al. [26] conducted a study on the output characteristics of a Darrieus water turbine with helical blade profiles. The study was conducted via hydrographical testing of various helical turbines and the results compared to that of the straight blade Darrieus turbine. Shino, et al. concluded that the helical turbines with different inclination angles do not affect the turbines start characteristics but the solidity of the turbine does. The torque on the turbine and subsequently the efficiency of the turbine increases with an increase in inclination angle of the turbine blades. The helical turbine however, was found to be best suited as the helical bladed turbine has a lower pulsation rate than that of the straight bladed Darrieus turbine.

Rossetti and Pavesi [27] conducted research on the different numerical methods used to analyse wind turbine self-start up characteristics. The analysis of the start-up characteristics of a turbine is of importance as this allows one to design and obtain a turbine which would require much less effort to extract energy from the flow medium. In the study the blade element momentum model was compared with a three-dimensional CFD model. Results of tip speed ratio versus power coefficient and the development of thrust coefficient highlighted the strengths and limitations of each of the mathematical predictions. The study compares the difference in 3D and 2D approaches in CFD analysis and further explains how 3D simulations, although more computationally expensive, show tip effects which have a

positive influence on the start-up of the turbine by increasing the torque coefficient for a tip speed of 1.

Gazzano, et al. [28] conducted their research to optimise the performance of a vertical axis wind turbine by means of obtaining the optimum blade pitch angle for the system in a cyclic manner. The concept ideas which lead to the investigation are better known as the “Giromill” and the basic principles were then applied to the Darrieus straight bladed turbine. The objectives of the study were to increase the performance of the Darrieus turbine by means of obtaining a suitable pitch angle formula and measuring the self-start characteristics of the turbine under the influence of a varied blade pitch. Gazzano, et al. concluded that by applying the cyclic changes in blade pitch, the turbine efficiency may be increased to a limit less than 30%. The understanding of blade pitch was used in the development of the turbine which was analysed in the current study.

2.6 Dynamic Stall and Vortex Structures

Research conducted by Ekaterinaris and Platzer [29] utilised a computational method for predicting dynamic stall on an airfoil. Wind turbines, turbo-machinery and flight vehicles rely on empirical methods for predicting dynamic stall on the aerofoils being utilised. In the case of a vertical axis hydrokinetic turbine, the phenomena of dynamic stall is prevalent and is required to be taken into account when developing such a turbine. The research expands on the approach methods utilized and results obtained and outline the deficiencies and possible avenues of improvements. The research describes the extent of the boundary layer, potential flow and the Navier-Stokes equations which are currently in use in the computational analysis of an airfoil. The various turbulence models which are used in the computational domain are briefly described and the mathematical formulations were expanded on in relation to each model’s development.

Rodríguez, et al. [30] conducted their research on the dynamic stall effects which occur on a symmetrical NACA 0012 blade. The researchers investigated the different mechanisms of flow separation across the blade and the transition to turbulence along the profile. Whilst monitoring this effect they also monitored the structures which were formed in the turbulent region with respect to low Reynolds numbers. It was found that at low to moderate Reynolds numbers, the flow separation occurs on a combination of the leading and trailing edge of the blade on the suction side. The results show that the vortices which were formed due to the

flow separation along the blade which is shed downstream of the blade and form, what appear to be a structure similar to a von Karman vortex street.

Mureithi, et al. [31] developed a simple mathematical model for a 2 Dimensional analysis of the von Karman vortex structure in a shedding wake formation. The overarching goal of the research was to develop a model which can approximate the behaviour of the nonlinear dynamics. The simple model could not replicate the complex, varying, Navier-Stokes equations and opted for the replication of the sequence of bifurcation from an oscillating blade. Under various circumstances the results proved too complex and sometimes chaotic wake structure formations. It was concluded that the model provides adequate insight into the complex domain of vortex creation and analysis and much can be learnt of the prediction of the bifurcation sequences in comparison to that of a 3 Dimensional model. The von Karman vortex street was an aspect of interest in relation to that of the vertical axis turbine as the cylindrical shape outputs a vortex structure similar to that of a von Karman vortex. However, if a simulation was conducted and outputted the same vortex structure as that of a cylindrical obstacle, it would prove that the simulation was not that of a rotating turbine.

Gim and Lee [32] studied the vortex structure around a NACA 0018 blade profile using a PIV flow method of visualisation in a recirculating water channel. The study analyses the blade profile subject to varying angles of attack. Velocity profiles are obtained for 1 chord length to 3 chord lengths which are measured from the trailing edge to understand the shed vortices. The authors concluded that vortex formation was changed at the end of the profile due to the roll-up phenomenon. The authors concluded that the attachment of an airfoil onto an endplate significantly stabilizes the Reynolds shear stress and decreases the affects from tip vortices. The Reynolds shear stress decreases with attack angle of 10° and 20° in the wake region. Along the leading edge of the foil a strong clockwise rotating vorticity emerges and towards the trailing edge a counter clockwise vorticity was generated.

It can be assumed that the pitch angle of a turbine can reduce the effect of dynamic stall on a turbine. Sarkar and Venkatraman [33] studied the effect of oscillating an airfoil profile between two different attack angle ranges at the same frequency. The work which was conducted indicates the behaviour of dynamic stall on the blade as the angle of attack changes which also changes significantly in relation to that of a pitched turbine blade. It was found that the variation in pitch angle does affect the dynamic stall on the blade as a higher attack angle range results in a stronger vortex structure formation from the leading edge of

the blade compared to that of the lower range of attack angles. By increasing blade pitch (Toe-Out), one seemingly reduces the range of attack angles which the blade can experience which impacts the dynamic stall on the blade.

Wang, et al. [34] conducted similar research to Sarkar and Venkatraman with respect to the effects of oscillating an airfoil blade, at low Reynolds numbers, on dynamic stall. A 2 Dimensional computational model was simulated for a NACA 0012 blade at a Reynolds number of 10^5 . The CFD analysis implemented two different sets of oscillating patterns; varying frequencies, mean attack angles and amplitudes of the blade were numerically solved. The researchers concluded that the CFD simulation captured the vortex structure adequately in comparison to that of the data which was captured experimentally. However, the results of the simulation do not have good agreement when the blade is at relatively higher Reynolds numbers.

Urbina, et al. [35] conducted a study on the effects of implementing a modified Beddoes Leishman into the free vortex method. This model was used to predict the performance for a Darrieus straight bladed turbine. The model incorporates the considerations which were concluded in the work conducted by Wanan, et al. [36]. The considerations outline the reduced pitch rate and its influence on dynamic loading over the airfoil. Sheng also revised the Kirchhoff flow equations for the calculation of the lift and drag coefficients for the blade. The researchers found a good comparison of their results to those of published and experimental research.

Wang, et al. [37] compared the model which was developed to that of other more commonly used numerical models for application on a vertical axis hydrokinetic turbine with varying blade pitch. The researchers had developed a potential flow model incorporating a 2 Dimensional vortex panelling method. It was found that the numerical results which outputted the instantaneous blade forces and the wake flow were in good agreement to that of the test data which was captured. The model which was developed was compared to that of the classical free vortex model and to that of a finite element model. The comparison proved that the model had good agreement, and was a simpler model than the previous two and would be far more suitable for the design and optimisation of a straight bladed vertical axis turbine

CHAPTER 3 TYPES OF OCEAN ENERGY

There are many ways of harnessing and extracting energy from the ocean. To understand these various methods one needs to first understand the various types of ocean resource which can be exploited. There are four main types of resources which may be exploited for energy harnessing purposes. They are the kinetic energy from waves; the thermal energy which arises from the thermal gradient difference of the upper and significantly lower ocean depths; the ebb and flow of variances on the ocean's tides, and; the ocean currents which have a tendency to be steadier than tidal currents as they are mostly influenced by the thermohaline circulation current. The following chapter expands on each type of energy resource in greater detail.

3.1 Wave Energy

Ocean waves represent a form of renewable energy which is created by wind currents passing over open water. The wind currents are created by the interaction of the sun's thermal irradiation entering the earth's atmosphere and impacting the ocean's surface water. As stated previously, the atmosphere is warmer in the equatorial regions and cooler in the polar regions. The winds are created as the warmer air travels to the poles and the trade winds arise as the cold, dense, polar air migrates towards the equatorial regions. The friction interaction of the wind on the surface of the open water transfers some of the kinetic energy of the wind to the water which results in the formation of waves. The wind energy is compounded and transferred to the wave which stores and transmits the energy along the ocean surface. This process can be seen in Figure 3-1 below. Once created the waves can travel immense distances (in the range of thousands of kilometres) with little energy being lost [3, 6]. The energy is only affected when the waves encounter opposing directional winds which tend to dissipate the energy in the wave due to surface friction.

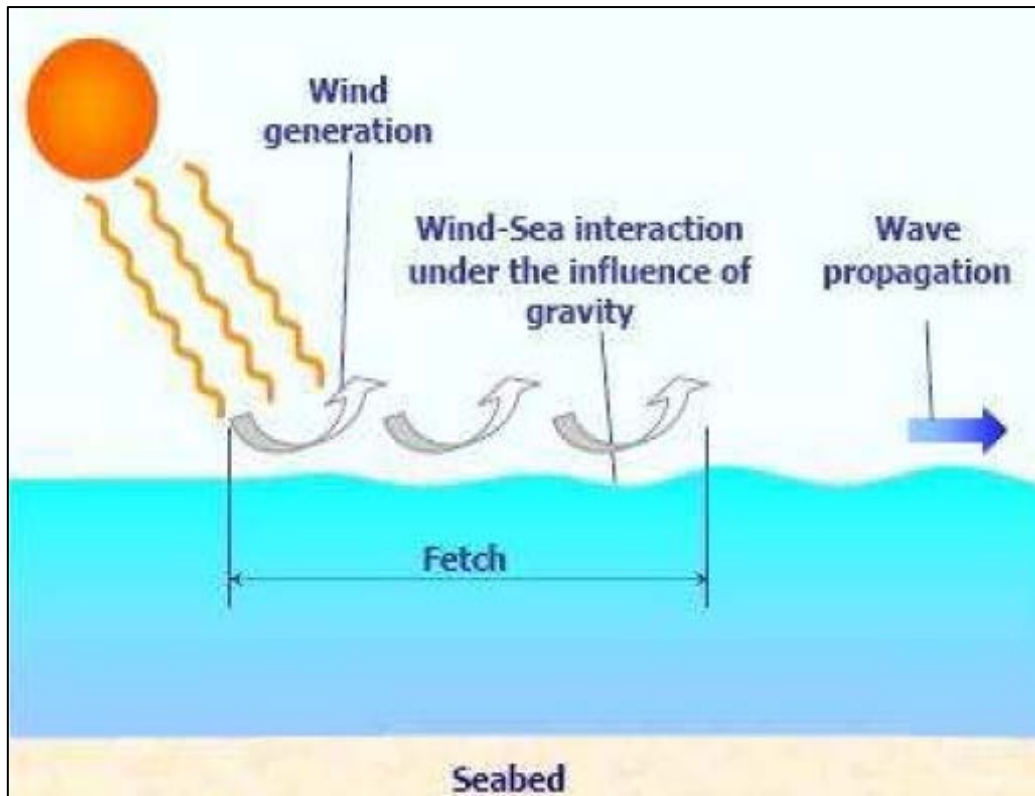


Figure 3-1: Formation of waves, Moreno, et al. [3]

Wave energy is strongest in the latitude band of 30 to 60 degrees from the equator which is depicted by Figure 3-2 [3, 6, 38]. This is due to the high concentration of wind which exists in this latitude band. Wave energy can be broken down into two forms of energy which is shown in Figure 3-3. The types of energy which exist in the wave are kinetic energy of the water molecules within the wave structure (which generally flows in circular formation) and the potential energy of the water molecules when the wave is at its highest point [3, 6]. The total energy contained within a wave structure depends on the linear length of the wave crest, the wave height and the wave's period through the ocean. The kinetic energy which is in waves is estimated to be thousands of times greater than that in wind energy. This can be due to the fact that the energy which is stored in a wave is higher than that of wind because the density of water is roughly 800 times more dense than air, Moreno, et al. [3].

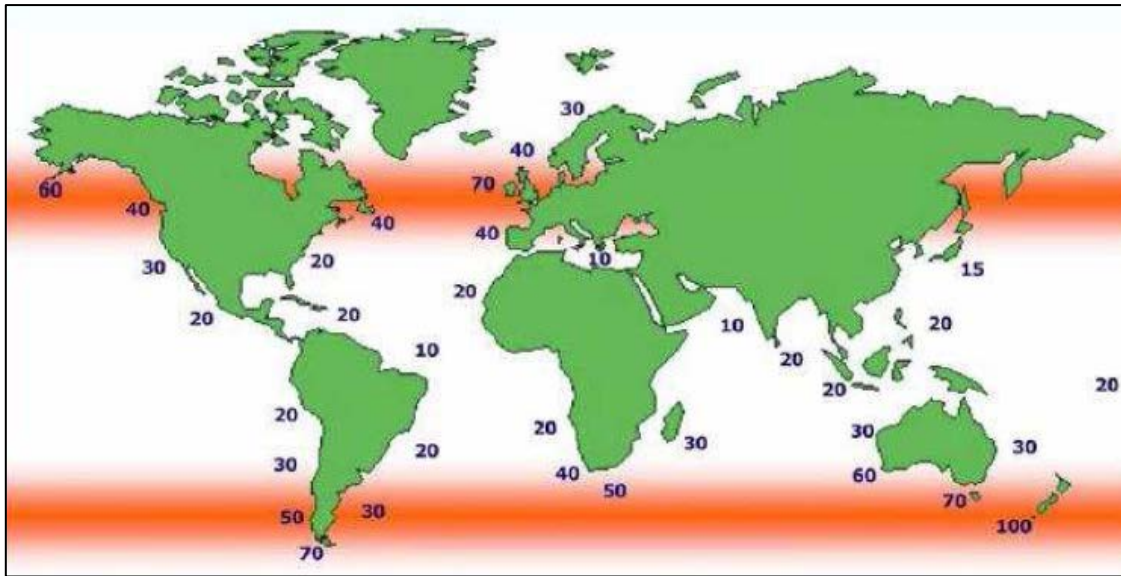


Figure 3-2: Areas of high kinetic wave energy, Moreno, et al. [3]

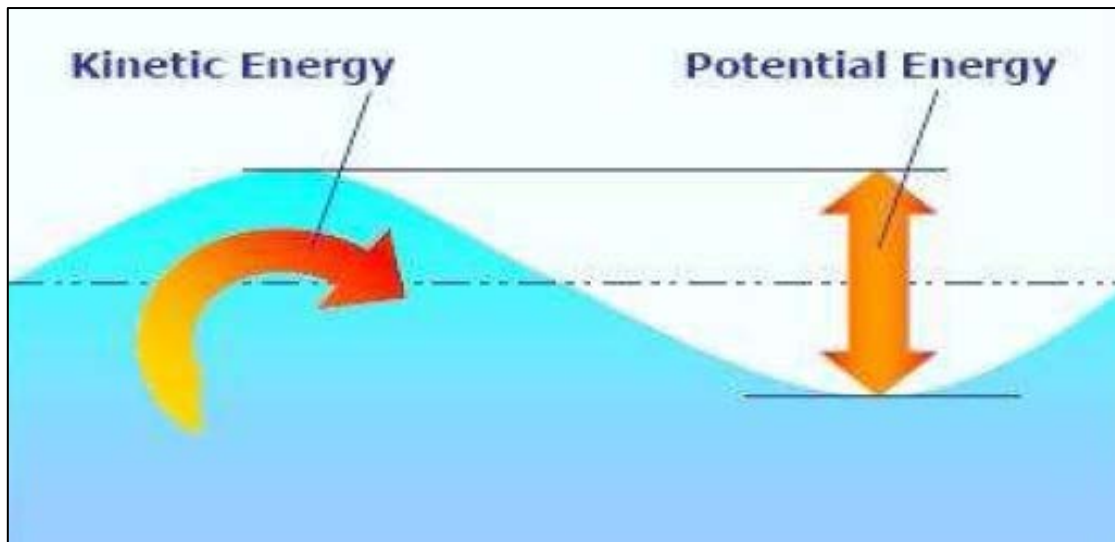


Figure 3-3: Kinetic and Potential energy of waves, Moreno, et al. [3]

Wave power density is accepted as the measure of natural wave energy, which is found in wind generated waves, Lutjeharms and Anson [6]. Wave power density is defined as follows:

$$\text{Wave Power density} = \frac{P}{L} = k H_s^2 T_z \quad (3.1)$$

where:

P	Power within the wave (kW)
L	Linear crest length (m)
k	Constant for waves
H_s	Significant wave height (m)
T_z	Mean zero crossing wave period (s)

Studies of the ocean which have been conducted, demonstrate that the ocean has approximately 290 GW of power which can be extracted or 29,500 terawatt-hours per annum (TWh/yr), [3, 6]. These values are inclusive of both the kinetic and potential energy of the waves. The values indicate a theoretical model of power within the ocean which does not take into account the practicality of extraction of the power. The amount of power which can be extracted will be determined directly by device interaction within the resource of the wave field, the machines' efficiency of extraction, environmental restrictions due to device impact on the environment, priorities such as fishing and shipping lanes and visual aesthetics, Lutjeharms and Anson [6].

3.2 Ocean Thermal Energy Converters (OTEC)

The ocean covers two thirds of the planet and this means it is the largest body that absorbs solar irradiation and thus the solar irradiation heat content within the ocean is high. The radiation from the sun warms the upper surface of the ocean and thus forms a temperature gradient between the upper and lower waters of the ocean. The regions of operation of an OTEC cycle are within the tropical, subtropical regions and equilateral regions as shown in Figure 3-4 [3, 39].

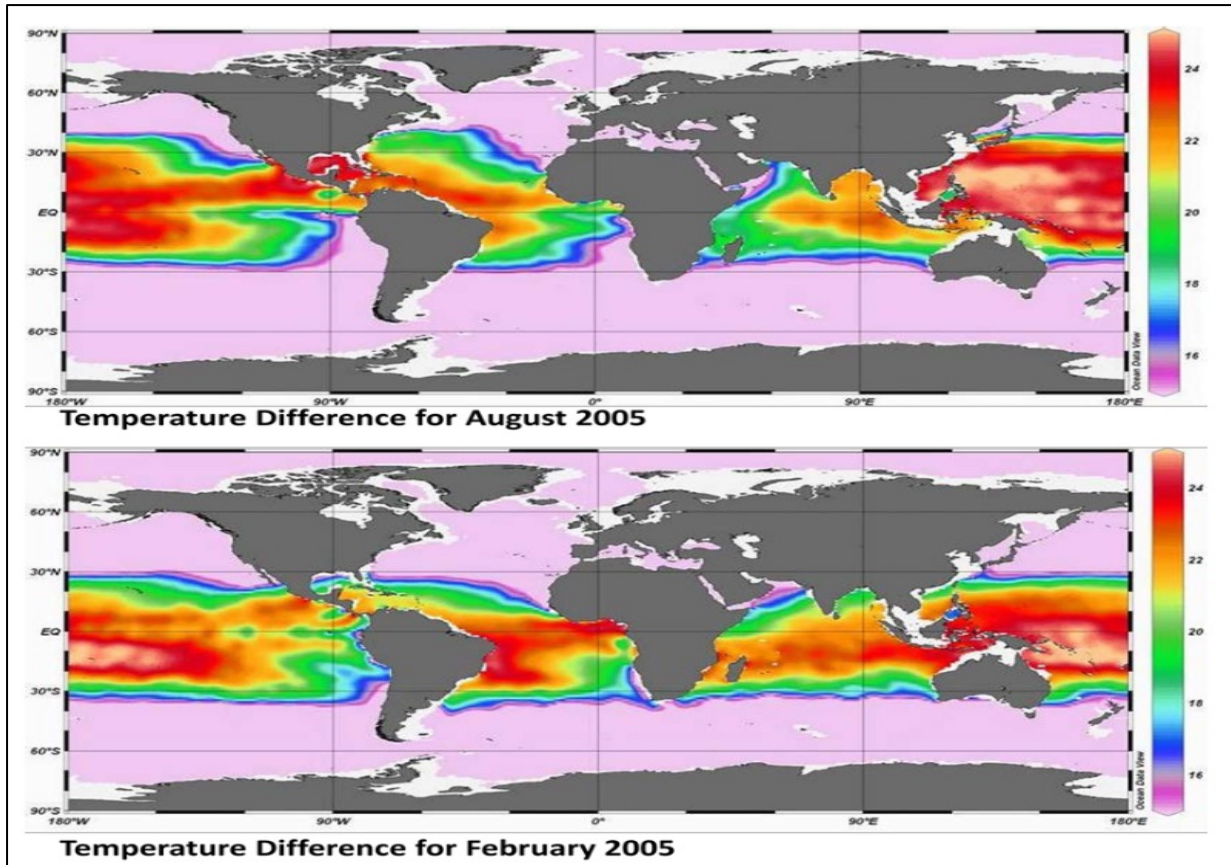


Figure 3-4: Latitude band of Ocean Thermal Concentration [5]

The ocean thermal energy process can be viewed as a thermal machine. This machine obtains thermal energy by using the temperature difference which exists between the upper warm, surface water and the lower cold, deep ocean water. The warm water from the surface can be used to vaporize a fluid with a seemingly low boiling point (Closed Cycle). The evaporated fluid expands through a turbine which extracts the energy from the fluid. The saturated fluid is condensed and either recirculated (Closed Cycle) or returns to the source or is used for desalination purposes [39-41].

To understand the amount of power an OTEC plant can produce two equations need to be understood. These equations have been derived due to previous studies on a modified temperature field within the OTEC temperature or latitude band, Faizal and Ahmed [41]. The OTEC power density P_{net} , can be determined from the following formulas which will give an estimate of the power output of the plant:

$$P_{net} = w_{cw} \frac{3\rho C_p \varepsilon_{tg} \gamma}{16(1+\gamma)} \frac{(\Delta T)^2}{T} - P_{Pump} \quad (3.2)$$

$$P_{Pump} = w_{cw} 0.30 \frac{3\rho C_p \varepsilon_{tg} \gamma}{4(1+\gamma)} \quad (3.3)$$

Where:

w_{cw} OTEC equivalent deep seawater vertical velocity (m/s)

ρ Average seawater density (kg/m³)

T Absolute temperature of OTEC warm seawater (K)

ΔT OTEC seawater temperature difference between surface and 1000 m depth (°C)

C_p Seawater specific enthalpy (J/kg K)

γ Ratio of OTEC surface seawater flow rate over OTEC deep seawater flow rate

ε_{tg} Combined OTEC turbo-generator efficiency

The power density which is described in Equation 3.3 is the auxiliary power which is associated with pumps that pump water to the evaporator and the condenser or the pump which is used to circulate the refrigerant in the closed cycle process. It can be seen that the power of the pumps is estimated to be 30% of the gross power output of the plant, Rajagopalan and Nihous [40].

3.3 Tidal Energy

Tidal energy is the energy produced from the ebb and flow of the tides which occur on a daily basis. The phenomenon occurs due to the gravitational and centrifugal forces illustrated in Figure 3-5 which are exerted onto the earth by the interaction of the earth, moon and sun, [42, 43]. The tides can be visualised as the regular rise and fall of the of the ocean's surface due to the gravitational forces that come from the sun and the moon on the earth. The centrifugal forces are produced by the rotation of the earth and moon about each other. The gravitational force of the moon which acts on the earth is estimated to be 2.2 times larger than the sun's gravitational force, Rourke, et al. [43].

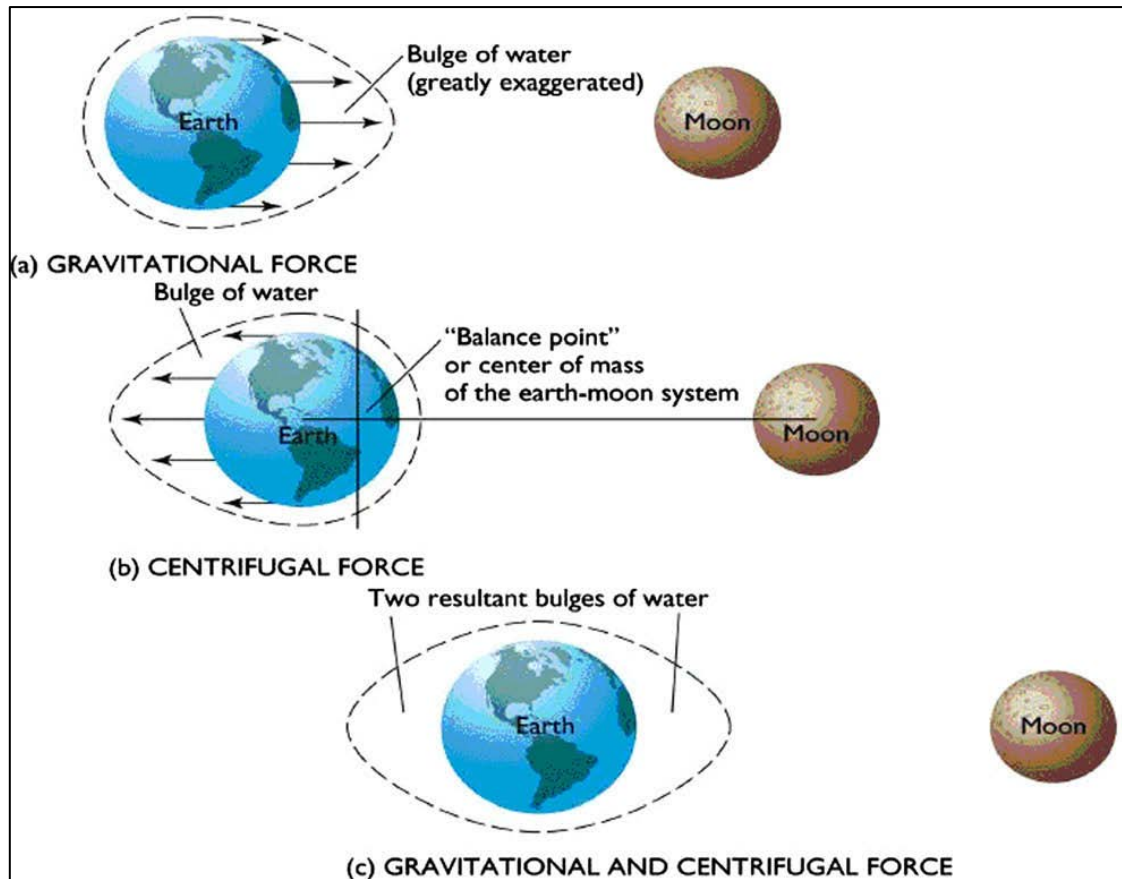


Figure 3-5: Forces which produce tides Clarke, et al. [10]

The tidal phenomena occur twice a day. The tides are formed as a bulge of water is created by the gravitational force on the earth and is greatest on the side that is closest to the moon. At the same time the centrifugal forces of the earth and moon system are acting on the ocean due to their rotational dependence. This relationship causes a bulge to form on the other side furthest away from the moon, Rourke, et al. [43]. When a landmass on earth comes into line with the earth-moon system the surrounding water is at high tide and when the landmass is perpendicular to the system the surrounding water is at low tide. This shows that every landmass experiences two tides, high and low, during each period of rotation of the earth, Clarke, et al. [44].

The moon orbits the earth every 29.5 days known as the lunar cycle. Tides vary during the year and in size between spring tides and neap tides. Spring tides are tides which occur when the sun and moon line up with the earth, whether they are pulling on the same side or on opposing sides of the planet which results in very high tides. Neap tides are tides which are formed when the sun and moon are perpendicular to one another which result in lower tides, Clarke, et al. [44].

Tidal currents occur in coastal areas and in places where the sea water has to flow through narrow channels. These currents flow in two directions, namely, the current which flows in the direction of the coast or towards the coast known as the flood current and the current which recedes from the coast known as the ebb current. The speed of the current varies in both directions from zero velocity to a maximum. The zero velocity speed refers to the slack period that occurs as the currents are changing. The maximum current occurs between the slack periods. The tidal variations of rising and falling tides and the currents can be harnessed to produce electricity, Clarke, et al. [44].

3.3.1 Types of Tidal Energy

The tidal energy which can be harnessed consists of kinetic energy and potential energy. The types of extraction however, can be broken up into two main types. These types are tidal barrages and tidal current turbines. These technologies use the potential and kinetic energy of the tides respectively [39, 43].

3.3.2 Tidal Barrages

The tidal barrage system of harnessing energy utilizes the potential energy of the tides. This system can be related to a dam which is constructed across a bay or estuary that experiences a tidal range in excess of 5 m. The electricity production from tidal barrages work on the same hydrokinetic principle as a dam would employ. A typical barrage would consist of turbines, sluice gates, embankments and ship locks. There are various different types of turbines which are used in tidal barrages which may range from unidirectional, bi-directional, rim turbines, bulb turbines and tubular turbines. The tidal barrage system can further be broken down into two types which consist of single basin barrages and double-basin systems, Rourke, et al. [43].

Single Basin Barrages

Single basin barrages use one basin and require a barrage across a bay or estuary. This method of operation has three methods of electricity generation within the single basin which is ebb generation, flood generation and two way generation [39, 43, 45].

Ebb generation is when the basin is filled with ocean water through the sluice gates during the flood tide period. The water is trapped in the basin when the gates are closed which

creates potential hydrostatic head for the turbines to extract energy from. When the water is trapped more water can be pumped into the basin when electricity demand is low which is typically at night. The gates are only opened when the tide has ebbed sufficiently to create a substantial hydrostatic head across the barrage [43, 46]. The water is allowed to flow through low-head turbines which generate electricity constantly until the hydrostatic head has depleted [39, 43].

Flood generation is when the sluice gates and turbines are closed off from the flood tide and a hydrostatic head is created by the barrage wall as the tide rises. The energy from this is extracted once a sufficient hydrostatic head is achieved by means of water flowing through the turbine and into the basin. This method of energy extraction is not favourable due to the impacts which it creates on shipping and the surrounding environment. These impacts are caused by the decrease in sea level within the basin, Rourke, et al. [43].

Two-way generation utilises both the ebb and flow of the tides to generate energy. The turbine sluice gates are kept closed until near the end of the flood cycle. After this point the water is allowed to flow through the turbines situated in the walls of the barrage. At high tide the sluice gates are closed and water is trapped behind the barrage to create a hydrostatic head for power generation as in the ebb generation. The water is released so generation occurs during the ebb mode. Two-way generation has an advantage in reduced periods of non-generation and in cost of generators due to low peak power [43, 45].

Double-Basin tidal barrages

The double basin system consists of two basins. This system works basically the same way an ebb generation single basin system works. The difference between the two is that a proportion of the energy generated during the ebb phase of the tide is used to pump water into the second basin. This means that the barrage uses the element of storage which can adjust delivery of electricity to match consumer demand. The advantage of this is that the system can deliver electricity at periods of high demand. This system however, is unlikely to become feasible due to the inefficiencies of low-head turbines. The feasibility of the system is also restricted due to the extra length of the barrage [39, 43, 45].

Electricity production using tidal barrages can be viewed as a mature method and various tidal sites worldwide are considered suitable for development; however are only four tidal

barrage plants operational at present. These four tidal barrages are further described below, Rourke, et al. [43].

3.4 Marine Current Turbines

Places which demonstrate high hydrokinetic tidal energy occur in areas that have relatively narrow passages between oceans and large estuaries or bays. This is because as the flow of water passes through the narrow passages, it has to accelerate to conserve mass flow along the passage way. By this conservation the velocity at the depth in which the flow accelerates subsequently increases. Another factor is that depending on the size of the estuary or bay in relation to the passageway with which it makes contact, a dynamic resonance may occur and thus result in a higher velocity profile for the water flow. The combination of these two processes can result in a high kinetic energy flow and this is ideal for harnessing to produce electricity, Thresher [47].

Tidal current turbines or marine current turbines utilise the surface currents which are generated due to the changes in tides and centrifugal forces which act on the planet from the earth-moon system. The energy is extracted from the kinetic energy of the flowing water. Tidal current turbines may be visualised as wind turbine technology which is implemented in the ocean. Tidal current turbines, however, have several differences in operating conditions. This is because the medium in which it operates (sea water) is approximately 832 times denser than that of air [43, 45].

Since the tidal current turbines operate in a denser medium than air, the turbine as a whole experiences greater forces and moments than that of wind turbines. The tidal current turbine must be able to generate electricity during the ebb and flow tides and also withstand high structural loads when inactive, Rourke, et al. [43].

No matter the design of the turbine which is to be used, a tidal turbine can only harness a fraction of the kinetic energy of the flow. This is because certain laws of conservation have to be met. The extractable power of the tidal current can be expressed by the following equation:

$$P = \frac{1}{2} C_{power} \rho A U_{\infty}^3 \quad (3.4)$$

where:

P	Hydrodynamic power (w)
C_{power}	Power coefficient of the turbine
ρ	Average fluid density (kg/m ³)
A	Cross-sectional area of the flow

Equation 3.4 depicts the amount of power which can be extracted from the tidal flow. It can be seen that the extractable power is dependent on the turbine's power coefficient (C_p), the density of the flow medium (ρ), the swept area of the turbine (A), and the mean velocity of the water (v). The theoretical upper limit for the coefficient of power for the turbine is taken as 59% of the fluid resource medium according to the Betz limitation. The coefficient of power changes with different turbine designs which means that the amount of power is directly affected by this variable, Lundin and Leijon [38].

A marine current turbine consists of various complex components. These components are the turbine blades which come in direct contact with the flow medium. The turbine blades are the components which use the flow to cause a pressure difference on either side of the airfoil profile creating a force to be induced onto them, so the resultant force on the blade profile causes rotational movement. Being attached to a rigid system the blades rotate the rotor which is situated at the centre of the blade structure. The rotating movement of the shaft is passed through a gearbox, in most cases, to increase the amount of revolutions of the moving rotor. The output of the gearbox is directly coupled to a generator which is used to generate electricity and this is transferred to the desired location via electricity cables.

The tidal current turbine is still in its infancy and the focus in this field of power generation is on product design reliability. Recent technological advancements have resulted in scaled down models and full-scale prototypes which are launched to conduct testing. The first dedicated test centre, The European Marine Energy Centre (EMEC) is located in Orkney, Scotland, and has been operational since May 2005 for the purpose of testing of marine

current technologies. This centre was set up for all renewable marine technologies to have an opportunity to test a full scale, grid connected prototype model in the excellent marine conditions in Orkney, Rourke, et al. [43].

CHAPTER 4 OCEAN ENERGY TECHNOLOGIES

In the previous chapter, the various ocean energy resources were expanded on. In order to exploit the resource, a suitable device needs to be deployed on or within the ocean to extract energy and transmit the extracted energy back to the shore for distribution. The following chapter expands on the many different ocean energy technologies which are in development or commercially available for exploitation of the many different ocean energy resources.

4.1 Wave Energy Technologies

At the present time there exist many different types of wave technology but most of the technologies are in a research and development stage while others work close to shore for testing purposes. A few of the various types of technologies, which extract energy from the waves, are further expanded on in the following section.

4.1.1 Oscillating Wave Column (OWC)

The Oscillating Wave Column which is illustrated in Figure 4-1 is a device which works with changing air pressure. The device harnesses the power from the waves by creating a pressure region in a cavity within which a turbine is situated. The pressure of air varies as a function of the level of water which enters the cavity. The water level varies as a result of the moving waves or “oscillating water”. When the water level increases so too does the pressure within the chamber. The relatively high pressure air passes through a Wells turbine which extracts energy from the air. When the level of water decreases the air pressure is reversed and the turbine extracts energy from the air in the same manner. The Wells turbine extracts energy from both directions of air flow. This is the advantage of the Oscillating Wave Column as energy is extracted by ascent and descent of the wave. The disadvantage, however, is that the Wells turbine requires energy to get started. Two of these systems have been deployed and are operational in Scotland by Wavegen, and in Australia. Each of these systems generates an estimated 500 kW of power, Meisen and Loiseau [39].

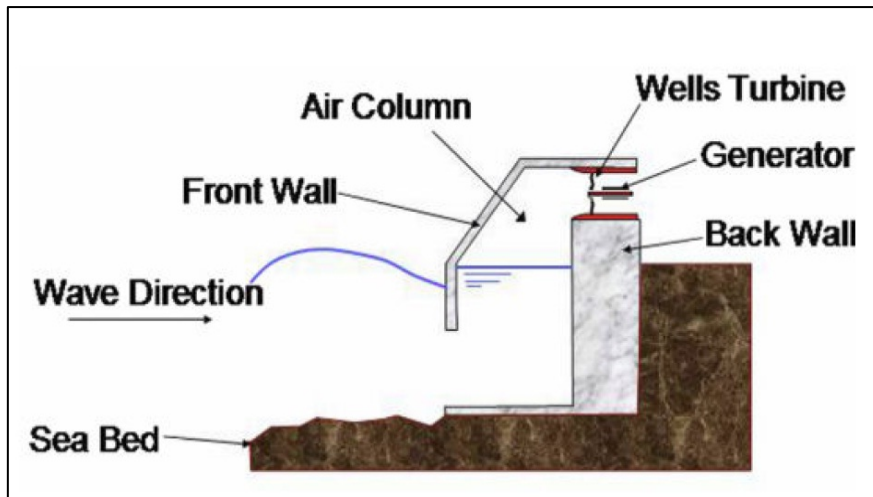


Figure 4-1: Oscillating wave column, Meisen and Loiseau [39]

4.1.2 The Pelamis

The Pelamis system shown in Figure 4-2 below is sometimes referred to as the “sea snake” due to its aesthetic properties. The system extracts energy from both the potential and kinetic energy of the waves by moving with the wave structure. The system comprises buoyant segments which are hinged to each other. Encased within the segments is a hydraulic generator. The generator is powered by oil which is pumped by the movement of the segments which gain kinetic energy when the waves ascend and descend. The hydraulic generator can be viewed as a smoothing system which allows a supported movement of the segments as they move with the waves, [39, 48].



Figure 4-2 The Pelamis, [48]

This structure is large and has a power rating of 750 kW, [48]. To be used on a large scale basis to power a country a farm of these structures would need to be implemented. The size of the system would impact shipping and fishing routes. The further away the system the more cabling is required so the energy generated can be transported to shore. The system also impacts the environment in regards to the visual aspect due to the size of the structure and the colour protruding on the surface of the ocean.

4.1.3 The Wave Dragon

The Wave Dragon which can be seen in Figure 4-3 below is a floating reservoir system which harnesses the potential energy of wave particles by exploiting the natural kinetic energy of the waves. Waves crash into the ramp of the reservoir which stores the kinetic energy of the crash and the water. Electricity is generated when the water returns back into the ocean. This form of wave energy harnessing can be closely related to a dam with three basic steps: absorption of the resource, storage of the potential energy and power generation, Meisen and Loiseau [39].

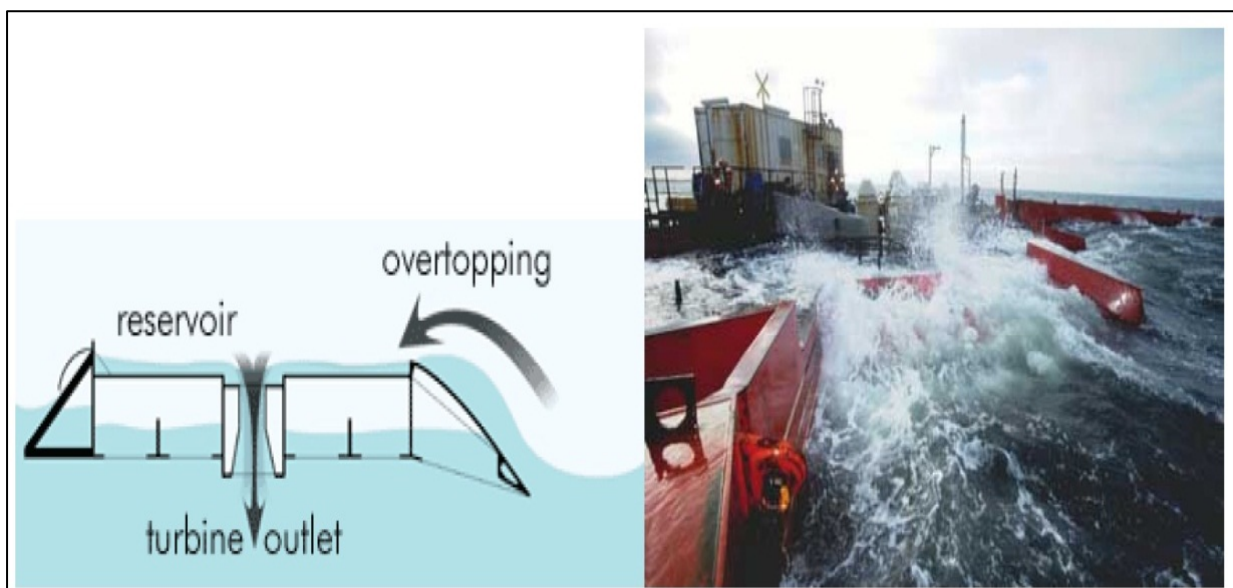


Figure 4-3 The Wave Dragon process of operation, Meisen and Loiseau [39]

This structure, however, is highly complex to design. Large optimization of the plant needs to be conducted due to the environment in which it is implemented. This system utilizes the potential energy of the wave and barely exploits the kinetic energy to transfer the potential energy into the floating reservoir. This device does not need the stability of the ocean shore and can be situated in harsh environments or regions of high wave activity. This system

however, like the Pelamis, is extremely large and can pose a threat to shipping lanes or impact the environment aesthetically, Meisen and Loiseau [39].

4.1.4 The Archimedes Wave Swing

The Archimedes Wave Swing (AWS) is a wave energy converter which uses the theory of float discovered by Archimedes. The system is a point absorber derivative and uses the pressure which is caused by a wave's motion onto a cylindrical buoy. The buoy moves in a vertical direction. The vertical movement is translated into electricity by means of a linear generator situated within the cylinder. The power generation is transmitted to shore by means of cables which run on the sea floor.

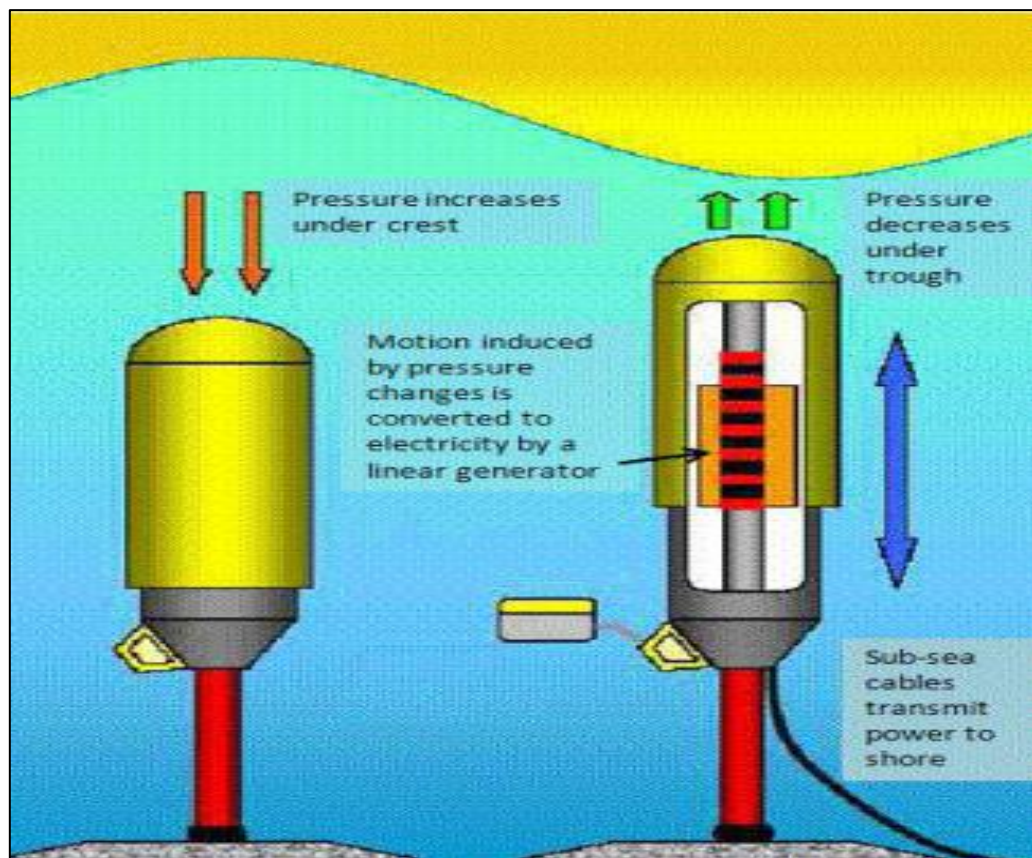


Figure 4-4: The Archimedes Wave Swing, Meisen and Loiseau [39]

This type of wave energy converter is a type of point absorber. Various types of point absorbers exist which are in development at present. The point absorber systems alone produce a small amount of power in relation to a county's power demand. This is why arrays of these devices are needed to produce a significant amount of power output, Meisen and Loiseau [39].

4.2 Ocean Thermal Energy Converter (OTEC) Technologies

Ocean thermal energy converters have a standard operating temperature of warm water being 20°C (300 K). These temperatures are found in the regions that are far off shore. Many types of OTEC plants are in circulation at present which include an on shore plant, on shelf plant and floating plant. There exist three basic cycles of ocean thermal energy converters: Closed Cycle, Open Cycle and the Hybrid Cycle. These cycles are to be further explained below [39-41, 47]. The following section expands on the three types of OTEC cycles.

4.2.1 The Closed OTEC Cycle

The closed OTEC cycle utilizes a second fluid as the working fluid and not the warm water which is obtained from the ocean. The working fluid is normally a fluid with a low boiling point (typically a refrigerant). The warm water collected from the surface of the ocean is used as a heat exchange fluid which boils the refrigerant. The vaporized fluid expands through a turbine which extracts the energy from the pressurized fluid. The cold water from the ocean's deep water reservoir is used to condense the working fluid in a heat exchanger. The condensed fluid is recirculated through the refrigerant cycle. India has constructed a closed-cycle floating plant which is rated at 1 MW [39, 41, 47].

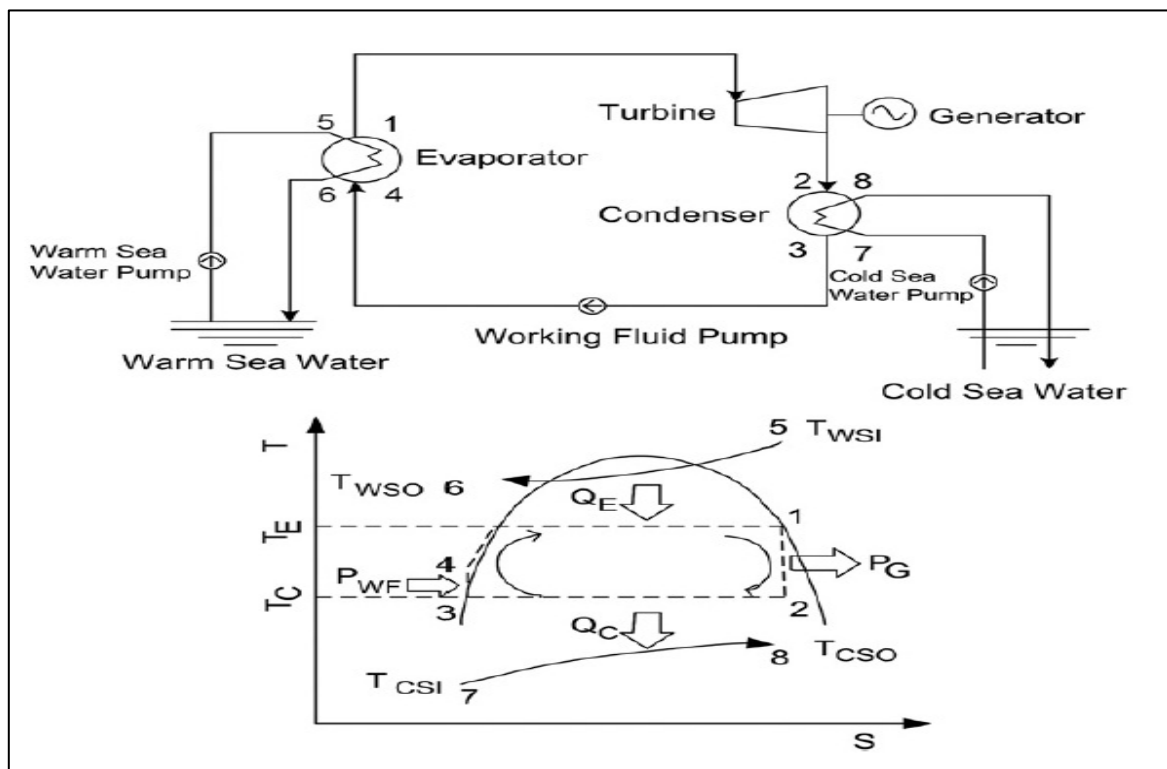


Figure 4-5: Closed OTEC Cycle, Faizal and Ahmed [41]

4.2.2 The Open OTEC Cycle

The open cycle is different from the closed cycle as the working fluid is the warm water which is obtained from the surface of the ocean. The warm water is pumped into a low pressure containing unit which flash evaporates the water into steam. The expanding steam passes through a low pressure steam turbine and the energy is converted into electricity. This system, however, can be coupled with a desalination system. As the saturated steam exits the turbine it is condensed using the cooler water from deeper waters. This pressurized, condensed water is fed into a desalination process where the water is then used as required [39, 40, 47].

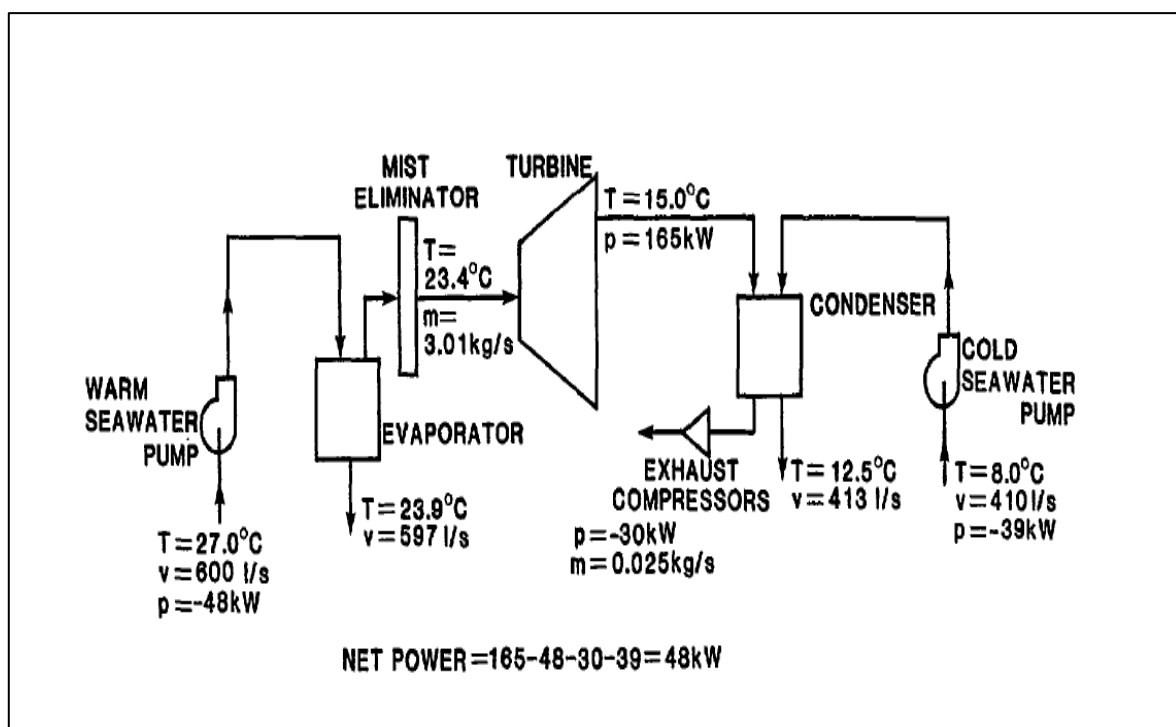


Figure 4-6: Open OTEC Cycle, Alam and Iqbal [8]

4.2.3 Hybrid OTEC Cycle

The hybrid cycle is a combination of the closed cycle and the open cycle. The sea water is vaporized in a vacuum chamber. The steam is used in a heat exchanger to vaporize a second working fluid as in the closed cycle to be passed through a turbine. The steam is condensed by the cooler water from the sea and then directed to a desalination process to provide fresh water whilst the saturated refrigerant is also condensed but recirculated through the refrigerant subsystem, Meisen and Loiseau [39].

4.3 Tidal Barrage Technologies

Tidal barrage systems, as mentioned in the previous chapter, utilises the same concept on which a traditional dam is built on by harnessing energy from the collected and compounded potential energy from the waves as they enter the capturing reservoir. The following section expands on the various commercial types of tidal barrages.

4.3.1 La Rance, France

The largest and longest running tidal barrage can be found in La Rance power facility located in France. The facility has a power capacity of 240 MW. The La Rance power facility was constructed between 1961 and 1967 and is situated over the river Rance in Brittany shown in Figure 4-7. This barrage is 720 m long and encloses 22 km² of water within the estuary. The facility consists of 24 reversible 10 MW bulb turbines operating with a hydrostatic head of 5 m. The facility exploits the use of two-way generation and also pumped storage. The facility is said to produce a net power output of approximately of 480 GWh per year, Rourke, et al. [43].



Figure 4-7: La Rance Tidal barrage Power Facility in France, Rourke, et al. [43]

4.3.2 Annapolis Tidal Generation, Bay of Fundy, Canada

The Annapolis tidal generation facility depicted in Figure 4-8 below was constructed between 1980 and 1984 and is located in the Bay of Fundy, Canada. The power facility construction was a government pilot project. This project was issued to explore the potential of harnessing the tidal energy. This facility's power capacity of 20 MW is connected to the national grid. The Bay of Fundy has the highest ocean tidal range worldwide and has a maximum tidal head of 16 m. The barrage utilises one turbine and it is the largest Straflo rim turbine in operation in the world which produces 30 GWh of electricity per annum. There is potential for further development of the tidal power in the Bay of Fundy. There have also identified two other potential basins which are the Minas Basin and the Cumberland Basin. The capacity of the Minas Basin is said to be approximately 5 GW of power, Rourke, et al. [43].



Figure 4-8: Annapolis tidal power facility, Rourke, et al. [43]

4.3.3 Kislaya Guba Power Facility, Russia

The Kislaya Guba facility is also a government pilot based project and was constructed in 1968 and has estimated capacity of 400 kW. This power facility is found in the Kola Peninsula near Murmansk in Russia. This power facility is the smallest tidal power facility in operation worldwide. This tidal facility has turned out to be successful and has led to feasibility studies which could lead to larger tidal power generating facilities in the north and

east of Russia which include the Mezen Bay in the White sea which is thought to have the potential power capacity of 15 GW and the Tugar Bay which has an estimated potential power capacity of 6.8 GW, Rourke, et al. [43].

4.3.4 Jangxia Creek, East China Sea

The Jangxia creek power generation facility was constructed during the same period as the La Rance tidal facility. This power plant has a power capacity of 500 kW and is situated in the East China Sea, Rourke, et al. [43].

There are other tidal barrage sites worldwide which are larger than the ones that were mentioned above. The larger sites are all currently undergoing feasibility studies and they include the Severn Estuary in the UK, Bay of Fundy in Canada, Mezen Bay and the Tugar Bay in Russia and other potential sites in the UK. The UK has the most potential as wave and tidal activity are high. In addition to the larger sites numerous small scale sites, estuaries and rivers are also being evaluated; smaller sites seem to be more feasible, Rourke, et al. [43].

The current issues which restrict the development of tidal barrage systems are the high cost of the projects due to construction and the environmental impact. The construction costs are high due to the vast amounts of materials required by a barrage to withstand the immense forces which it is subjected to by the damming of the ocean water. The maintenance of the turbines can now be considered as a minor issue in relation to the entire barrage because of the developments in turbine design.

The main issue for tidal barrages are the environmental impacts the barrage has on the surrounding environment. By enclosing a large amount of water in an estuary or bay the barrage may change the flow of the tidal currents which directly affects the marine life which is dependent on it. The impacts however, vary from site to site. The presence of turbines also affects the transport of marine life within the estuary which is being enclosed as the marine life would sometimes travel between the turbines, Rourke, et al. [43].

The concept of tidal barrage systems is mature in nature, reliable and has excellent current future potential. The issues which need to be resolved or minimised are the environmental impacts and the high cost of construction of a facility. The advantage of this form of renewable energy is that this technology has stood the test of time and power generation from this technology is readily available when required, Rourke, et al. [43].

4.4 Types of Tidal Current Turbines

There are two common types of tidal current turbines which are used at present to extract energy from the ocean. These types are horizontal axis turbines and vertical axis turbines. The horizontal axis turbine blades rotate in the horizontal plane relative to the incoming flow. The axis of rotation with this turbine is parallel to the direction of flow. The vertical axis turbine blades rotate in the vertical plane relative to the flow and the axis of rotation is perpendicular to the incoming flow [39, 43]. Turbines are not the only forms of technologies which are used to extract the tidal energy; tidal Hydrofoils are also used to extract energy from the tides, Rourke, et al. [43]. The following section further expands on the different types of technologies.

4.4.1 Delta Stream Turbine

The Delta Stream turbine is a turbine which was developed in the UK by a company called Tidal Energy Ltd. This turbine device is rated to generate 1.2 MW of power and consists of three, three-bladed, horizontal axis turbines as depicted in Figure 4-9 below. Each turbine blade has a diameter of 15 m and the turbines are mounted on a triangular frame which is used to produce a low centre of gravity. This is done so the structure as a whole has increased structural sustainability. This device, however, has yet to undergo testing and full production is planned to commence in the summer of 2009, Rourke, et al. [43].

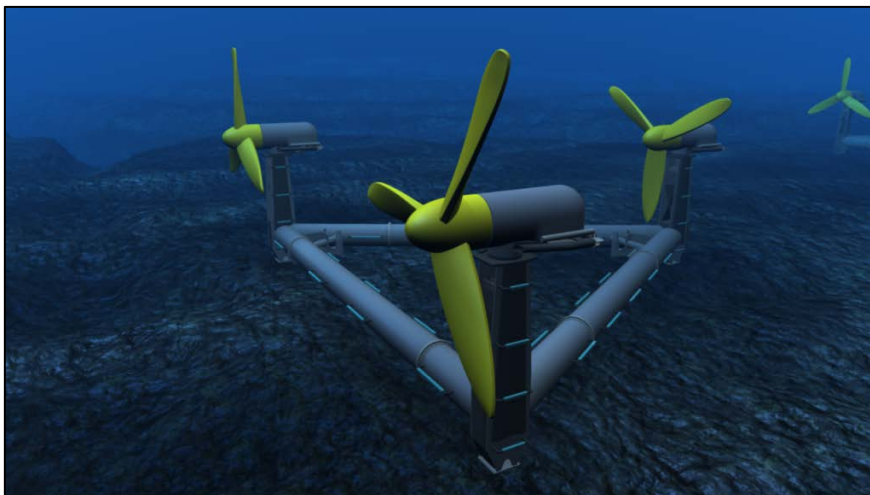


Figure 4-9: Delta Stream Turbine, [49]

4.4.2 Evopod Tidal Turbine

The Evopod Tidal turbine shown in Figure 4-10 below is a horizontal axis turbine which consists of five blades. It is a floating system and the main structure is moored to the sea floor which allows the floating system to maintain optimum heading into the oncoming tidal stream. The mooring system is designed such that the structure is anchored using gravity anchors to the seabed but has the freedom of motion as the tidal streams change due to the lunar cycle. This technology comes in a mono, twin or multi-turbine structure depending on the environment being exploited and power output required. There is a scaled down model which is currently undergoing tests in Strangford Lough, Northern Ireland. This technology was developed by a company called Ocean Flow Energy Ltd. based in the UK, Rourke, et al. [43].



Figure 4-10: Evopod Tidal Turbine, [50]

4.4.3 Lunar Energy Tidal Turbine

The Lunar Energy Tidal turbine illustrated in Figure 4-11 below is a bidirectional horizontal axis turbine which was developed by Lunar Energy Ltd. based in the UK. This structure consists of a gravity base and is rated to produce 1 MW with a turbine diameter of 11.5 m. This system turbine consists of a duct which is 19.2 m long and 15 m in diameter which

tappers down to the diameter of the turbine. This is done to increase the flow rate and thus velocity of the tide so more energy may be extracted. This turbine, however, is still at a developmental stage and nothing has been built and tested as yet, Rourke, et al. [43].

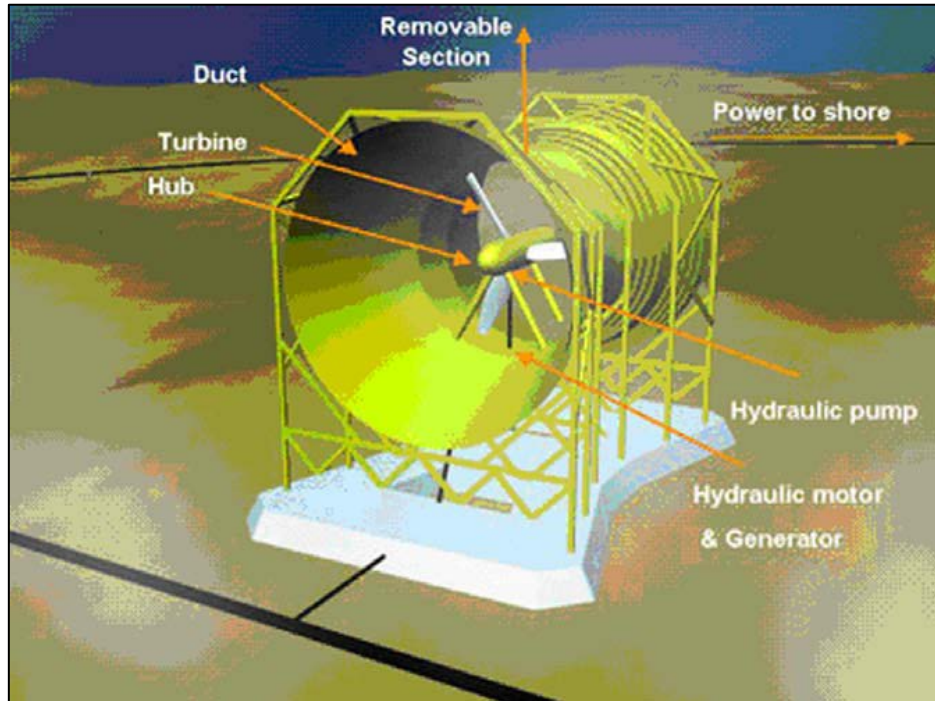


Figure 4-11: Lunar Energy Tidal Turbine, Rourke, et al. [43]

4.4.4 Free Flow Turbine

The Free Flow turbine is a horizontal axis, three bladed turbine which is developed by Verdant Power Ltd. based in the USA and Canada. The diameter of this turbine is 4.68 m and a prototype is currently being tested in New York City's East River. The system is rated to produce a power of 1 MWh of electricity per a day, Rourke, et al. [43]. The system was first tested to deliver power to a nearby grocery store and car parking arcade to test the systems power delivery and grid connection system. Currently this turbine system, consisting of more than one turbine, is generating 70 MWh of electricity and is connected to the grid with no power delivery problems. The turbine is a modular system and is in its fourth generation of turbine design.

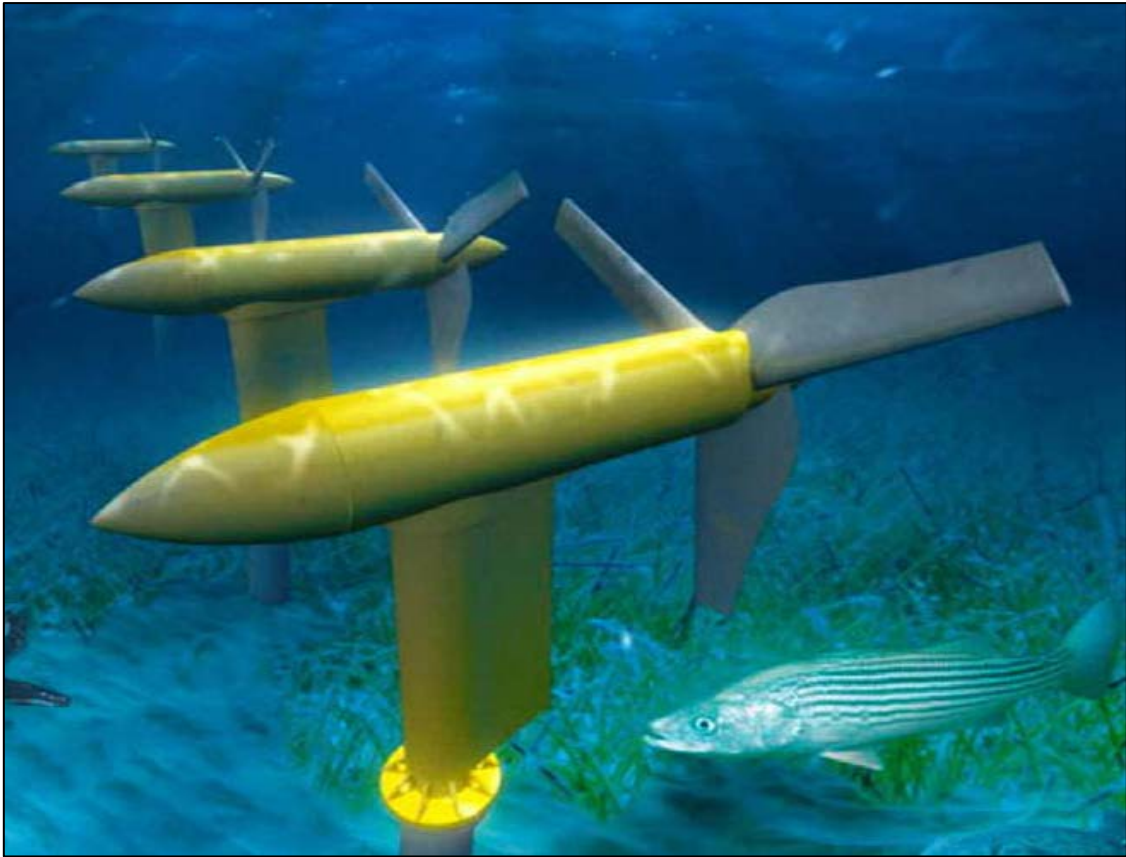


Figure 4-12: Free Flow Turbine, Rourke, et al. [43]

4.4.5 Neptune Tidal Stream Device

The Neptune tidal turbine device was developed by a company called Aquamarine Power Ltd. which is based in the UK. This device was rated to generate a power output of 2.4 MW. The tidal generator consists of two horizontal axis turbines, each of which has three blades mounted on a monopole structure. This device can generate power in both the ebb and flood tides, Rourke, et al. [43]. The system was scheduled to be tested in Orkney, Scotland in 2010 before commercialisation of the technology. The system was highly influenced by wind turbine technology and the close integration of electrical and mechanical components ensures a fault tolerant design system which can be safely connected to the UK electricity grid [51].

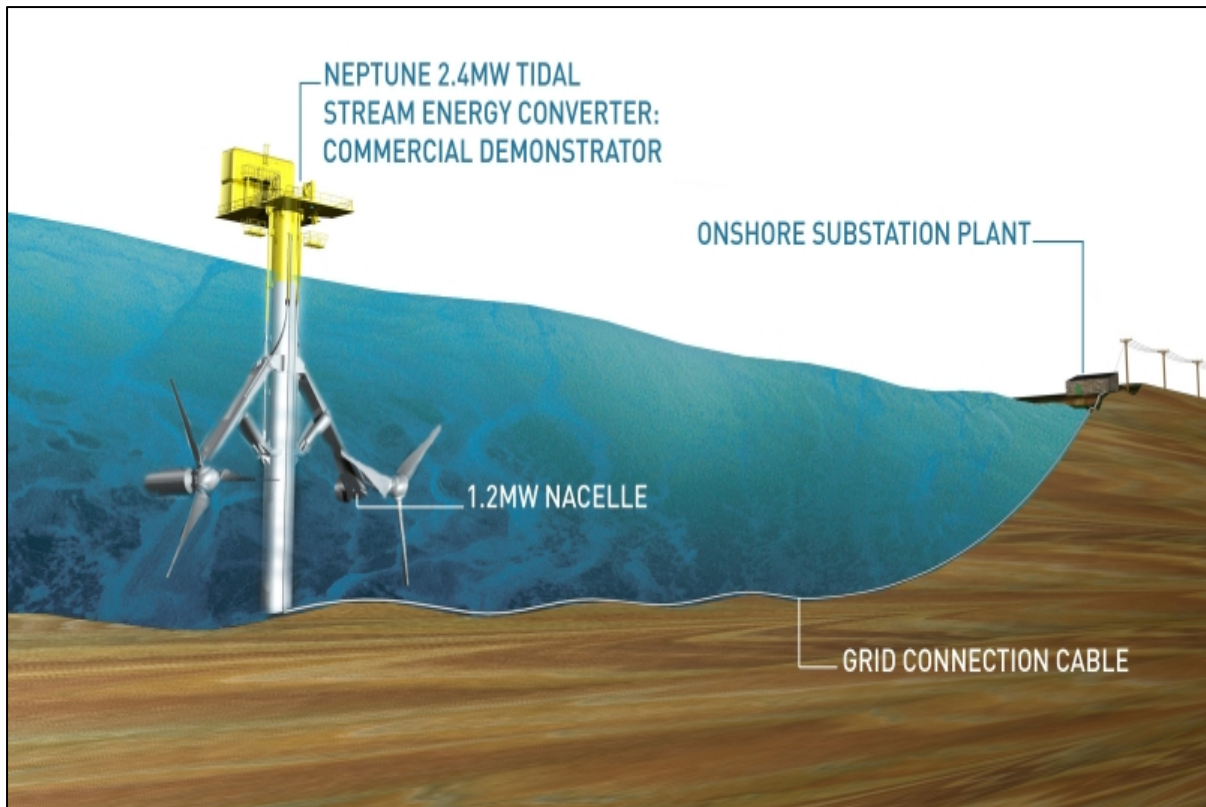


Figure 4-13: Neptune Tidal Stream Device, [52]

4.4.6 Nereus and Solon Tidal Turbines

The Nereus and Solon Tidal turbines were developed by the Atlantis Resource Corporation Ltd. which is based in Singapore. The Nereus Tidal turbine is a shallow, horizontal axis turbine which has been grid connected in Australia. The system was rated to output 400 kW and was successfully tested in July 2008. As seen in Figure 4-14, the turbine is of robust design and has the capability to withstand flow with large amounts of debris. The Solon turbine is a deep sea turbine which is ducted like the Lunar Energy Tidal turbine. The technology was rated to produce 500 kW and this turbine was successfully tested in August 2008, Rourke, et al. [43].



Figure 4-14: Above the Nereus Turbine and below the Solon Turbine, Rourke, et al. [43]

4.4.7 SeaGen

SeaGen, short for Sea Generation, is a horizontal axis tidal turbine which was developed by Marine Current Turbines Ltd. which is based in the UK. The technology is rated as a 1.2 MW tidal current turbine. This technology is the next step after the 300 kW, SeaFlow project which was successfully installed off the coast of Devon in the UK in 1993. A trial prototype of SeaGen was installed and connected to the electricity supply grid in May 2008 in Strangford Lough, Northern Ireland [43, 53]. SeaGen consists of two, two bladed horizontal axis rotors, each of 16 m in diameter. The rotors are connected to a gearing system which increases the revolutions of the rotor which is used to generate electricity via a generator. The rotor blades are pitch controlled which means that the turbine can operate in both ebb and flood tides. The pitch control system can also be used as a braking mechanism for maintenance to be conducted on the turbine. The SeaGen system was successfully installed and operating at full power on January 18th 2009, Rourke, et al. [43].

CHAPTER 5 ANALYSIS OF THE AGULHAS CURRENT

The Agulhas transport system has been an area of interest for researchers for many years. The research conducted on this system was mainly focused on transport behaviour and the integration of the entire system with the Thermohaline current. The Agulhas contributes to the Thermohaline system by recirculating flow from the equator which passes down the Southern African coast and starts to break up off from the Eastern Cape coast. The current retroflects back towards the Indian Ocean by means of cyclonic eddies which span over a kilometre, Lutjeharms and Anson [6]. These cyclonic eddies impact the Agulhas in an adverse manner which is to be further expanded upon and depicted within this chapter.

Eskom has identified the potential of the Agulhas current as a renewable energy resource which may be harnessed for electrical energy production. Eskom, the national supplier of energy, have conducted various lengthy investigations which analyse the flow velocity, flow direction and temperature of the Agulhas current at various locations along the east coast of South Africa. The performance parameters, which will subsequently affect the hydrokinetic turbine, are also subjected to natural and geological factors which affect the flow of the Agulhas current.

In this chapter the two factors which affect the Agulhas current, which are mentioned above, will be linked to the resource analysis for the three potential harnessing sites which were made public by Eskom as of August 2013, Eskom [54]. The same analysis was then conducted on new data which was updated and made public as of May 2014, Eskom [55]. As a result of the resource analysis performed on each of the potential sites, a general conclusion on suitable site location was made for the cross flow turbine being investigated.

In addition to the site selection for deployment of the turbine, estimated potential kinetic energy predictions were made on the parameters from the specific site. The predictions depict theoretical power density within the fluid and the energy density for the flow in relation to flow velocity.

5.1 Agulhas Current Potential Site Locations

As stated in the introduction of this chapter, site location for deployment of the hydrokinetic turbine is of importance to the performance of the system. Eskom had evaluated three potential sites along South African east coast. These sites are Port Edward, Cape Morgan and East London. The analysis was conducted by using an Acoustic Doppler Current Profiler (ADCP) which was situated at various depths at each site at different times of the year. For each site a set of three files were analysed, each containing measurements of date and time, range of unit from receiver, depth of the ADCP, magnitude of the flow resource and direction of the flow. To arrive at a proper analysis of the data, a more statistical approach was chosen. Frequency distribution, directional and power analysis was conducted on the data. The power which could be generated by the turbine from the data analysis was calculated in relation to the power curve assigned and constructed for the turbine.

5.1.1 Port Edward

Situated south of Durban, Port Edward was the first site which was chosen to be analysed by Eskom. For each chosen site, three sets of readings were conducted, each of which were at different depths. Figure 5-1 and Figure 5-2 depict the velocity profile of the Agulhas current off the coast of Port Edward, at depths of 60 m and 30 m respectively over a two month duration from September to December.

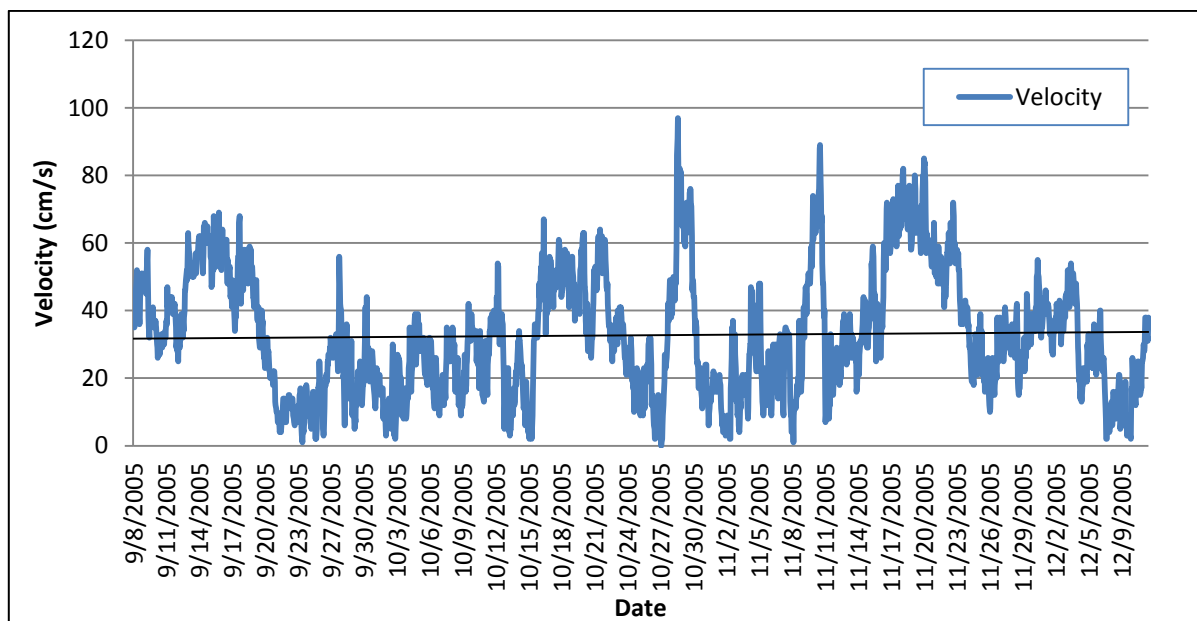


Figure 5-1: ADCP measurement, Port Edward 60 m

Figure 5-1 and Figure 5-2 depict velocity patterns of the current over the period of the measurement. These figures depict erratic raw data simulation over the duration of the measurement and cannot be used as a general consensus for the evaluation of a site. Arriving at a conclusion on site selection based on the average mean, depicted by the black trend line, would not be an accurate indication of an appropriate analysis. A frequency or distribution is depicted in Figure 5-3 and Figure 5-4 respectively. The histogram plot indicates the frequency or occurrence of the current's velocity as a percentage of the duration of the measured data.

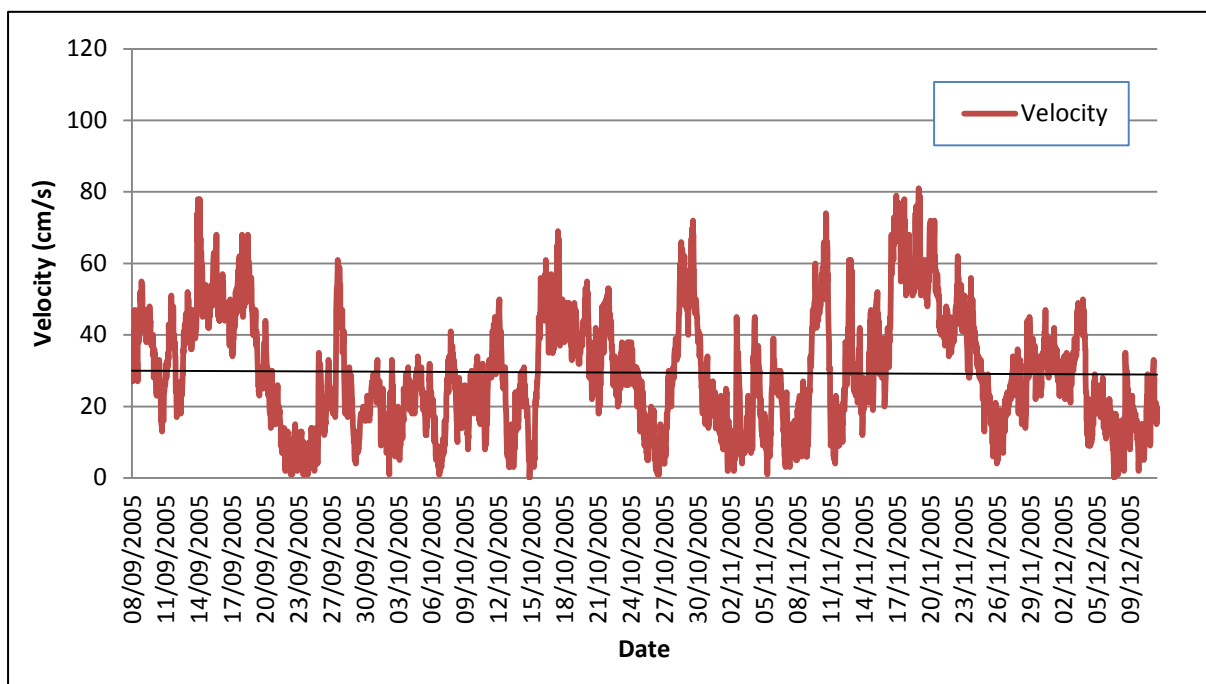


Figure 5-2: ADCP measurement, Port Edward 30 m

Analysing Figure 5-3 and Figure 5-4 below, one can assume that the distribution follows a Weibull distribution. The Weibull distribution, however, is a generalisation of the Rayleigh distribution which would approximate the distribution of the data more accurately as this is most commonly used in the analysis of wind resources. It can also be noted, by comparison of both the distributions, that the profile of the current's distribution does not vary significantly with depth variation for this specific site.

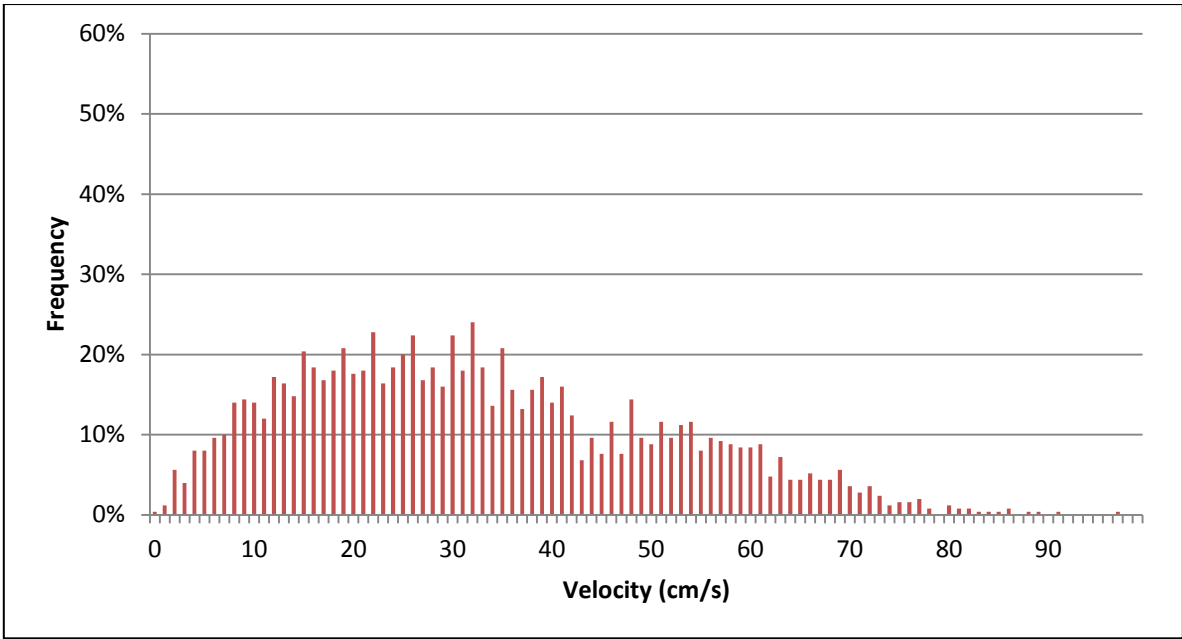


Figure 5-3: Frequency Distribution, Port Edward 60 m

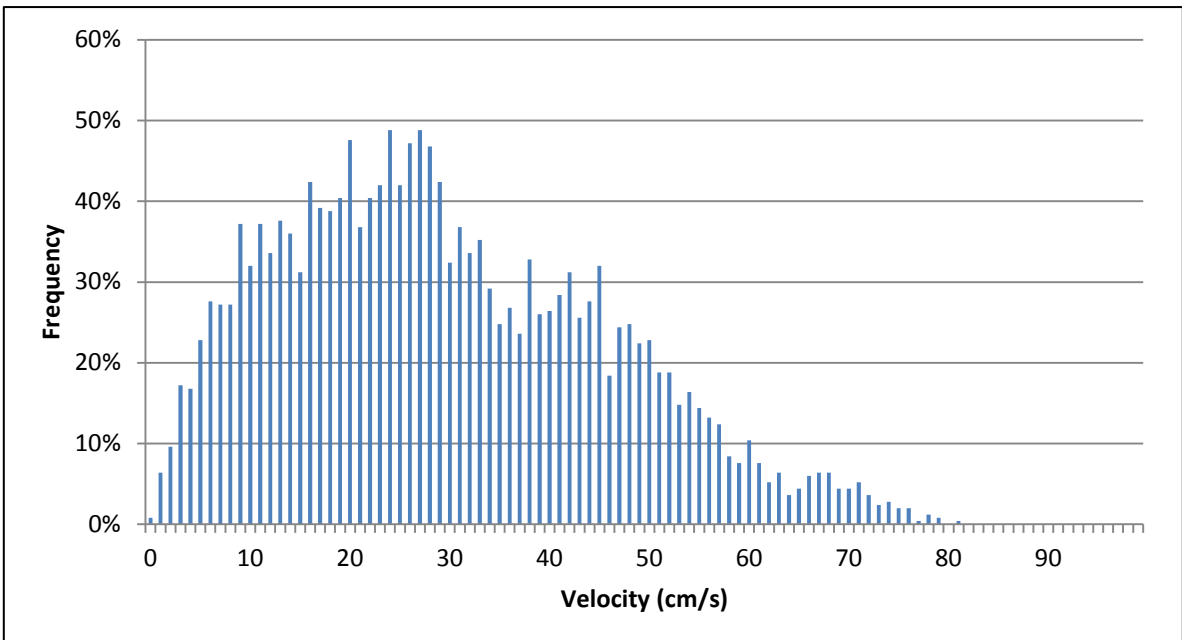


Figure 5-4: Frequency Distribution, Port Edward 30 m

Based on this analysis, it can be noted that the velocity of the current at this specific site increases as the depth decreases (moves towards the surface). This can be seen by the increase in frequency of velocity within the range of 10 to 40 cm/s.

Figure 5-5 below depicts polar distribution plots which were generated for the Port Edward site at the two depths which were analysed. It can be seen that at the deeper depth of 60 m in comparison to the depth of 30 m, the current's behavioural profile can be seen to be different.

This could be due to many affects. Effects on the current can be attributed to environmental topology causing swirl and directional changes. An effect which may have a more dominating role is that of the Natal Pulses or cyclonic eddies which retroreflect from the south and disturbs the almost constant flow patterns of the Agulhas.

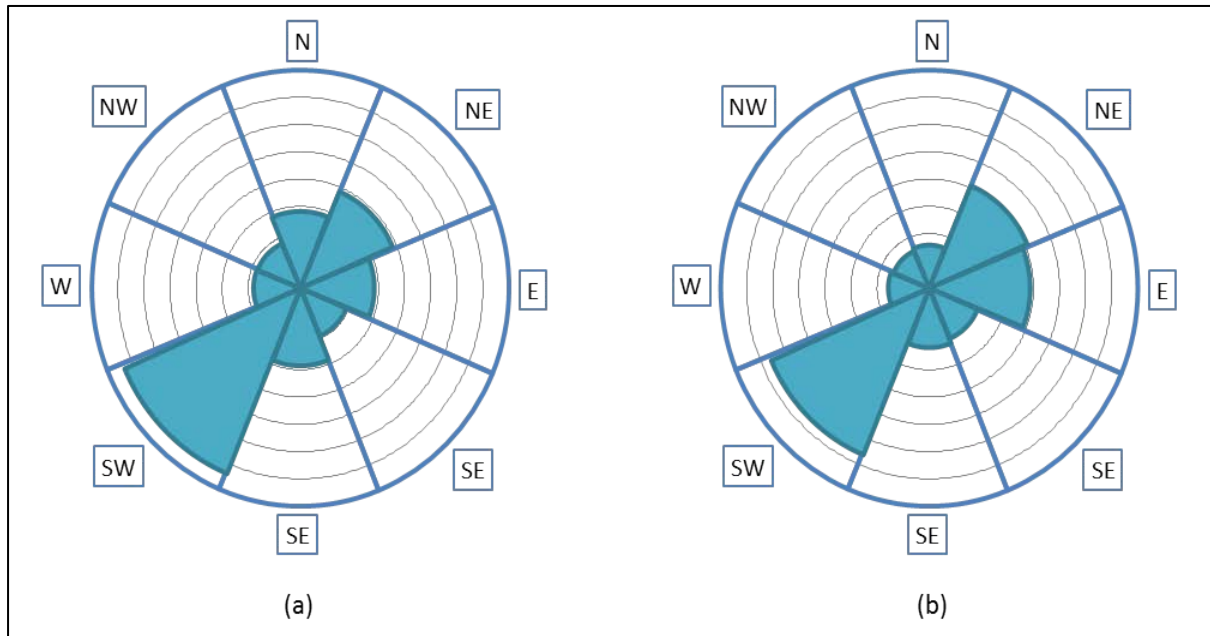


Figure 5-5: Polar Plots - (a) 60 m Depth; (b) 30 m Depth

5.1.2 Cape Morgan

Cape Morgan is situated south of Port Edward near Morgan's Bay and is a tourist attraction due to its beautiful sunrises and sunsets. The data which was collected by Eskom was conducted off the coast of Morgan's Bay. A similar analysis for the data obtained was conducted for Cape Morgan which is depicted in Figure 5-6 and Figure 5-8 below.

Figure 5-6 depicts the current velocity profile at a depth of 80 m from the surface of the ocean. It was observed that the current fluctuated continuously over the recorded time. This was suspected to be due to the tidal influence on the upper surface current and frequent large scale eddy interactions which occur from the Agulhas retroflexion. On closer inspection of the mean velocity line a positive gradient slope was depicted. This suggested that the mean velocity of the current was on the rise over the recorded time.

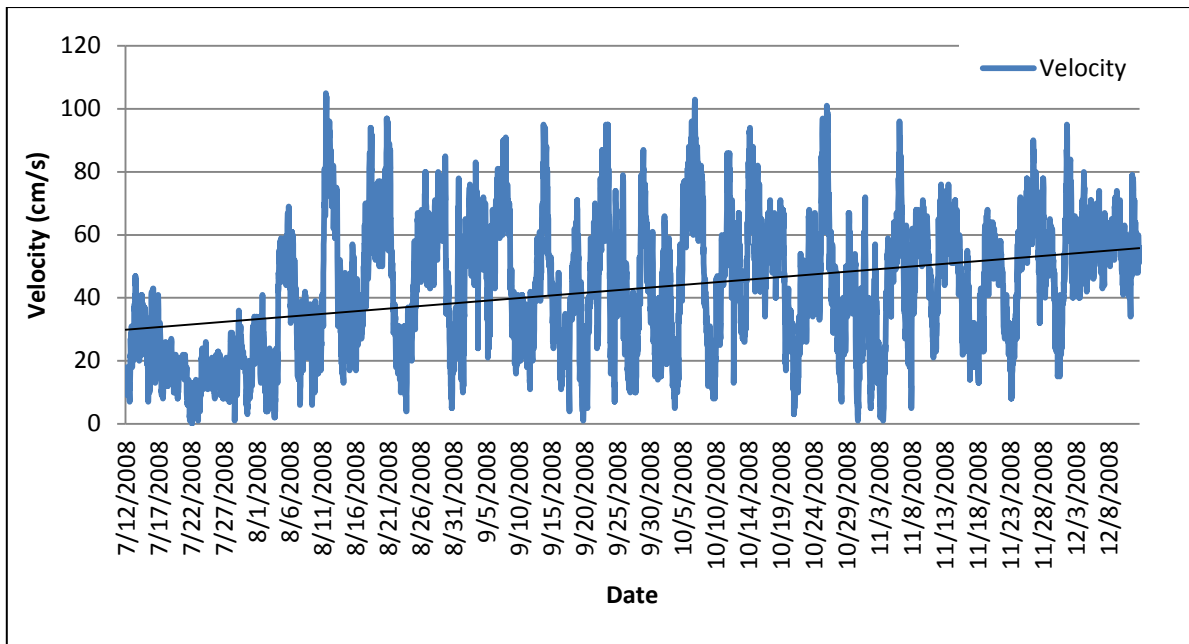


Figure 5-6: ADCP measurement, Cape Morgan 80 m

Figure 5-7 depicts the velocity profile of the Agulhas current at a depth of 83 m. As seen with Figure 5-6, the current is highly unstable at this location. However, the unsteady velocity profile is fairly consistent in its unsteady pattern. Inspection of the mean velocity line for Figure 5-7 yielded a relatively constant gradient line. This suggested that the current at this depth does not change over time even with the interactions with the cyclonic eddies stemming from the south.

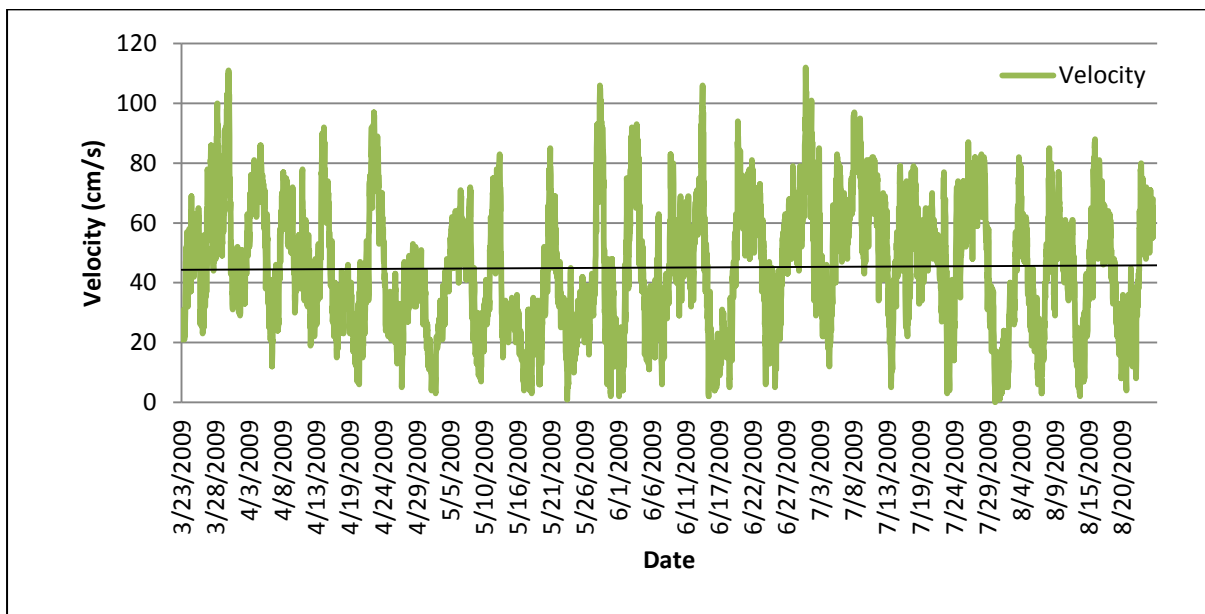


Figure 5-7: ADCP measurement, Cape Morgan 83 m

Figure 5-8 depicts the Agulhas current velocity profile at a depth of 85 m from the ocean surface. The current at this depth was seen to be slower than the previous depths which were analysed.

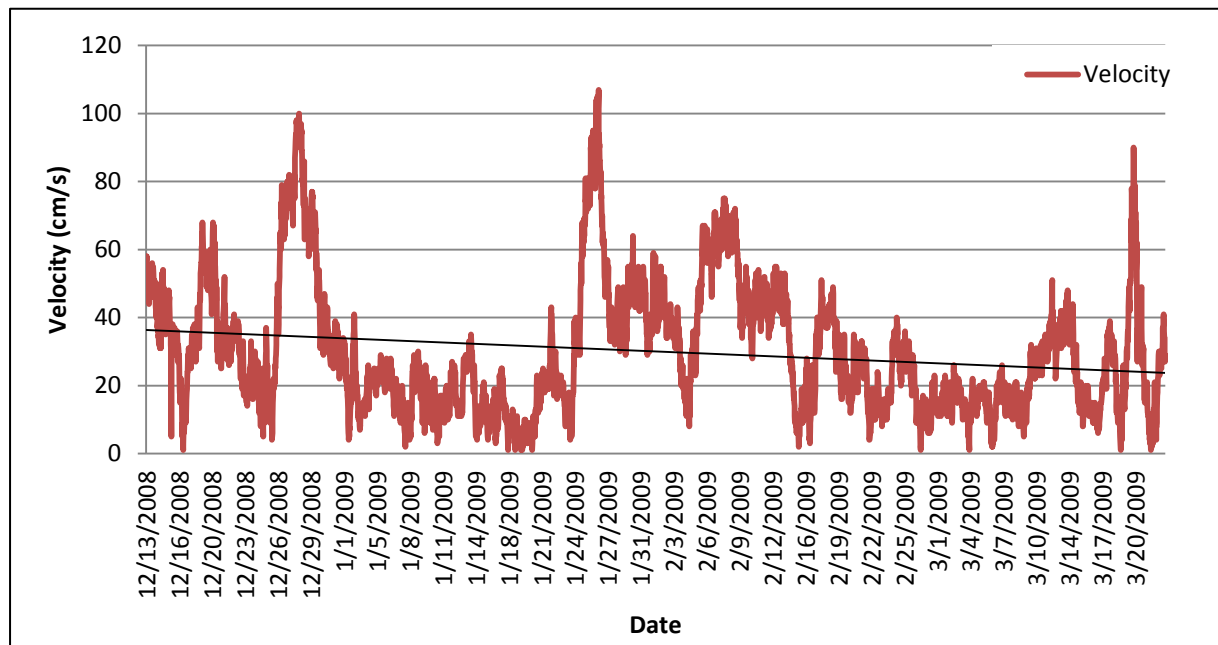


Figure 5-8: ADCP measurement, Cape Morgan 85 m

From the results, Figure 5-8 is the slowest velocity profile which was obtained from the Eskom results for Cape Morgan. The occasional spikes which do occur in this period can be assumed to be due to the interaction of the upper current with cyclonic eddies which are a result of the retroflection. Further inspection of the mean velocity of the profile generated a negative gradient. This depicts a decrease in mean velocity of the current as one ventures deeper.

Figure 5-9 to Figure 5-11 indicates the frequency distribution of the current's velocity profile for the Cape Morgan site. It can be seen, from the comparison of the results below, that the velocity tends to increase as the depth decreases and approaches the surface of the ocean. It can be seen here as well that the distribution of the current's profile follows one similar to that of a Weibull distribution.

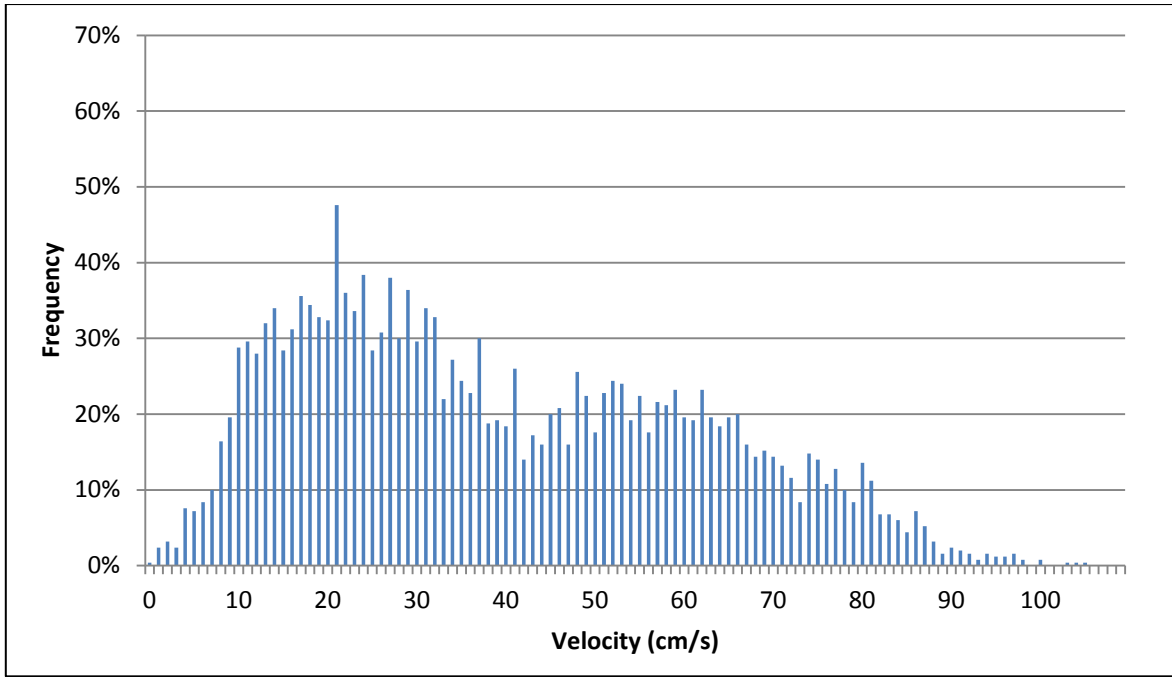


Figure 5-9: Frequency Distribution, Cape Morgan 80 m

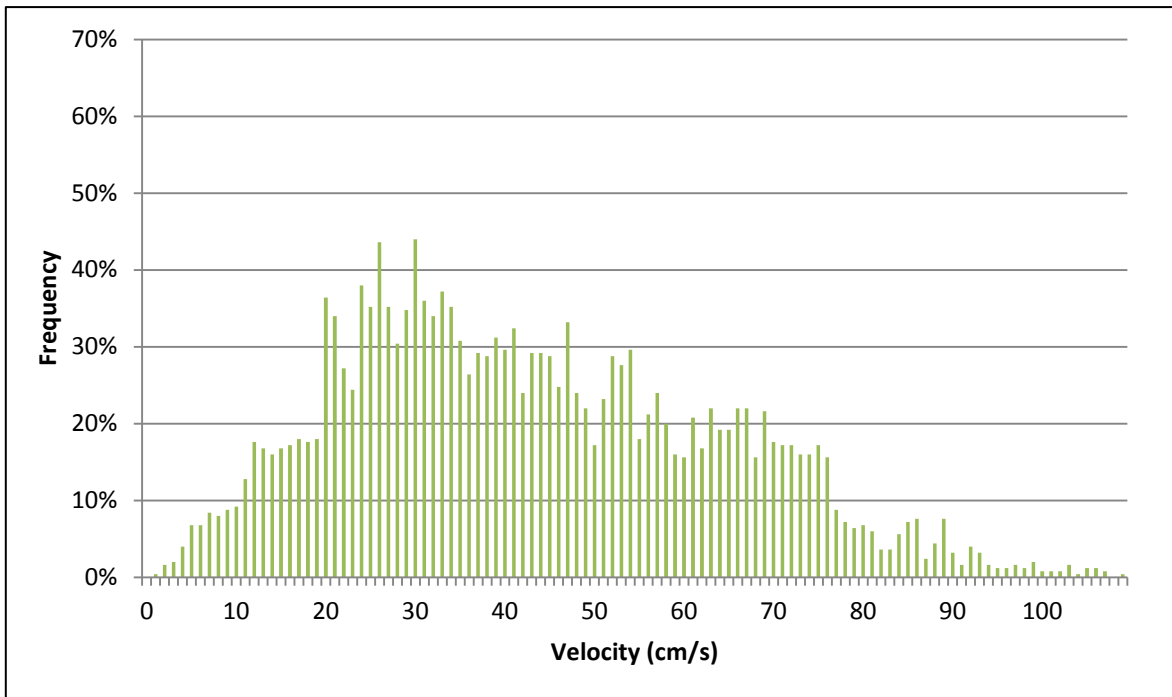


Figure 5-10: Frequency Distribution, Cape Morgan 83 m

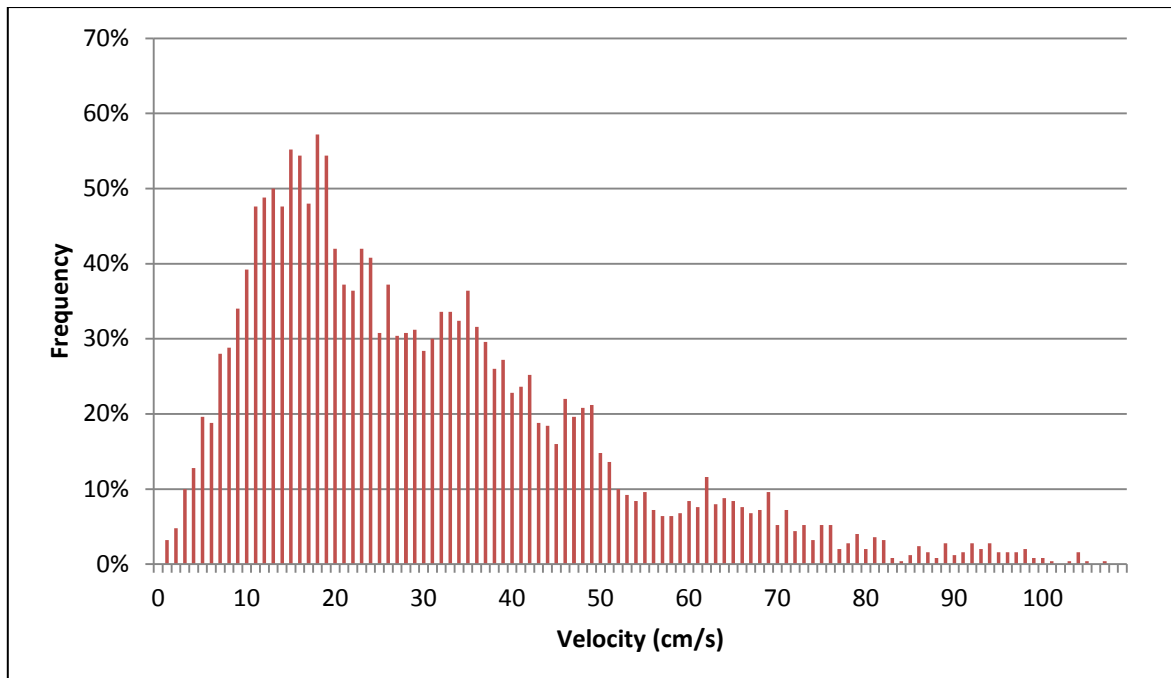


Figure 5-11: Frequency Distribution, Cape Morgan 85 m

Figure 5-12 below depicts the average velocity profile from each of the average depths recorded for the Cape Morgan site. It can be seen that as one approaches the surface of the ocean the current average velocity profile increases. As only three sets of readings were made public, it is suspected that the velocity of the current found within the surface current of the Agulhas holds higher kinetic potential energy, in relation to mean velocity strength, than what was analysed within this section.

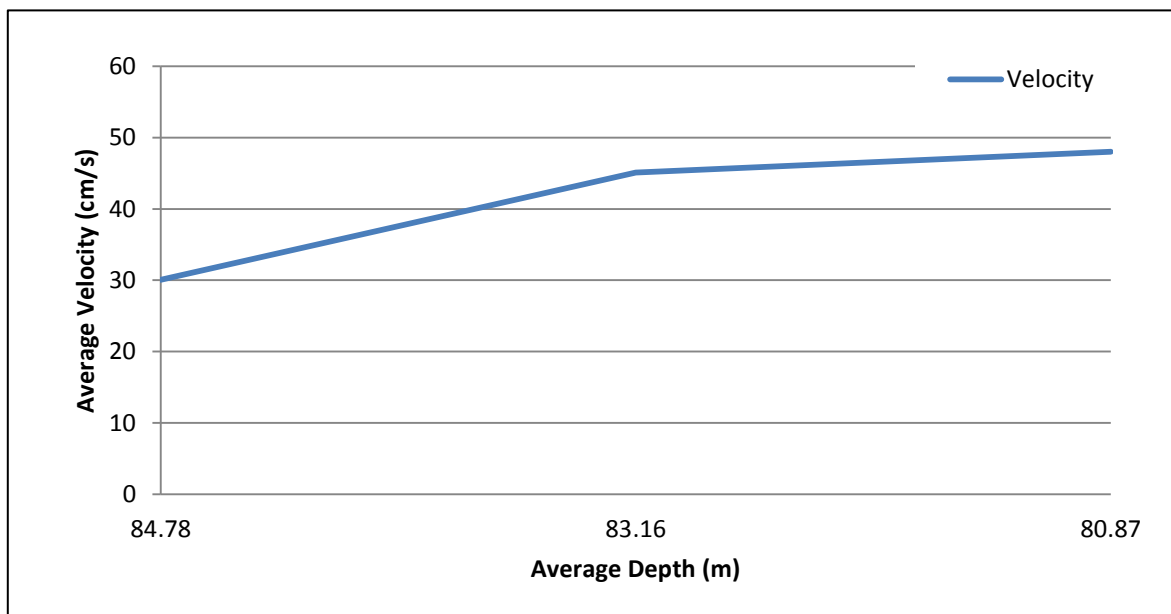


Figure 5-12: Average Velocity Vs. Average Depth for Cape Morgan

Figure 5-13 below illustrates the polar distribution plots for the Cape Morgan site and can be seen to be seemingly different from the previous site which was analysed. The plots depict that the variation in current speed tends to stabilise as the depth is increased. This could be misread however, as the data is only for large depths and not relatively shallow depths which might depict a similar, possibly more stable, trend as seen below.

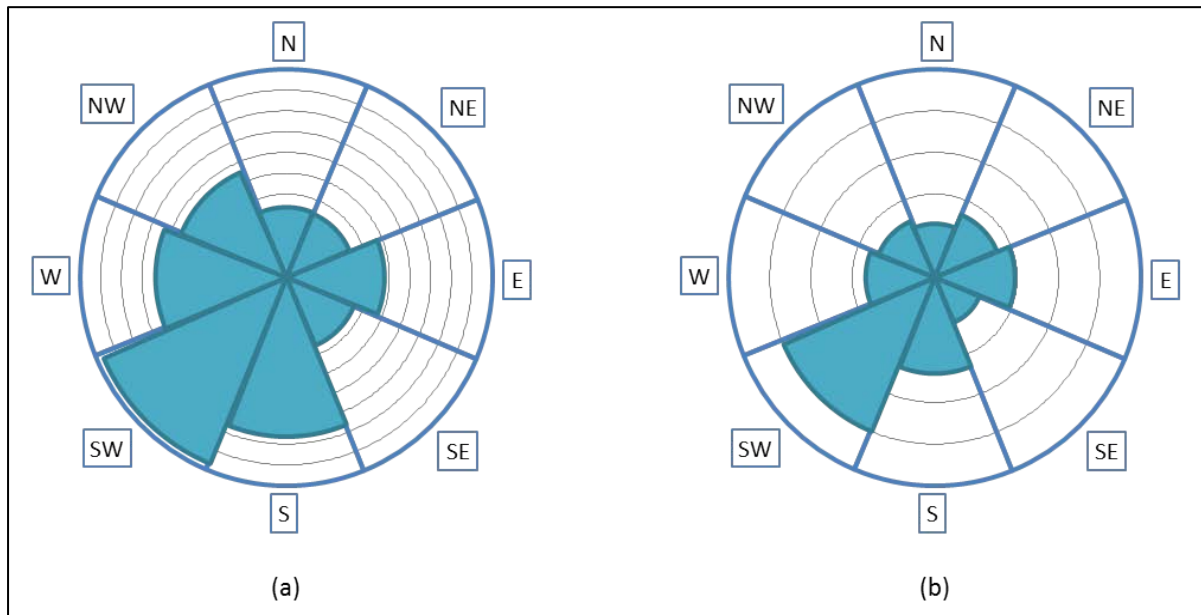


Figure 5-13: Polar Plots - (a) 80 m Depth; (b) 85 m Depth

5.1.3 East London

East London is the location which is located the furthest south of all the sites which were recorded by Eskom over the period which was chosen first for ocean data collection in 2006. The following section will expand on the data which was analysed for East London. Figure 5-14 to Figure 5-16 depict the velocity profile generated for a depth of 87 m. It was noticed during the analysis that the three sets of data consisted of a split of a year's data capture and Figure 5-16 depicts the results obtained for a depth of 94 m.

Figure 5-14 depicts the first half of two readings for the east London site at a depth of 87 m. The results show an unsteady plot as previously seen in the Cape Morgan analysis. A mean velocity of the results was also generated and closer analysis of this trend resulted in a positive gradient. Conversely when the same analysis was conducted on the latter half of the year's results, shown in Figure 5-15, the velocity mean line generated resulted in a negative gradient being produced. On analysis of the whole year, the results suggest that the velocity

of the current slowly increases with kinetic strength and then the energy decreases as the year ends. The combination of the two sets of results would lead to a mean velocity which would be relatively stable at the given depth of 87 m below the ocean's surface. Relating this finding to that of previous results at a similar depth, the conclusion of a constant mean velocity at this depth can be justified.

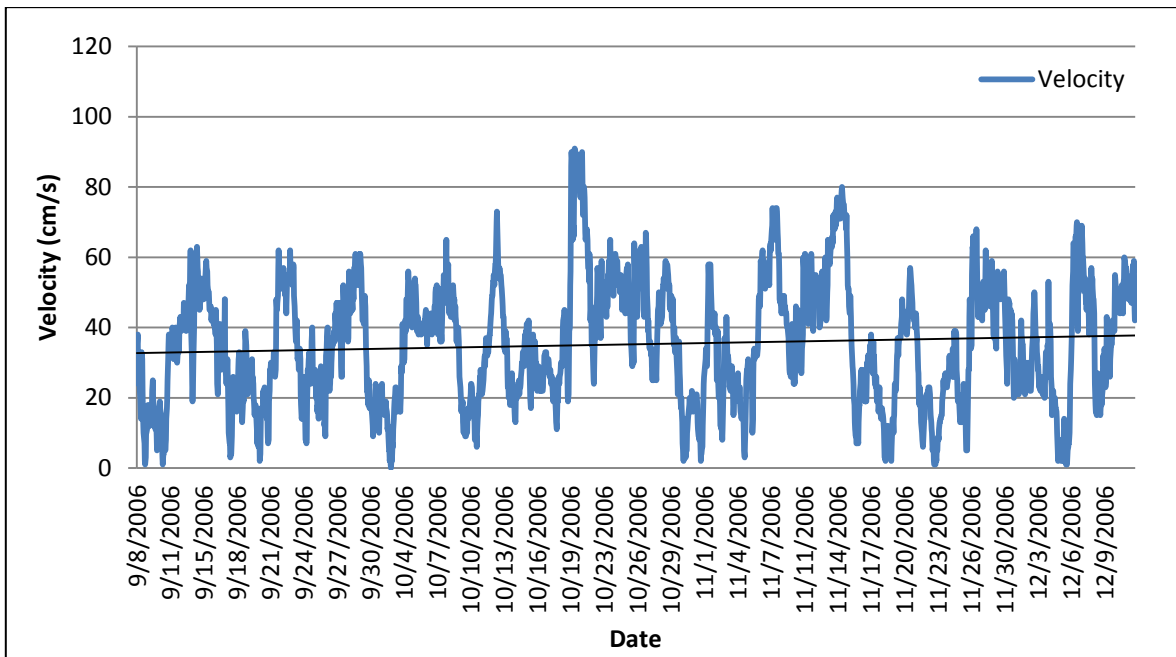


Figure 5-14: ADCP measurement, East London 87 m

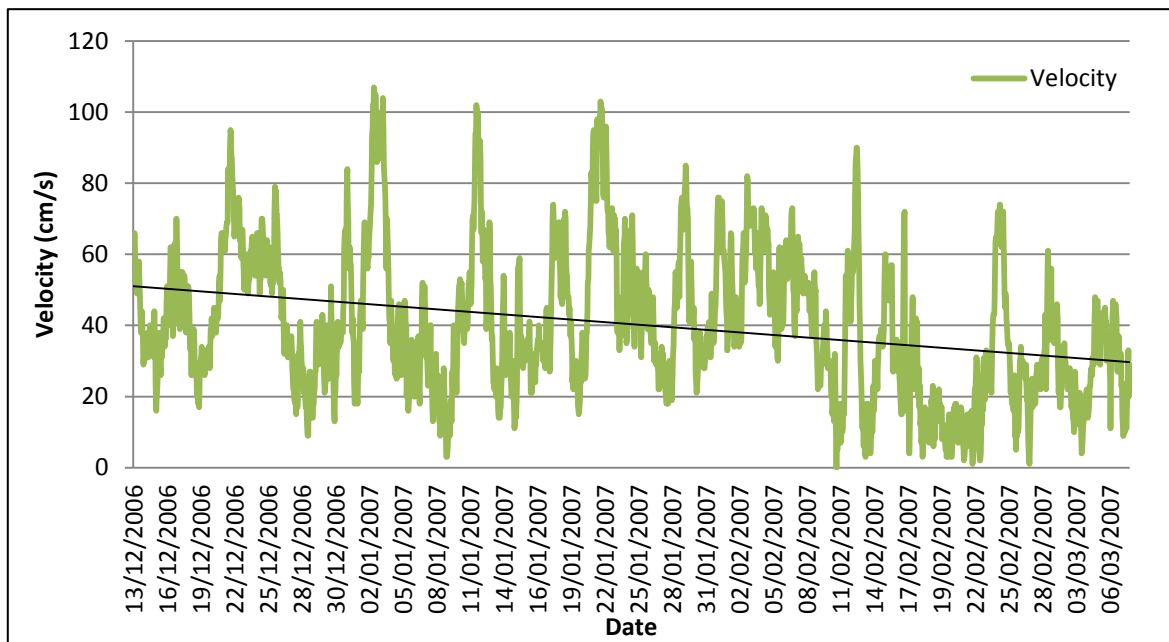


Figure 5-15: ADCP measurement, East London 87 m

Figure 5-16 illustrates the velocity profile which was generated using the last set of data for East London which is at a depth of 94 m below the surface of the ocean. The current profile is highly unsteady as compared to the previous results. On examination of the mean velocity trend line, a positive gradient was generated. This suggests that the mean velocity at this depth, for the recorded time, increases at a steady pace.

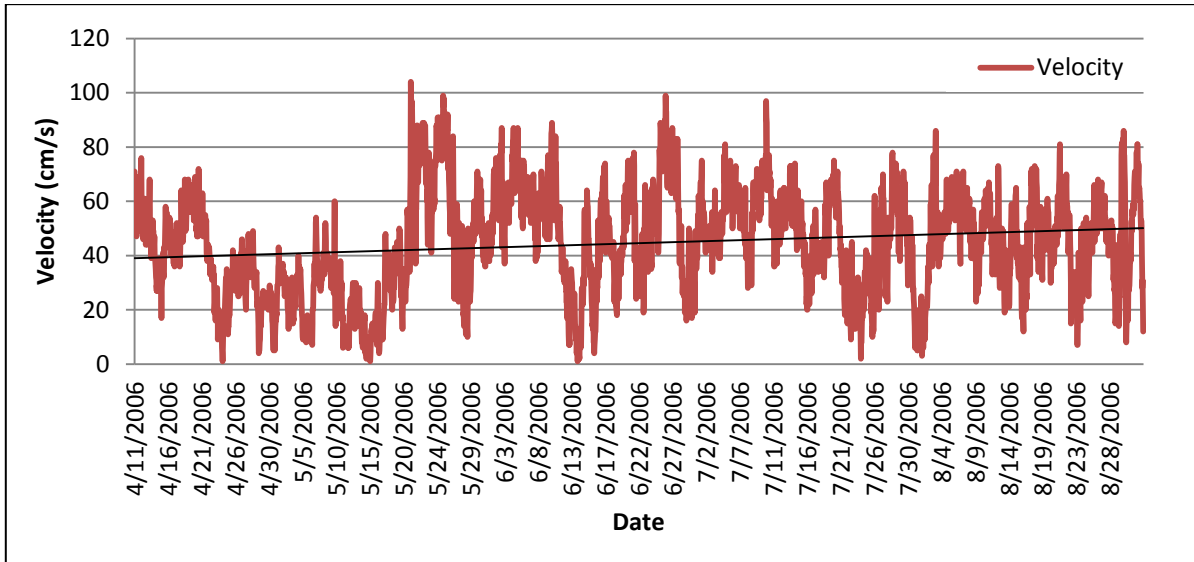


Figure 5-16: ADCP measurement, East London 94 m

Figure 5-17 to Figure 5-19 depict the frequency distribution for the three depths which were analysed above.

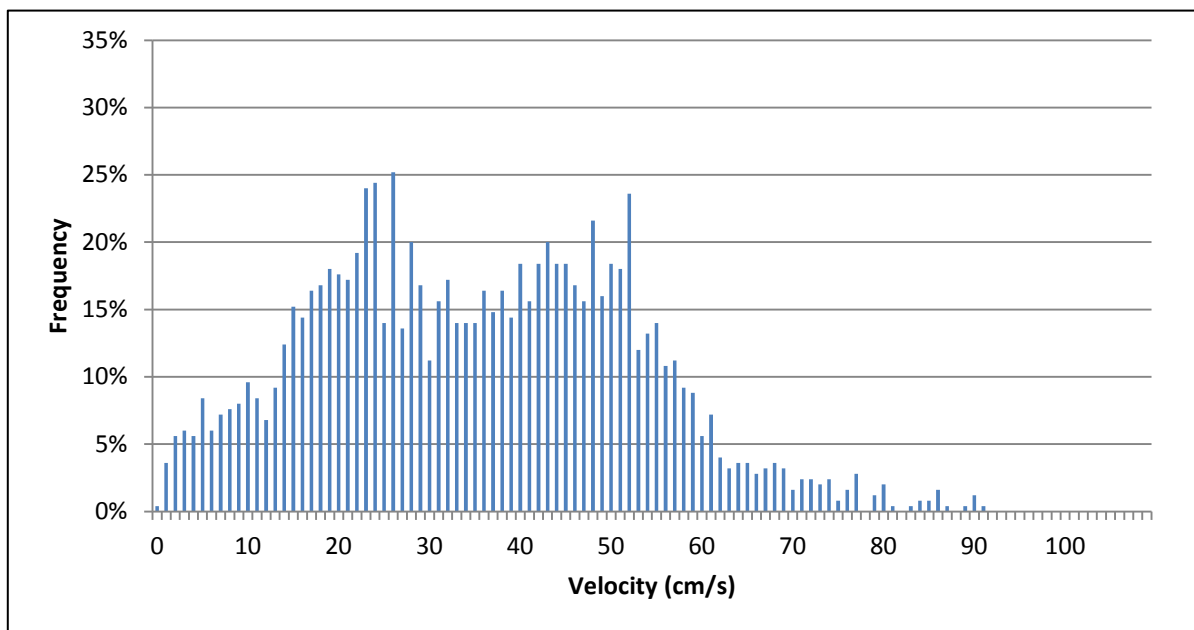


Figure 5-17: Frequency Distribution, East London 87 m

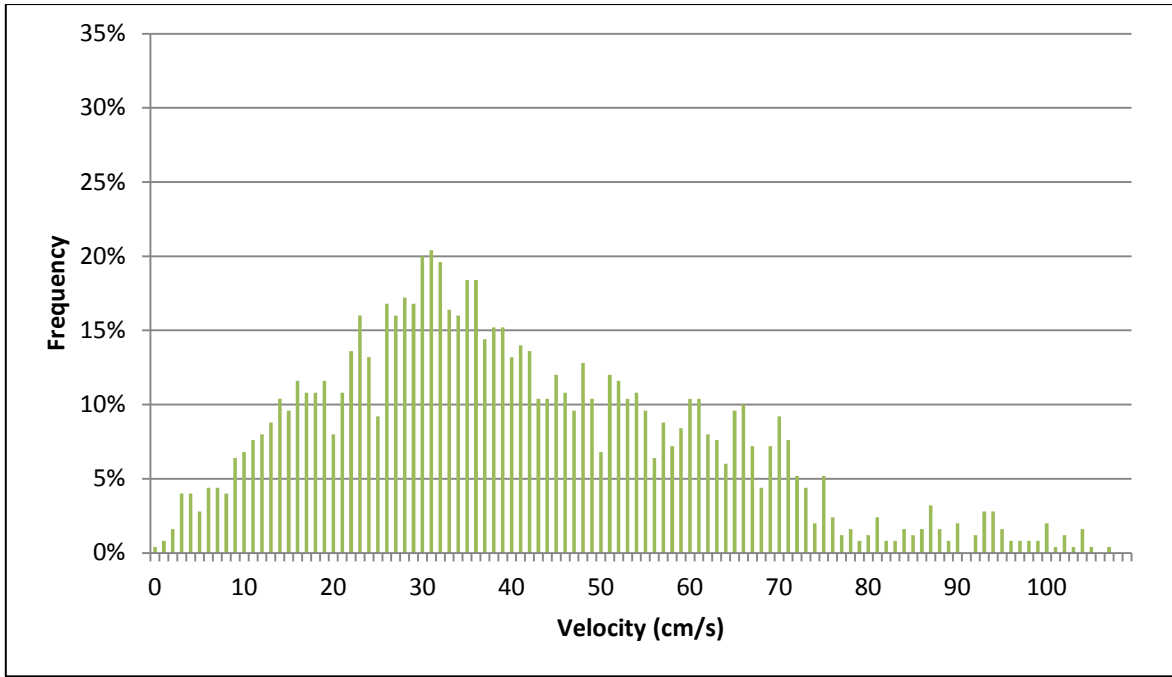


Figure 5-18: Frequency Distribution, East London 87 m

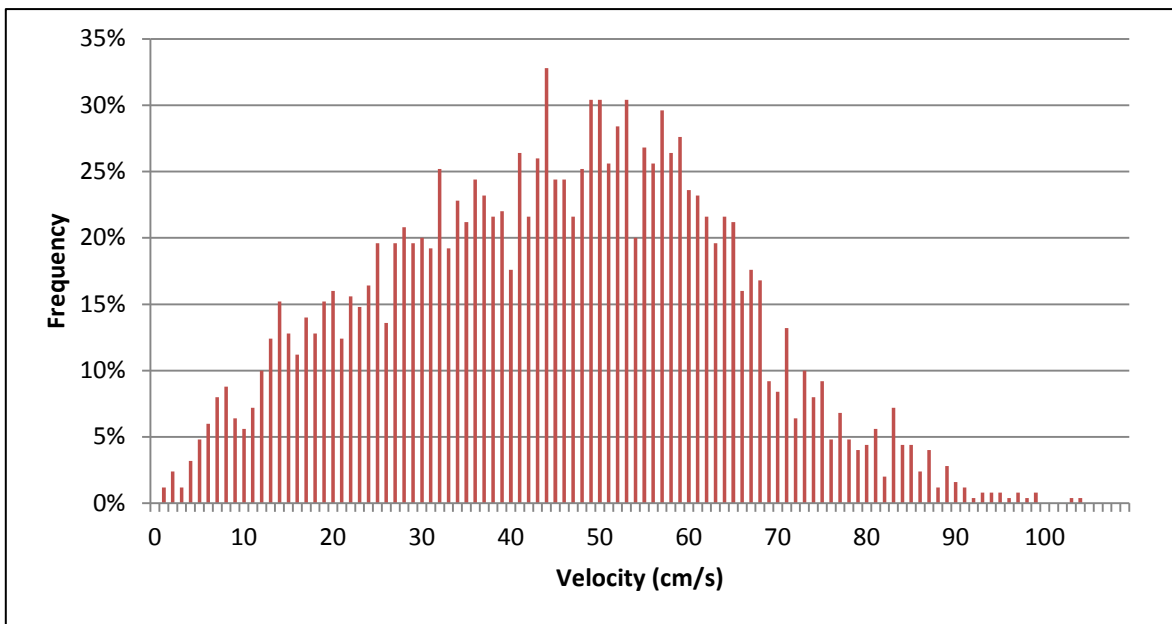


Figure 5-19: Frequency Distribution, East London 94 m

Figure 5-17 illustrates the average velocities for each depth reading against the average depth for each set of data which was analysed. It was observed that for the site of East London, the average velocity of the Agulhas current decreased as depth decreased which is an inverse relationship to that of Cape Morgan. This could be a resultant of geological factors which were not looked into for the current dissertation as it is not in the given scope of work. Bearing this in mind, if the ADCP was conveniently located in a vertically converging

channel which subsequently increased the flow of the current, then this would be a plausible reason for the given result.

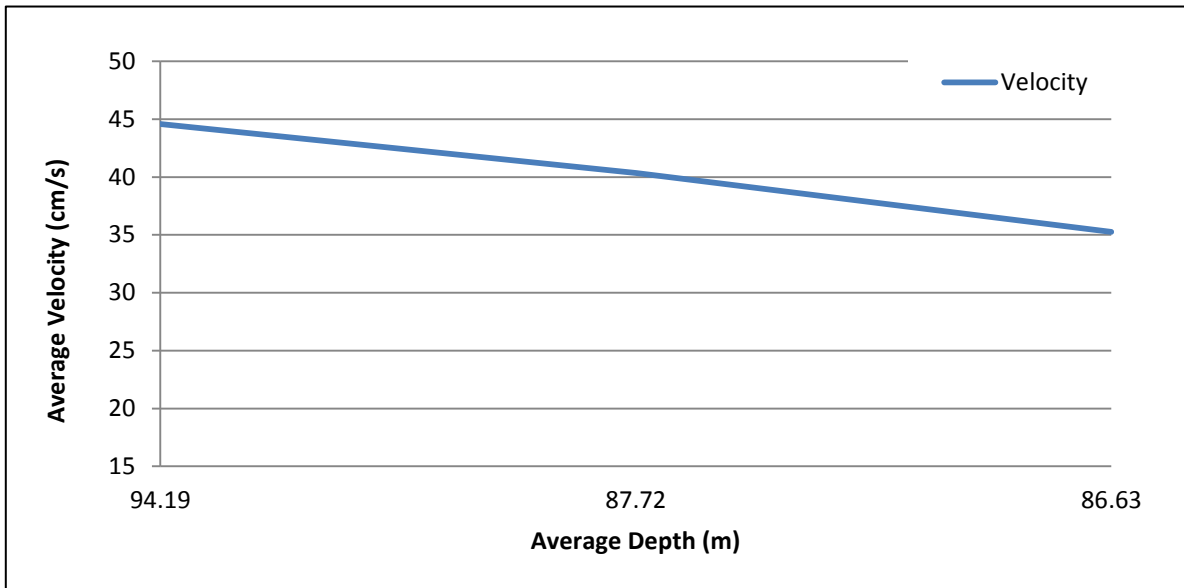


Figure 5-20: Average Velocity Vs. Average Depth for East London

Figure 5-21 below shows the final polar distribution plot which was generated for the East London site. This plot however, shows that the current's profile tends to be more stable as the depth increases towards the surface. Large disturbances and imbalances can be seen in the second plot. This could depict the impact of a Natal pulse at this specific measurement time step as the distribution seems to be moving anti-clockwise with the rotation of the eddy.

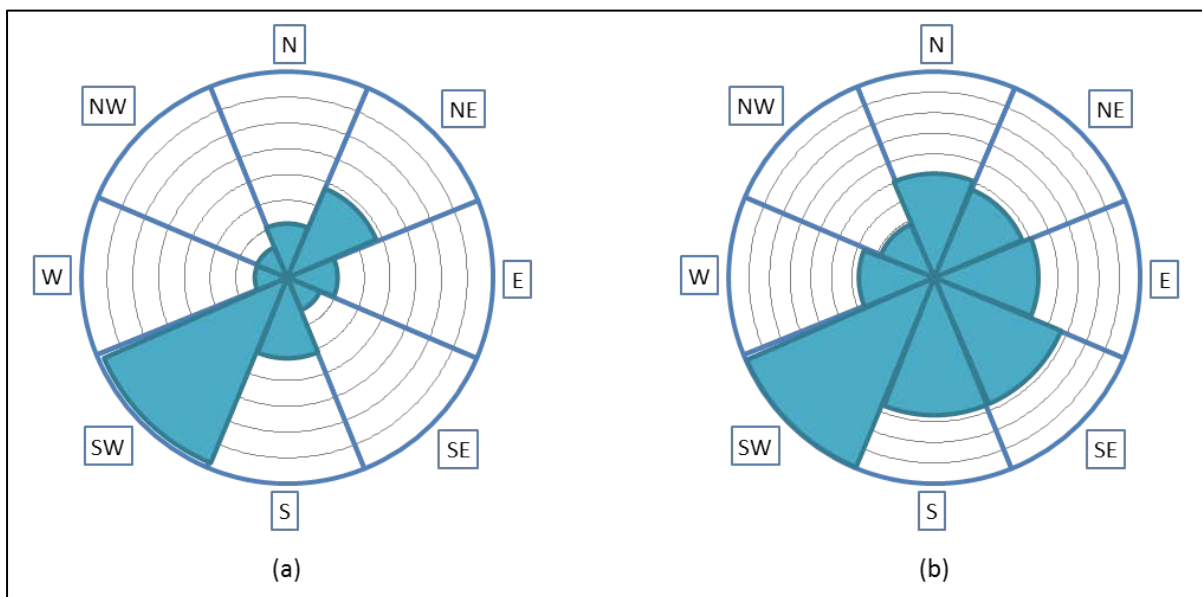


Figure 5-21: Polar Plots - (a) 87 m Depth; (b) 94 m Depth

As stated previously, further study in regions closer to the surface of the ocean would be required with more data for the shallower depths. This is due to the vagarity of the data and inadequate amount of comprehensive data which was made public by Eskom. This data, however, serves as a starting point for the understanding of the Agulhas current at various different sites along South Africa's east coast. Furthermore it allows one to use the results obtained from the data to aid in site selection for deployment of a hydrokinetic turbine system. The site selection analysis will be elucidated in the following section.

5.2 Site Selection

By conducting the relevant analysis on the Port Edward, Cape Morgan and East London sites, a suitable site selection may be chosen based on the results obtained from the analysis. The turbine which was researched in this dissertation is dependent on velocity of the flow medium. By using each site average depth against average mean velocity one can come to a suitable conclusion on site selection, based on frequency and strength of the mean velocity.

As explained in 5.1.1, the mean velocity gradient for the average depth of the recorded results at the Port Edward site yielded a constant gradient line. This meant that the current was a constant value irrespective of the depth that the turbine is deployed. The average speed of the Agulhas flow medium was found to be approximately 30 cm/s.

In 5.1.2, the Cape Morgan site was evaluated for a given period of time. This site data proved to be the most detailed and documented compared to that of the other three site's data. On closer inspection of the average depth against mean velocity of the flow, it was noticed that the flow medium increased in mean velocity as depth from the ocean surface decreased. It was also suspected that the mean velocity would increase substantially at a depth of 20 – 30 m of depth. One could not deploy the turbine higher as this would pass into wave energy and have effects on human factors such as shipping lanes, fishing nets etc. The maximum mean velocity of the flow which was generated by the analysis was found to be 50 cm/s.

In 5.1.3 East London was evaluated on the mean flow velocity against the average depth. It was found on analysis of the generated graph that the data produced a negative gradient. This suggested that the mean velocity of the flow was stronger at deeper depths. One possible explanation for this result was that the ADCP, which was used to measure the current flow and profile it according to direction and temperature, was accidentally deployed in a

converging channel. As the ADCP was left deeper the channel area decreased which increased the flow. The maximum mean velocity for East London was found to be 45 cm/s.

The site for deployment of the turbine was chosen to be Cape Morgan as it is assumed that the velocity of the flow would be higher at shallower depths compared to that of the other sites. This, however, could be corrected in future studies of the ocean's current profiles along the coast of the country. The data which was analysed could change as depth decreases due to the topology of the ocean floor and many other factors. Thus, an adequate site selection cannot be implicitly specified and is beyond the scope of this dissertation.

Wright, et al. [56] conducted research on the Agulhas current ADCP data which was seemingly more extensive than the public data, which was made available to the researchers by Eskom. The analysis for the depths which were analysed in this chapter is in excellent correlation to that of the researchers, proving that the methodology behind the analysis was correct. All of the above data analysis was justified with the respective distribution plots adhering to a similar result as the trend lines associated with each site.

Williams, et al. [57] conducted a similar study using more data which was made available to the researchers from Eskom. The study evaluated the potential amount of power which could be extracted from the Agulhas current based on the ADCP data which was analysed. It was concluded, due to power estimations and the results of the simulations, that the most suitable site would be East London as the surface current tends to be stronger but seemingly more erratic as well. The second most favourable site would then be Cape Morgan, which is what was concluded from the analysis in this chapter as well as stated above.

5.3 Estimated Energy Yield

Figure 5-22 depicts the theoretical power available for various water speeds which is based on the general power equation. This gives a generalised idea on the power density for a given site by knowing the mean velocity for the site being analysed. The figure is a clear indication of the cubic function embedded within the general power equation.

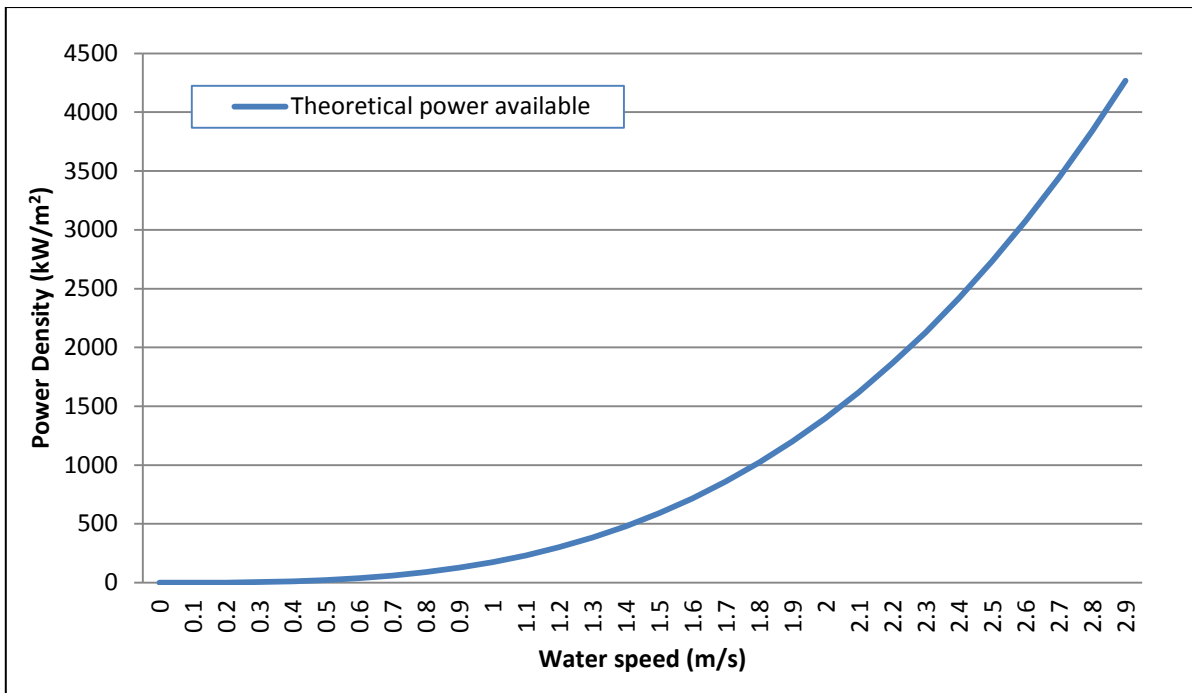


Figure 5-22: Theoretical power available

That being noted, this does not mean that all the power from this curve may be extracted. At higher velocities, most turbines shut down due to potential damage which can be caused to the generator unit. In most designs, a braking system is incorporated where either a mechanical brake is applied to the driving shaft to stop rotation or the blades of the turbine are manoeuvred so as to not generate any lift force or torque onto the drive shaft.

The Weibull distribution is a statistical approximation and generalisation of the Rayleigh distribution. This distribution is often used for energy predictions for wind resource analysis. Due to the similarity of flow between water and wind, the same statistical logic may be implemented in forecasting the resource energy predictions. The Weibull distribution was implemented to an average value (mean) of the current velocity shown in Equation 5.1. The average speed for the Cape Morgan site, which was obtained from the Eskom data, was utilised in the equation. A suitable shape parameter was chosen for the resource based on the current speed, and an annual resource power density was generated. The scale parameter was taken to be the average speed of the flow of the fluid and a shape parameter of 2 was used to avoid a Gaussian convergence, Patel [58]. The chosen shape factor is also typically used for wind resource undergoing the same analysis.

$$h(v, k_s, c) = \frac{k_s}{c_s} \left(\frac{v}{c_s}\right)^{k_s-1} \exp\left[-\left(\frac{v}{c_s}\right)^{k_s}\right] \quad (5.1)$$

where:

v Velocity of flow (m/s)

k_s Shape factor (-)

c_s Scale parameter (m/s)

Equation 5.2, gives the expected power that may be extracted by a given turbine from the flow resource, Hodge [59]. The equation utilises the root mean cubed of velocity coupled with the Weibull distribution to accomplish this. A power coefficient of 0.35 was chosen on the basis of experimental data obtained by Gorlov [11] which directly relates to the Betz limit.

$$\text{Power}_{ext} = C_p \frac{1}{2} \rho V_{rmc}^3 \quad (5.2)$$

where:

C_p Coefficient of Power (-)

ρ Density of fluid (Kg/m³)

V_{rmc} Root mean squared velocity of fluid (m/s)

$$\text{Energy}_{rmc} = C_p \frac{1}{2} \rho \int_0^{\infty} h(v, k, c) \cdot 8750 \cdot V^3 dv \quad (5.3)$$

Figure 5-23 depicts the potential energy of a flow medium for various velocities over a given year based on the average speed of the Agulhas current data taken from the Cape Morgan site. This analysis illustrates that with an average speed of 1 m/s there exists, potentially, an estimated 1 GW of power in the flow medium.

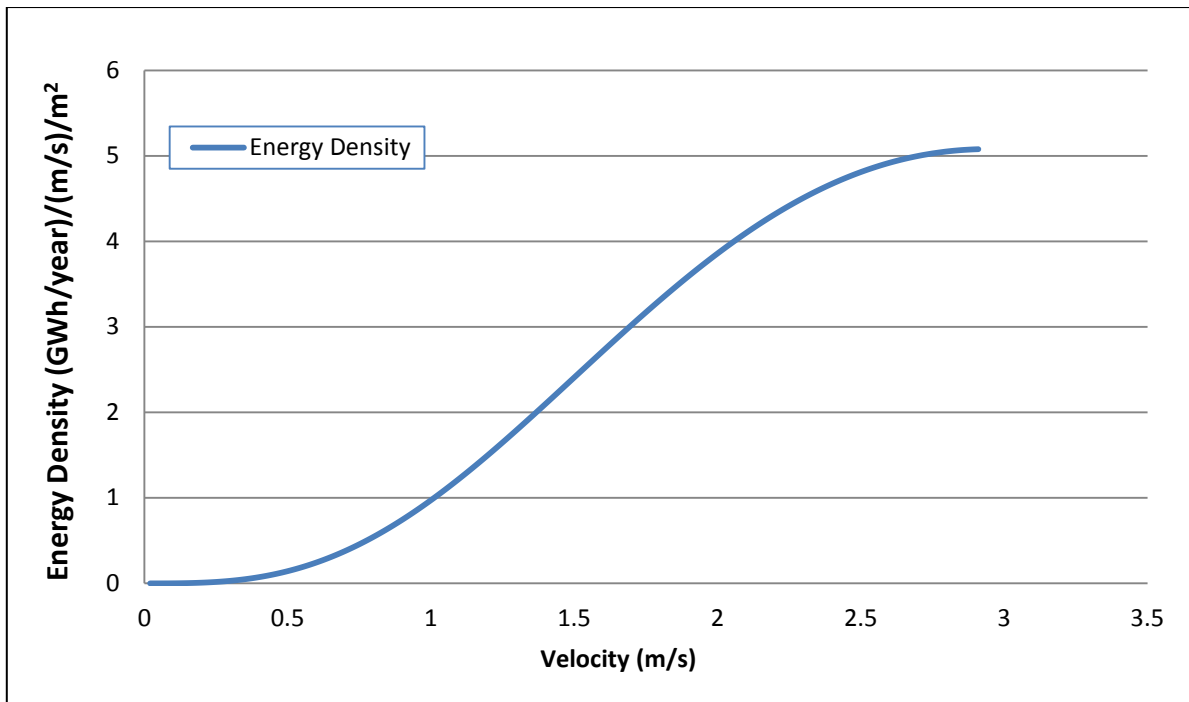


Figure 5-23: Energy density for various current speeds

This power estimation is based on the fact that the turbine will be generating power for the entire year without fail. In reality this cannot be the case and thus a power capacity factor arises. The capacity factor of a power plant is taken as the ratio of the power plant's actual power output, for a recorded period of time, to the power output of the plant if it were to be generating indefinitely at its assigned nameplate generating capacity. The capacity factor is dependent on various factors which the turbine is subjected to and was not simulated.

The analysis of the Agulhas proved to be of significance as it broadened the knowledge and understanding of the ocean resource. The analysis of the Eskom data also gave indications of a potential site which may be of value for extraction of energy. The Agulhas current resource has the potential kinetic energy which may be harnessed for production of commercial energy.

This however does not mean that the turbine may extract all of the energy predicted for the year as the turbine efficiency is directly affected by the generator, drive train efficiencies and other minor losses which occur as the power is transmitted back to shore. Once the turbine has reached its peak efficiency in relation to the generator's peak efficiency, one can determine the amount of energy a single turbine may extract from the flow.

CHAPTER 6 DESIGN OF TURBINE SYSTEM

There are three types of vertical axis marine current turbines. These types of turbines are categorised depending on the forces which they exploit and are as follows: lift based turbines, drag based turbines and hybrid configurations. The following chapter presents a brief review of the different types of vertical axis turbines, the performance parameters of marine current turbines, design of a helical turbine and design of a simple shrouding mechanism used in a turbine system.

6.1 Selection of Turbine

In order to design the helical cross-flow turbine, an understanding of the different types of vertical axis turbines needs to be established. The following section of the chapter briefly describes the three different types of vertical axis turbines which are in existence.

6.1.1 Drag Based Turbines

A drag based turbine exploits the drag force created by the flow medium onto the turbine blades. An excellent example of this turbine is the Savonius turbine which consists of two or more cup like components which are, most commonly, rigidly coupled onto the turbine's central shaft. Figure 6-1 illustrates a simple Savonius turbine component layout. The free stream velocity enters the turbine area and exerts a force on the obstructing area of the turbine cup used causing the turbine to rotate. This form of harnessing energy, however, causes a large amount of flow obstruction which consequently decreases the amount of power which may be extracted from the flow. Additionally, the turbine harnesses the drag force which is created by the flow causing multiple stagnation points on the turbine cup. This requires the turbine to be structurally stable and could lead to extra support being incorporated which may decrease the performance of the turbine substantially.

On a positive note, the Savonius turbine generates substantially greater torque than that of a lift based turbine which is the main factor when operating generators which require high torque input from their source input devices. The added torque from the turbine easily overcomes the starting or "cogging" torque from the generators excitation components. New developments in turbine generators lead to lower cogging torque by removing the excitation component. An example of these generators is the permanent magnet generator (PMG) which also reduces the need for a step up gearing or pulley mechanism. By reducing the amount of

components between the source generating unit (Turbine) and the electrical generating unit, one in effect, increases the efficiency of the system.

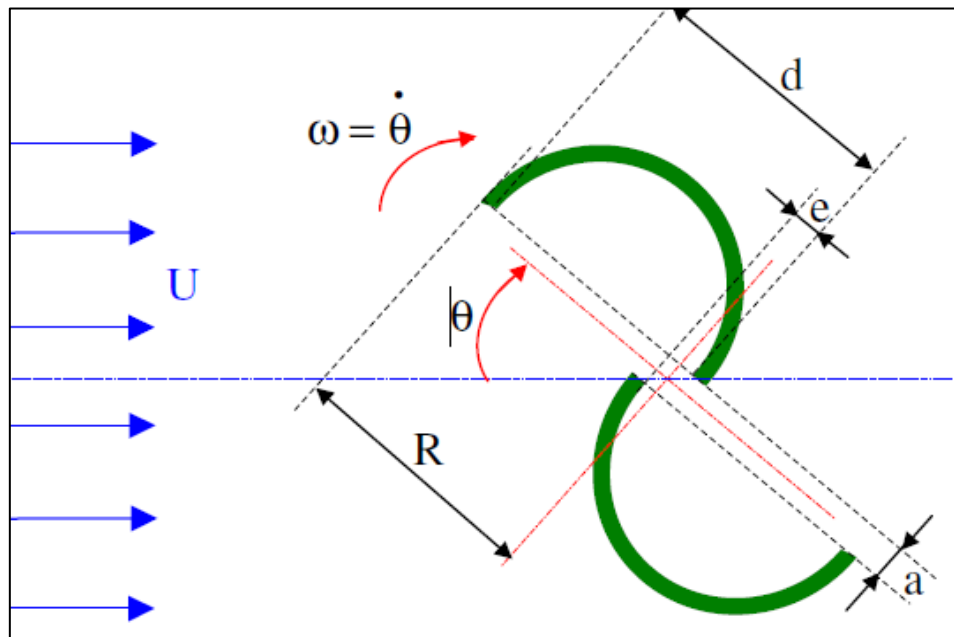


Figure 6-1: Savonius turbine, Menet [60]

The concept of a drag based turbine is attractive to most individuals as it becomes instinctive that the capturing area of the cup like blades would result in a more effective turbine. However, this is a misconception as the efficiency of this type of turbine dramatically decreases as the flow speed increases. This is due to high turbulence, swirl and blockage within the shaft region.

6.1.2 Lift Based Turbines

A lift based turbine uses aerofoils or, in a hydrodynamic environment, hydrofoils to exploit the lift force generated by the profile from the flow resource medium. This type of turbine is conventionally used by the wind turbine industry. These types of turbines are being incorporated into ocean and river current turbines. The first research conducted on this type of turbine was done by G.J. Darrieus and his turbine was patented in the 1920's. The two most common types of Darrieus turbines are the troposkein turbine and the Darrieus straight bladed turbine which are illustrated in Figure 6-2 below.

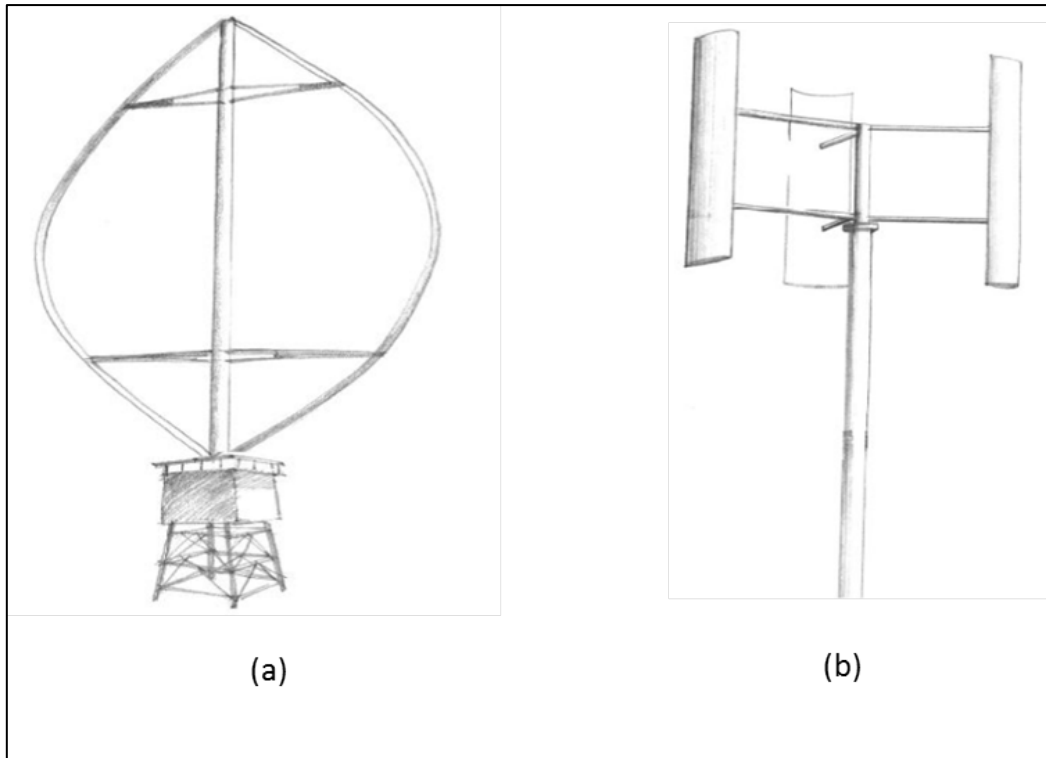


Figure 6-2: (a) Darrieus troposkein turbine, (b) Darrieus straight bladed turbine, Niblick [15]

The straight bladed Darrieus turbine incorporated airfoil profiles which generated a higher lift force compared to the drag force. The airfoil profiles which are oriented in a vertical orientation allow the turbine to accept flow from any direction and is thus termed a cross-flow turbine. By exploiting the lift force of the aerofoils, the resultant force results in rotation of the central shaft creating torque about the axis of rotation.

Figure 6-3 depicts the vector diagram of the straight bladed cross-flow turbine at the four main areas of the turbine's rotation. This diagram also depicts the angle of attack at these different positions of the blades. The lift based turbine operates at a higher tip speed ratio than that of the Savonius turbine which means that a higher operating speed is created by a lift based turbine. This is advantageous as the torque to speed relation of a lift based turbine is more compatible with conventional generators than that of the Savonius turbine. By incorporating the new PMG's, the lift based turbine relatively low cut in speed allows for some power generation at low speeds as the PMG can operate fairly well under low input revolutions.

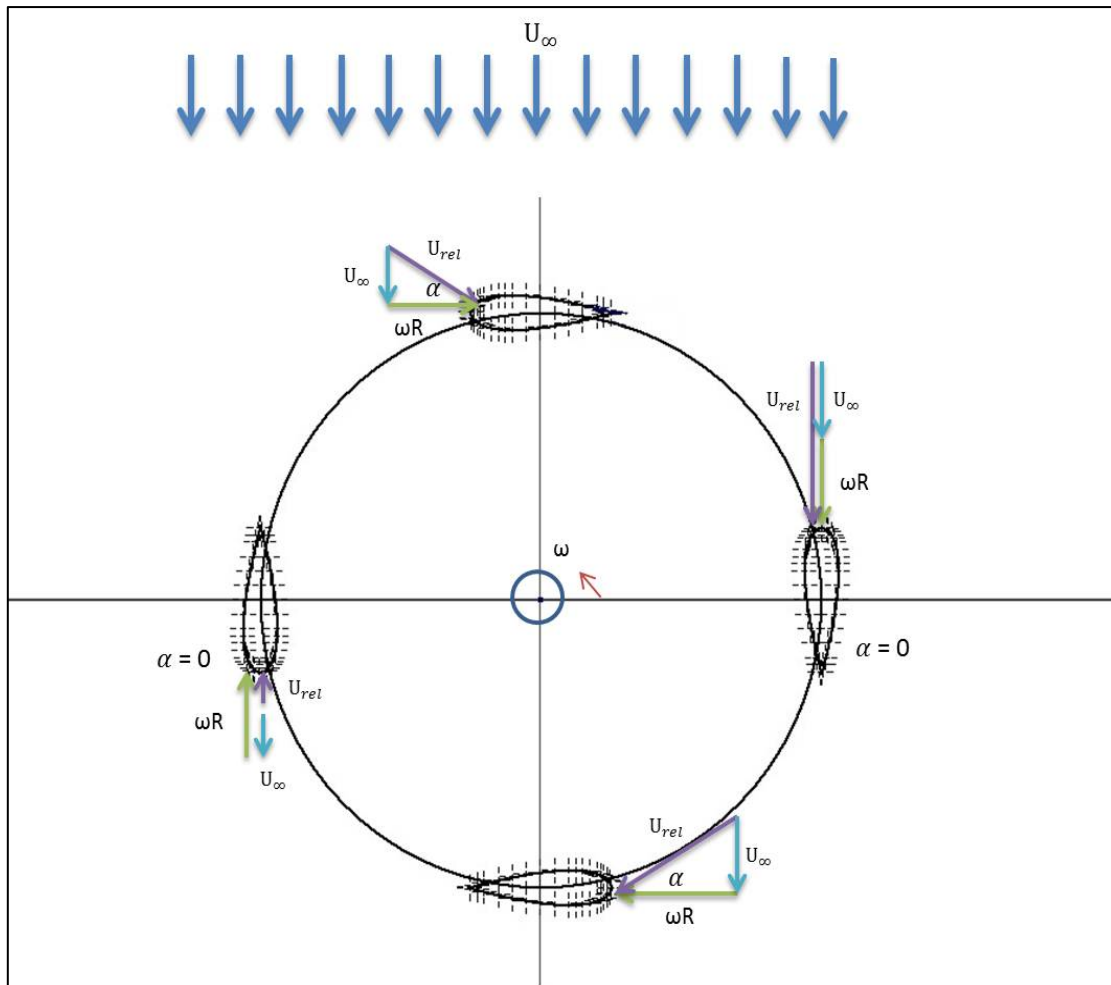


Figure 6-3: Vector diagram of turbine

The cross-flow turbine designed by Darrieus was further examined by various other researchers and the general conclusion of this turbine was that it exhibited torque fluctuations on the central transmitting shaft when the turbine is in operation. These fluctuations increased proportionally to the tip speed of the turbine. Gorlov found that the straight bladed turbine exhibited high amounts of vibration and concluded this to be a result of torque fluctuations which stemmed from void space between the turbine blades as a result of no blade overlap. The effect of these vibrations directly influenced the fatigue life of the turbine blades and that of the generated power. Gorlov [11] used the straight bladed turbine as a basis for his cross flow turbine which incorporated a helical blade profile rather than a straight blade which can be seen in the designed turbine in Figure 6-4 below. By this new addition of the helical blade profile Gorlov seemingly created a turbine with blade overlap thus eliminating the void space between blades. Through various tests and simulations, Gorlov concluded that his turbine exhibited far less torque fluctuations compared to that of the Darrieus turbine which was a result of the helical blade profile.

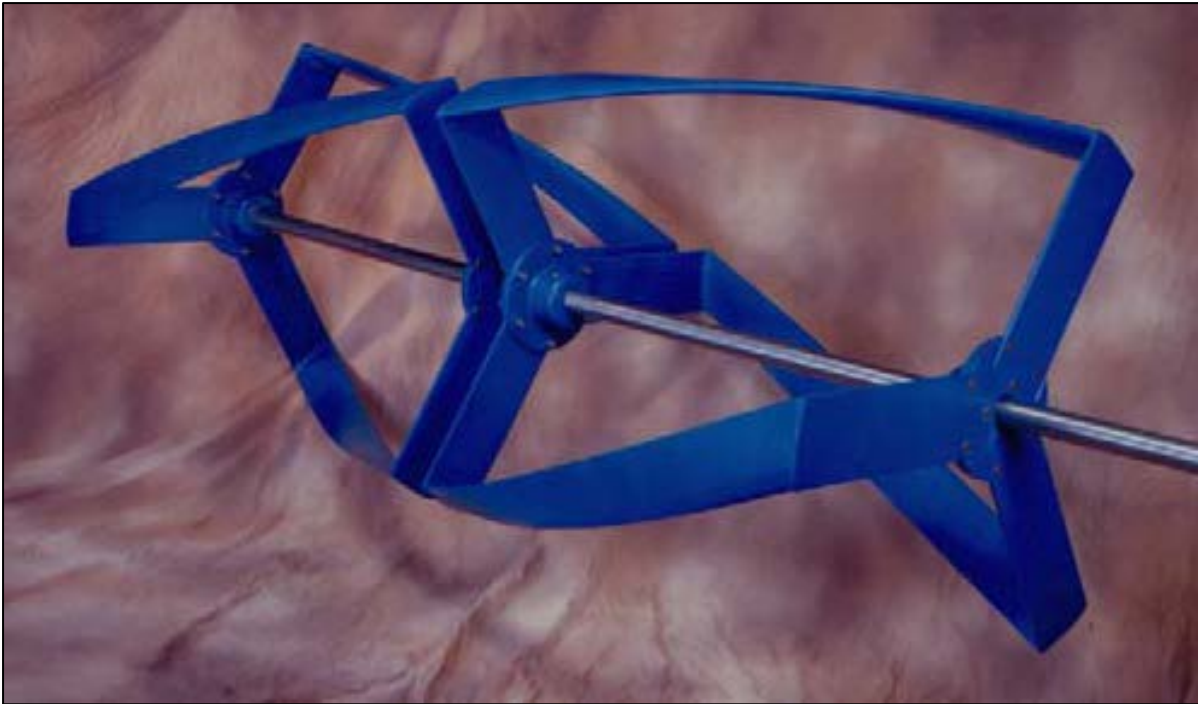


Figure 6-4: Gorlov helical turbine, Gorlov [61]

Another common flaw with the Darrieus straight bladed turbine is its poor self-start capabilities. To improve this, a Savonius turbine was coupled to the Darrieus turbine's central shaft to increase the torque and allow the turbine to start at low Reynolds numbers which is briefly described in the next section. Other methods such as increasing blade pitch to induce lift more rapidly is also being investigated to increase self-start capabilities and torque which subsequently increases turbine performance.

Khan [62] and Shino, et al. [26] conducted various experimental tests on Darrieus straight bladed turbines used for marine current applications. The joint conclusion was that even with the poor self-start characteristics, torque fluctuations and excessive turbine vibrations, the efficiencies were as high as 33% for flow speeds of 1.2 m/s. Taking into consideration that the torque and vibrational characteristics are minimised for the Gorlov helical turbine, it may be assumed that the turbine would exhibit higher efficiencies under the same loading conditions as the Darrieus turbines.

6.1.3 Hybrid Turbines

As mentioned in the previous section, the self-start characteristics of the Darrieus turbine was of concern and thus a hybrid system was used which consisted of a straight bladed Darrieus turbine which incorporated a Savonius turbine within it. Alam and Iqbal [8] conducted

experimental tests on the combination of turbines to prove that the addition of the Savonius turbine increased the torque of the turbine at low tip speed ratios and once the start-up torque threshold was overcome, the Darrieus turbine's lift forces would take over to allow the turbine to reach the full operating speed. Figure 6-5 below shows the hybrid configuration of the Darrieus and Savonius turbine.

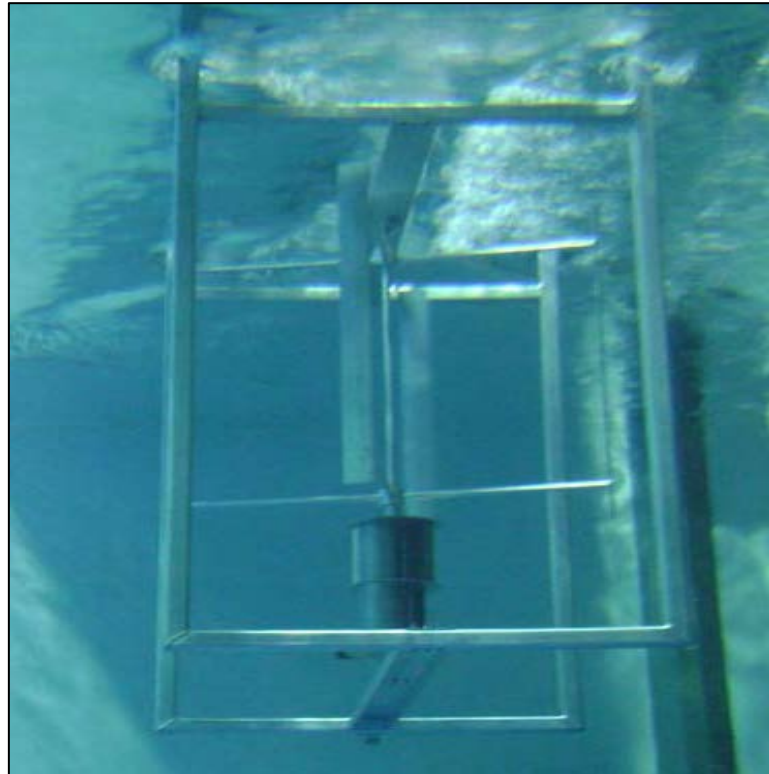


Figure 6-5: Hybrid turbine tested in water, Alam and Iqbal [8]

One of the design challenges faced by this type of configuration is the difference in the individual turbine optimum tip speeds. The Darrieus turbine operates at its peak efficiency at a relatively higher tip speed than that of the Savonius turbine. The most optimum solution to this challenge was to scale each turbine accordingly so that both reach optimum efficiency relative to the tip speed of the entire system. If the scaling of both turbines is incorrect, then the Savonius turbine results in increased drag force onto the Darrieus turbine and reduces efficiency of the entire system. The results obtained by Alam and Iqbal depicted very low power output. This could be due to inadequate research into the scaling of both turbines to both reach optimum efficiency as stated previously.

6.2 Hydrodynamics of the Cross-Flow Turbine

The notion of using a cross-flow turbine as a potential energy generating source is not new but the understanding of the hydrodynamics and physics of the turbine's behaviour is still in development. Although the development of wind turbines and hydropower turbines has increased in recent years, there still is no complete characteristic comparison to hydrokinetic turbines. There exist differences between traditional wind turbines and hydrokinetic such as very different changes in Reynolds number, varying inflow conditions, different blade stall characteristics and in some cases the possibility of cavitation. These factors are addressed in order to successfully implement a marine current cross-flow hydrokinetic turbine. This section describes the basic hydrokinetic behaviour that a cross-flow turbine would normally encounter.

One of the main characteristics which is monitored for any turbine is the amount of power which is extracted from the flow medium. This requires an understanding of the available power that exists within the resource fluid flow that is to be harnessed. This is done by applying the standard power equation which is a measure of the rate of passing kinetic energy. The power available in the flow medium is given by:

$$P_{available} = \frac{1}{2} \rho A_c U_{\infty}^3 \quad (6.1)$$

Equation 6.1 shows that the amount of power is directly proportional to cube of the speed of the fluid flow medium. All the components of the equation play an integral role in designing a cross flow turbine. The turbine cross-sectional area (A_c) which is where the flow enters the turbine is a key component on having a rough estimate of the amount of power which to be extracted. Although the average speed of the ocean current to be considered in this study is roughly 1 m/s to 1.5 m/s, which is significantly lower than that of wind speed, this does not mean that a hydrokinetic system extracts less power since the density of water to air is roughly 832 times greater.

The dynamics of the cross-flow turbine is in itself quite complex as the fluid interaction and flow field is highly unsteady and is mostly three dimensional. This is due to the interaction of the shed vortices produced by the blades in the upwind side of the turbine which impacts the downwind side of the turbine negatively. In addition to these factors, dynamic stall also

affects the turbine adversely as the blades are constantly changing the angle of attack throughout the rotation of the turbine. Bearing in mind the complex nature of the problem, an excellent starting point for understanding the problem is to apply the Blade Element Momentum (BEM) theory.

Figure 6-6 depicts the velocity triangles of an infinitesimally small cross-section view of the turbine's blade at various different positions of its rotation. The blade position is illustrated by its azimuthal coordinate θ . As the blade changes its position the blade is rapidly changing its angle of attack (α) and subsequently experiences resultant velocities (U_{Rel}) which are a function of azimuthal angle.

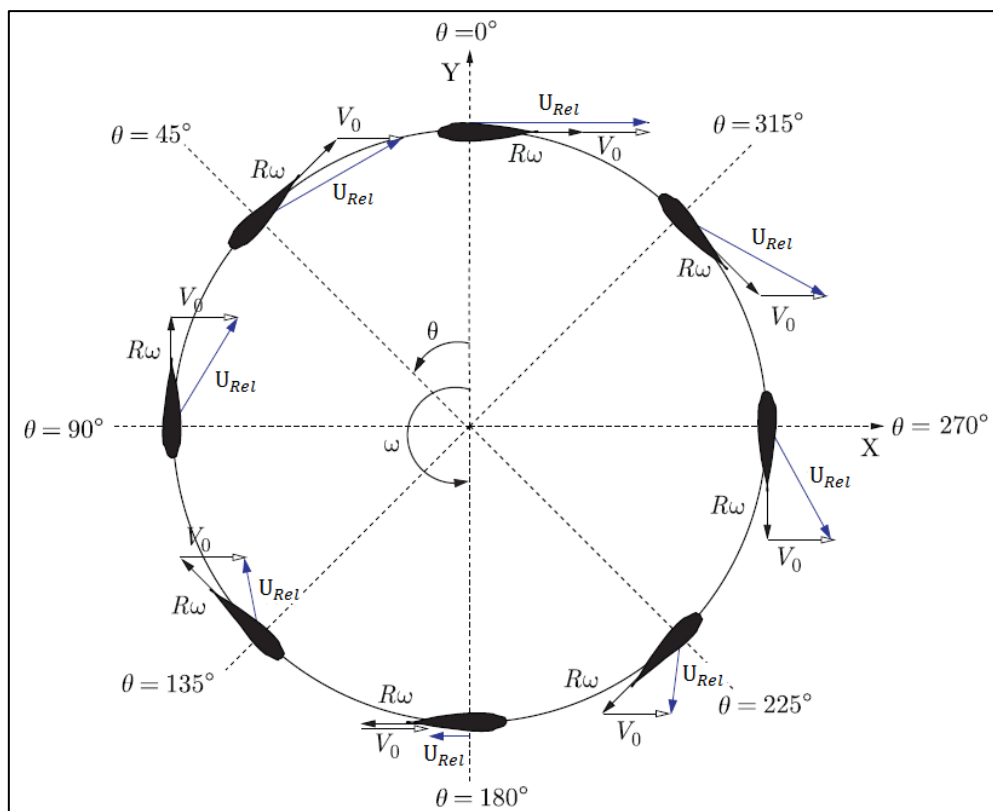


Figure 6-6: Velocity triangle for cross flow turbine, Antheaume, et al. [63]

U_{Rel} is the resultant velocity that is created from the free-stream (U_∞ depicted as V_0 above) and rotational ($R\omega$) velocity components. A blade is a continuously changing velocity component; the velocity changes as a function of azimuthal position of the blade in the local coordinate system of the turbine and is calculated as follows, Biadgo, et al. [16]:

$$U_{Rel} = \sqrt{(U_\infty + \omega R \cos \theta)^2 + (\omega R \sin \theta)^2} \quad (6.2)$$

Where:

U_{Rel}	Relative Velocity (m/s)
U_{∞}	Free Stream Velocity (m/s)
R	Radius of the turbine (m)
ω	Rotational Speed (rad/s)
θ	Azimuthal Angle ($^{\circ}$)

The angle of attack is determined by incorporating a relationship between the resultant velocity and the tip speed ratio of the turbine. This method of determining the angle of attack allows one to fully understand the theoretical attack angle of the blade through one full revolution of the blade. The angle of attack (α) is calculated as follows:

$$\alpha = \frac{\sin\theta}{\cos\theta + \lambda} \quad (6.3)$$

Where:

α	Angle of Attack ($^{\circ}$)
θ	Azimuthal Angle ($^{\circ}$)
λ	Tip Speed Ratio (-)

Figure 6-7 depicts the attack angle for various tip speed ratios. This also helps one to understand and visualise how and where the changing of attack angles for various azimuthal positions coincide with the stall angles determined for the hydrofoil which is being implemented. It can also be seen that the angles of attack change rapidly during the turbine blade's rotation. The rate of change of angle of attack is directly proportional to the tip speed of the turbine. Low tip speed ratios of the turbine affect the turbine performance negatively as the angles of attack at these tip speeds coincide with dynamic stall angles.

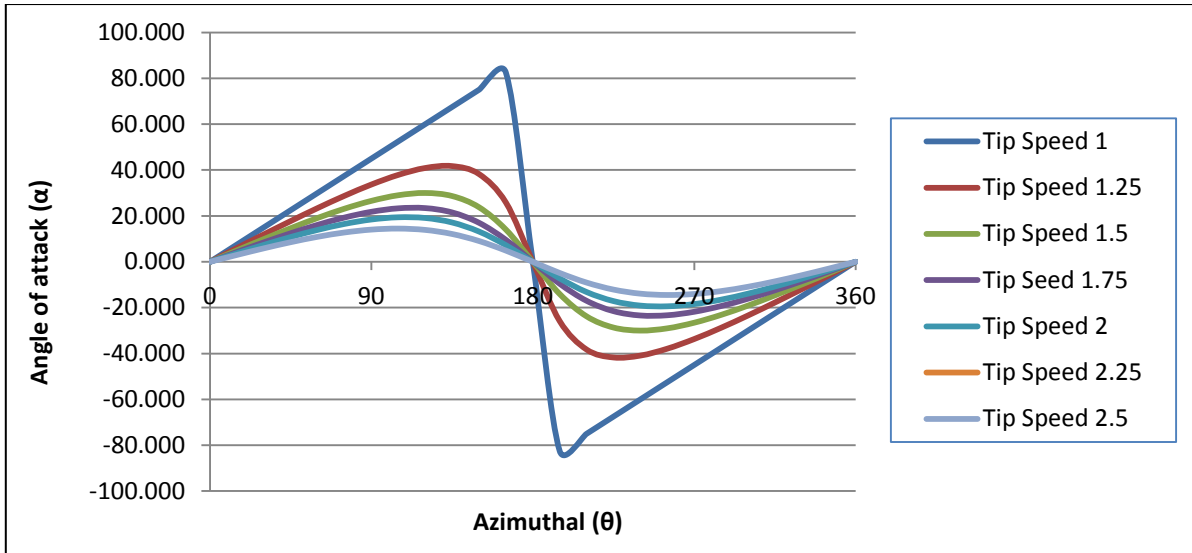


Figure 6-7: Angle of attack Vs. Azimuthal Angle

The turbine circumferential area is divided into two sections which are described by using the turbine central shaft as a reference point. The upstream pass (flow entering the turbine before interacting with the turbine shaft) results in positive attack angles and the downstream pass (flow leaving the turbine after interaction with the turbine shaft) results in negative attack angles. This sectional division of the turbine is also used in analytical momentum modelling. The sectional division of the turbine circumferential area is illustrated in Figure 6-8.

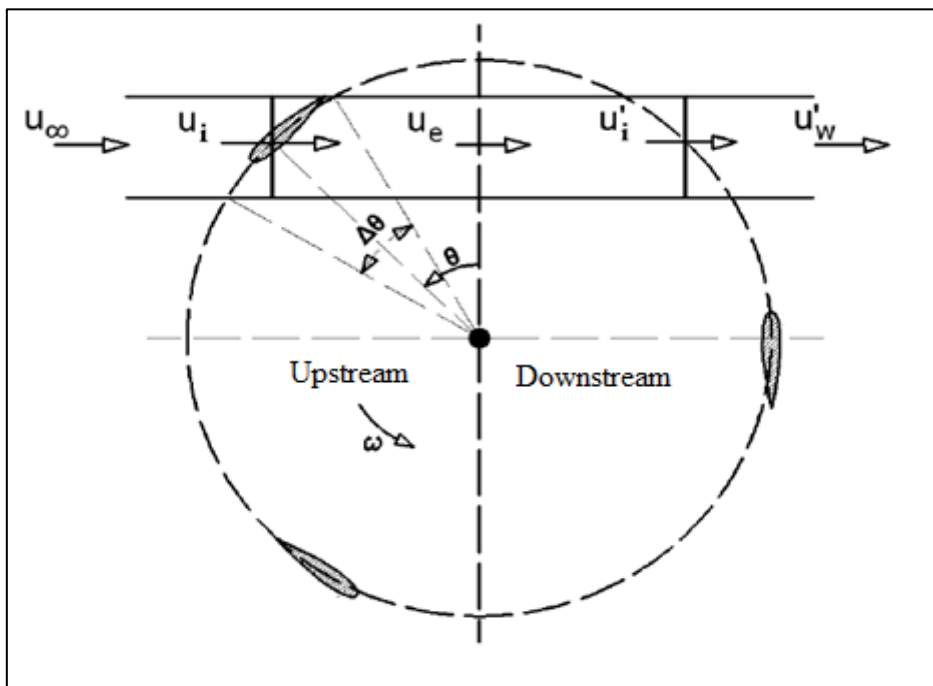


Figure 6-8: Upstream and downstream of turbine, Biadgo, et al. [16]

Further investigation into the turbine blade Reynolds number was conducted to understand the flow regime around the blade at various tip speed ratios. This was conducted by holding the rotational speed constant and obtaining the various free stream velocity for various tip speed ratios. This was conducted so as to vary the relative velocity which consequently varies the blade Reynolds number. Figure 6-9 depicts the blade Reynolds numbers for various tip speed ratios for a full revolution of the turbine blade. The figure depicts that the Reynolds number is directly influenced by the relative velocity of the turbine blade. As the Reynolds number increases, the lift and drag coefficients change respectively. This also allows one to obtain a rough understanding of the optimum tip speed that the turbine should operate under to achieve maximum power output.

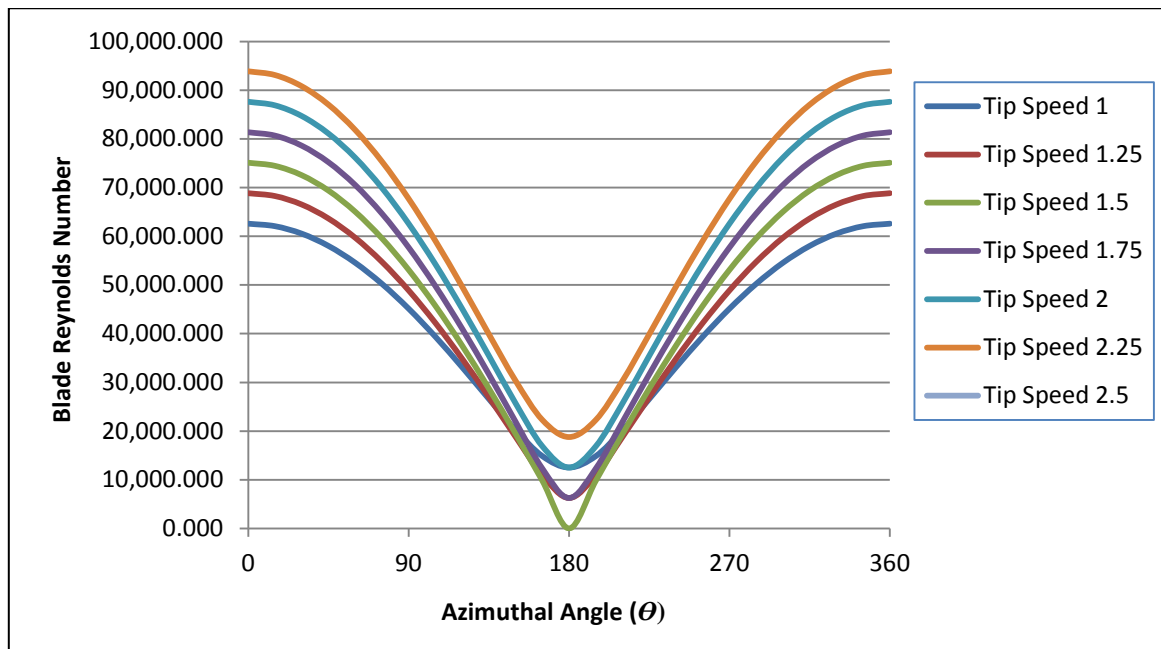


Figure 6-9: Blade Reynolds number for one full blade revolution

Initially the turbine blade analysis was conducted on a turbine with 0° blade pitch. Research conducted by Fiedler and Tullis [64] found that a toe-out blade pitch configuration is advantageous for the performance of the turbine compared to that of a toe-in blade pitch configuration. Fiedler and Tullis also found that the most optimum toe-out angle was between 3° and 8° . The angle of attack changes incorporating the pitch angle of the blade (β) is calculated as follows as described in [64]:

$$\alpha = \frac{\sin\theta}{\cos\theta + \lambda} - \beta \quad (6.4)$$

The cross flow turbine was chosen so as to exploit the lift force generated by the fluid flow on the turbine blades. The blades however, do still experience drag as they rotate. The lift (C_L) and drag (C_D) coefficients are directly related to the lift and drag force for the given blade geometric profile. The coefficients of lift and drag were obtained from Sheldahl and Klimas [65] as this provided various lift and drag coefficients for various Reynolds numbers. The lift and drag coefficients are respectively given as follows:

$$C_L = \frac{L}{0.5 \rho U_{rel}^2 c H} \quad (6.5)$$

$$C_D = \frac{D}{0.5 \rho U_{rel}^2 c H} \quad (6.6)$$

Where:

- L Lift force on profile centre of pressure (N)
- D Drag force on profile centre of pressure (N)
- c Chord length of airfoil profile (m)
- H Turbine height (m)
- ρ Density of fluid (Kg/m³)

Applying equations 6.5 and 6.6 to different azimuthal positions of the blade provide a very basic understanding of the forces generated by the flow but this does not give an accurate depiction of the flow behaviour within the vicinity of the turbine. The resultant of these forces generates torque on the turbine shaft which is used to drive the coupled generator. This forms the basis for obtaining the torque coefficient (C_Q).

$$T = R(L \cos \alpha - D \sin \alpha) \quad (6.7)$$

where:

- T Torque (Nm)
- R Radius of turbine (m)

The blade element model provides a good starting point to understand the physics for the cross flow turbine but to obtain a more refined analytical result, the double multiple stream tube model was adopted. Another issue which could not be properly modelled using the basic lift and drag equations are the shed vortices which are caused by the turbine blades in the upwind section of the turbine. There was also the dynamic stall component of the blade profiles which demonstrates that the coefficients of lift and drag are not solely dependent on the angle of attack, but also directly dependent on the rate of change of the angle of attack for a sectional piece of the blade nearing the theoretical stall angle of that blade profile. These concepts are further explained in the turbine modelling section of the dissertation.

6.3 Turbine Performance Parameters

For any turbine, performance parameters need to be understood and properly used in order to understand how the turbine would perform under various different operating conditions. Hydrokinetic and wind turbines are characterized by a set of well-known non-dimensional parameters which outlay the turbine's performance. This section outlines the parameters which were used in the development of the hydrokinetic cross-flow turbine.

One of the principal parameters which are used is the turbine tip speed ratio (λ). This is a ratio of the turbine's blades rotational speed relative to the free stream speed of the resource which is being harnessed and is expressed as follows:

$$\lambda = \frac{R\omega}{U_{\infty}} \quad (6.8)$$

where:

λ Tip Speed Ratio (-)

R Turbine Radius (m)

ω Rotational speed of the turbine (rad/s)

U_{∞} Free stream velocity (m/s)

The torque coefficient of the turbine (C_Q) is defined as the ratio of torque generated by the turbine as a result of the flow resource being harnessed if all the kinetic force of the fluid medium could be concentrated from the full radius of the turbine. The torque may be taken as

the cross product of the force which acts at the centre of pressure of the hydrofoil which is being implemented.

$$C_Q = \frac{T}{0.5\rho U_\infty^2 R A_c} \quad (6.9)$$

where:

- C_Q Coefficient of torque (-)
- T Torque on turbine (Nm)
- A_c Turbine cross-sectional swept area (m^2)
- ρ Density of fluid (Kg/m^3)

When the torque produced by the turbine is measured or calculated, the amount of power which can be extracted from the turbine shaft may also be calculated by means of the power coefficient (C_p). The power coefficient is the ratio of extracted power from the turbine to the theoretical power of the fluid resource. The unit-less value can also be directly related to the torque coefficient and tip speed ratio. The power coefficient may also be viewed as the turbine's efficiency.

$$C_p = \frac{T\omega}{0.5\rho U_\infty^3 A_c} = C_Q \lambda \quad (6.10)$$

As in any design which involves an application in a fluid flow environment, there exist various Reynolds numbers which need to be considered when designing. In the case of a hydrokinetic turbine the turbine Reynolds number (Re_T) and blade Reynolds number (Re_B) are highly important parameters. The turbine Reynolds number describes the fluid flow from the perspective of the turbine relative to the free-stream velocity entering the turbine.

$$Re_T = \frac{U_\infty D}{\nu} \quad (6.11)$$

The blade Reynolds number describes the fluid flow from the perspective of the blade to the flow entering the turbine circumferential blade area. In both instances the same kinematic viscosity (ν) is used for water.

$$Re_B = \frac{U_{Rel}c}{\nu} \quad (6.12)$$

Another key parameter is the solidity ratio of the turbine. This is the measure of solid space to void space of the turbine. The term may be defined in many ways but for the purpose of this dissertation is defined as follows:

$$\sigma = \frac{Bc}{\pi D} \quad (6.13)$$

Where:

σ	Solidity Ratio (-)
B	Number of Blades (-)
c	Chord Length (m)
D	Diameter of the turbine (m)

The above equation depicts that the solidity is dependent on the turbine's physical parameters. Previous research indicates that for a low solidity ratio the turbine would operate at peak efficiency at a higher tip speed ratio and for a higher solidity ratio the turbine would achieve peak efficiency at a lower tip speed ratio. Gorlov [11] concluded that for a helical turbine with a solidity of 0.27, an efficiency of 35% was achieved.

6.4 Helical Turbine design parameters

When designing the helical turbine several parameters needed to be examined. While some of these parameters were similar to most turbine designs, other parameters were unique to the development of the helical turbine examined in this dissertation. The following section describes parameters which were obtained with the aid of previous experimentation and analytical modelling with regards to previous helical and Darrieus turbine designs.

6.4.1 Hydrofoil Profile

For any turbine which may be examined the components which are of extreme importance are the turbine blades. These are the components which facilitate the extraction of energy from the fluid flow medium. The forces from the fluid flow onto the obstructing blades occur

on the centre of pressure of the blade profile. The fluid exerts both a normal and tangential force on the blade resulting in a substantially greater lift force to drag force on the blade which causes the rotation.

Some of the parameters which directly affect blade design are blade profile thickness, chord length, leading and trailing edge profiles, blade thickness-to-chord ratio and blade camber. The chord length of a blade is the line which connects the blade leading edge to the trailing edge of the profile. Blade camber can be defined as the location of the blade's mean thickness along the length of the blade. There are symmetrical and unsymmetrical blade profiles which may be considered when selecting hydrofoil shapes for the turbine. The symmetric blade (uncambered) blade is a profile which is symmetrical about the chord line.

Originally the standard NACA 4 digit series blade profiles were implemented for previous vertical axis wind turbines (VAWT's) due to the availability of a vast number of lift and drag coefficient data for various different Reynolds numbers. Islam, et al. [66] conducted research on the performance of other profiles and compared the data to that of the NACA series and concluded that the NACA series profiles performed poorly compared to other blade profiles. Their results showed that for optimum turbine performance the hydrofoil needs to be cambered facing concave outwards from the turbine centre of rotation, and have a relatively thick blade profile where a large leading edge radius exist in conjunction to a sharper trailing edge.

Islam, et al. [66] noted the blade profiles which were superior to the standard NACA 4 digit symmetrical profile series. Experimentation was conducted for a low Reynolds number as the starting capabilities for a standard VAWT system is low. Examination of the same profiles was conducted for a high Reynolds number for a helical turbine using Islam, et al. superior blade profiles. A low high Reynolds number was chosen for the helical turbine as the helical shape of the turbine blade configuration eliminates the self-start problem encountered by standard VAWT systems.

On analysis of the turbine's requirements to produce power, it was concluded that a larger torque is required from the turbine shaft to operate a generator which is to be coupled to it. Niblick [15] found that symmetric airfoil profiles generated a higher torque compared to that of cambered profiles in the downstream part of the turbine when the attack angle is negative. Kirke [67] explains that the majority of power extracted from a vertical axis turbine is

obtained in the upstream pass of the blades. This would conclude that a suitable cambered blade profile would be highly advantageous compared to that of a symmetrical profile. Figure 6-10 depicts the lift coefficient for the various airfoil profiles. The coefficient of lift was of interest as the helical turbine exploits the lift force from the blades to achieve rotation.

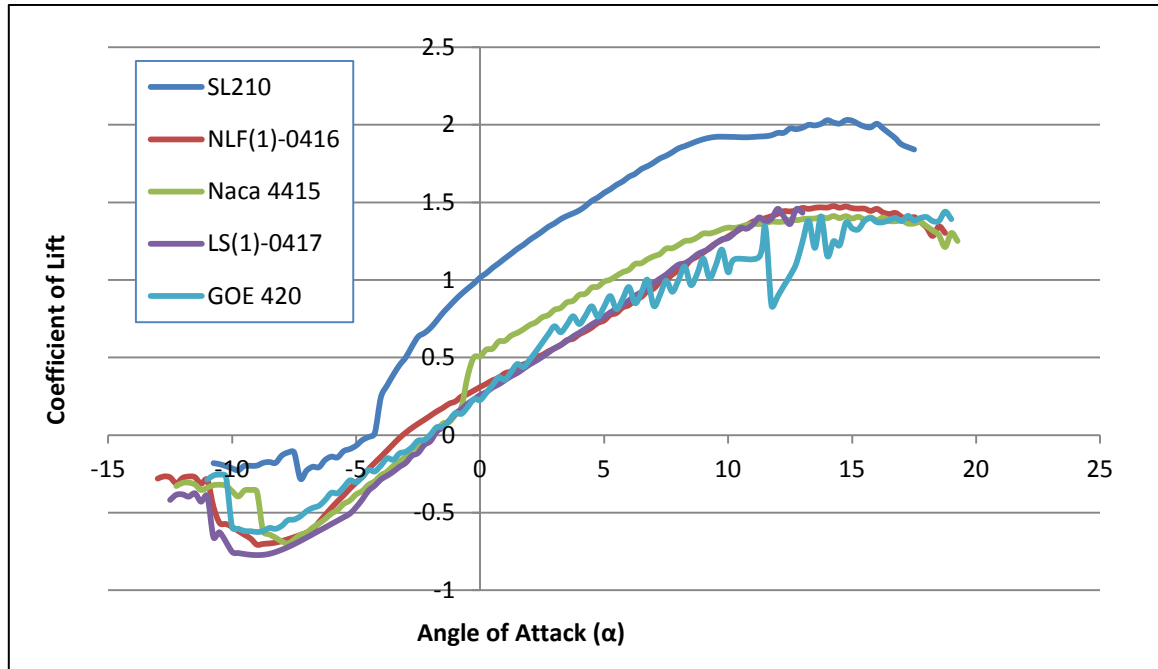


Figure 6-10: Coefficient of lift for superior cambered blade profiles

A symmetrical profile was chosen for the design of the turbine for this project as a cambered blade profile proved costly and difficult to manufacture. The sharp trailing edges of the cambered profiles render the blades fragile and unsusceptible to high loading. The symmetrical profile hydrofoil would produce an adequate amount of torque in both the upstream and downstream pass to generate the required amount of power without significant losses compared to that of a cambered profile.

Figure 6-11 depicts the coefficient of lift plotted against the angle of attack for various NACA symmetrical profiles. It can be seen that the NACA 0024 blade profile exhibits a greater lift coefficient trend compared to that of the other commonly used airfoil profiles. This profile is also in agreement with Islam, et al. [66] attributes, such as high leading edge radius and sharp trailing edge even though it is a symmetrical profile.

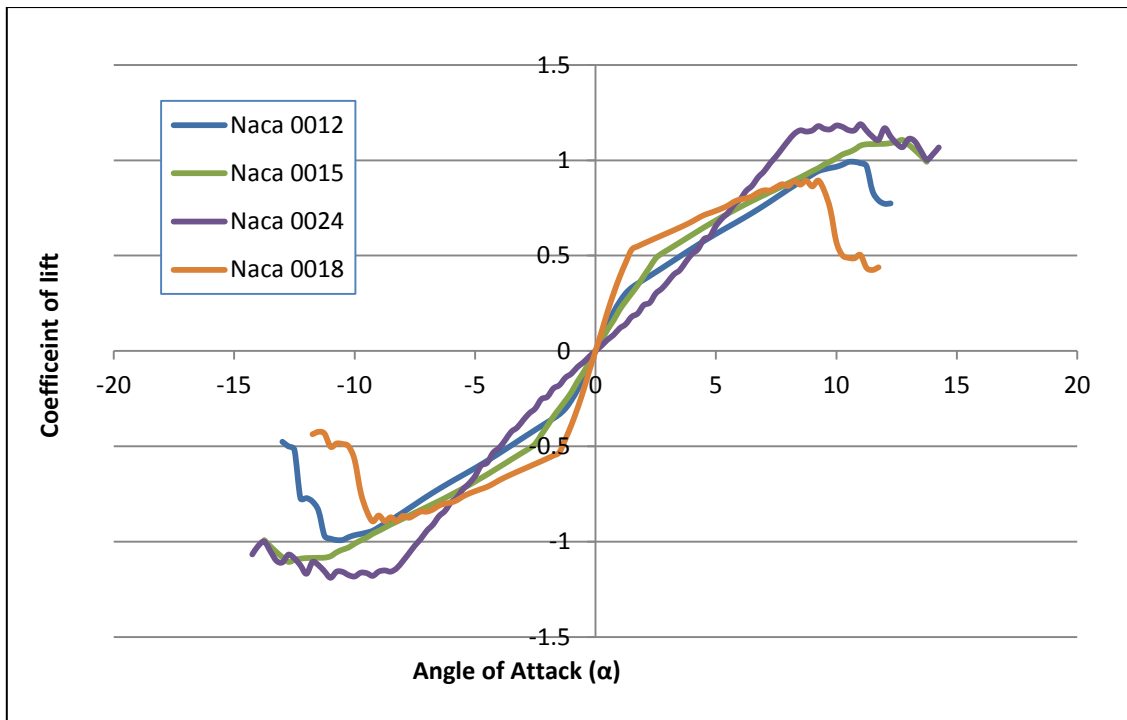


Figure 6-11: Coefficient of lift Vs. Angle of attack

For a turbine to be designed based on the concept of exploiting the lift force generated from the blade profiles, the relationship between the coefficients of lift versus the coefficient of drag (C_l/C_d) is of importance to understand. For the lift based turbine one would want to obtain a C_l/C_d which is relatively high. This would indicate that the drag coefficient is almost negligible compared to that of the lift coefficient. Figure 6-12 below illustrates the C_l/C_d for the NACA 0024 blade profile which was selected for the helical cross-flow turbine. As the turbine is in rotation the angles of attack change throughout the cycle. An angle of attack of -20° to 20° was chosen for analysis. It can be seen that the C_l/C_d relationship is adequate as the values are high. If the values for C_l/C_d predominantly tend to zero, it would mean that the coefficient of drag values outweigh those of the coefficient of lift values.

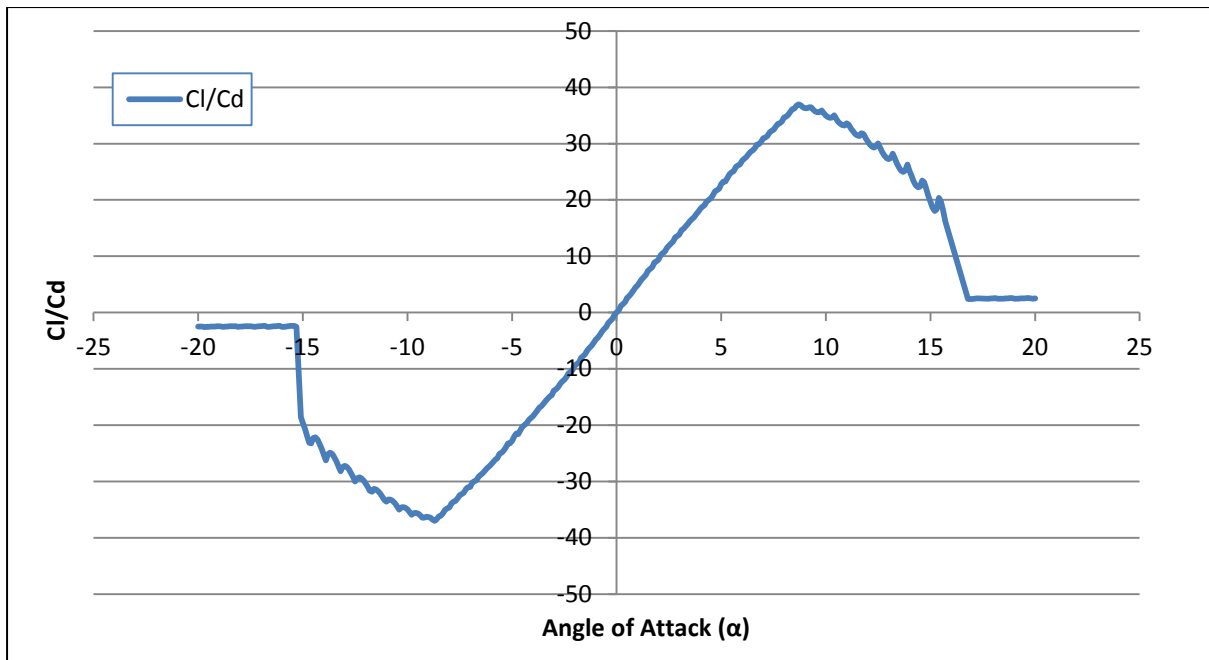


Figure 6-12: Cl/Cd for NACA 0024

6.4.2 Blade Wrap

The term blade wrap is commonly associated with turbine design and blade geometry. The term may be defined as the percentage of a turbine's radial circumference which is occupied by the collective amount of blades of the turbine. The blade wrap (ω) of the turbine may be calculated as follows:

$$\omega = \frac{BH}{\pi D \tan \delta} \quad (6.14)$$

where:

- B Number of blades (-)
- H Height of turbine (m)
- D Diameter of turbine (m)
- δ Helix angle (°)

Niblick [15] concluded that with a blade wrap ratio of 100% there would exist no void space between the trailing edge of one blade and the leading edge of the next blade throughout the span of the turbine. If a blade wrap ratio of less than 100% was used there would exist azimuthal angles where void space would occur resulting in an increase in torque fluctuations

and thus excess machine vibrations. This would be detrimental to the life span of the turbine and the entire power generation system. The use of airfoil profiles as hydrofoils still means that the turbine blades will develop stall vortices. Neglecting the blade tip and stall effects, a blade wrap of 100% would theoretically decrease the amount of torque fluctuations on the turbine shaft due to a constant blade interaction with the fluid flow. For the purpose of the following turbine design, a blade wrap of 100% was used, Cunden and Inambao [68].

6.4.3 Turbine Aspect Ratio

Aspect ratio (A_R) of a turbine is a method in which one may visualise and obtain the turbine's swept area. This relationship may be defined as the ratio of turbine height (H) to turbine Radius (R) which is represented as the following equation:

$$A_R = \frac{H}{R} \quad (6.15)$$

On observation of a straight bladed Darrieus turbine, the aspect ratio is defined as the blade length to chord length as concluded by Chu, et al. [69]. On analysis of a double multiple streamtube momentum modelling for a straight bladed Darrieus turbine, Chu, et al. concluded that the performance coefficient of the Darrieus turbine increase with an increase in aspect ratio, however the starting torque of the turbine was affected negatively and thus the turbine require a higher flow speed to get started.

A turbine's cross sectional swept area may be determined from the product of turbine height to diameter. As cross sectional swept area is one of the main factors influencing the turbine's ability to extract power from a fluid, it would be natural to assume that an increase in aspect ratio would result in a subsequent increase of the turbine cross sectional swept area. This would be beneficial only if the turbine blades can support the loading of the fluid under various tip speed ratios. As the blades increase with length and diameter increases with respect to aspect ratio, the structural strength of the turbine blades needs to be carefully examined. Once the loading threshold of the blades is exceeded to the point of deflection, support struts need to be implemented so as to reduced deflection and maintain the blades shape to produce the required power output. By implementing support structures, the turbine performance could be impacted adversely as the supports can cause extra shed vortices which mix with the stall vortices caused by the blades in the upwind cycle of the turbine. It was

found that the proposed turbine of diameter 0.2 m and height of 0.3 m did not require extra blade supports and was more than adequate to perform under the assumed loading conditions, Cunden and Inambao [68].

6.4.4 Number of Blades

The number of blades of the turbine directly affects the turbine solidity. It was noted that if the number of blades of a turbine was increased, the chord length of the blades was subsequently decreased to maintain a specific solidity ratio. For the proposed turbine a solidity ratio was chosen by acquiring a 100% blade wrap ratio. Figure 6-13 depicts the results obtained for two turbines which consisted of three and four blades respectively. As the turbine diameter and aspect ratio was chosen on the bases of the experimental results from Gorlov [11], various helical pitch angles were used to determine which turbine would achieve a blade wrap ratio of 100% and from this the turbines helical pitch angle was obtained. As shown in Figure 6-13, the most appropriate number of turbine blades was found to be four blades as this resulted in a blade wrap of 100%, [68].

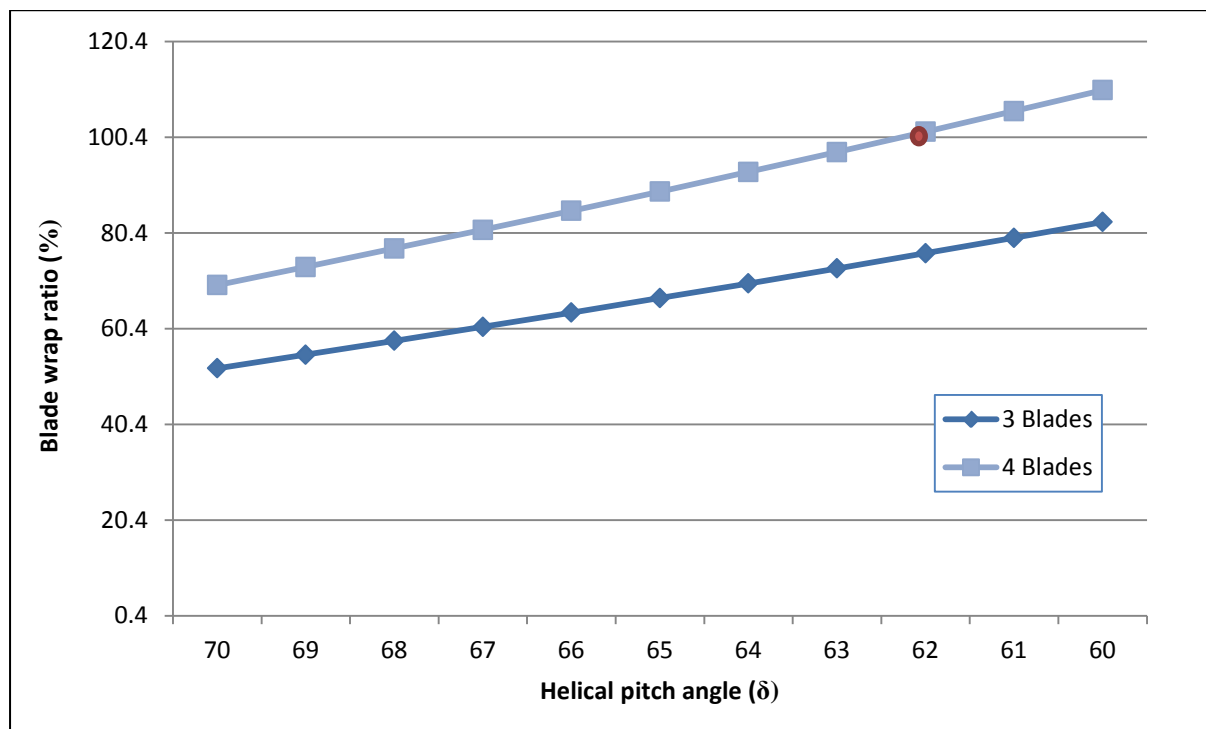


Figure 6-13: Blade wrap ratio Vs. Helical pitch angle

6.4.5 Blade Geometry

Helical pitch angle (δ) may be defined as the angle to which the helical blade makes with the base of the turbine hub. Figure 6-14 depicts the mathematical modelling and Cartesian coordinates used to model the helical turbine. By using the results obtained from the blade wrap analysis, the most suitable helical pitch angle to use was found to be 62° . This meant that the helical blades would be inclined at an angle of 62° to that of the base hub diameter at every point of the blade profile.

Figure 6-14 also depicts the angle of twist (φ) which is defined as the angle that is created between the centre point of the blade hydrofoil profile at the top of the turbine hub and the hydrofoil profile at the bottom of the turbine hub. This twist angle follows a path along the cylindrical profile of the turbine. The angle of twist is of key importance to the turbine modelling as it allows one to know the start and end co-ordinates of the blade which results in the length of the blade.

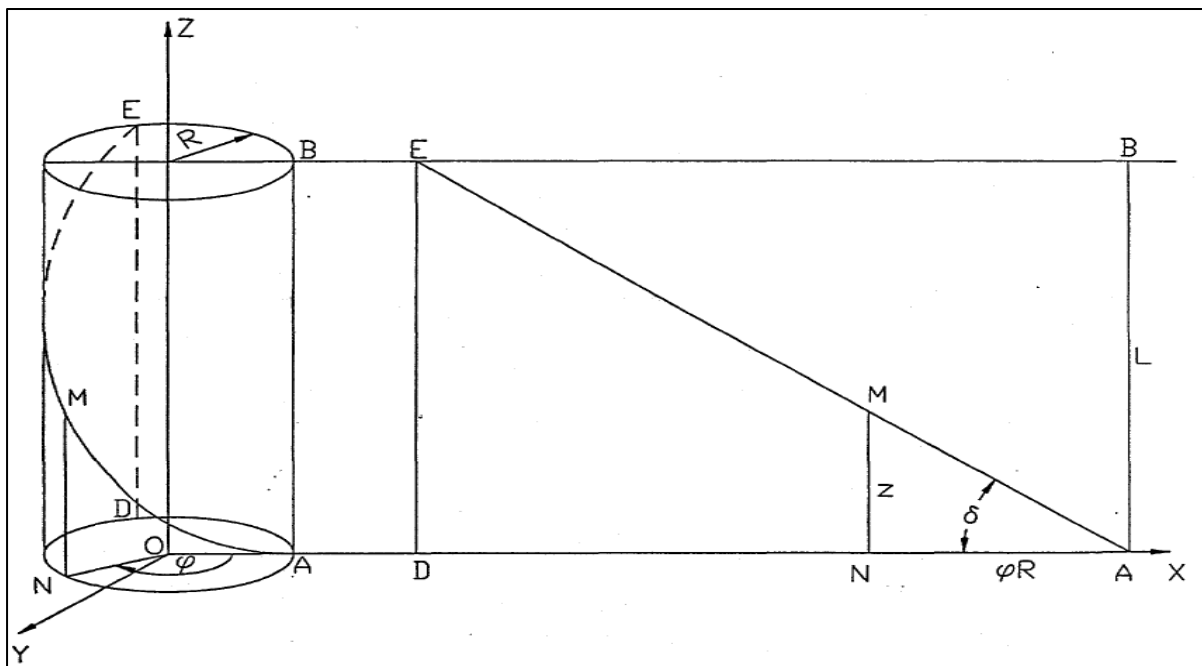


Figure 6-14: Mathematical layout of helical turbine, Gorlov [11]

Shino, et al. [26] concluded from their results that a turbine's performance increases as the helical pitch angle increases up to an angle of 90° , which is equivalent to the straight bladed Darrieus turbine. This type of turbine however has its own set of flaws as outlined in previous sections, with respect to self-start capabilities and torque fluctuations due to void spaces.

Gorlov [11] derived parametric equations for the helical turbine which he designed to allow one to successfully design the turbine based on a few constant parameters, such as the turbine diameter and aspect ratio which was used in this design. Gorlov related the angle of attack of the blade at any given point along the blade to the angle of twist of the blade by the following equation:

$$\sin \alpha = \cos \varphi \text{ and } \cos \alpha = \sin \varphi \quad (6.16)$$

The angle of attack of a blade is the angle which the blade relative velocity creates with the chord line of the blade profile. A simple illustration of the velocity vectors on the blade is given by Figure 6-15. It can be noted that as the turbine blades move along the path of rotation, the angles of attack for each blade change at a rate relative to the tip speed of the turbine. For blade force analysis, it was taken that the lift and drag forces act at the centre of pressure of the blade element which was taken to be at “1/4-chord” from the leading edge of the blade profile which corresponds to the research conducted by Anderson [70].

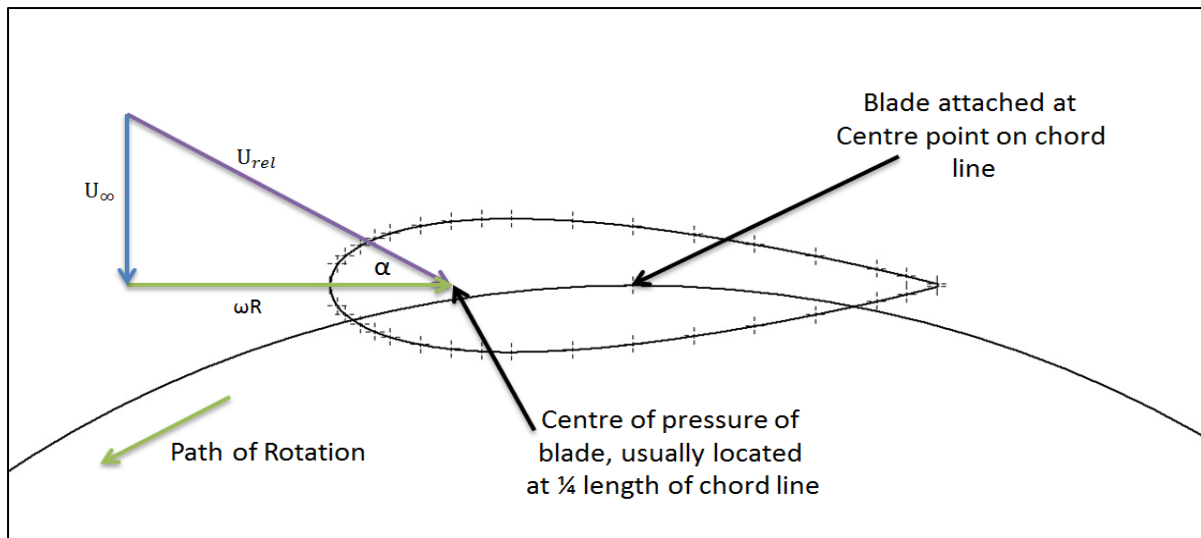


Figure 6-15: Angle of attack for 0° blade pitch

Blade pitch is the degree of tilt that the blade chord line creates in relation to the tangent line of the turbine circle of revolution. Figure 6-16 illustrates the concept of blade pitch in relation to angle of attack. Previous research proved that a toe-in blade pitch angle is highly undesirable for the vertical axis turbine system as it decreases the performance and efficiency of the turbine. Toe-out pitch angles, however, can boost performance but the most optimum angle of pitch has not yet been clearly established. A toe-out angle is dependent on the

geometric profile of the blades and also depends of the camber of the blades. Although the literature which was used to understand and apply this theory was for a straight bladed Darrieus turbine, the resulting performance of the helical turbine may be altered due to the helical profile of the blades. Using the conclusion from Fiedler and Tullis [64] on how a toe-out blade pitch benefits the vertical axis turbine performance coefficient, a 7.5° toe-out angle was implemented on the turbine and compared to a turbine with 0° blade pitch.

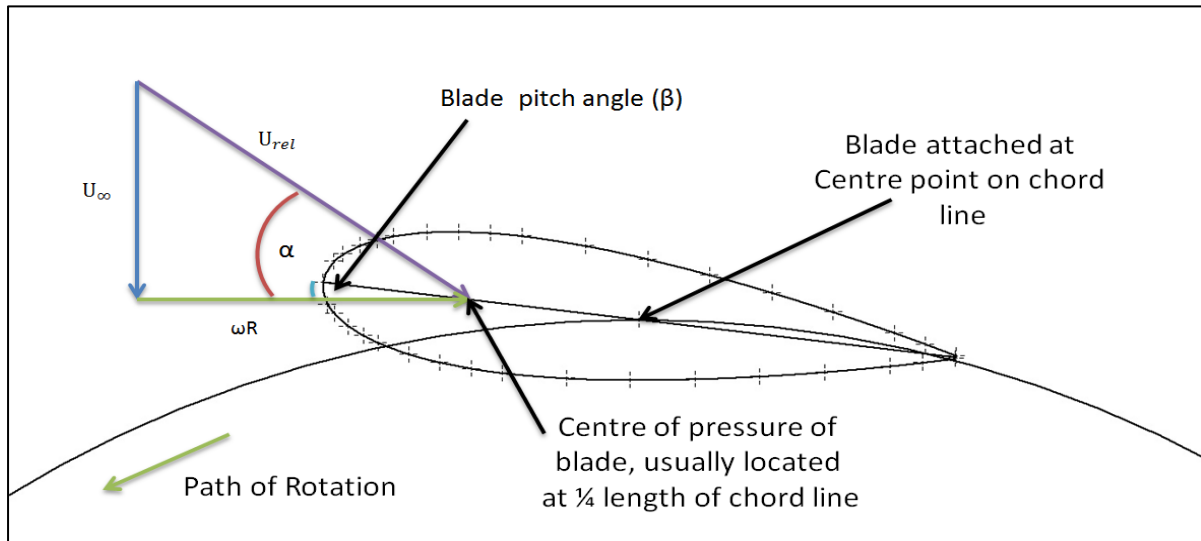


Figure 6-16: Blade pitch toe-out angle of 7.5°

6.4.6 Central Shaft Design

For a hydrokinetic marine current turbine to transfer power from the fluid medium to a generator which is to be coupled to the turbine, a central shaft is required to connect the turbine to the drive train used to link the generator and turbine. The drive train is used to step up the rotation that the turbine has to the generator. A central shaft also provides structural support for the turbine and aids alignment for the turbine when being implemented. Khan [62] conducted experiments on a shaftless turbine and concluded that the low performance of the turbine was due to the lack of central shaft and that the turbine was structurally weak. The central shaft does affect the performance of the turbine as it obstructs flow and causes vortices to be created which interacts with the downstream section of the turbine which reduces the hydrokinetic lift for the blades which are in the downstream section of the turbine. The vortices created by the central shaft may be rendered insignificant, however, as the shed vortices created in the upstream section of the turbine means that the central shaft is located in a highly turbulent zone. This also means that the shed vortices from the central

shaft mix with that of the shed vortices from the turbine blades in the upstream region creating a highly turbulent region in the downstream section of the turbine.

6.4.7 Turbine Strut Design

Initially the Darrieus concept which was used incorporated no strut design and used troposkein blades with a parabolic, variable radius profile which converged to the central shaft of the turbine, Sheldahl and Feltz [71]. Lucid energy used a similar approach and created a spherical shaped turbine to be used within water pipelines. The norm which is now used for vertical axis turbines are constant radius blades from the central shaft. This means that a means of connection was needed. A strut is a means by which to support turbine blades and provides a means of ridged connection between the central shaft and the turbine blades. The blade strut design is of importance as the strut also rotates with the turbine blade. This means that drag stemming from the interaction of the strut with the flow directly impacts the efficiency of the turbine. Previous designs such as the one used by Gorlov [11] incorporated a thin circular plate which connected the ends of the blades to the central rotating turbine shaft.

The turbines which were used by Shino, et al. [26], Khan [62] and Biadgo, et al. [16] used strut arms at the end of the blades which linked directly back to the central shaft. The affects caused to the turbines performance however, are not discussed in the literature for the turbine's research and experiments. Khan [62] performed various experimental tests of different vertical axis turbines using different strut designs but at the same time varying the blade geometry and number of blades which were used, hence confounding the implications of the different strut designs on the turbine's performance.

The effects of a strut on a vertical axis turbine are drag forces induced onto the turbine. The drag force which is caused by the strut is skin friction drag and pressure drag. The skin friction drag is the tangential drag as a result of the fluid flow creating a viscous boundary layer over the strut. Pressure drag is caused by the area of the strut which is normal to the flow which is developed from a fluid boundary layer separation due to that area of the strut. This highlights the importance of strut design which effects the performance of the turbine due to wake interference shed from the strut.

6.4.8 Turbine Blade Attachment

Turbine blades are essentially the components which generate the forces required for rotation and hence power generation. The blades may be secured at either the midpoint, close to the ends of the blades or a combination of both to form a more rigid connection between the turbine hub and the blades. As the blade length increases in proportion to aspect ratio of the turbine, extra struts may be required to be installed at various calculated blade lengths to provide structural support against induced vibration, stress loading and deflection due to fluid blade interaction.

Blade attachment to the turbine hubs may be overlooked as a small and nonessential factor when constructing a vertical axis turbine. However, blade attachment plays a role in understanding the complex physics stemming from the turbine such as blade shed vortex formation, and vortex structure and strength of the vortex in the wake field. Incorrect blade attachment may also impact blade pitching moment. Built in blade pitch may be a result of incorrect alignment of attachment points to the radial path of rotation which is detrimental for the turbine performance and blade life as stresses along the blade arise from this. A well designed vertical axis turbine should account for the pitching affects caused by attachment points.

After all the parameters for the turbine and hydrodynamics of the turbine were considered, a conceptual design was conducted. Figure 6-17 below depicts the turbine which was designed to undergo simulation. Four blades were selected for the turbine with a chord length of approximately 20 mm and a turbine height of 300 mm. The aspect ratio for the turbine was selected to be 3 to obtain a reasonable turbine diameter of 100 mm. These values were selected so as to accommodate a small scale turbine for testing purposes.



Figure 6-17: Designed Turbine, [68]

The turbine has a solidity ratio of 32% which means that the turbine has 32% of its cylindrical space occupied by the blades of the turbine. Using these parameters and based on the mathematical relationships of Figure 6-14, the turbine helix angle was calculated for a blade wrap of 100%. The helix angle for the turbine designed was calculated to be approximately 62° . From the same methodology the angle of twist of each blade was found to be 91° from a singular reference point on the circumference of the turbine base diameter.

6.5 Shrouding Device

Shrouding systems have been used in many different applications to increase flow into turbines or devices which require increased flow. In the renewable energy portfolio of resources, wind and ocean technologies are the only two which harness flow mediums. Shrouding structures have been incorporated in existing wind turbines to increase flow entering the turbine and also decrease the amount of wake interference with other turbines which are usually off set in a farm like configuration. The following section will describe a shrouding device which was used in conjunction with the designed turbine. The shroud was included so as to increase flow entering the turbine and hence, theoretically, increase energy output.

6.5.1 Selection of Shroud

Ponta and Jacovkis [21] conducted numerous amounts of research which focused on the incorporation of channelling devices for vertical axis marine current turbines. The research conducted by Ponta and Jacovkis [21] and Ponta and Shankar Dutt [22] gives adequate insight into shrouding for vertical axis turbines and the consequences stemming from the addition of the device. The device which was designed was shared as non-dimensional schematic drawings within the research and was incorporated within the shrouding system which was selected for the helical turbine which was designed.

The shroud system which was used for the turbine designed above was based on the assumptions and design parameters which were mentioned in the research studies. This was done as an entirely new design was out of the scope of this dissertation. The assumptions which were made were for increased flow entering the turbine and for the flow which is exiting to be partially restored to ambient conditions. The desired shroud parameters are as follows:

1. A nozzle entrance to increase the flow as it enters the turbine section.
2. A normalised straight channel so as to induce a partial amount of flow linearity as it passes through the turbine section.
3. A diffuser section which minimises wake interference with the downwind section of the turbine and thereby increases turbine performance.

Figure 6-18 depicts two schematics of possible shrouding devices which can be incorporated into the turbine system. The devices vary on the aspect of flanges which are located on the exit side of the shroud or the exhaust. The addition of the various styles of diffusers was to analyse the effect of hydrodynamic loading on the walls of the shroud and to minimise the negative effects of the wake which is created by the turbine as the fluid passes through it.

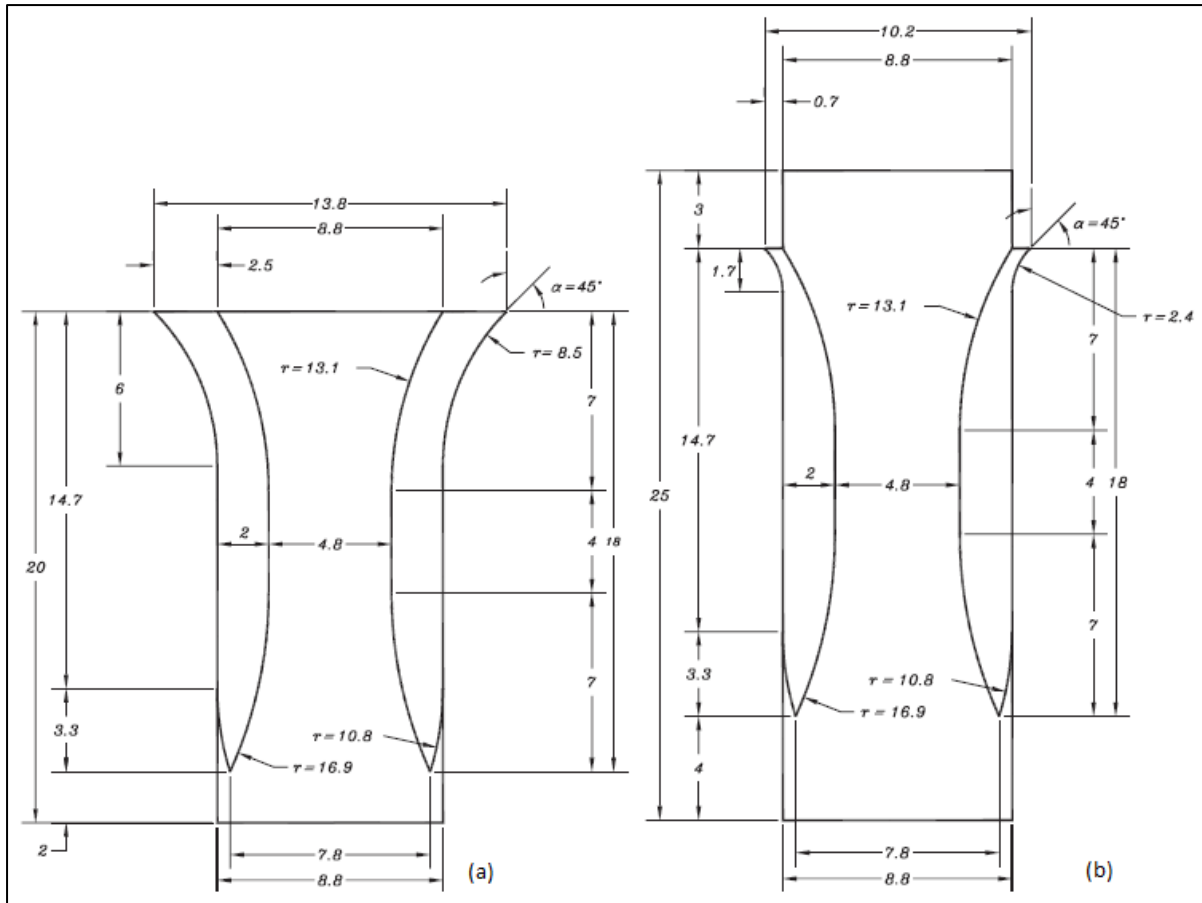


Figure 6-18: Non-Dimensional Schematic of Shroud, Ponta and Jacovkis [21]

Figure 6-18 (a) was the layout which was chosen to be augmented with the designed turbine. This was due to the fact that this device was found to be the most optimum by the researchers. A similar simulation was conducted for the turbine as verification was required even though experimental verification was conducted by the researchers within the study.

The fluid dynamic fundamentals need to be established for the further analysis of the shrouding mechanism which is to be augmented with the designed turbine. For the chosen augmentation some assumptions were made on the flow in the channelling device, as follows:

1. The channel is completely submerged as the turbine is to operate completely underwater.
2. The flow is incompressible, adiabatic, isothermal and one dimensional.
3. There is no mechanical exchange of work with the surrounding environment and medium.

6.5.2 Channel Flow Theory

Ponta and Jacovkis [21] research was based on open channel flow and the turbine shroud which is chosen for the following analysis is based on flow in a closed channel and at a deeper depth which is not related to open channel flow. Traditional research indicates that a turbine can only extract a certain amount of energy from a flow. The restriction is based on the concept which was derived by Betz and is given by $16/27$ or approximately 59% of the flow. However, this concept was derived under the basis that there are no restricting walls which affect or constrict the flow entering the turbine. This is one of the main reasons why the Betz limitation cannot be used for channelling devices as the amount of power which is extracted from the fluid by the turbine is now a function of the following equation based on the estimates by Garrett and Cummins [72]:

$$P_{MAX} = \frac{C_{P,Max} 0.5 A_C \rho U_0^3}{(1 - \varepsilon)^2} \quad (6.17)$$

where:

P_{MAX}	Maximum Power which can be extracted by the channel (W)
$C_{P,Max}$	Maximum power coefficient for free flow (-)
A_C	Cross-sectional area of the turbine (m^2)
U_0	Asymptotic flow velocity (m/s)
ρ	Density (Kg/m^3)
ε	Blockage Ratio (-)

Figure 6-19 depicts the divergence which was explained above in comparison to the amount of power which is available in the flow medium without any constrictions. The power from the channel which is depicted below was taken for a blockage ratio of 0.85. As this value decreases the amount of power which is within the flow passing through the narrower channel increases exponentially due to the denominating term of equation 6.17. However, there is a practical limitation behind this term which is not explicitly clarified in most research. The practical limitation is the amount of tolerance which needs to be accommodated for between the turbine and the channel wall.

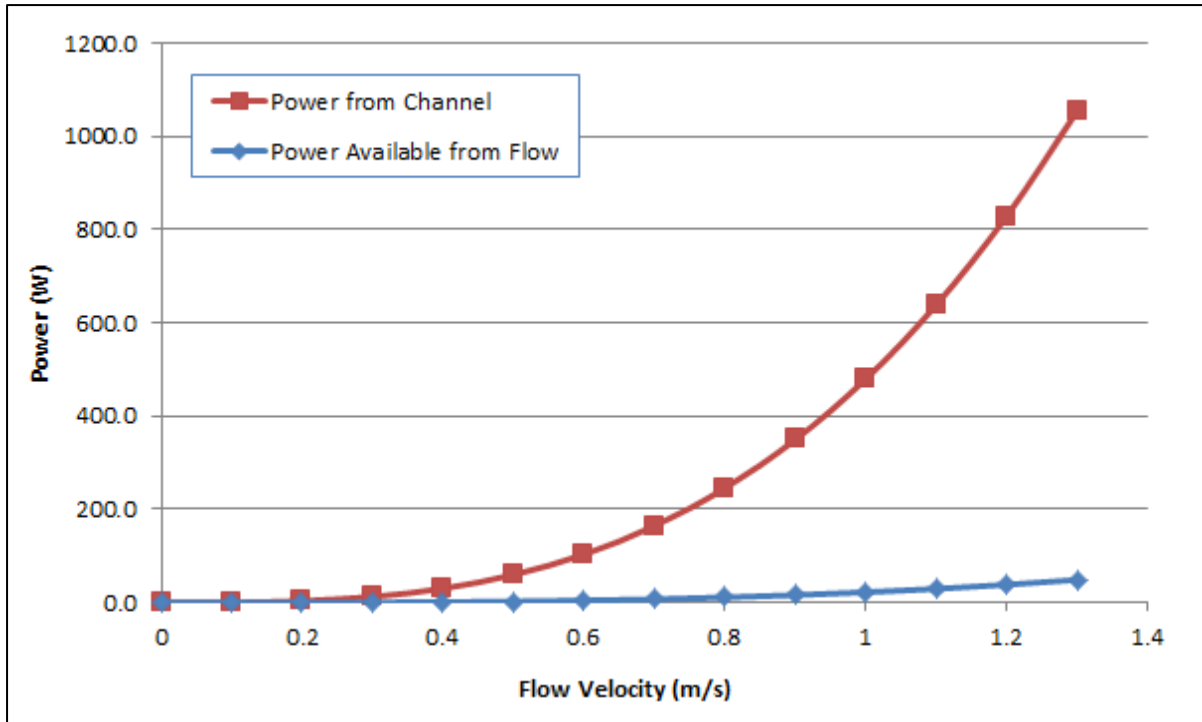


Figure 6-19: Power available in the flow vs. Power from channel

Equation 6.17 above is based on streamtube theory and does not take into account the level of the fluid in relation to the channel. For a more realistic simulation for the turbine and channel system, water level would have to be accommodated for as this directly affects the pressure differential and will not be able to diverge. Goude and Ågren [73] explain the term of blockage ratio in relation to Garrett and Cummins [72] studies as the relationship of the cross sectional area of the turbine with the cross sectional area of the channel. The relationship can be expressed by the following equation:

$$\varepsilon = \frac{A_C}{A_{Ch}} \quad (6.18)$$

Where:

ε Blockage ratio (-)

A_{Ch} Cross-Sectional area of the channel (m²)

On closer examination of the above Equation, it is evident that the amount of power which can be extracted by the turbine cannot be limited by the Betz limitation of 59%. This is due to the fact that the amount of power which can be extracted by the turbine with the addition of

the channel will diverge as the cross sectional area of the turbine encompasses the area within which it is situated in the channelling device, Goude and Ågren [73].

Interesting enough Goude and Ågren [73] expand on the work by Garrett and Cummins [72] by including the pressure drop between a point which exists far ahead of the turbine and a point far behind the turbine, but not as far as where viscous effects would have to be incorporated. The pressure drop (ΔP) between the two points also diverge which is a clear indication of the power being extracted by the turbine and given by the following equation:

$$\Delta P = \frac{4\varepsilon(3 - \varepsilon)}{9(1 - \varepsilon)^2} U_\infty^2 \quad (6.19)$$

Where:

ΔP Pressure Difference (Pa)

ε Blockage ratio (-)

U_∞ (m/s)

For the analysis which is conducted for the turbine system incorporating a shroud in this dissertation, the blockage ratio was varied by varying the shroud cross sectional area with the turbine cross sectional area. This was accomplished by relating the shroud width to that of the turbine diameter which effectively is the turbine width.

One of the fundamental equations which govern flow in any respect is the continuity equation which describes the conservation of mass within the flow. Mass flow rate is conserved and accepting that the density of the fluid does not change due to the initial assumption of incompressible flow, it can be concluded that the volumetric flow rate is constant and is express by the following equation:

$$Q = V_1 A_1 = V_2 A_2 = \text{Constant} \quad (6.20)$$

Where:

Q	Volumetric flow rate (m^3/s)
V	Velocity of flow (m/s)
A	Cross sectional area (m^2)

By taking into account the blockage ratio and practical limitations, one can design a simple shrouding device which can help increase flow entering the turbine. By knowing the parameters of the entrance, turbine section and exit of the shroud device, the volumetric flow can be calculated at any specific point within the shroud. It is obvious that within the region of the turbine, however, the continuity equation does still apply but has to be reconfigured to account for the extraction of energy from the turbine. By extending the length of the turbine region towards the entrance and exit slightly, one can calculate the velocity which is entering the turbine which can be used for simulating the amount of power which can be extracted by the turbine due to an increase in flow speed.

Figure 6-20 depicts the velocity flow profile through the channelling device for the turbine based on the continuity equation. It can be seen in the figure that the velocity increases until it reaches the region of the turbine but what it does not clearly depict is the loss of velocity through this region due to the extracting of kinetic energy from the flow by the turbine.

Within the analysis of the turbine and augmented shroud system, the velocity which is found to be at in the region of the turbine in Figure 6-20 will be used. This was found to be the optimum velocity which was based on the blockage ratio concept. By increasing the blockage ratio further than what was taken for the above case, the velocity of the system would not have increased as much. Conversely, one could increase the velocity in the region of the turbine by increasing the entrance of the channel and keeping the turbine section constant. The width of the channel which was chosen in the above case was found to be the most practical solution if the shroud device had to be constructed.

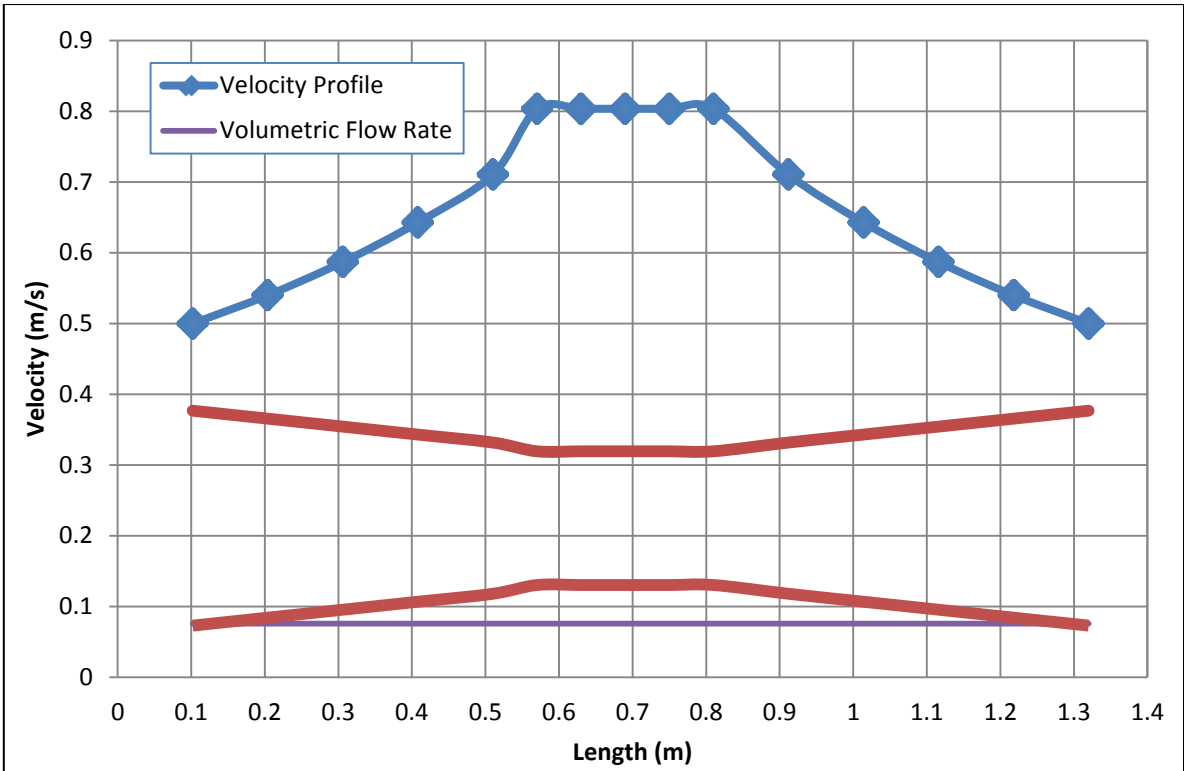


Figure 6-20: Velocity Profile for the Channel

The design of the channel was not completed within this dissertation as it falls outside its scope, however, the result which was obtained from the mathematical model used to construct Figure 6-20 was used for the velocity which enters the turbine in the simulation and analysis of the turbines with and without blade pitching angles.

CHAPTER 7 MODELLING OF VERTICAL AXIS TURBINE

Various models have been developed and implemented to simulate the performance of a cross-flow turbine. Biadgo, et al. [16] explain the use of the most common technique of modelling of a vertical axis cross-flow turbine. The following chapter consists of an explanation of the blade element theory which is most commonly used for vertical axis turbines and the momentum models which accompany them. An in-depth discussion of vortex formation and modelling is also presented.

7.1 The Blade Element Theory

The blade element theory was derived from finite element methods to analyse the forces on a turbine blade element which is caused by the surrounding fluid medium. For a given rotating blade element, the relative velocity (U_{Rel}) at the blade element is influenced by the free stream velocity (U_{∞}) and the tip speed (λ) at which the turbine is rotating. As a result of the blade's angle of attack (α) created by the relative velocity angle with the chord line of the blade, the hydrofoil profile experiences a pressure difference on either side of the profile resulting in a net lift force exerted on the centre of pressure of the profile. The hydrofoil also experiences drag forces which are created by viscous skin friction and pressure drag as the hydrofoil moves through the working fluid. For the hydrofoil which was chosen for the purpose of this dissertation the data for lift and drag coefficients was extracted and interpolated from Sheldahl and Klimas [65] and verified with software tools.

The existing data in literature are for static airfoils and from this it may be noted that the lift and drag coefficients are functions of the Reynolds number of the fluid and the angle of attack of the hydrofoil profile. As mentioned previously, the resulting force acts at the "1/4 chord" point. This is a point which is assumed to be the centre of pressure of the hydrofoil profile and is located $1/4^{\text{th}}$ length from the leading edge of the profile which corresponds to Anderson [70]. This assumption however does not incorporate the dynamic effects which are impacted onto the blade. Examples of these effects are vortex interaction from the upwind section propagating to the downwind section of the turbine and pitching moment. The implementation of these effects on the blade meant that a different mathematical approach had to be implemented to the already existing momentum models. Strickland, et al. [74] developed a model which evaluates the lift generated by the profile based on the angle of

attack of the profile at the “3/4 chord” and the drag force based on the angle of attack at the “1/2 chord” which takes into account the pitch rate effects.

A similar relationship may be expressed for the lift and drag coefficients in terms of the turbine tangential force coefficient (C_T) and normal force coefficient (C_N) which are calculated as follows respectively, [16]:

$$C_T = \frac{F_T}{0.5 \rho U_{rel}^2 CH} \quad (7.1)$$

$$C_N = \frac{F_N}{0.5 \rho U_{rel}^2 CH} \quad (7.2)$$

The tangential force is usually directed towards the positive leading edge of the profile and the normal force directed inward, towards the centre of rotation of the turbine. However the tangential and normal forces may be difficult to obtain, so a relationship between the lift and drag coefficients and the relative angle of attack at the 1/4 chord was used to obtain the tangential and normal coefficients. The tangential and normal force coefficients may be calculated by the following equations respectively, [16]:

$$C_N = C_L \cos(\alpha) + C_D \sin(\alpha) \quad (7.3)$$

$$C_T = C_L \sin(\alpha) - C_D \cos(\alpha) \quad (7.4)$$

Figure 7-1 depicts the tangential and normal force vectors in relation to the lift and drag force vectors which impact the blade profile. From this we may conclude how the turbine exploits the lift force generated by the hydrofoil. Figure 7-1 depicts a pitched blade profile and the component vectors induce rotation of the turbine.

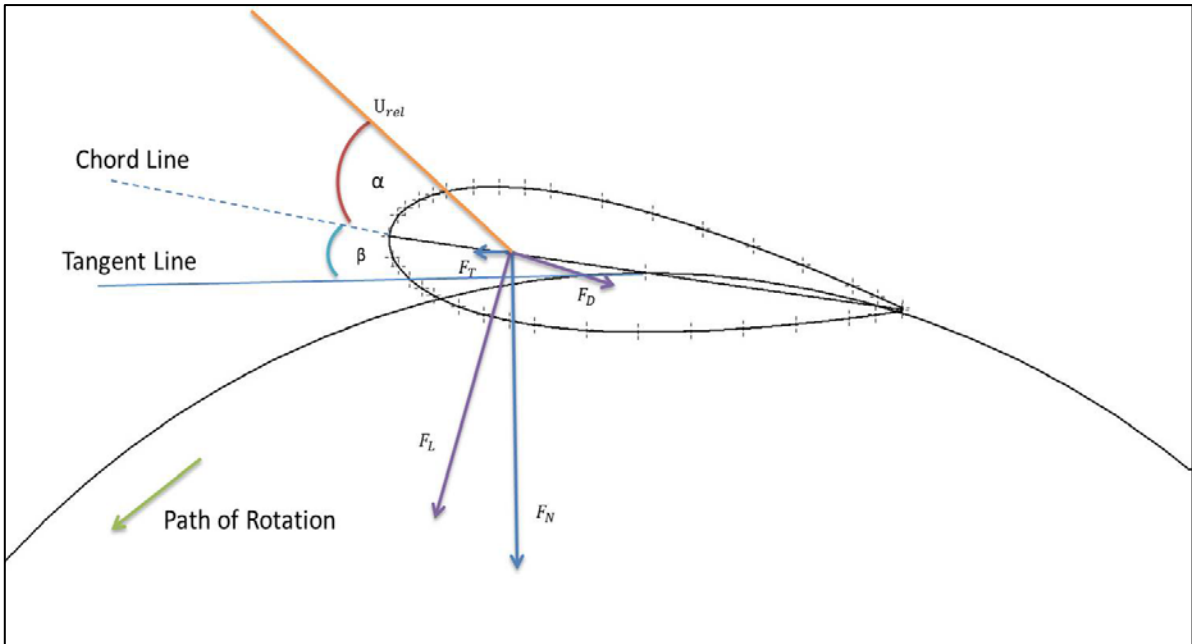


Figure 7-1: Normal and Tangent coefficients

7.2 Momentum Modelling

When it is recognised that a moving fluid has the potential for energy production, a suitable turbine is used to extract the energy from the moving fluid. As the moving fluid passes through the swept area of the turbine, the turbine extracts energy from the fluid flow which causes a deficit in momentum in the fluid, Alidadi [75]. This conclusion of the fluid energy relationship with the turbine forms the basis for any momentum model used for analysing hydrokinetic or wind turbines. Momentum modelling used for analysing turbines uses a thin actuator disc or rectangular plate to represent the turbine as depicted by Figure 7-2.

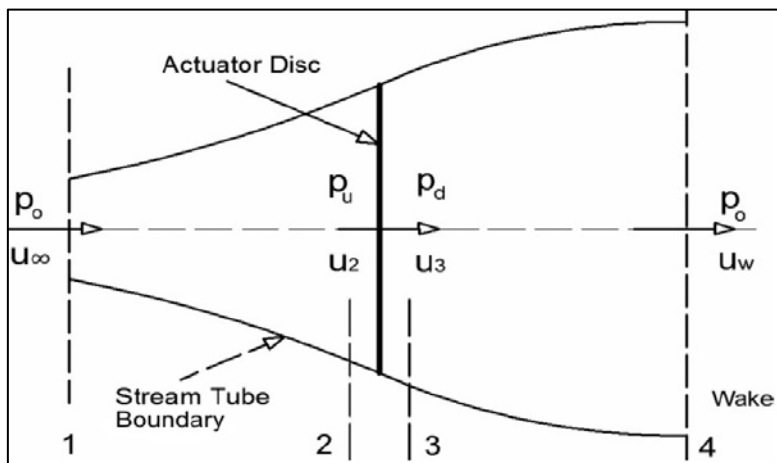


Figure 7-2: Simple actuator disc model, Biadgo, et al. [16]

When the fluid passes through the turbine a pressure difference occurs across the turbine which is due to the turbine extracting energy from the flow. This means that the free stream velocity which enters the turbine decelerates in the region of the turbine to adhere to the conservation of mass and momentum as seen in Figure 7-3.

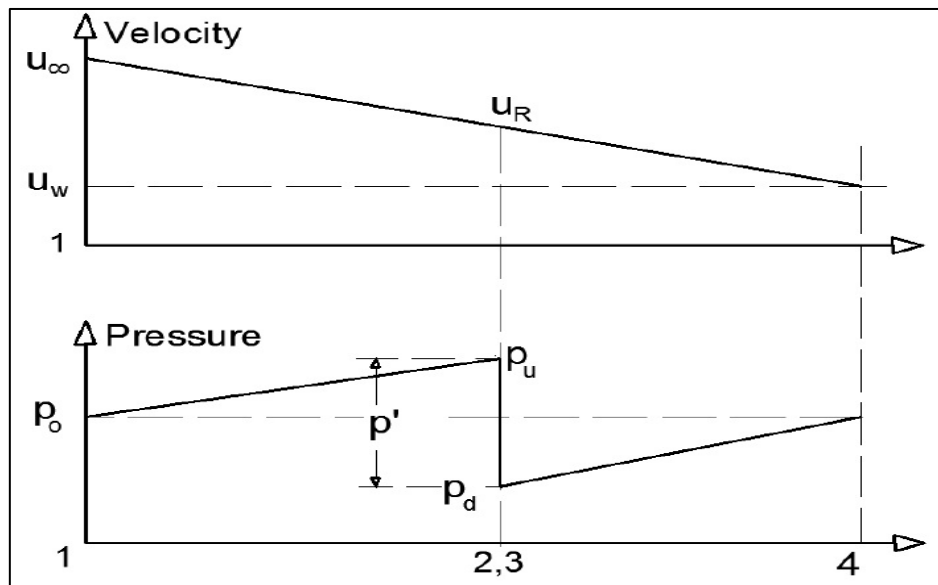


Figure 7-3: Pressure and velocity change across turbine, Biadgo, et al. [16]

On observation of the area behind the turbine, the wake formed by the turbine shed vortices continue to expand until such time that the pressure within the wake formation reaches equilibrium with the free stream pressure which is downstream from the turbine. Further downstream the wake and free stream fluid continue to mix with each other until the downstream velocity reaches uniformity. As previously stated, the blade element theory is used to calculate the forces which act on the blade by using the lift and drag coefficients corresponding to the angle of attack of the blade element at the relative Reynolds number of the working fluid from the perspective of the blade.

The first model which was used to analyse turbines was a single streamtube model which is a direct relation to Figure 7-2. This model was first introduced by Milne-Thomson [76] which was used for a Sandia troposkein Darrieus turbine. The actuator disc theory which Templin's model is based on consists of one single, uniform, expanding streamtube which accommodates the momentum change across the turbine rotor section. Within this model there exists some flaws as the single streamtube does not account for the fluid flow directly as it interacts with the blade as the blade moves within the streamtube.

Strickland [77] had identified the limitations of the Templin momentum model. Strickland developed a new momentum model that incorporated multiple streamtubes. This provided a higher degree of accuracy compared to the single streamtube model as the single streamtube which was used by Templin is divided into multiple discrete streamtubes from a 2-Dimensional spatial orientation as viewed by the plane perpendicular to the incoming free stream velocity. The addition of multiple streamtubes in the momentum model allowed for the user to analyse the forces on the turbine rotor multiple locations as the blade changes azimuthal position within the relevant streamtube.

This momentum model was an accurate way of analysing the forces acting on the turbine blades as they pass through the upwind section of the turbine. The model however also had limitations as it modelled the downwind section similarly to the upwind section of the turbine. This was inaccurate as the downwind section of the turbine had different physics conditions to that of the upwind turbine as the downwind section experienced more turbulence than the upwind section. Paraschivoiu [78] built on the multiple streamtube theory and developed a double multiple streamtube momentum model. This model divides the turbine into two sections which are the upwind and downwind sections and incorporates multiple streamtube theory separately for both sections. Paraschivoiu used two actuator discs to model the turbine separately in the upwind and downwind zones. Biadgo, et al. [16] give an excellent description of the induced and relative velocities of the turbine in the upwind and downwind sections of the turbine. Figure 7-4 depicts the multiple and double multiple streamtube models.

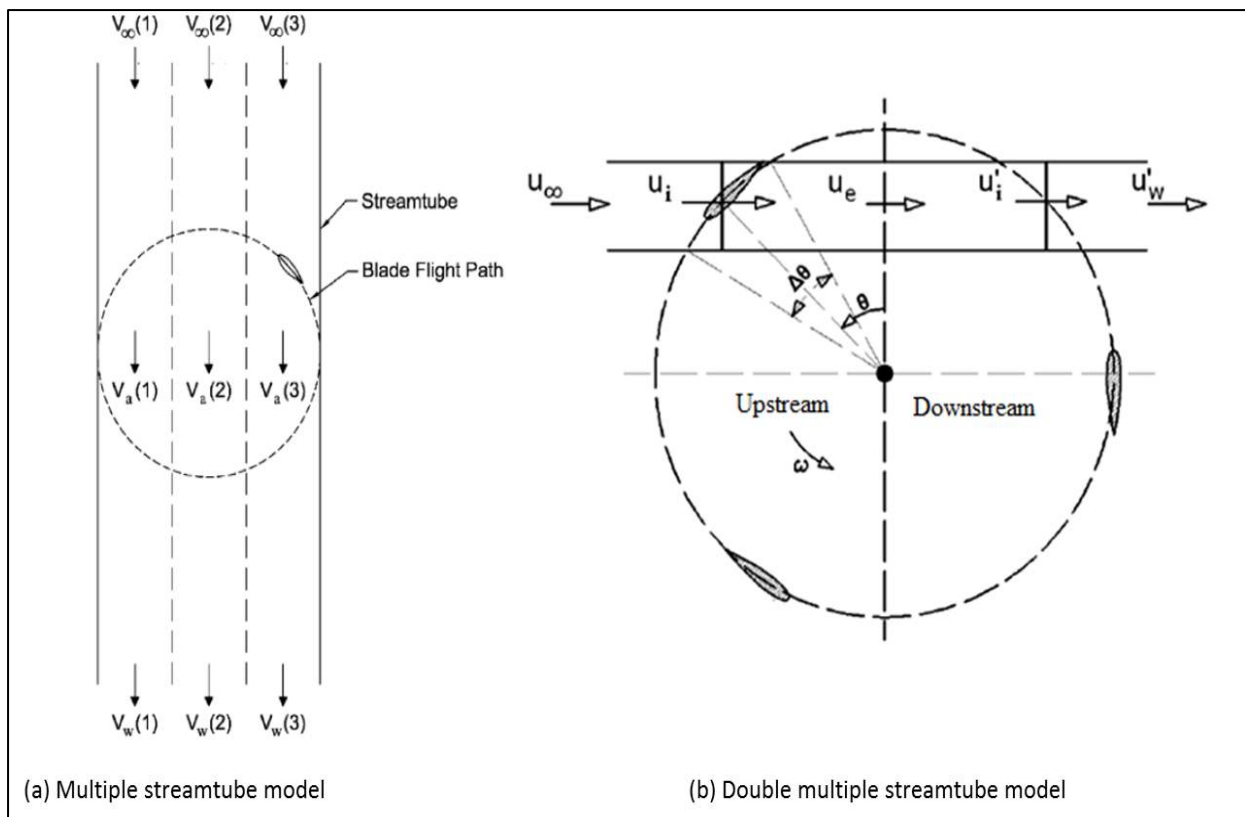


Figure 7-4: Momentum models, Biadgo, et al. [16], Paraschivoiu [78]

Another momentum model which is used for cross-flow which is similar to the double multiple streamtube model is the Cascade model which was developed by Fung [79]. The momentum model utilises a factor of empirical correction which is used for high solidity turbines. This is done by using an empirical formula for velocity and thus calculating the influence of a modelled turbine blade and relating it to the pressure and velocity of the other blades of the turbine. The momentum model represents the turbine blades by outlaying them equally spaced on a plane surface as if to unfold the turbine and using the circumference joining the attachment points as a reference line. The Cascade model also includes vortex modelling which significantly impacts the analysis of the turbine which is discussed further in the next section. The Cascade model is depicted in Figure 7-5.

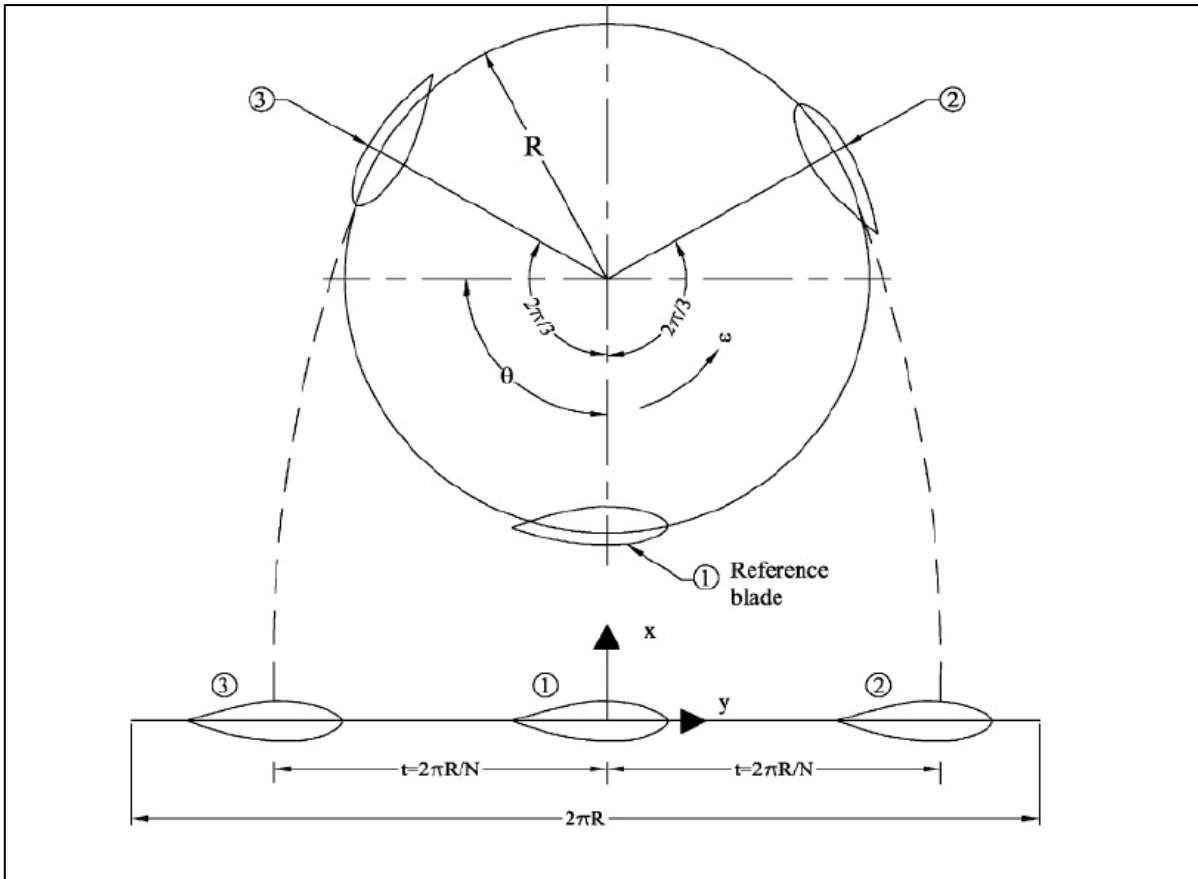


Figure 7-5: Cascade momentum model, Ciffone and Orloff [80]

7.3 Vortex Modelling

The unducted turbine undergoes various loading conditions. The turbine blades experience unsteady loading conditions which may be due to many different effects. In the case of no stall experienced by the blades then the blades would experience effects which may be generally referred to as “Added mass effects” and “circulatory effects”, Alidadi [75]. On the case of stall however, the unsteady loading experienced by the blades and turbines performance is mainly connected to “Dynamic stall”.

7.3.1 Added Mass Effects

Added mass effects can be simply explained as the inertia which is added to the body or system which occupies the flow domain because the acceleration or deceleration of the body must move some fluid volume as it is moving. This is because the fluid may not occupy the same physical space as the body which is moving through the fluid domain. What is usually modelled is the fluid moving with the moving body. In reality however, the fluid would not

move in this way and will be moved in various different paths in relation to that of the moving body, Milne-Thomson [76].

7.3.2 Circulatory Effects

The hydrofoils which are moving through the fluid medium inherit a pitching moment. This pitching moment results in changes in the fluid circulation and adjustments to the numerical modelling need to be conducted to satisfy the Kutta condition. Conversely, the change of circulation results in the formation of an unsteady wake which may be seen as continuous shed vortices from the trailing edge of the hydrofoil, as demonstrated by the total vorticity conservation constraint, Katz and Polotkin [81]. Figure 7-6 depicts the unsteady wake that was observed from the CFD analysis. The unsteady wake created by the shed vortices changes in direct relation due to the changes of circulation.

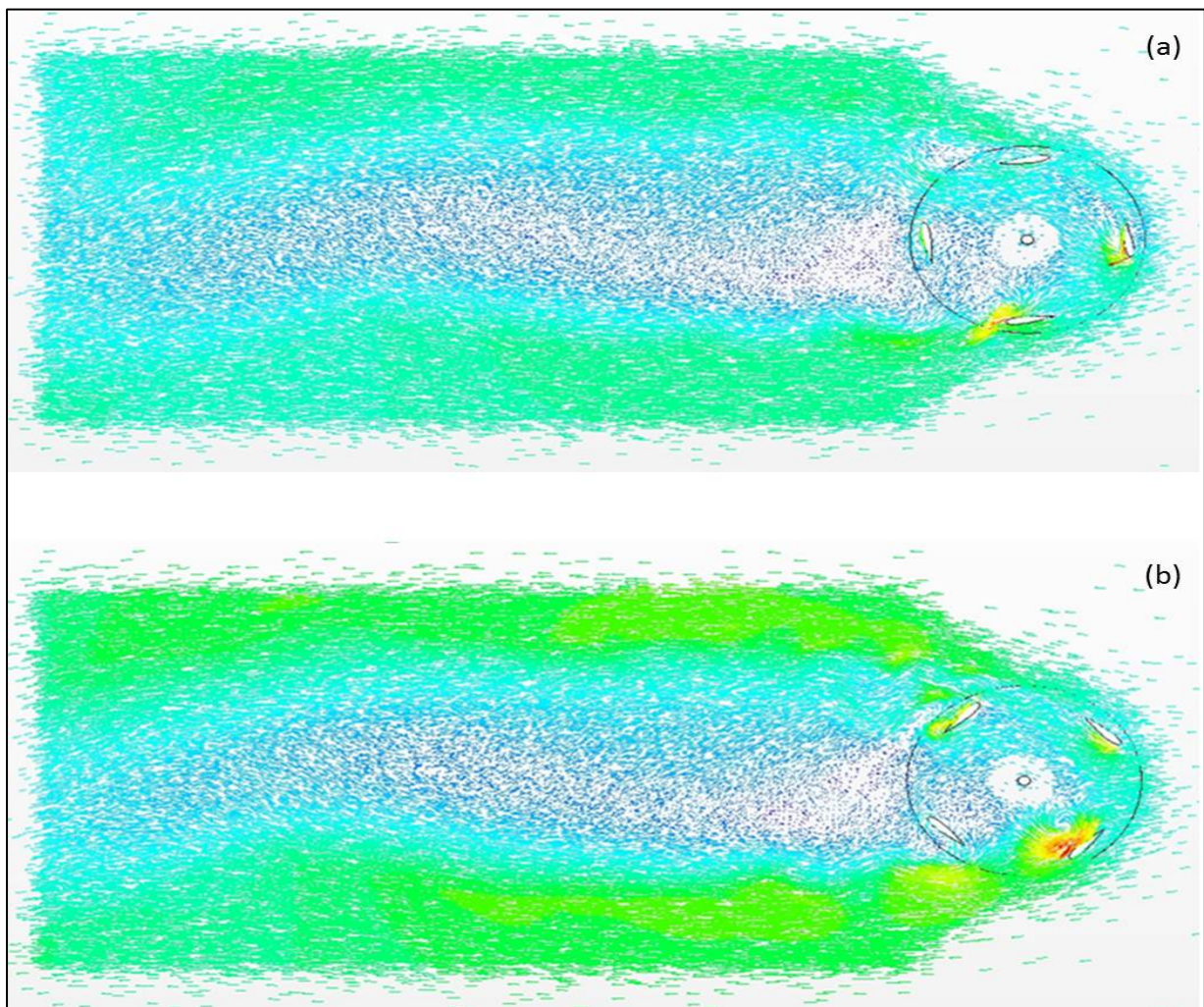


Figure 7-6: Wake comparison at 0.5s and 4s time steps

Researchers have attempted to simulate and thus approximate the added mass effects and circulation effects on the turbine. Fung [79] in his research, made use of the classical thin airfoil theory which he used as a basis to calculate the lift and drag of a pitching and conversely, plunging foil profile. By using a quasi-steady analysis, Fung ignored the unsteady wake effects and proved that the lift created by the foil is proportional to the angle of attack of the profile but at the “3/4 chord” point. This point is located at a distance which is equal to 3/4 of the chord length from the leading edge of the foil profile.

Strickland, et al. [74] developed a method to model the vortices which leave the hydrofoil profile. This method was developed using the analysis conducted by Milne-Thomson [76]. This analysis replaced the profile with a cylindrical shape to represent the blade and then estimate the circulation and loads caused by the moving profile. The results from this analysis lead to the development of expressions which depict additional circulation which exists around the profile shape which is a direct result of the object’s rotation and the added mass effects which are independent of the rotational body. Strickland found that the tangential force on the blade profile is directly proportional to the angle of incidence (Angle of Attack) which is located at the profile mid-chord position. The normal force is shifted to the “3/4 chord” position and the added mass term is proportional to the normal acceleration of the foil profile. Strickland also stated that in order to justify the omission of the added mass term and pitching moment which arises within the foil profile as conducted by Fung, an order of magnitude analysis needs to be done. The results which were obtained by Strickland give a good insight into the unsteady physics behaviour on the circulatory effects and the various forces which are exerted on the blades. The normal force which was calculated would not represent a reasonable approximation of the normal force on the hydrofoil profile. This is because the force was calculated based on a cylindrical representation of the profile which does not physically resemble the profile shape, Alidadi [75].

Fujisawa and Shibuya [82] proposed another method which was used to calculate the loads on the blade profile by incorporating a mapped flat plate to a cylindrical profile and then applying the theory which was developed by Milne-Thomson. Wilson, et al. obtained different expressions compared to that of Strickland, et al. but the general conclusion based on the conclusions made by them stated that the added mass effects and pitching moment do not significantly affect the net power which is extracted from the flow medium. This

conclusion indirectly states that the assumption made by quasi-steady analysis is sufficiently accurate to calculate the net power which the turbine may extract.

7.3.3 Dynamic Stall

When considering a pitching airfoil profile with an equivalent magnitude angle of attack and a sufficient rate of change of the angle of attack, a phenomenon referred to as dynamic stall begins to occur. The phenomenon arises when a vortex is formed at the leading edge of the airfoil profile and propagates back towards the trailing edge. This motion of the vortex causes the airfoil to experience a delayed stall angle and an increase in lift. As this vortex finally disperses off the trailing edge of the profile, the airfoil experiences a deeper stall until the stall vortex is fully shed off the profile and the blades lift and drag characteristics are returned to static values, Armstrong, et al. [83]. This phenomenon is known as dynamic stall.

There are different types of dynamic stall models which have conflicting agreements over the magnitude of the stall delay of the profile; maximum generated lift and the non-dimensional pitch rate parameter, k . The dynamic stall models were first developed for the study of helicopter blades undergoing the same phenomena but the dynamic stall in a vertical axis turbine is far more complex compared to that of helicopter blades due to the higher thickness ratio of the turbine blades, higher angles of attack and rate of change of angle of attack which is experienced by the vertical axis turbine blades.

Various experiments have been conducted by past researchers devoted to the topic of dynamic stall of turbine blades. The tests included measuring the forces and pressure distributions on the pitched foils within a wind tunnel and monitoring the changes of the measured values. The general consensus of the tests depict that the magnitude of the stall delay and peak loading on the foil is a function of the non-dimensional pitch rate parameter Alidadi [75] expressed by equation below:

$$k_p = \frac{\dot{\alpha} C}{2U_\infty} \quad (7.5)$$

where:

k_p Pitch rate parameter

$\dot{\alpha}$	Rate of change of angle of attack (deg/s)
C	Chord length (m)
U_{∞}	Free stream velocity (m/s)

With the analysis of cross-flow turbines, there are two models which simulate dynamic stall and these are the Boeing-Vertol model, McLaren, et al. [84] and the Leishman-Beddoes model, Li, et al. [85]. These models use different analysis methods of calculating the changing forces which act on a blade due to the induced forces created by shed vortices which subsequently result in dynamic stall of the turbine blade.

7.3.4 Shed Vortex Structure

According to fluid dynamic theory, the vorticity created by any given fluid due to the fluid interaction with a foreign object may be recognised as a pseudo-vector field. The field describes the fluid circulating motion near a given point as would be observed if one was located at the specific point and traveling along the path of the fluid.

Figure 7-7 depicts a three dimensional model of how the shed vortices from a hydrofoil profile move through the fluid. The shed vortices ($\Gamma_1 - \Gamma_2$) are depicted as being perpendicular to the axis of rotation of the turbine. It can be seen that the fluid imparts an imbedded vortex within the blade section located at the centre of pressure axis of the profile. The trailing vortices, however, have the same strength as the bound vortex (Γ_1) and are circulating perpendicular to the blades path of motion. In the figure the control volume used to understand the vortex behaviour is represented as a quadrilateral shape. Each shape represents an increment in the time step of the blade as it moves through the fluid medium.

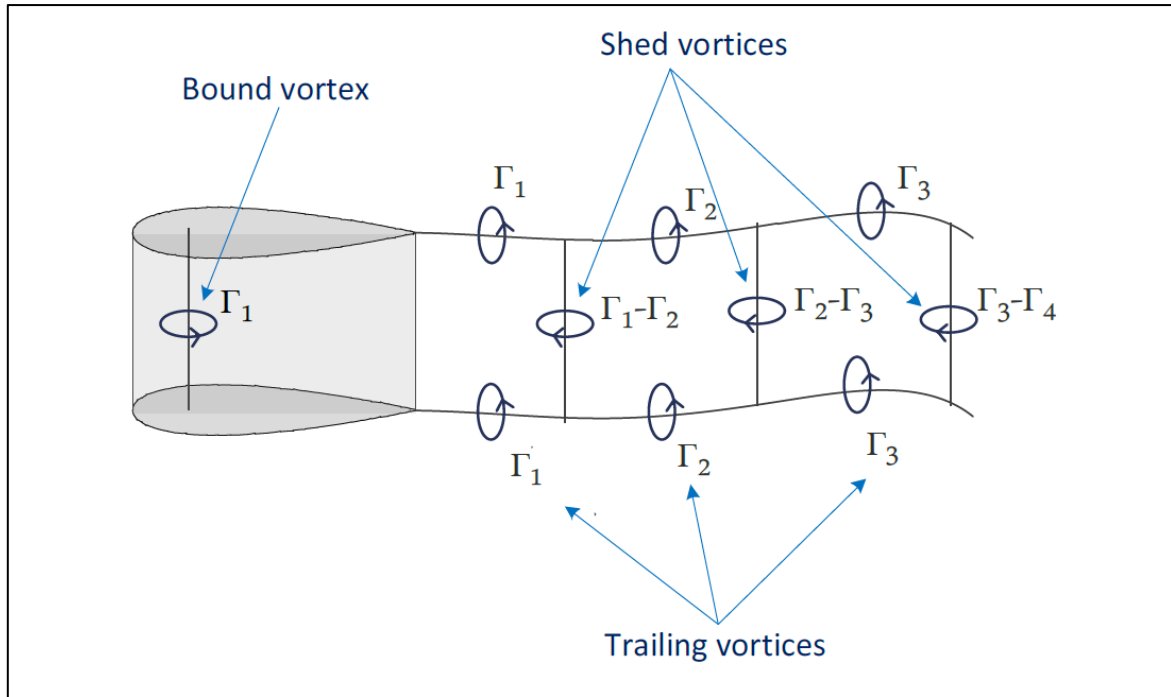


Figure 7-7: Shed vortices from hydrofoil profile, Strickland [77]

As mentioned previously, the total vorticity conservation constraint results in the formation of an unsteady wake structure which comprises of continuous shed vortices from the trailing edges of the hydrofoils of the turbine. It may be seen in Figure 7-8 that as the blade moves through the fluid from its initial position having a circulation of Γ_C^n to a new position having a circulation Γ_C^{n+1} a shed vortex commonly referred to as “nascent vortex” which has strength γ_s is calculated as follows:

$$\gamma_s = -(\Gamma_C^{n+1} - \Gamma_C^n) \quad (7.6)$$

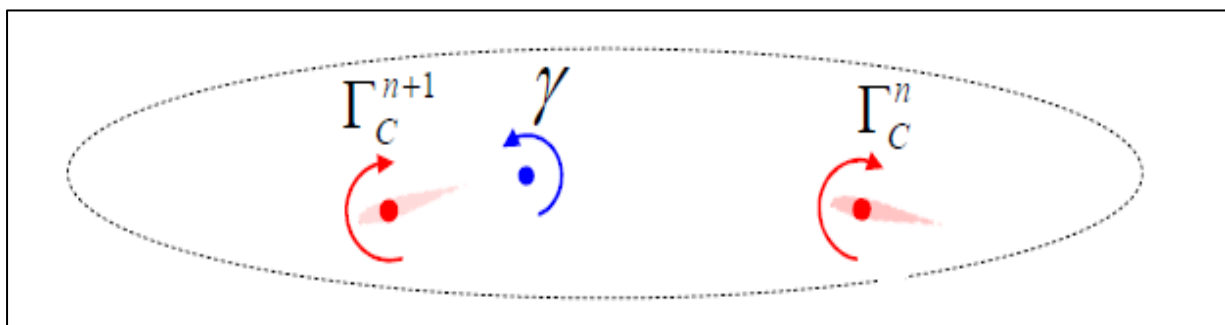


Figure 7-8 Formation of nascent vortex, Alidadi [75]

Alidadi [75] further researched the position of the nascent vortex relative to the blade profile as it moved from its taken initial position to that of its next position. The nascent vortex was calculated by using the DVM and the effects of this vortex on the induced velocities (W_v^i)

acting on the blade was assumed to have the same effect as that of a vortex sheet. This assumption was based on the Biot-Savart Law at the mid-point of the blade chord length, Katz and Polotkin [81].

Ciffone and Orloff [80] conducted experimental studies on the far field wake vortex characteristics and they concluded that the shed vortex from the airfoil rotates from the trailing edge of the blade as a single solid body which is confined within a distance of R_c which stems from the centre of the vortex referred to as the “vortex core”. This theory may be applied to the current situation of water as the shed vortices from the hydrofoil profile behaves in a highly similar way to that of the shed vortex of air under the same environmental and experimental conditions. On closer inspection of the tangential velocity (W_c) which impacts the blade, it was noted that the tangential velocity induced on the blade from the shed vortex increases linearly within the vortex core. The maximum tangential velocity is reached at the extremity of the vortex core. Figure 7-9 depicts the linear behaviour of the tangential velocity and also depicts how the tangential velocity strength has an inverse relationship with the vortex as the distance from the vortex centre exceeds the core radius (R_c).

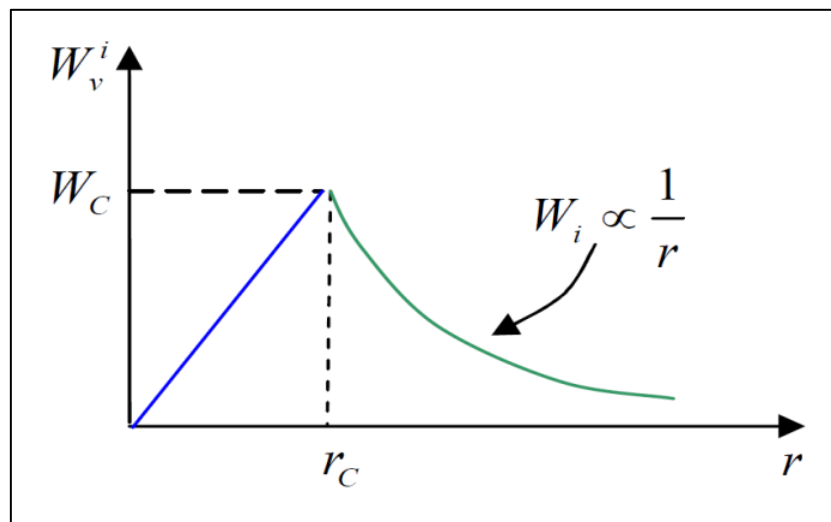


Figure 7-9: Relationship of induced vortex strength to vortex core, Alidadi [75]

The tangential vortex strength was calculated by using the theory of Alidadi [75] and the DVM model and comparing it with the vortex sheet model. The methodology which was used was based on the methods used by Strickland, et al. [74]. Figure 7-10 depicts a vortex sheet which starts from the trailing edge of a blade element and produces counter clockwise shed vortices.

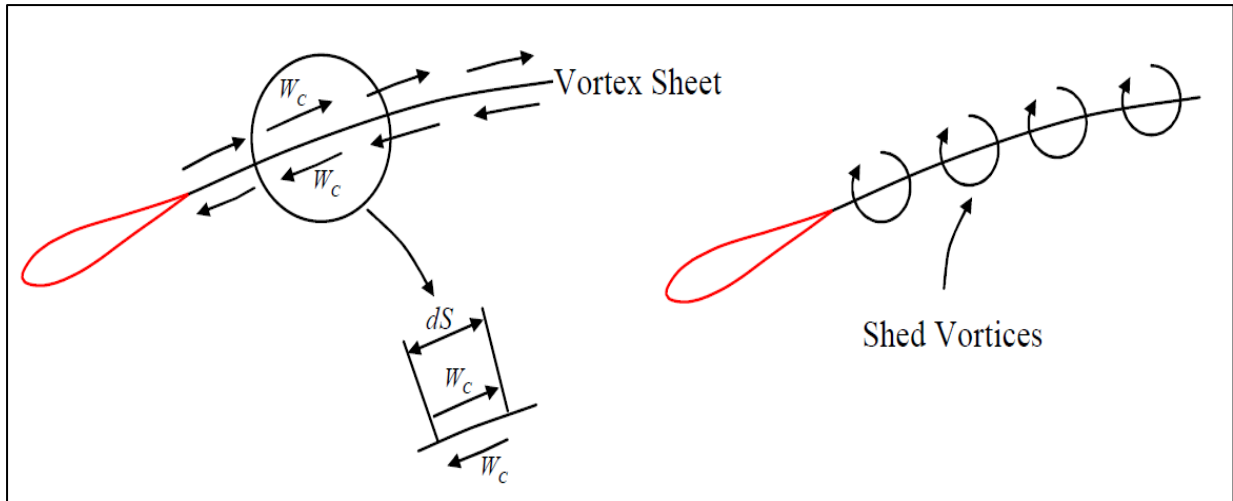


Figure 7-10: Formation of counter clockwise shed vortex, Alidadi [75]

For a point which lies outside the vortex core structure the induced tangential velocity of the counter clockwise vortex was found to be as follows based on the Biot-Savart Law:

$$W_v^i = -\frac{\gamma_s}{2\pi r} \text{ for } r \geq r_c \quad (7.7)$$

where:

W_v^i Induced velocity

γ_s Vortex strength

r Distance from the vortex center outside the vortex core

By assuming that the formation of the induced velocity stems from the trailing edge of the foil profile associated with Figure 7-10 one can come to a relationship of the induced velocity as a function of position of the shed vortex. By the definition of circulation applied to the above case the resultant induced velocity by a counter clockwise shed vortex is given as follows, Alidadi [75]:

$$W_v^i = -\frac{\gamma_s}{2R\Delta\theta} \text{ for } r \leq r_c \quad (7.8)$$

Using the above theory of vortex structure and strength the relative induced velocity on the hydrofoil blade due to all vortex components may be consolidated in the following equation, Niblick [15]:

$$U_{Rel} = U_{\infty} + U_{Tip} + \sum (U_{Bound} + U_{Trailing} + W_v^i) \quad (7.9)$$

where:

U_{Rel}	Relative velocity due to vortex interference
U_{∞}	Free Stream Velocity
U_{Tip}	Blade tip speed
U_{Bound}	Induced bound vortex velocity
$U_{Trailing}$	Induced velocity from trailing vortex
W_v^i	Induced velocity from shed vortex

This equation defines the relative velocity which the blade experiences as it moves through the fluid medium. By obtaining the relative velocity vector of the fluid acting on the blade, the bound vortex within the blade element may be calculated. This bound vortex located at the centre of pressure of the profile may also be referred to as the pitching moment within the blade. The included effects of vortex interaction with the incoming flow may be viewed as advantageous compared to that of the momentum models which do not account for the vortex structure and interference to the free stream and rotational components of the flow.

7.4 Numerical Analysis of Turbine

The following section expands on the analytical modelling of the helical cross-flow turbine by using theoretical equations and numerical analysis. A double multiple streamtube model was developed by adapting the modelling approach which was used in Biadgo, et al. [16]. This method of analysis logic was also used by various other researchers and stems from the original double multiple streamtube model constructed by Strickland [77]. The mathematical approach was compared with a Computational Fluid Dynamic (CFD) model designed to analyse the complex vortices created by the aerofoil's flow separation and the interaction with the downstream wake.

7.4.1 Numerical Model

Various computational models were developed in the effort of analysing a vertical axis Darrieus type turbine, each of which has its own specific strengths and weaknesses. Islam, et

al. [86], Paraschivoiu [78] and Paraschivoiu, et al. [87] conducted surveys on the various types of models which are used to analyse and predict the behaviour of vertical axis wind turbine (VAWT) systems. The three major models are the momentum models as explained previously, the vortex models and computational fluid dynamics (CFD) models. Figure 7-11 shows the expansion of the momentum model theory from the single actuator disc theory, Biadgo, et al. [16]. The double multiple streamtube model using a fixed interference factor was used in the built model as the variable interference factor had to be built into an empirical iterative solver within numerical solver.

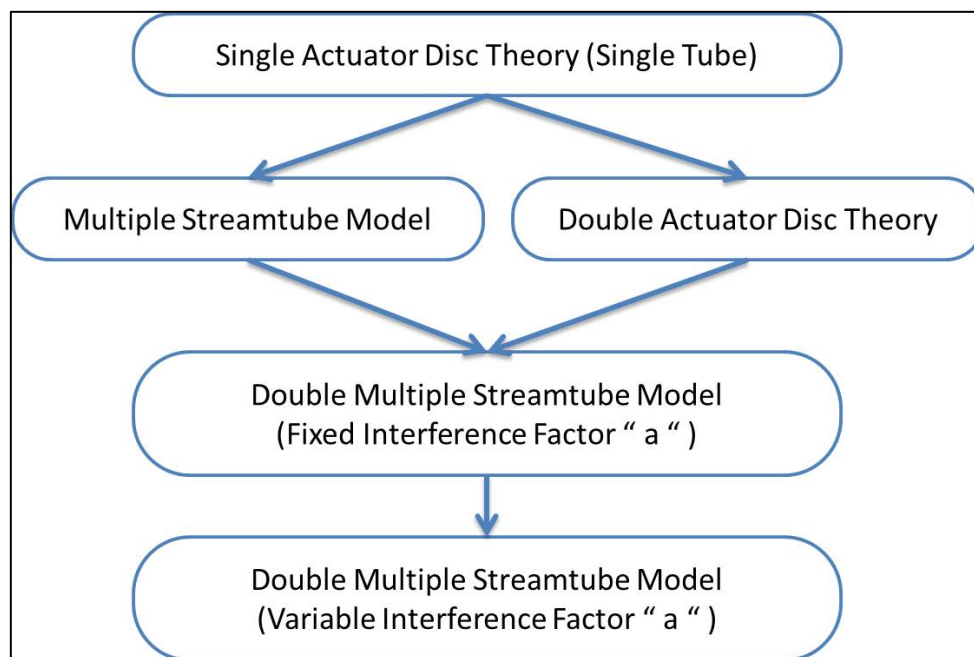


Figure 7-11: Expansion of actuator disc theory

In section 7.2 the conventional concept of a singular streamtube model was expanded on by elaborating on the multiple streamtube model. As the name suggests, multiple streamtubes occupy the assumed control volume surrounding the turbine. However, in the case of the double multiple streamtube model, the turbine section is subdivided into an upwind and downwind section as previously depicted in Figure 7-4. These two separate sections have specific parameters linked to them. The double multiple streamtube model was best described by Loth and McCoy [88] and Paraschivoiu and Delclaux [89]. They elaborate on the fact that by combining the multiple streamtube theory with the double actuator disc theory, the double multiple streamtube theory allows for the accurate modelling of the velocity variations which occur across the turbine. Looking back on the previous models of analysis, which the following theory was built on, it is evident that they could not evaluate the significant

influence of the upwind and downwind characteristics and direct influence on the turbine performance, Cunden [90].

By analysing the characteristics of the turbine, regarding the upwind and downwind sections it can be concluded that the upwind section influences the analysis of the downwind section of the turbine. The velocity of the upwind section is higher than the velocities found in the downwind section. The changes in velocity profiles are due to the upwind interaction of the blades as they extract energy from the incoming flow which is in direct relation to the second law of thermodynamics. In the double multiple streamtube model, the upwind extraction occurs in the multiple streamtubes across the global control volume. Focusing on the multiple streamtube control volumes, it was concluded by Strickland [77] that each streamtube's induced velocity is reduced by what is referred to as interference factor “ a ” and “ a' ” for the upwind and downwind sides respectively. These interference factors accommodate for the loss of velocity between the two extremities of the relevant streamtube due to the blade interaction with the flow and extraction of energy from the flow.

The equations governing the two sections were derived from the existing aerodynamic characteristics associated with the standard straight bladed Darrieus turbine. As the approach analyses discrete sections of the blade, the double multiple streamtube model can be used to determine the characteristics of a helical profiled bladed turbine, such as the Gorlov turbine which is considered in this dissertation. On closer examination of the double actuator disc theory which is depicted in Figure 7-12, it can be graphically seen how the free-stream velocity changes through interaction with the blades and creates induced velocities.

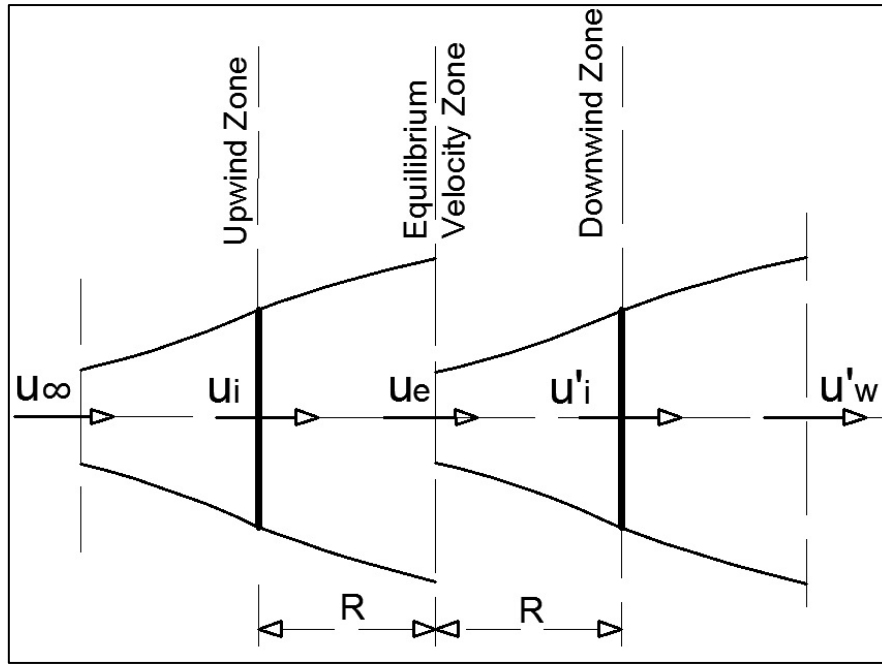


Figure 7-12: Multiple Actuator Disc Theory, Biadgo, et al. [16]

The induced velocities for the upwind and downwind sections are illustrated in equations 7.10 and 7.11 respectively. It can be concluded that the induced velocity of the downwind actuator is dependent on the exit velocity of the upwind actuator. These equations provide the basis for calculation of the relative velocity of the fluid flow and the constantly changing attack angles of the turbine blades, by using the interference factors which are obtained via an iterative method, Biadgo, et al. [16].

$$u_i = (1 - a)U_\infty \quad (7.10)$$

where:

- u_i Induced velocity (Upwind)
- a Interference / Induction factor (Upwind)
- U_∞ Incoming free-stream velocity

$$u'_i = (1 - a')(1 - 2a)U_\infty \quad (7.11)$$

where:

u_i'	Induced velocity (Downwind)
a'	Interference / Induction factor (Downwind)
a	Interference / Induction factor (Upwind)
U_∞	Incoming free-stream velocity

This analysis takes the interaction of the turbine blades in the upwind separately to the downwind section. The main assumption is that the wake created from the flow in the upwind section expands to its full extent and the resultant wake velocity reaches the downwind section before the flow interacts with the blades in the downwind pass. Due to this assumption, the downwind blades interact with a reduced “free-stream” velocity. It can be safely assumed that this method of mathematical analysis, which takes into consideration the variation in flow velocity at discrete points in the control volume, is the most accurate mode of analysis for an ideal case.

The double multiple streamtube model solves the equations allocated for the upwind and downwind sections simultaneously. The equations are linked to the stream-wise force at each actuator disc. The following equations are obtained from the conservation of momentum and the aerodynamic coefficient characteristics of the turbine blade profiles being implemented. The equations for the upwind and downwind sections of the turbine, including the attack angle, are as follows, Biadgo, et al. [16]:

$$w = \sqrt{(u_i \sin \theta)^2 + (u_i \cos \theta + \omega R)^2} \quad (7.12)$$

where:

w	Relative velocity (Upwind)
u_i	Induced velocity (Upwind)
ω	Rotational velocity of the turbine
θ	Azimuthal Angle
R	Radius of the turbine

$$\alpha = \tan^{-1} \left(\frac{(1-a)\sin\theta}{(1-a)\cos\theta + \lambda} \right) \quad (7.13)$$

where:

- α Attack Angle (Upwind)
- a Interference / Induction factor (Upwind)
- λ Tip Speed Ratio
- θ Azimuthal Angle

$$w' = \sqrt{(u_i' \sin \theta)^2 + (u_i' \cos \theta + \omega R)^2} \quad (7.14)$$

where:

- w' Relative velocity (Upwind)
- u_i' Induced velocity (Upwind)
- ω Rotational velocity of the turbine
- θ Azimuthal Angle
- R Radius of the turbine

$$\alpha' = \tan^{-1} \left(\frac{(1-a')\sin\theta}{(1-a')\cos\theta + \lambda} \right) \quad (7.15)$$

where:

- α' Attack Angle (Downwind)
- a' Interference / Induction factor (Downwind)
- λ Tip Speed Ratio
- θ Azimuthal Angle

To correctly use these equations within an iterative solver, there needs to be a common value to compare to the analytical data. By reverting back to the multiple streamtube model and the hydrodynamics of the turbine various new equations can be resolved using the multiple streamtube approach, Cunden [90].

As stated previously, the tangential (C_t) and normal (C_n) coefficients of the turbine are highly important in the calculation of the performance of the turbine. As the multiple streamtube model analyses the turbine performance for one full revolution from 0° to 360° , the previously stated coefficient methods cannot be directly incorporated in the model, hence a relationship with the constantly changing attack angle (α) needs to be established. Equations 7.3 and 7.4 accurately depict the tangential and normal coefficients respectively.

The common relating value was found between the analytical equations and the numerical models were found to be the thrust coefficient. The accuracy of the double multiple streamtube model is directly dependant on the total number of discrete streamtubes being used. The momentum balances for each of the streamtubes are calculated individually. The separate calculations results in the model having to acquire the “ N ” amount of induction factors for each streamtube. The induction factor for each streamtube will be different due to blade attack angle and resulting relative velocity being different in each streamtube. The average aerodynamic thrust on a turbine, with “ B ” number of blades can be expressed by Equation 7.18. Equation 7.18 was derived on the basis that each of the turbine blades spends $\Delta\theta/\pi$ percent of the rotational time in the streamtube, Biadgo, et al. [16].

$$T_{avg} = 2 \left(\frac{B\Delta\theta}{\pi} T_i \right) \quad (7.18)$$

where:

T_{avg}	Average Torque
B	Number of turbine blades
θ	Azimuthal Angle
T_i	Instantaneous Torque on a single blade

Taking into consideration that the streamtube has a wetted swept area of $A=hR\Delta\theta\sin\theta$, similarly to the torque coefficient of the entire turbine, the non-dimensional thrust coefficient of the turbine may be derived, as seen in equation 7.19, Biadgo, et al. [16]:

$$C_{Thrust} = \left(\frac{Bc}{2R}\right) \left(\frac{w}{U_\infty}\right)^2 \frac{2}{\pi} C_t \left(\frac{\cos\theta}{\sin\theta} - C_n\right) \quad (7.19)$$

where:

C_{Thrust}	Thrust coefficient
B	Number of turbine blades
θ	Azimuthal Angle
w	Relative velocity
U_∞	Free stream velocity
C_t	Tangential Coefficient
C_n	Normal Coefficient

Within the computational model the average torque on a rotor with, “ B ” number of blades, in one complete turbine revolution and blade length “ h ” is given by equation 7.20, Biadgo, et al. [16]:

$$Q_{avg} = B \sum_{i=1}^{N_\theta} \frac{Q_i}{N_\theta} \quad (7.20)$$

where:

Q_{avg}	Average torque on turbine
N_θ	Number of streamtube
θ	Azimuthal Angle
Q_i	Instantaneous torque on a single turbine blade

The corresponding torque coefficient can be derived from the average torque and is shown in Equation 7.21, Biadgo, et al. [16]:

$$C_Q = \left(\frac{Bc}{2R} \right) \sum_{i=1}^{N_\theta} \frac{\left(\frac{w}{U_\infty} \right)^2 C_t}{N_\theta} \quad (7.21)$$

The numerical model uses the known relationship of tip speed ratio and torque coefficient to obtain the performance coefficient of the turbine and is given by Equation 7.22:

$$C_P = \lambda C_Q \quad (7.22)$$

The equations which were discussed at the beginning of this section were adapted and implemented in a built numerical solver. This was done within QBlade software developed by Marten, et al. [91] which was built especially for the purpose of calculating a turbine's performance based on its coefficients of lift and drag as well as the corresponding tangential and normal coefficients for various attack angles. Figure 7-13 shows the basic methodology logic behind the programming based on the research conducted by Biadgo, et al. [16]

The coefficients of lift and drag were generated within an external program, which is used widely for the generation of lift and drag coefficients, called Xfoil. The various different coefficients of lift and drag may be found in Appendix A for various Reynolds numbers and discrete attack angles. The analysis was conducted on 6 types of turbines to validate the theory of using a fixed pitch turbine within a limit of 0° to 5°. The most suitable blade profile was chosen to be the NACA 0024 profile as the lift to drag ratio is the highest compared to the other symmetrical profile. Parameters regarding the entire turbine was taken from Chapter 6 and implemented accordingly. The analysis was conducted for tip speed ratios from 0.05 to 2.95 in increments of 0.1. This range was chosen based on previous literature performance on similar turbine designs. For the angle of attack for each tip speed, an increment of 30° was initially chosen and then reduced to 5° to refine the resolution of the performance curve. Within the code of the numerical solver, a Glauret empirical formula had to be imbedded so as to calculate the thrust coefficient from the analytical equation for $0.4 < a < 1$, as this is not possible for an induction factor of 0.5.

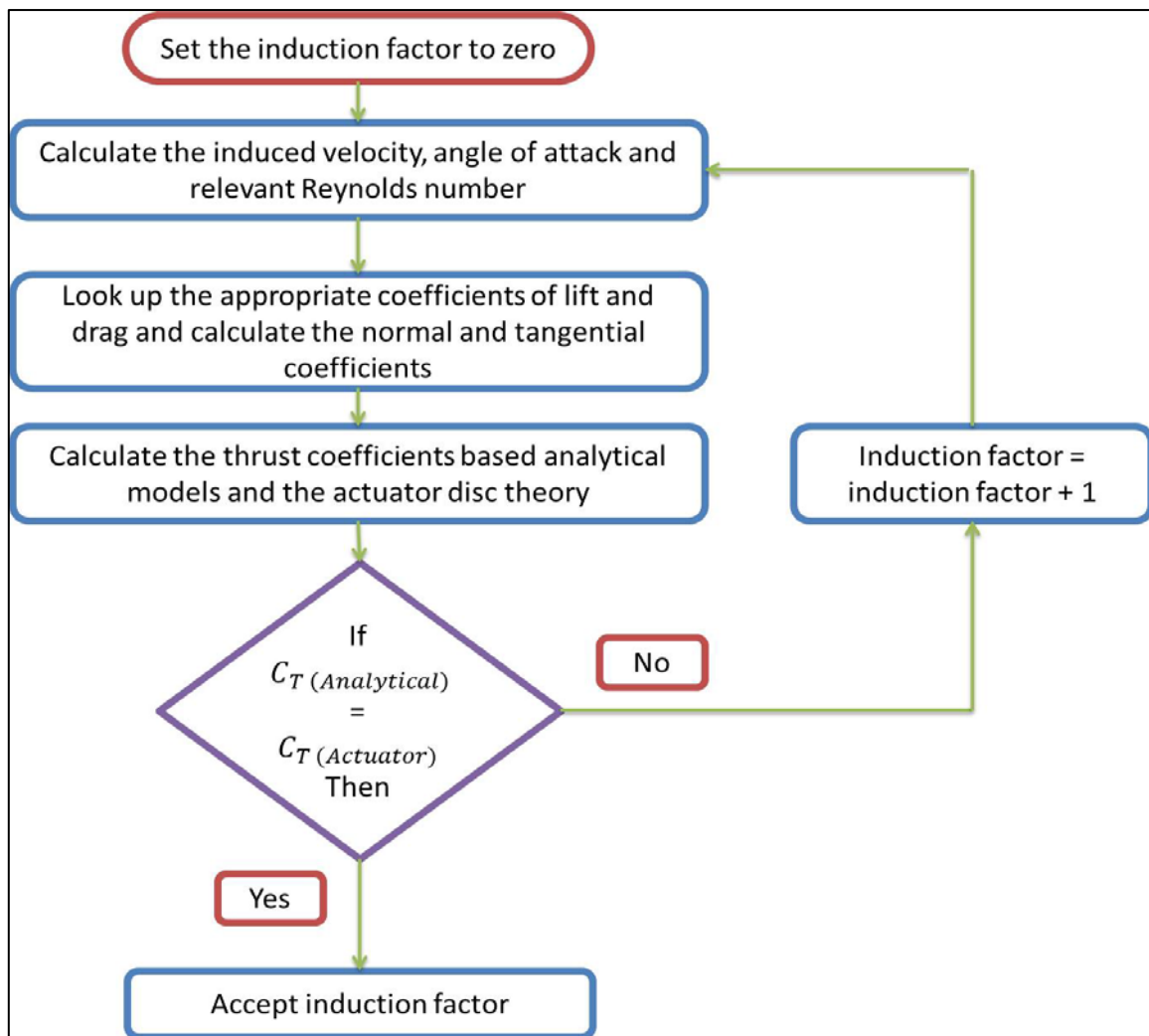


Figure 7-13: Flow Diagram of Program Logic, Biadgo, et al. [16]

Within this iterative solver, vortex modelling of the turbine was not included which may lead to somewhat of an inaccurate result but the effects may be taken as minimal. The vortex modelling of the system was omitted due to the complexity of the model which could not be adequately coded within the numerical solver but the tip loss factors were included. This type of model can be obtained via external programs such as SANDIA Labs CACTUS modelling program.

7.4.2 Computational Fluid Dynamic Model

Most of the research conducted on vertical axis wind turbines recently has included a computational model to validate the numerical solvers which were either used in conjunction with testing or developed from scratch. Various types of simulations can be conducted for the turbine depending on the output which is required. The type of solver which is chosen for the simulation directly affects each of these variations and does impact the various outputs respectively which was found by examining Li, et al. [85] and Nobile, et al. [92]. These final results, however, were not immensely impacted by the different solver choice between the two.

The following section outlines the methodology and steps which were taken to conduct the CFD model. The software which was utilised to conduct the simulation was CD-Adapco's Star CCM+ flow simulation software. A 2 Dimensional simulation and a 3 Dimensional simulation were conducted to obtain the power coefficient of the turbine which may be recognised as the turbine's efficiency and to understand the flow around the turbine respectively.

Geometry Parameters

On initialization of the simulation a 3 Dimensional CAD rendering of the turbine needed to be imported into the simulation software. However, to import this into the software a flow region needed to be constructed which indicates to the programme the region which the flow is moving in. A cavity within the flow region was formed, within the CAD domain, which was used for the turbine section. Doing this indicates to the flow simulation that the flow medium is obstructed by the cavity within the flow region.

Figure 7-14 below depicts the 2 Dimensional top view of the combined flow region and turbine region. The flow region was designed based on a simple relationship of the turbine diameter to that of the various flow region extremities. The distance of the turbine to the inlet and the surrounding walls were taken to be four times the turbine diameter ($4D$). This was to allow for enough spacing between the inlet and the surrounding walls for the fluid flow. If this spacing was inadequate, a blockage effect would arise and seemingly increase flow around those areas. This is the norm which was also followed by various other researchers who have examined similar turbines.

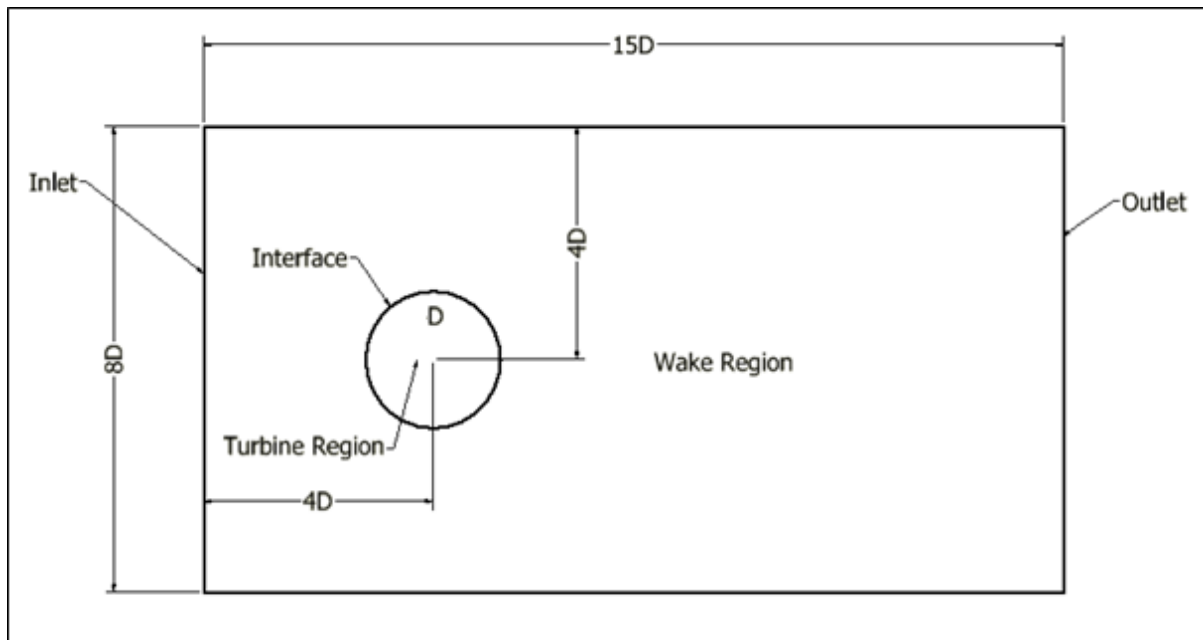


Figure 7-14: Turbine and Flow Region

Once this has been imported into the simulation software one still needs to edit the geometry so as to obtain useful results from the simulation. For the simulation which was conducted, the turbine was separated into key components such as the turbine blades, the turbine central shaft and the turbine end hubs. Included in this partitioning of the geometry was the interface region which provides the simulation with an indication of where the flow will be transitioning from one flow region to another. This was highly important because if this was not defined the simulation would result in flow around a cylindrical body at the various flow velocities and not include the turbine rotation. The sections of the flow region also needed to be portioned into inlet, outlet and slip wall surfaces so as to allow for the various input conditions for the simulation. Once these parameters are set the discretization of the model can be conducted.

Mesh Conditions

In order to adequately simulate the flow through a body or around a restrictive surface, the flow field is required to be discretized. Discretization of the flow field is basically breaking down the flow field into smaller regions by means of a discretizing element structure. There are many different types of meshing structures which can be used for the discretization process. For the CFD simulation a polyhedral mesh condition was selected for the volume discretization of the flow field. This was done as it has 14 faces with multiple nodes points all

implementing the fundamental flow parameters such as the continuity equation and the Navier-Stokes equations for the flow condition.

The mesh models first needed to be selected before commencing the discretization of the imported geometry. The models which were selected were surface, prism layer and polyhedral mesh models. The surface mesh model is an initial mesh model which allows the user to identify any possible deviations or errors within the imported geometry and allows for modification to correct the model.

The prism layer mesh model identifies the boundaries within the flow domain which possibly restrict flow and assign boundary layers to these regions. The prism layer mesh model generates a mesh which is a separate mesh from that of the core mesh. This is so the boundary layer thickness can be defined from the wall to the thickness which is selected. Figure 7-15 depicts the difference between the prism layer thickness from the wall surface in conjunction to that of the core mesh, CD-Adapco [93].

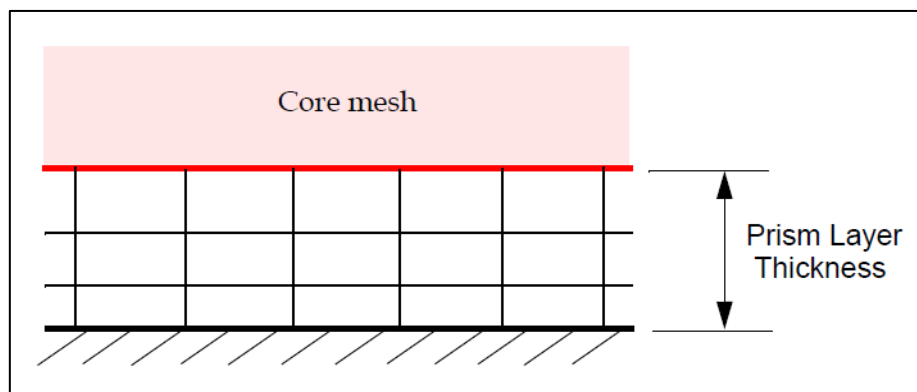


Figure 7-15: Prism Layer, CD-Adapco [93]

When the mesh is generated, it will expand upwards to that of the core mesh by the specified prism layer stretching factor. The prism layer thickness was set to be 25% of the base element size of 100 m and the stretching factor was set to be 1.5. The number of prism layers directly affects the resolution of the prism layer as an increase in this parameter would increase the discretization of the prism layer thickness. The boundary wall properties of the flow domain were changed to slip wall as this would eliminate the prism layer meshing model from creating boundary layers on the flow domain boundary walls.

The polyhedral mesh model is the meshing model which creates the cells which are used to calculate the various flow conditions for the simulation. The cell shape is arbitrary; however,

this cell is bounded by the base element sizing condition which is set before running the meshing procedure. Figure 7-16 below depicts a threshold visualization which illustrates the volume mesh which was generated for the simulation of the vertical axis turbine. The equations of fluid flow and interaction are conducted by the nodes of the cells which are the end points of each face of the cell.

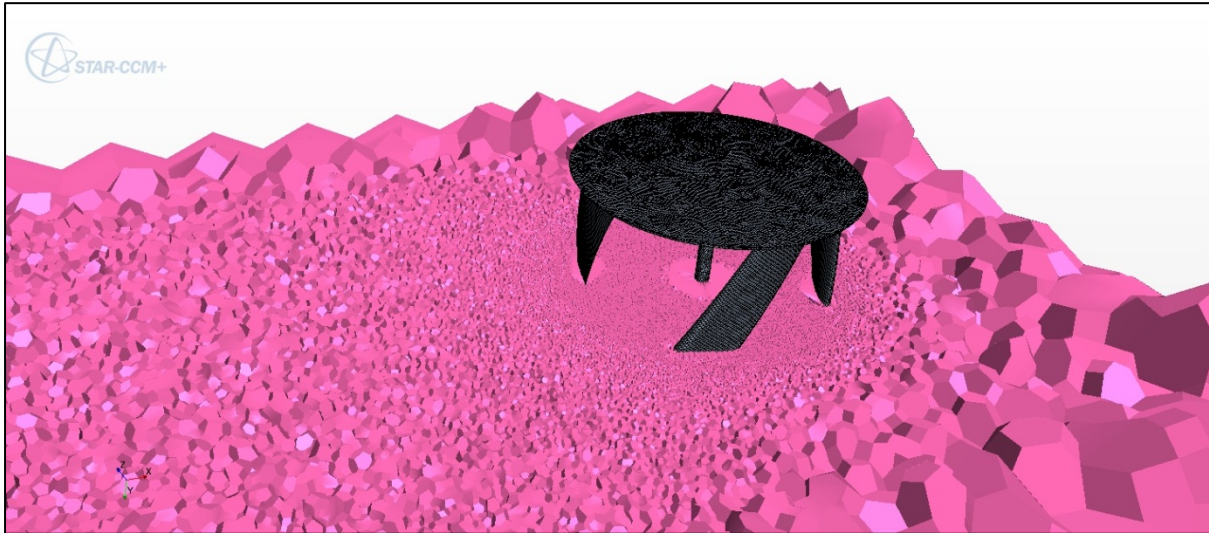


Figure 7-16: Threshold Mesh of Flow Field and Turbine

The mesh was refined by means of a mesh control volume which was configured for the simulation to increase the density of the mesh within the control volume. Figure 7-17 below depicts the two control volumes which were utilised to decrease the element size and increase the number of elements within the control volume which resulted in a finer mesh within that specific section of the geometry.

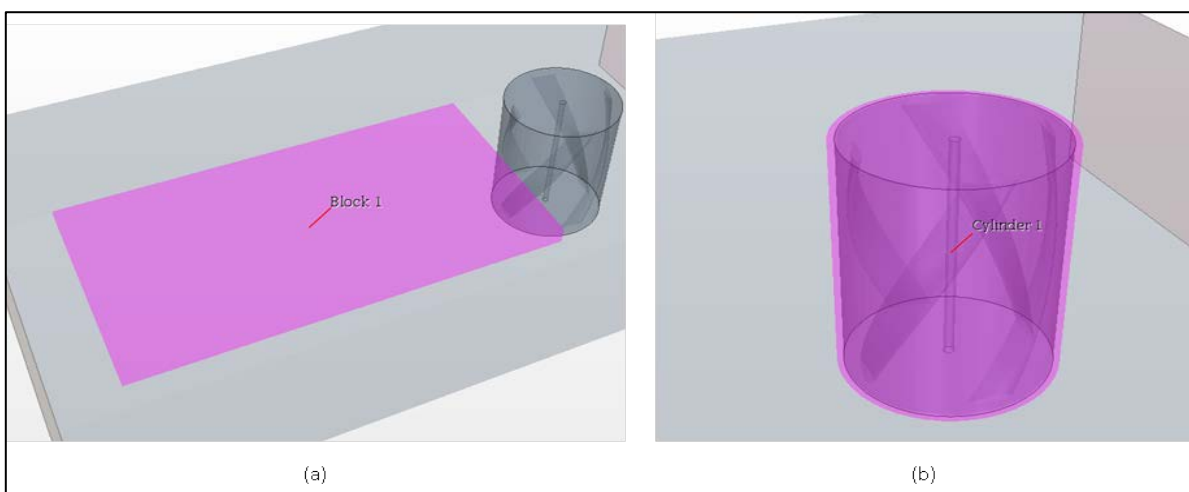


Figure 7-17: Volumetric Control of Mesh

Figure 7-18 depicts the flow field and turbine discretization which was conducted within Star CMM+. It can be seen that there are various different mesh densities within this discretization. The variation in mesh densities was done so as to obtain a refined solution for the turbine region with respect to the turbine blades and the turbine shaft. The section behind the turbine was refined so as to understand the complex wake formation which stems from the turbine as it rotates within the flow.

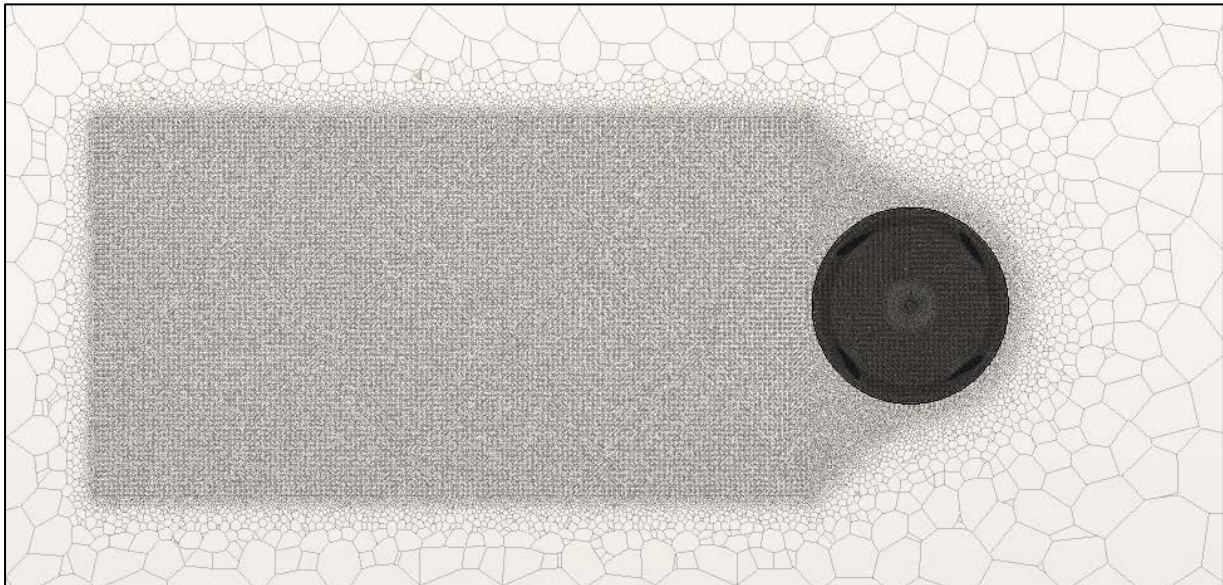


Figure 7-18: Discretization of Flow Field & Turbine

In order to reduce computational time a 2 Dimensional mesh was derived for the flow field and turbine to obtain a numerical solution for the force and moment on the turbine blades as well as the moment on the turbine shaft. This can be done for this type of turbine as the turbine blade wrap means that a blade will always be in contact with the flow medium.

Physical Conditions

The physics conditions are the parameters which are used by the cells of the mesh to conduct the bounding flow equations. For the simulation of the turbine the following physical parameters were chosen:

1. Liquid Fluid Medium.
2. Constant Density Flow.
3. Implicit – Unsteady solver.
4. K – Ω Turbulence model.
5. Average Navier-Stokes solving criteria.

6. Turbulence Suppression.

For the rotation of the turbine within the model an interface plane was required. This plane links both the regions so the solver can distinguish the transition of flow from the entire flow domain and the turbine flow region. A new co-ordinate system was constructed for the turbine region and assigned a motion constraint with the parameters of rotation equivalent to the rotational speed of the turbine for the given tip speed ratio. This value had to be altered for the various simulations as the programme cannot use inertial predictions for the turbine's rotation. By assigning a rotational constraint to the reference co-ordinate, the co-ordinates of the region of the turbine was changed to the reference co-ordinates and the relative physics conditions were changed to specify rotational motion of this region.

Solver Selection

As stated above, an implicit unsteady solver was chosen for the simulation of the vertical axis turbine. This was done as a steady state solver would not simulate accurately the effects of the turbine blades rotation within the flow field. It was found that in order to accurately simulate the flow conditions in the highly turbulent region of the turbine, a further discretization was required coupled with a turbulence model which is commonly used for turbine or aerofoil analysis.

An implicit unsteady solver further discretizes the turbine's rotational path into finite time steps within the revolution. Within a single time step a number of iterations are conducted for the given spatial and time domain co-ordinates of the turbine blade during its rotation. For the simulation which was conducted, a time step of 1.4 s was selected based on the time step relationship to the rotational path. CD-Adapco [94], indicates that as a rule of thumb one should select 1° per time step. The equation which governs this is as follows:

$$Time_{step} = \frac{60}{RPM \times 360} \quad (7.23)$$

Where

TimeStep Time Step for the solution (s)
RPM Revolutions per Minute of the turbine

Within each time step convergence is required which depicts that the solution within that time step has reached a point solution which is more accurate than that of a steady model.

Reports & Monitors

In order to obtain results from the CFD simulation a report needed to be created within the programme which identifies the key areas which one needs to monitor. In the case of the vertical axis turbine, the turbine's coefficient of power was the main output which was required from the simulation. In order to achieve this, the torque on the turbine shaft was monitored as the torque has a direct relationship to that of the power coefficient of the turbine. Along with this result a report was set up to monitor the torque on the blades of the turbine and the force on the blades of the turbine.

From the reports which were created, monitor plots were created to visualise through the simulation for convergence of a solution for the three factors. These results will be further expanded on and compared to the numerical model for the same conditions in Chapter 8.

CHAPTER 8 RESULTS AND DISCUSSIONS

This chapter of the dissertation outlays the results which were found from the numerical and CFD simulations which were conducted for the turbine which was designed. The results are also reflecting the effect of pitch angle on the turbine blades and the channel augmentation on the flow speed.

8.1 Helical Turbine - No Pitch Angle

As stated previously, for the numerical solvers iterative process to run successfully, the lift and drag coefficients needed to be calculated and stored in a data array bank so the solver may access and check for values which are in the specific range as the multiple equations are run. For this, lift and drag coefficients were generated for the selected profile for the Reynolds numbers in relation to flow velocity as shown in Table 8-1 for a hydraulic diameter of 0.1m and kinematic Viscosity of $1.004 \times 10^{-6} \text{ m}^2/\text{s}$.

Table 1: Reynolds Numbers for increasing flow velocity

Reynolds	Flow Speed (m/s)
0.00	0
19 920.32	0.2
39 840.64	0.4
59 760.96	0.6
79 681.27	0.8
99 601.59	1
119 521.91	1.2
139 442.23	1.4
159 362.55	1.6
179 282.87	1.8
199 203.19	2
219 123.51	2.2
239 043.82	2.4
258 964.14	2.6
278 884.46	2.8
298 804.78	3

The coefficients of lift and drag was generated with the use of Xfoil solver in conjunction with the numerical solver so as to calculate the performance coefficient for the overall turbine, the force on a turbine blade as well as the resultant torque on the rotor of the blade.

To run the numerical solver, the blade of the turbine was required to be modelled within the program as this served as a platform of discretizing the blade into multiple blade elements similar to that of meshing an object in the CFD environment. Figure 8-1 below depicts the turbine which were discretized within the numerical solver which was built by Marten, et al. [91].

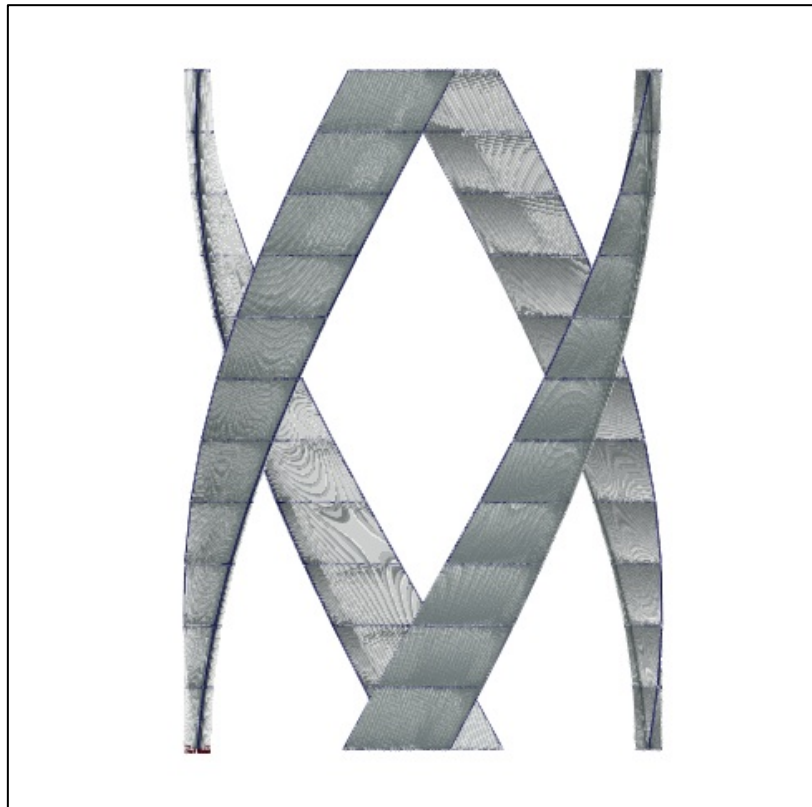


Figure 8-1: Discretization of Turbine

As mentioned earlier, Gorlov concluded in his research on the straight bladed Darrieus turbine that one of the factors which hinders a straight bladed turbine's performance is the varying torque loading on the central shaft which is created by an inherent void between the turbine blades. This is due to the fact that within the straight bladed turbine's design there is no blade overlap. However, in the helical design, a 100% or multiples thereof, steers towards a reduced force loading with respect to fluctuations on the rotor and hence the subsequent torque loading on the turbine shaft as the torque loading is the force loading product with the turbine radius.

Flow curvature needed to be considered within the QBlade model. As indicated within Chapter 7 of the dissertation, induction factors are highly important in the accurate prediction of the turbine's performance. It was also indicated that the 3 Dimensional vortex effects were

important as the downstream wake formation also affects the amount of power which is extracted by the turbine. Figure 8-2 depicts the effects of the factors on the performance curve of the turbine for a 0.5 m/s flow. The performance curve was chosen as the basis for understanding the effects as this parameter can be correlated with that of previous experimental results on similar turbines and from previous literature, [65]. For the simulation of the turbine which was designed, both induction factors and tip losses were included to obtain the most accurate prediction of performance parameters.

By not including tip losses or variable induction factors it was found that the performance prediction for the turbine was extremely high and obscure from the conventional results, [21,28,63,65,66]. As the CFD simulation took into account the variation in flow as it was discretized which served as multiple layers of varying induction factors, the mathematical model with variable induction factors only can be seen to be a good representation of the performance curve for similar turbines; however, this curve was drastically over exaggerated and surpasses Betz Limit for the turbine. The importance of variable induction factors can be seen as the prediction seemingly increases as if the turbine was not restricting flow during extraction. The last simulation included variable induction factors and tip losses of the blades which resulted in a more accurate performance prediction.

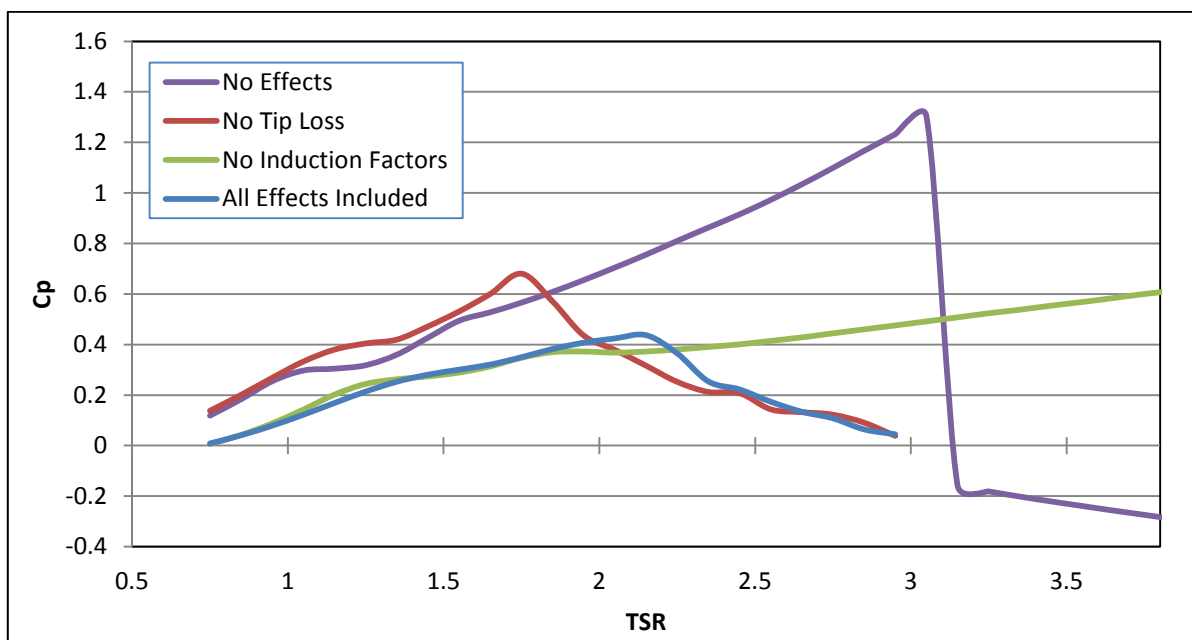


Figure 8-2: Effects of Flow Curvature

Figure 8-3 below depicts the tangential force loading profile which stems from a single blade within the helical turbine for one full revolution. It can be seen that the CFD result is in good

relation to that of the numerical model indicating that the two models were conducted correctly as this result also corresponds with the literature which was mentioned previously. However, it can be seen from the CFD analysis the effect of the shed vortices on the turbine blade during the last degrees of revolution. The CFD result indicates a slight fluctuation in force as the blade passes through 240 to 330 degrees. This is due to the blade overcoming the force of the vortex which has shed from the blade.

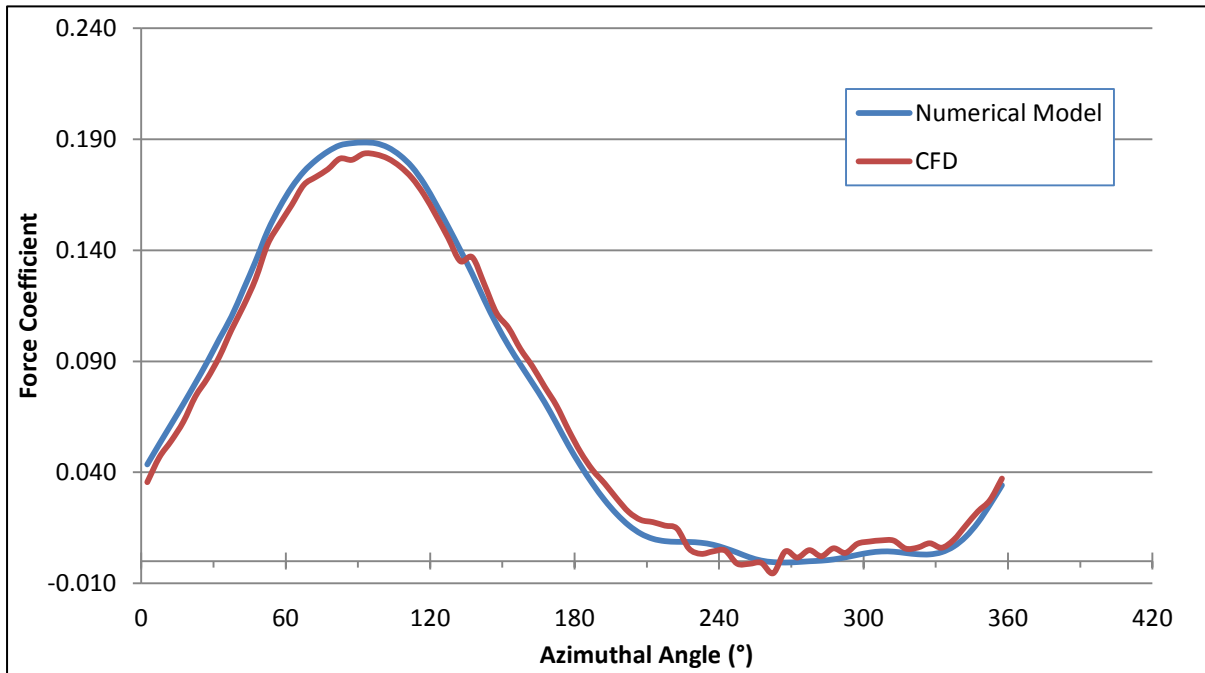


Figure 8-3: Force Coefficient on a Single Blade

The force coefficient on the blades is of importance as the lift force which is generated by the blade profiles forms the fundamental basis for the power generation from the turbine as a whole. Figure 8-4 illustrates the torque coefficient of a single blade for the turbine for various tip speed ratios for a given flow velocity. The area plot clearly depicts the change in torque, and hence the resultant torque on the rotor, as the tip speed ratio increases till its maximum operating point for the flow speed. As the torque on the blade decreases in relation to the increasing tip speed ratio, it was noted that the power coefficient is also decreasing in proportion.

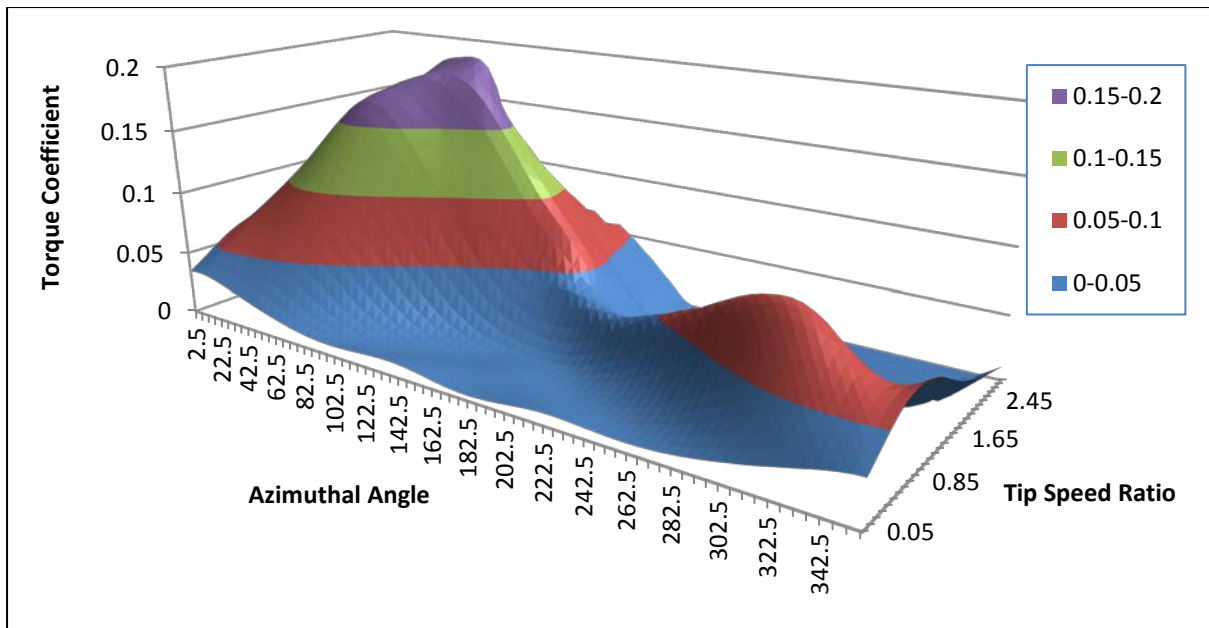


Figure 8-4: Torque Coefficient Plot for a Single Blade

The theory states that as blade overlap is increased the remaining blade torque profiles will seemingly dissipate the fluctuation of torque from a single blade. The summation of the individual blade torque loading profiles would result in a torque loading which is fairly constant and almost periodic. Figure 8-5 below illustrates the combination of all the blade torque coefficients on the turbine's central shaft.

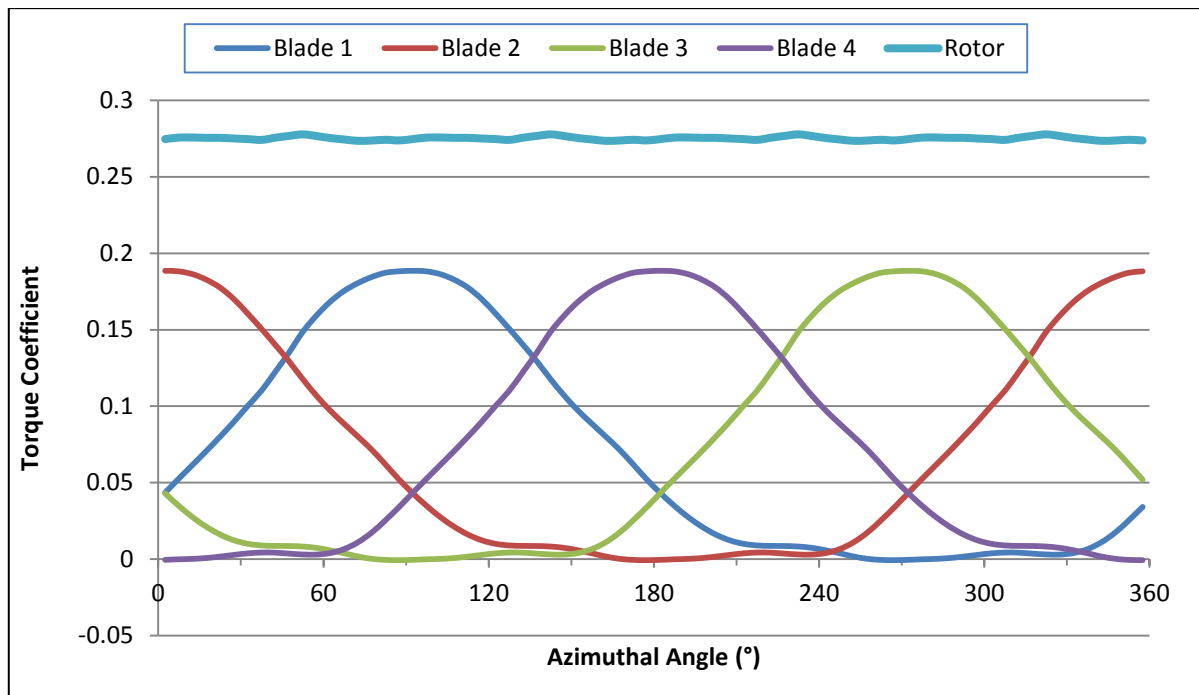


Figure 8-5: Combined force distribution on each blade and resultant torque coefficients on rotor

The most important results from the simulations were the power coefficients and the force coefficients on the blade of the turbine to understand the torque loading on the central shaft of the turbine. Figure 8-6 below depicts the power coefficient for the helical turbine which was designed. The simulation was conducted for a flow speed of 1 m/s for both the turbines as this is taken to be the maximum stable velocity of the Agulhas current.

It can be seen from this that the CFD model is of adequate agreement to that of the numerical model. The result can also be matched in good relation to that of the results obtained by Raciti Castelli, et al. [95] and Shiono, et al. [96].

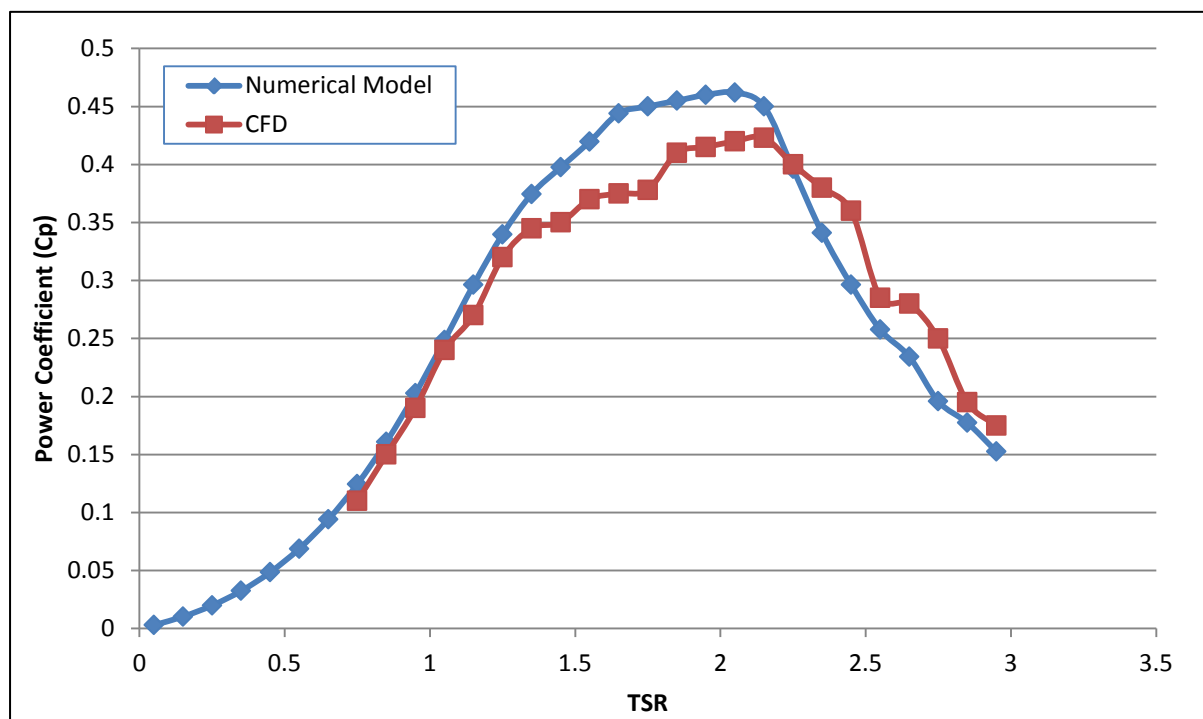


Figure 8-6: Cp for Turbine at 1 m/s

It can be seen that the CFD model is in good correlation with that of the numerical model and does not deviate by a large degree. The error which does arise at the maximum power coefficient of the curve can be attributed to the complex vortex shedding and vortex interaction with that of the turbine downstream section. Due to the complexity of the shed vortex formation and the fact that its motion is in three dimensions, the circulatory effects could not be modelled within a two dimensional space.

It can also be noted after a tip speed ratio (TSR) of 2.25 the CFD model has various fluctuations which are a result of flow separation from the turbine blades which result in shed

vortices. Within this region is where dynamic stall is more prevalent as the rate of change of the blades attack angle are increased due to the increase in TSR.

Figure 8-7 below depicts the resultant torque loading on the turbine central shaft taken for the various TSR based on the above power coefficient curve for a flow speed of 1 m/s obtained from the numerical solver. It can be seen that as the turbine starts up from TSR of 0.55 to its maximum power coefficient point at TSR of 2.15 the torque on the central shaft increases. This is due to the direct relationship of the torque coefficient with the power coefficient as stated previously in Chapter 6.

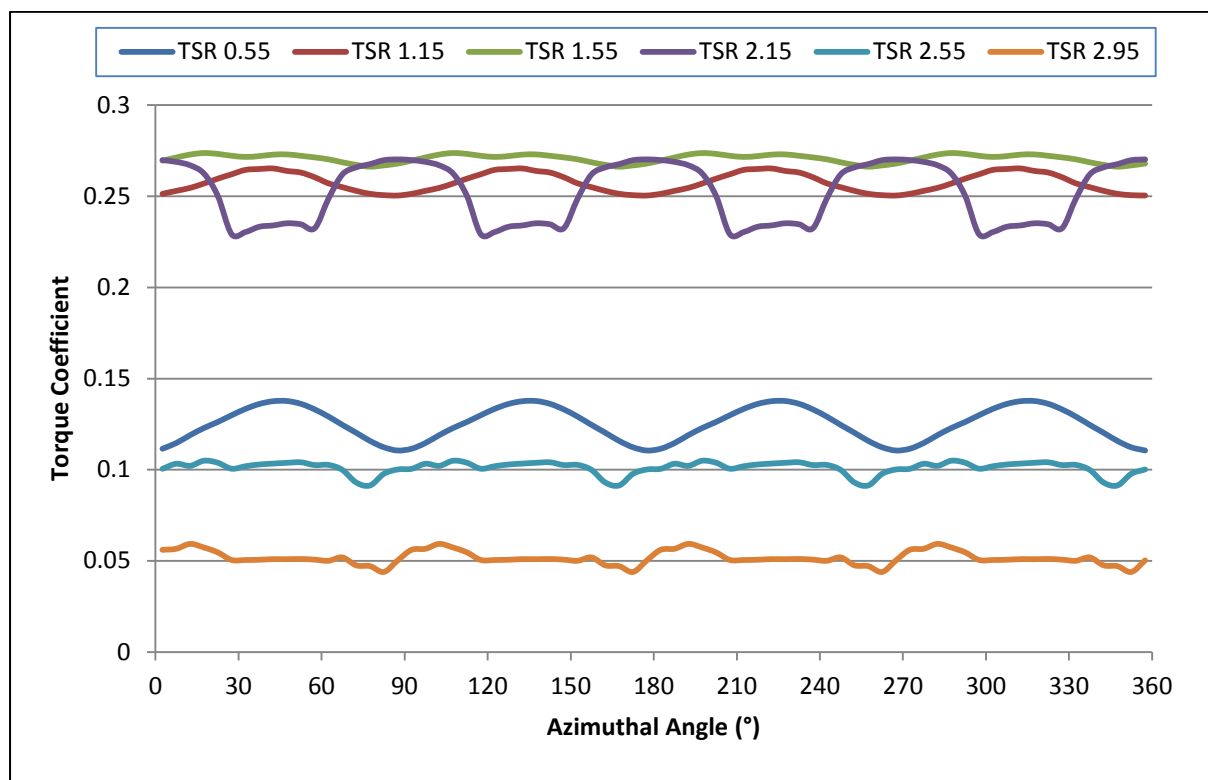


Figure 8-7: Resultant Torque Loading on Turbine Central Shaft

Even though the unsteady behaviour of the torque loading may seem periodic this can be taken as an indication of vibration on the shaft. These vibrations can be potentially harmful to the turbine if they occur within the same natural frequency of the shaft material or one of the modes of frequencies because this will result in failure. This type of loading also increases life cycle fatigue on the shaft unless it was designed for these conditions.

Figure 8-8 illustrates further the torque coefficient generated from the blade and the associated power coefficient from that single blade which is represented by a polar plot for the blade's full 360° rotational path. This result varies for the various tip speeds as can be

seen in Figure 8-4. Figure 8-8 below is based on the optimum tip speed ratio for a flow velocity of 1 m/s, before fluctuations occur at the peak of the power coefficient in relation to the flow velocity.

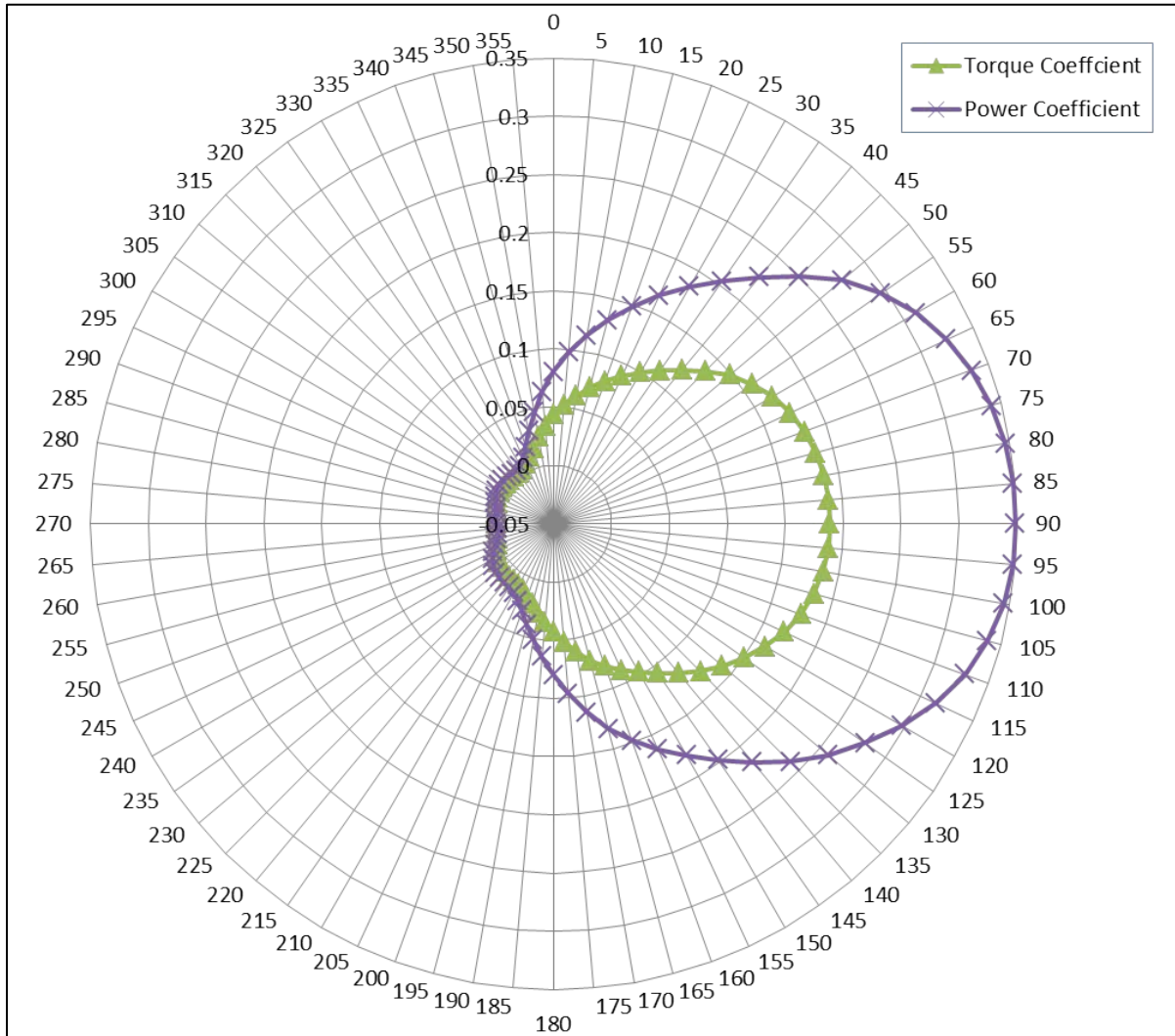


Figure 8-8: Polar plot of single blade torque and power coefficient – TSR 1.85

It would not be advisable to design a turbine to operate at its maximum power point as the torque loading on the shaft, as depicted below, is not constant and can result in failure. This unsteady loading on the turbine shaft also directly affects the amount of electric power which may be generated as the generator has to be synchronised with the turbine. Catastrophic failure can occur if these two key components are not synchronised correctly. From this result it would be advisable to design a turbine to operate just under its maximum power coefficient and corresponding TSR as this would yield a more controllable power output in comparison to the unsteady loading which not only has a lower yield but vibrational effects.

8.2 Helical Turbine – Addition of Pitch Angle

As stated in Chapter 6 in conjunction with the research which was conducted by Fiedler and Tullis [64], a toe-out angle of 0° to 7.5° was implemented to the turbine with increments of 1° . The theory is based on the assumption that the turbine would experience an increase in lift force as the blade pitch is increased, in the specified region of 0° to 7.5° , as more of the blade is exposed to the flow medium. It was found, however, that from a blade pitch of 4° onwards the turbine power coefficients decreased and thus the analysis was only conducted from 0° to 5° .

Figure 8-9 below depicts the variation of power coefficients for the turbine for the different blade pitch angles. The decrease in power coefficient indicates that the pitch angle does not positively increase the turbine's power coefficient. This is evident for various speeds of the simulation. Figure 8-9 depicts the power coefficient for a flow velocity of 1 m/s for each blade pitch angle chosen.

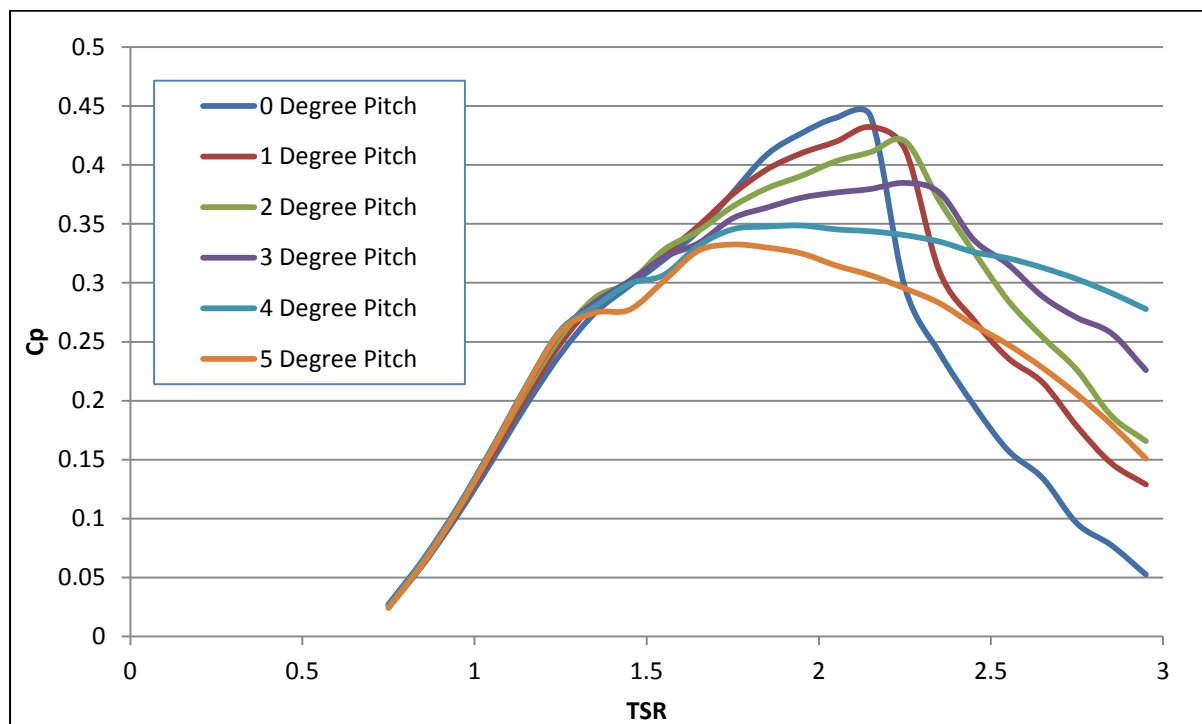


Figure 8-9: Cp for various blade pitch angles

It was noted that the increase in blade pitch angle for the turbine, the peak power coefficient decreases and shifts towards a higher tip speed ratio. This was peculiar as the power coefficient curve also tended to smoothen out in comparison to the turbine with no pitch angle modification.

Figure 8-10 below depicts the polar plots of the torque coefficients of a single turbine blade for a single rotation for the various pitch angles which were analysed. The blade torque coefficients were taken for the peak power coefficient for each of the pitch angles to identify the variations of individual blade torque for the change in blade pitch angle. It would seem as if the turbine with a blade pitch of 5° is in good comparison to that of the blade with no pitch and would seemingly output the similar power; however, each of the blades which was analysed in Figure 8-10 was taken for its own individual peak power coefficient as depicted in Figure 8-9.

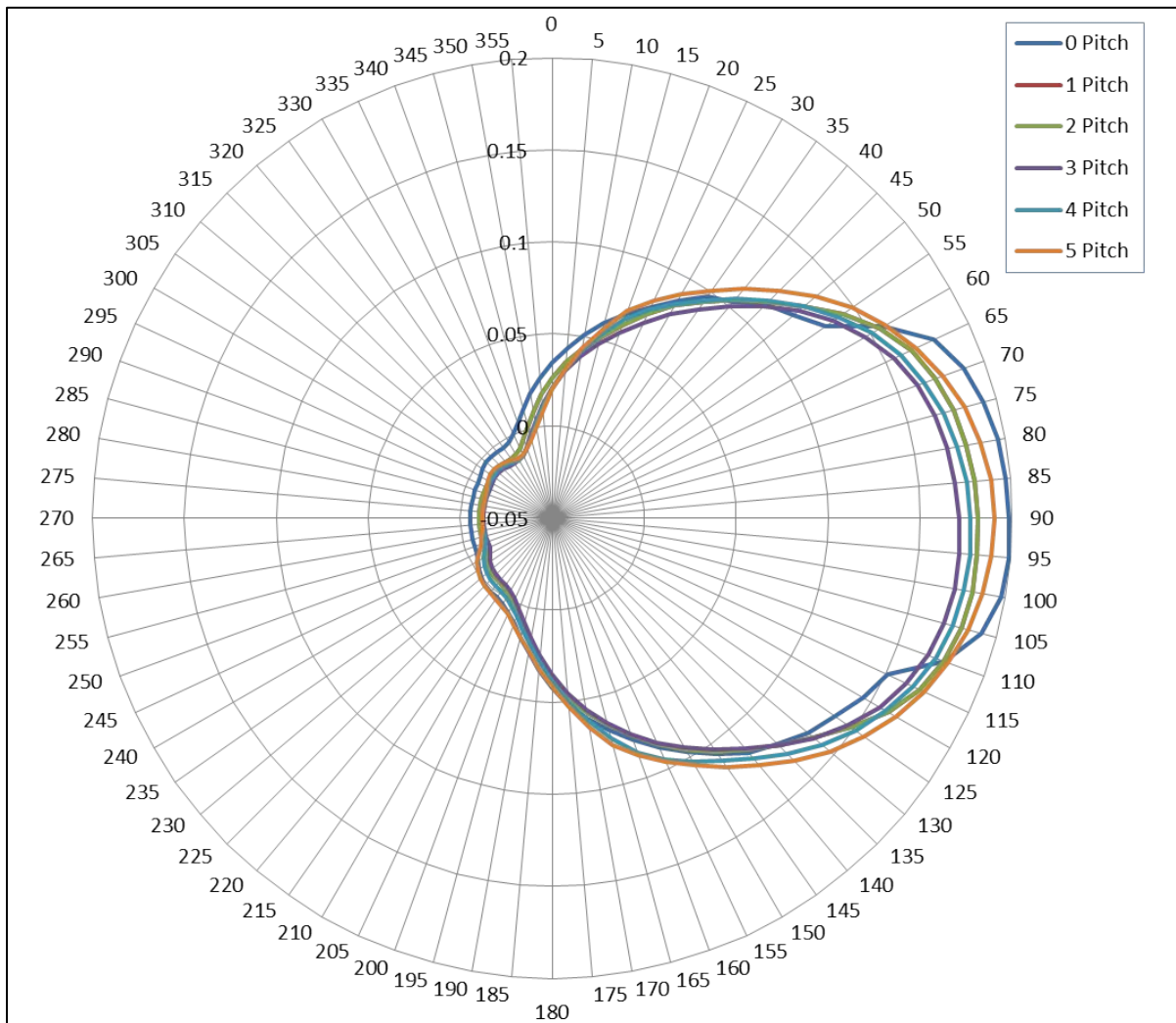


Figure 8-10: Polar plot of blade torque for various blade pitch angles

Figure 8-11 below compares the combined turbine blades loading at the maximum power coefficient of 2.15 which is equivalent to that of a turbine which does not utilise blade pitch. This was conducted so as to understand how the torque on each blade for each pitch angle

behaves for the maximum power coefficient of a turbine with 0° pitch as this resulted in the most power extracted.

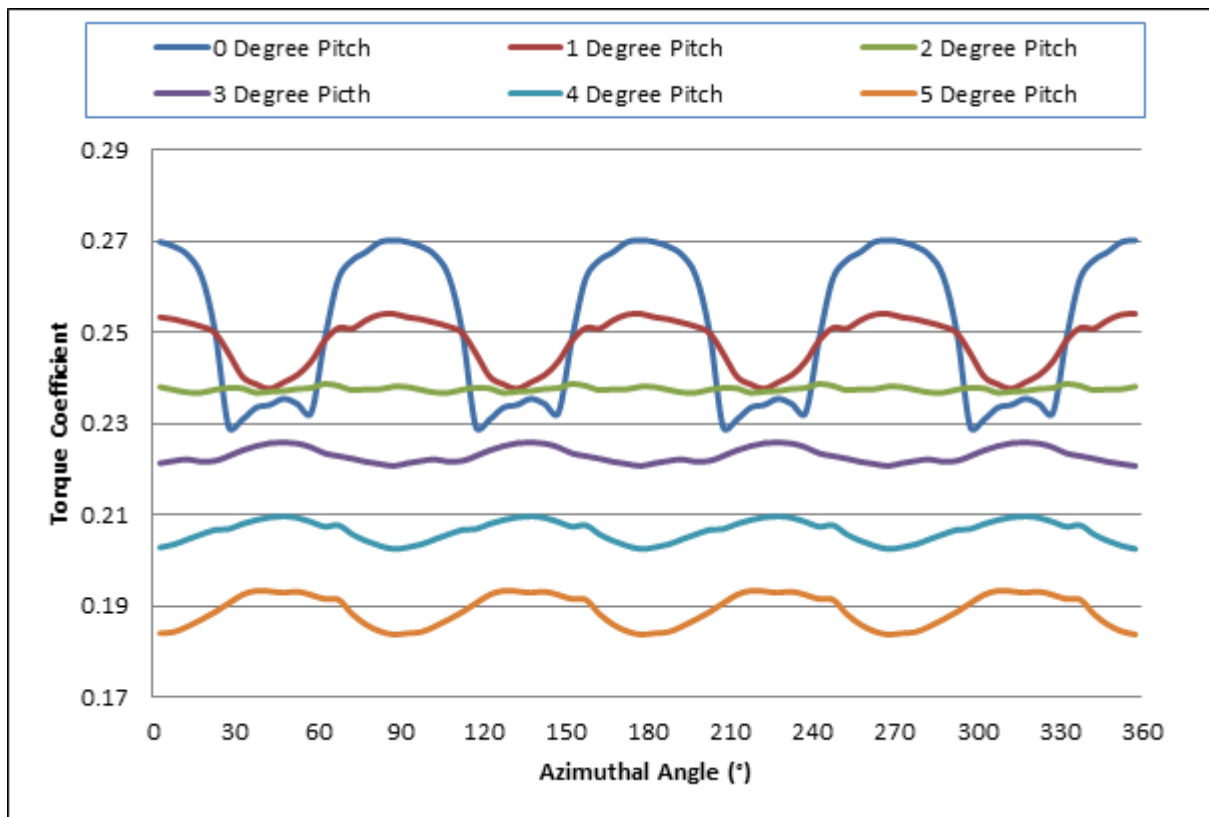


Figure 8-11: Torque Coefficient for various blade pitch angles

8.3 Helical Turbine – Addition of Channel

It was found in Chapter 7 that by introducing a channelling device that the velocity of the fluid medium increases depending on the channel design. As the design of a channel is out of the scope of this study, an increasing factor of 60% was assumed for the channel to be implemented for this turbine system. Table 8-1 depicts the increase in flow velocity which enters the turbine. These figures were used in the numerical analysis of the turbine to further understand the effect of flow velocity on the turbine’s efficiency.

Figure 8-12 depicts the various performance curves of the turbine for the various flow speeds for a pitch angle of 0°. It can be seen from the figure that the performance of the turbine does increase and also the tip speed ratio of the increased performance shifts towards the left, towards a relatively lower tip speed ratio when the flow speed entering the turbine is increased.

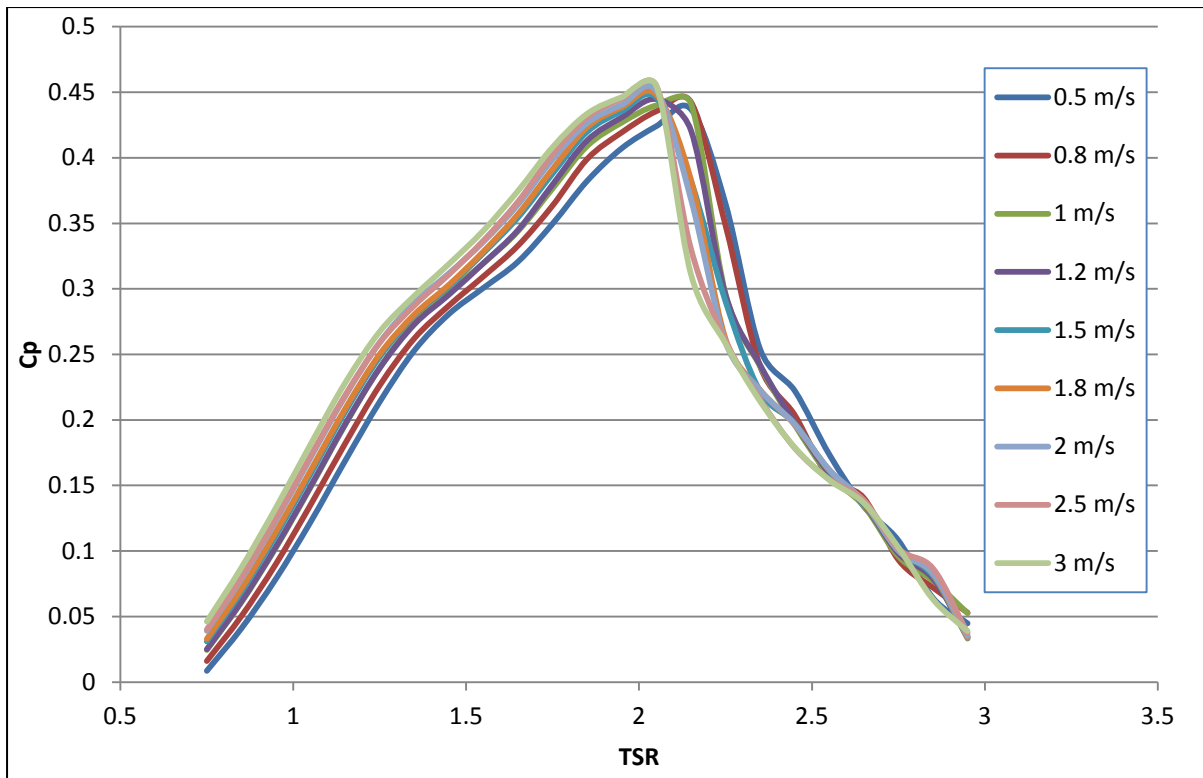


Figure 8-12: Cp for various flow speeds

The same simulation was conducted for all the pitch angles for the turbine for the given specified range which was obtained from Fiedler and Tullis [64]. It was found that for the increase in flow velocity, the change in pitch angle of the turbine blades did vary the performance of the turbine. Figure 8-13 shows the performance curve for the turbine for the blade pitch ranging from 0° to 2° for a standard 0.5 m/s flow and an increased flow due to the channelling device. The extreme of 3 m/s was chosen for the analysis for a clear depiction of the increased flow effect on the turbine. It was found that the variation of the amount of power which could be extracted by the flow for the blade pitch angle range of 0° to 2° was not extremely high. The trailing edge slope of the performance curves did vary and as stated previously this was found to have a positive effect on the turbine's shaft torque fluctuations. As the trailing edge slope tends to increase, the amount of torque fluctuations tend to reduce.

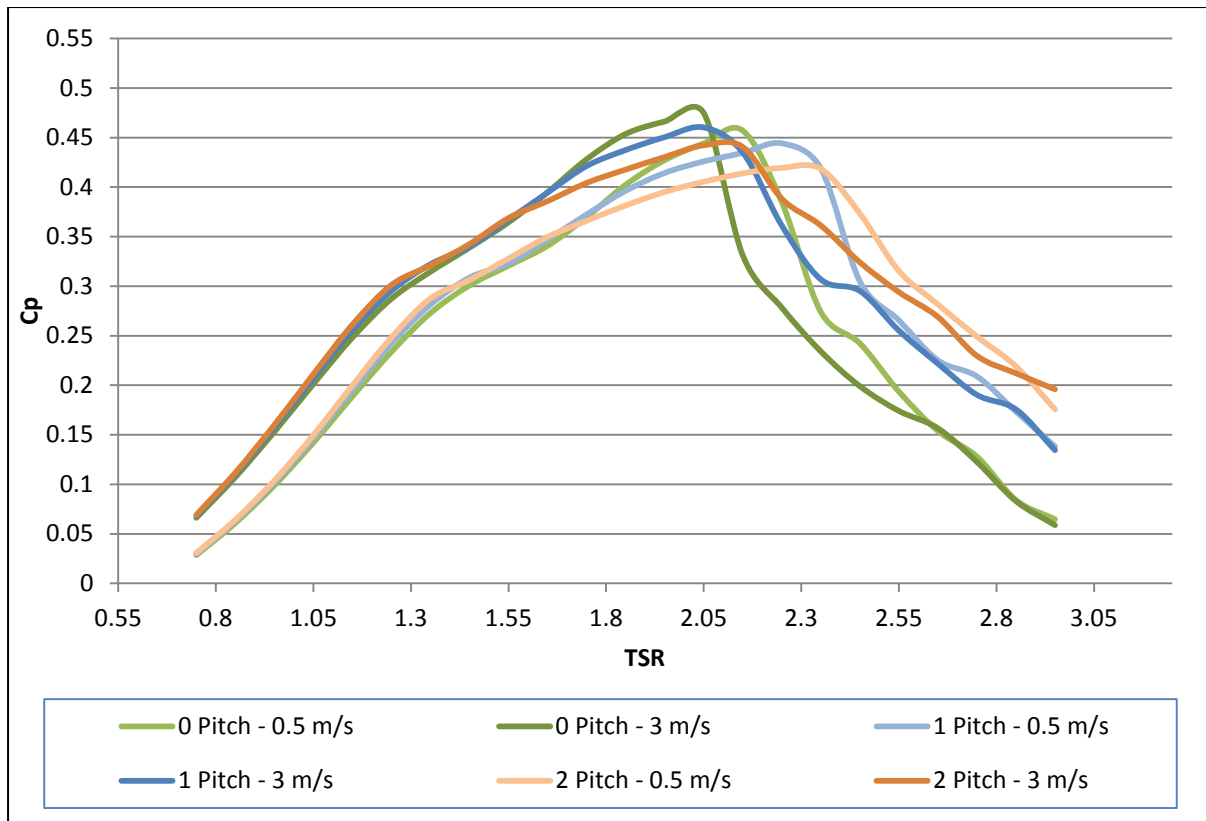


Figure 8-13: Cp Vs. Blade Pitch for Normal & Increased Flow

Figure 8-14 depicts the comparison of 0° blade pitch and 3° blade pitch with and without the effect of the channelling device. It can be seen that in relation to Figure 8-13 the performance of the turbine with blade pitch of 3° is far less than that of the turbine with no blade pitch. It was found that as the blade pitch was increased, even with the addition of the channelling device to increase the entering flow, the performance of the turbine decreased as depicted in Figure 8-9. This indicates the theoretical maximum limit for the amount of turbine blade pitch which can be utilised by this type of turbine. The performance of the turbine decreased due to an increase in vortex formation as the pitch of the turbine blades increased.

The main reason one would consider blade pitch in this design would be to reduce the amount of torque fluctuations on the generator shaft. The lower but smoother decrease in power coefficient from an increase in blade pitch can also be utilised for rapidly increasing flow velocities. Once the turbine tip speed ratio increases rapidly the amount of power being extracted by the turbine does not decrease drastically which would give the operator enough time to respond to the situation via control systems designed for the turbine.

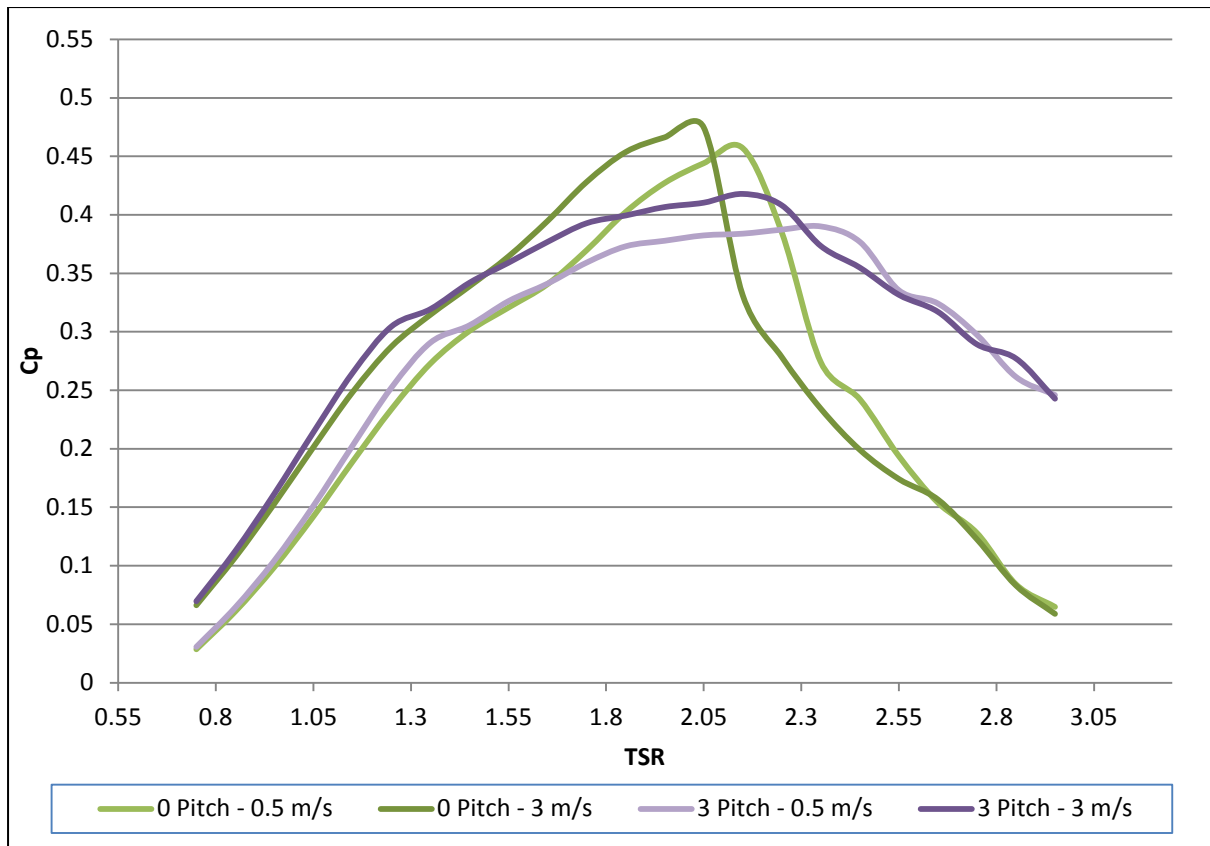


Figure 8-14: Cp - Comparison of Blade Pitch with Normal & Increased Flow

These results show that both numerical modelling approaches were in good agreement to one another and the correct parameters were chosen in both the simulations. It can also be seen that the approximate maximum efficiency of the turbine was 47% with no blade pitch angle implemented; however, blade pitch has a positive result on the torque fluctuations on the turbine shaft. It was also found from the results that the increase in velocity does increase the peak efficiency point and the turbine operates at a lower tip speed ratio. It can be seen that the major influence on the turbine performance is a result of altering the blade pitch of the turbine. The implementation of blade pitch can only be made by understanding parameters such as generator starting torque, resource flow speed and size of the turbine to state a few.

CHAPTER 9 Conclusions and Recommendations

The aim of this study was to design a suitable cross-flow turbine which is based on the Gorlov Helical turbine but with added blade pitch to increase the turbine efficiency and to prove that the proposed turbine is capable of supplying energy from the flow. The main conclusions and recommendations drawn from the study are summarized below.

9.1 Conclusions

The dissertation proved to be insightful regarding the potential amount of energy which could be extracted from an ocean resource such as the Agulhas current. Chapter 5 illustrated a resource assessment and proved valuable to an extent. It was found that within the Agulhas current there is a potential of approximately 5 GWh of energy per square meter on a flow velocity of 3 m/s. The average velocity of the Agulhas was found to be between 0.8 m/s and 1.2 m/s which results in an estimated 0.5 to 0.8 GWh of energy per square meter. As the flow profile is analogous to that of wind energy, the statistical approach was based on the analysis for wind energy but was modified to accommodate the density difference between the two mediums. This result was obtained by analysing the Eskom ADCP data, which resulted in an average flow speed of 0.5 m/s, and was incorporated within the statistical approach used to outlay a prediction of potential kinetic energy within the Agulhas.

On the basis of the amount of energy which was found from the analysis of the Agulhas current, a hydrokinetic turbine was designed. The design of the turbine was based on the Gorlov wind turbine design as this turbine was said to overcome the torque fluctuations due to the void spaces between the blades. The turbine blade profiles were selected from the NACA series of symmetrical profiles. The selection process was based on the lift versus drag coefficient as the turbine is a lift based turbine, meaning it exploits the lift force generated from the blade profile. The turbine was designed with helical profiled blades as Gorlov stated that this type of blade profile decreased the amount of torque fluctuations on the turbine shaft.

Analysis of the turbine in the mathematical model and CFD model proved this theory as the torque variation on the turbine shaft was cyclic and reduced in comparison with literature on conventional Darrieus turbines. Blade pitch angle was also incorporated into the designed turbine and analysed to understand its effects on the turbine performance and torque challenges. The use of blade toe-out angle was to try and increase the efficiency of the

turbine but it was found that as the blade pitch increased the performance of the turbine decreased accordingly. However, the blade pitch did have an advantage on the torque on the turbine shaft. As the performance of the turbine decreased the peak performance curve tended to plateau out. Examination of the torque on a turbine with no blade pitch after its peak performance point indicated high unsteadiness in the torque on the turbine but for the turbine with blade pitch, the torque after the peak performance point was more stable on the shaft.

The main aim of the dissertation was to obtain the performance of the turbine and assess whether it would have a significant impact if situated to exploit the Agulhas current. However, in all engineering cases there are limiting factors which effect the situation. In the case of the designed turbine the limiting factors were the airfoil profile selection, the blade profile geometry, the amount of blade pitch incorporated into the design and the number of blades that the turbine has. It was found in the literature that asymmetrical blade airfoil profiles exhibited more than adequate lift to drag ratios but the amount of turbulence and wake interference as well as dynamic stall was high. This was the reason for selecting a symmetrical NACA profile which did not produce high wake interference. As stated previously the helical blade profile design was chosen as this eliminated, to a large extent, the amount of vibration on the turbine shaft due to torque loading fluctuations.

The number of blades of the turbine directly impacts the speed of the turbine as the solidity ratio increases with an increase in the number of blades. As the number of blades increase the cut in speed of the turbine decreases as the turbine poses more flow resistance but this reduces the performance of the turbine and lowers the the peak performance tip speed ratio. Conversely, if the number of blades is decreased the turbine experiences less flow resistance but does not harness enough torque from the flow even though the rotational speed is high. The number of turbine blades was selected based on the blade wrap of the turbine which also aids in the reduction of torque fluctuations. It was found that to obtain a blade wrap of 100%, four blades were needed.

The turbine was found to perform at an efficiency of approximately 45% without any blade pitch incorporated and has a peak tip speed ratio of 2.25. When blade pitch toe-out angles were introduced to the turbine the performance of the turbine dropped to 41%. This was not a major decrease in efficiency of the turbine but when the pitch angle surpassed 2° the performance of the turbine dropped incrementally below 40%. With the addition of a channelling device the performance of the turbine increased and the operating tip speed ratio

decreased accordingly. This indicated that the addition of a channelling device does positively impact the turbine and help increase the performance of the turbine to an extent depending on the blockage ratio between the turbine blades and the channel walls as well as the blade pitch angle.

9.2 Recommendations

This study was successful in understanding the performance of the designed helical turbine. The study can be taken further by constructing a small scale turbine according to the design expressed in this dissertation. The small scale turbine should be simulated within a controlled environment where the velocity of the flow can be controlled. This would allow the simulation of a varying current as the Agulhas does not have a constant velocity and varies throughout the year.

Within the manufacture of the small scale turbine there also are limiting factors which influence the turbine's performance. Factors such as the selection of airfoil come into the practical world as one needs to accommodate for the manufacturability of the blade which has a helical profile. It is suggested that the NACA series which was selected for this turbine be used as this would be the easiest profile to manufacture. The turbine size needs to be accommodated for in relation to the flume which it would be tested in as well as the blockage ratio. Structural integrity of the turbine blades as well as the method of attachment and reinforcement, if necessary, need to be researched as these normally do affect the flow curvature around the turbine.

Refinement of the channelling device should be further researched as the amount of flow is increased. Research into the percentage increase of flow which can be utilised from the resource should be considered in the design of the channelling device. Further research of the trailing edge of the channel would result in a channel which outputs a velocity of flow which is less but close to that of the inlet.

REFERENCES

- [1] J. R. Toggweiler and R. M. Key, "Ocean Circulation - Thermohaline Circulation," in *Encyclopedia of Atmospheric Sciences*, R. H. James, Ed. Oxford: Academic Press, 2003, pp. 1549-1555.
- [2] S. Rahmstorf, "Glacial Climates - Thermohaline Circulation," in *Encyclopedia of Quaternary Science*, A. E. Scott, , Ed. Oxford: Elsevier, 2007, pp. 739-750.
- [3] N. Moreno, R. Sallent, A. Espi, D. Bao, and Y. Teillet, "Ocean Current's Energy: How to produce electrical energy thanks to marine currents?," Hogskolan I Gavle 2008.
- [4] M. Anyi and B. Kirke, "Evaluation of small axial flow hydrokinetic turbines for remote communities," *Energy for Sustainable Development*, vol. 14, pp. 110-116, 6// 2010.
- [5] (May, 2013). *Britanica Kids*. Available: <http://kids.britannica.com/comptons/art-166557/This-chart-indicates-the-principal-ocean-surface-currents-during-winter>
- [6] J. R. E. Lutjeharms and I. J. Ansorge, "The Agulhas Return Current," *Journal of Marine Systems*, vol. 30, pp. 115-138, 8 2001.
- [7] L. Bryden, L. Beal, and L. Duncan, "Structure and transport of the Agulhas Current and its temporal variability," *Journal Of Oceanography*, vol. 61, pp. 479-492, 2005.
- [8] M. J. Alam and M. T. Iqbal, "Design and development of hybrid vertical axis turbine," in *Electrical and Computer Engineering, 2009. CCECE '09. Canadian Conference on*, 2009, pp. 1178-1183.
- [9] M. J. Khan, M. T. Iqbal, and J. E. Quaicoe, "Dynamics of a vertical axis hydrokinetic energy conversion system with a rectifier coupled multi-pole permanent magnet generator," *Renewable Power Generation, IET*, vol. 4, pp. 116-127, 2010.
- [10] H. Akimoto, K. Tanaka, and K. Uzawa, "A conceptual study of floating axis water current turbine for low-cost energy capturing from river, tide and ocean currents," *Renewable Energy*, vol. 57, pp. 283-288, 9// 2013.
- [11] A. Gorlov, "Development of the helical reaction hydraulic turbine. Final technical report," July 1, 1996--June 30, 1998," 1998.
- [12] T. Ikoma, K. Masuda, S. Fujio, H. Nakada, H. Maeda, and C. K. Rheem, "Characteristics of hydrodynamic forces and torque on Darrieus type water turbines for current power generation systems with CFD computations," in *OCEANS 2008 - MTS/IEEE Kobe Techno-Ocean*, 2008, pp. 1-8.
- [13] B. Yang and C. Lawn, "Fluid dynamic performance of a vertical axis turbine for tidal currents," *Renewable Energy*, vol. 36, pp. 3355-3366, 12// 2011.

- [14] X.-W. Zhang, S.-Q. Wang, F. Wang, L. Zhang, and Q.-H. Sheng, "The hydrodynamic characteristics of free variable-pitch vertical axis tidal turbine," *Journal of Hydrodynamics, Ser. B*, vol. 24, pp. 834-839, 12// 2012.
- [15] A. L. Niblick, "Experimental and analytical study of helical cross-flow turbines for a tidal micropower generation system," Master of Science in Mechanical Engineering, Department of Mechanical Engineering, University of Washington, 2012.
- [16] A. M. Biadgo, A. Simonovic, D. Komarov, and S. Stupar, "Numerical and analytical investigation of vertical axis wind turbine," *FME Transactions*, vol. 41, pp. 49-58, 2013.
- [17] S. M. Camporeale and V. Magi, "Streamtube model for analysis of vertical axis variable pitch turbine for marine currents energy conversion," *Energy Conversion and Management*, vol. 41, pp. 1811-1827, 11/1/ 2000.
- [18] J. N. Goundar and M. R. Ahmed, "Marine current energy resource assessment and design of a marine current turbine for Fiji," *Renewable Energy*, vol. 65, pp. 14-22, 5// 2014.
- [19] B. K. Kirke, "Tests on ducted and bare helical and straight blade Darrieus hydrokinetic turbines," *Renewable Energy*, vol. 36, pp. 3013-3022, 11// 2011.
- [20] B. V. Davis, "Low head tidal power: a major source of energy from the worlds oceans," in *Energy Conversion Engineering Conference, 1997. IECEC-97., Proceedings of the 32nd Intersociety, 1997*, pp. 1982-1989 vol.3.
- [21] F. L. Ponta and P. M. Jacovkis, "Marine-current power generation by diffuser-augmented floating hydro-turbines," *Renewable Energy*, vol. 33, pp. 665-673, 4// 2008.
- [22] F. Ponta and G. Shankar Dutt, "An improved vertical-axis water-current turbine incorporating a channelling device," *Renewable Energy*, vol. 20, pp. 223-241, 6// 2000.
- [23] R. Luquet, D. Bellevre, D. Fréchu, P. Perdon, and P. Guinard, "Design and model testing of an optimized ducted marine current turbine," *International Journal of Marine Energy*, vol. 2, pp. 61-80, 6// 2013.
- [24] J. Giles, L. Myers, A. Bahaj, J. O'Nians, and B. Shelmerdine, "Foundation-based flow acceleration structures for marine current energy converters," *Renewable Power Generation, IET*, vol. 5, pp. 287-298, 2011.
- [25] B. Yang and X. W. Shu, "Hydrofoil optimization and experimental validation in helical vertical axis turbine for power generation from marine current," *Ocean Engineering*, vol. 42, pp. 35-46, 3// 2012.
- [26] M. Shino, k. Suzuuki, and S. Kiho, "Output characteristics of Darrieus water turbine with helical blades for tidal current generation," presented at the Proceedings of The Twelfth (2002) International Offshore and Polar Engineering Conference, Kitakyushu, Japan, 2002.

- [27] A. Rossetti and G. Pavesi, "Comparison of different numerical approaches to the study of the H-Darrieus turbines start-up," *Renewable Energy*, vol. 50, pp. 7-19, 2// 2013.
- [28] R. Gazzano, M. Marini, and A. Satta, "Performance calculation for a vertical axis wind turbine with variable blade pitch," *International Journal of Heat and Technology*, vol. 28, pp. 143-139, 2010.
- [29] J. A. Ekaterinaris and M. F. Platzer, "Computational prediction of airfoil dynamic stall," *Progress in Aerospace Sciences*, vol. 33, pp. 759-846, 4/14/ 1998.
- [30] I. Rodríguez, O. Lehmkuhl, R. Borrell, and A. Oliva, "Direct numerical simulation of a NACA0012 in full stall," *International Journal of Heat and Fluid Flow*, vol. 43, pp. 194-203, 10// 2013.
- [31] N. W. Mureithi, K. Huynh, M. Rodriguez, and A. Pham, "A simple low order model of the forced Karman wake," *International Journal of Mechanical Sciences*, vol. 52, pp. 1522-1534, 11// 2010.
- [32] O.-S. Gim and G.-W. Lee, "Flow characteristics and tip vortex formation around a NACA 0018 foil with an endplate," *Ocean Engineering*, vol. 60, pp. 28-38, 3/1/ 2013.
- [33] S. Sarkar and K. Venkatraman, "Influence of pitching angle of incidence on the dynamic stall behavior of a symmetric airfoil," *European Journal of Mechanics - B/Fluids*, vol. 27, pp. 219-238, 5// 2008.
- [34] S. Wang, D. B. Ingham, L. Ma, M. Pourkashanian, and Z. Tao, "Numerical investigations on dynamic stall of low Reynolds number flow around oscillating airfoils," *Computers & Fluids*, vol. 39, pp. 1529-1541, 10// 2010.
- [35] R. Urbina, M. L. Peterson, R. W. Kimball, G. S. deBree, and M. P. Cameron, "Modeling and validation of a cross flow turbine using free vortex model and a modified dynamic stall model," *Renewable Energy*, vol. 50, pp. 662-669, 2// 2013.
- [36] S. Wanan, A. M. G. Roderic, and N. C. Frank, "Applications of low speed dynamic stall model to the NREL airfoils," in *46th AIAA Aerospace Sciences Meeting and Exhibit*, ed: American Institute of Aeronautics and Astronautics, 2008.
- [37] L. B. Wang, L. Zhang, and N. D. Zeng, "A potential flow 2-D vortex panel model: Applications to vertical axis straight blade tidal turbine," *Energy Conversion and Management*, vol. 48, pp. 454-461, 2// 2007.
- [38] M. G. U. Lundin and M. Leijon, "*Ocean Energy*," Uppsala University, Sweden.
- [39] P. Meisen and A. Loiseau, "Ocean energy technologies for renewable energy generation," Global Energy Network Institute. 2009.
- [40] K. Rajagopalan and G. C. Nihous, "Estimates of global Ocean Thermal Energy Conversion (OTEC) resources using an ocean general circulation model," *Renewable Energy*, pp. 532-544, August 2012.

- [41] M. Faizal and M. R. Ahmed, "Experimental studies on a closed cycle demonstration OTEC plant working on small temperature difference," *Renewable Energy*, pp. 234-240, October 2012.
- [42] O. Alan , "Tidal Current Energy: Origins and Challenges," *Future Energy: Improved, sustainable and Clean options for our planet*, pp. 111-289, 2008.
- [43] F. O. Rourke, F. Boyle, and A. Reynolds, "Tidal Energy Update," *Applied Energy*, vol. 87, pp. 398 - 409, September 2009.
- [44] J. A. Clarke, G. Conner, A. D. Grant, and C. M. Johnstone, "Regulating the output characteristics of tidal current power stations to facilitate better base load matching over the lunar cycle," *Renewable Energy*, pp. 173 - 180, February 2006.
- [45] I. Bryden, T. Grinsted, and G. Melville, "Assessing the potential of a simple tidal channel to deliver useful energy," *Applied Ocean Resource*, vol. 26, pp. 198 - 204, 2004.
- [46] D. Prandle "Simple theory for designing tidal power schemes," *Advances in Water Resources*, vol. 7, pp. 21 - 27, March 1984.
- [47] R. Thresher, P. Denholme, G. Hagerman, G. Heath, S. O'Neil, J. Paquette, D. Sandor, and S. Tegen, "Chapter 9. National Renewable Energy Laboratory. Renewable Electricity Futures Study," *Ocean Energy Technologies*, vol. 2, pp. 1 - 36, 2012.
- [48] Pelamis Wave Power. (2013, March). *Pelamis Wave Power – Image Library*. Available: <http://www.pelamiswave.com/image-library/12>
- [49] Tidal Energy. (2013, June). *Tidal Energy: The DeltaStream Technology*. Available: <http://www.tidalenergyltd.com/cms/wp-content/uploads/2013/04/DeltaStream-%C2%A9-Tidal-Energy-Ltd1.png>
- [50] Ocean Flow Energy. (2013, June). *Ocean Flow Energy*. Available: <http://www.oceanflowenergy.com/index.html>
- [51] Power Engineer. (2013, March). *Power Engineer - Engines Turbines*. [Online Magazine].
- [52] Power Engineer. (2013, March). *Power Engineer - Engines Turbines* [Online Magazine].
- [53] E. Denny, "The Economics of Tidal Energy," *Energy Policy*, vol. 37, pp. 1914 - 1924, 2009.
- [54] Eskom. (2013, September). *Eskom Renewable Energy - Ocean Data*. Available: <http://www.eskom.co.za/c/article/1054/ocean-current-data/>
- [55] Eskom. (2014, June). *Renewable Energy - Ocean Current Data* Available: http://www.eskom.co.za/AboutElectricity/RenewableEnergy/Pages/Ocean_Current_Data.aspx

- [56] S. H. Wright, S. P. Chowdhury, and S. Chowdhury, "A feasibility study for marine energy extraction from the Agulhas current," in *Power and Energy Society General Meeting, 2011 IEEE*, 2011, pp. 1-9.
- [57] A. Williams, M. Nthontho, S. Chowdhury, and S. P. Chowdhury, "Modelling South African Agulhas marine current profile data for electricity generation," in *Power System Technology (POWERCON), 2012 IEEE International Conference on*, 2012, pp. 1-7.
- [58] M. R. Patel, *Wind and Solar Power Systems* (2nd ed.). New York: Taylor and Francis, 2005.
- [59] B. K. Hodge, *Alternative Energy Systems and Applications* Hoboken, NJ: John Wiley & Sons, 2006, pp. 69-72.
- [60] J. L. Menet, "Increase in the Savonius rotors efficiency via a parametric investigation," presented at the 2004 European Wind Energy Conference and Exhibition, London, 2004.
- [61] Maine Tidal Power (2013, May). A. Gorlov, "Helical turbine and fish safety" . Available: <http://www.mainetidalpower.com/files/gorlovrevised.pdf>
- [62] M. N. I. Khan, "A micro seafloor marine current energy conversion system," Memorial University of Newfoundland, 2008.
- [63] S. Antheaume, T. Maître, and J.-L. Achard, "Hydraulic Darrieus turbines efficiency for free fluid flow conditions versus power farms conditions," *Renewable Energy*, vol. 33, pp. 2186-2198, 10// 2008.
- [64] A. J. Fiedler and S. Tullis, "Blade offset and pitch effects on a high solidity vertical axis wind turbine," *Wind Engineering*, vol. 33, pp. 237–246, 2009.
- [65] R. E. Sheldahl and P. C. Klimas, "Aerodynamic characteristics of seven symmetrical airfoil sections through 180 degree angle of attack for use in aerodynamic analysis of vertical axis wind turbines," United States. Department of Energy, Sandia National Laboratories, 1981.
- [66] M. Islam, D. S. K. Ting, and A. Fartaj, "Desirable airfoil features for smaller-capacity straight-bladed VAWT," *Wind Engineering*, vol. 31, pp. 165-196, 05/01/ 2007.
- [67] B. K. Kirke, "Evaluation of self-starting vertical axis wind turbines for stand-alone applications," PhD Thesis, Griffith University, Nathan, Australia, 1998.
- [68] K. Cunden and F. Inambao, "Design and Numerical Simulation of a Small Scale Helical Cross Flow Turbine," in *Proceedings of 13th Botswana Institution of Engineers Biennial Conference*, Botswana, 2013.
- [69] F. Q. Chu, P. Chen, X. X. Shen, and X. H. Yan, "Parameter selection of straight bladed vertical axis wind turbine," presented at the Sixth Miami International Conference on Alternative Energy Sources, Washington, D.C., 1983.

- [70] J. D. Anderson, *Fundamentals of Aerodynamics* (3rd ed.). Boston: McGraw-Hill, 2001.
- [71] R. E. Sheldahl and L. V. Feltz, "Aerodynamic performance of a 5-metre-diameter Darrieus turbine with extruded aluminum NACA 0015 blades," Sandia National Laboratories, Albuquerque, NM1980.
- [72] C. Garrett and P. Cummins, "The efficiency of a turbine in a tidal channel," *Journal of Fluid Mechanics*, pp. 243 - 251, October 2007.
- [73] A. Goude and O. Ågren, "Simulations of a vertical axis turbine in a channel," *Renewable Energy*, vol. 63, pp. 477-485, 3 2014.
- [74] J. H. Strickland, B. T. Webster, T. Nguyen, A Vortex Model of the Darrieus Turbine: An Analytical and Experimental Study: *Journal of Fluids Engineering*, vol. 101, no. 4, pp. 500-505, Dec 1979.
- [75] M. Alidadi, "Duct optimization for a ducted vertical axis hydro current turbine " PhD thesis, Mechanical Engineering, The University of British Columbia, Vancouver, 2009.
- [76] L. M. Milne-Thomson, *Theoretical hydrodynamics*, Mineola, NY: Dover Publications, 1996.
- [77] J. H. Strickland, "The Darrieus turbine: A performance prediction model using multiple streamtubes," Sandia National Laboratories, Albuquerque, NM1975.
- [78] I. Paraschivoiu, "Double multiple streamtube model for Darrieus wind turbines," *Journal of Propulsion and Power*, vol. 4, pp. 370-377, 1988.
- [79] Y. C. Fung, *An Introduction to the Theory of Aeroelasticity*, North York, ON, Canada: General Publishing Company, 2002.
- [80] D. L. Ciffone and K. L. Orloff, "Far-field wake-vortex characteristics of wings," *Journal of Aircraft*, vol. 12, pp. 464-470, 1975.
- [81] J. Katz and A. Polotkin, *Low seed aerodynamics*. Cambridge, United Kingdom: Cambridge University Press, 2001.
- [82] N. Fujisawa and S. Shibuya, "Observations of dynamic stall on Darrieus wind turbine blades," *Journal of Wind Engineering and Industrial Aerodynamics*, vol. 89, pp. 201-214, 2// 2001.
- [83] S. Armstrong, A. Fiedler, and S. Tullis, "Flow separation on a high Reynolds number, high solidity vertical axis wind turbine with straight and canted blades and canted blades with fences," *Renewable Energy*, vol. 41, pp. 13-22, 5// 2012.
- [84] K. McLaren, S. Tullis, and S. Ziada, "Measurement of high solidity vertical axis wind turbine aerodynamic loads under high vibration response conditions," *Journal of Fluids and Structures*, vol. 32, pp. 12-26, 7// 2012.

- [85] C. Li, S. Zhu, Y.-l. Xu, and Y. Xiao, "2.5D large eddy simulation of vertical axis wind turbine in consideration of high angle of attack flow," *Renewable Energy*, vol. 51, pp. 317-330, 3// 2013.
- [86] M. Islam, D. K. Ting, and A. Fartaj, "Aerodynamic models for Darrieus-type straight-bladed vertical axis wind turbines," *Renewable and Sustainable Energy Reviews*, vol. 12, pp. 1087 - 1109, 2008.
- [87] I. Paraschivoiu, F. Saeed, and V. Desobry, "Prediction capabilities in vertical axis wind turbine aerodynamics," presented at the The World Wind Energy Conference and Exhibition Berlin, Germany, 2002.
- [88] J. L. Loth and H. McCoy, "Optimization of Darrieus turbines with an upwind and downwind momentum model," *Journal of Energy*, vol. 7, pp. 313-318, 1983.
- [89] I. Paraschivoiu and F. Delclaux, "Double multiple streamtube model with recent improvements (for predicting aerodynamic loads and performance of Darrieus vertical axis wind turbines)," *Journal of Energy*, vol. 7, pp. 250-255, 1983/05/01 1983.
- [90] D. Marten, J. Wendler, G. Pechlivanoglou, C. N. Nayeri, and C. O. Paschereit, "QBlade v0.6," ed. Berlin, Germany, 2013.
- [91] K. Cunden, "Numerical simulation of a vertical axis cross-flow helical hydrokinetic turbine," presented at the First Eskom Power Plant Engineering Institute Student Conference Eskom Academy of Learning, 2014.
- [92] R. Nobile, M. Vahdati, J. F. Barlow, and A. Mewburn-Crook, "Unsteady flow simulation of a vertical axis augmented wind turbine: A two-dimensional study," *Journal of Wind Engineering and Industrial Aerodynamics*, vol. 125, pp. 168-179, 2// 2014.
- [93] CD-Adapco, "Working with a prism layer mesh," in *Star CCM+ User Guide*, ed, 2012.
- [94] CD-Adapco, "Rigid body rotation tutorial," in *Star CCM+ User Guide*, ed, 2012, p. 7914.
- [95] M. Raciti Castelli, A. Englaro, and E. Benini, "The Darrieus wind turbine: Proposal for a new performance prediction model based on CFD," *Energy*, vol. 36, pp. 4919-4934, 8// 2011.
- [96] M. Shiono, K. Suzuki, and S. Kiho, "Output characteristics of Darrieus water turbine with helical blades for tidal current generation," presented at the International Offshore and Polar Engineering Conference, Kitakyushu, Japan, 2012.

APPENDIX A – NACA 0024 COEFFICIENTS OF LIFT AND DRAG

NACA 0024 Coefficients of Lift and Drag

Table 2: NACA 0024 Coefficients of Lift & Drag for Reynolds Number 50 000		
AoA	CL	CD
-25	-0.7049	0.27645
-24.5	-0.6802	0.26937
-24	-0.6677	0.26553
-23.5	-0.6469	0.26012
-23	-0.6288	0.25478
-22.5	-0.6231	0.25386
-22	-0.5923	0.24478
-21.5	-0.5777	0.24031
-21	-0.5663	0.23748
-20.5	-0.5385	0.22978
-20	-0.5231	0.22503
-19.5	-0.5173	0.22294
-19	-0.4868	0.21515
-18.5	-0.4664	0.20943
-18	-0.4524	0.20469
-17.5	-0.4401	0.2006
-17	-0.4266	0.19653

Table 3: NACA 0024 Coefficients of Lift & Drag for Reynolds Number Reynolds 100 000		
AoA	CL	CD
-25	-0.7201	0.27106
-24.5	-0.6894	0.26402
-24	-0.6845	0.26059
-23.5	-0.6566	0.25382
-22.5	-0.6216	0.24363
-22	-0.6205	0.23972
-21.5	-0.5864	0.23331
-21	-0.5793	0.22816
-20.5	-0.5521	0.22286
-20	-0.5394	0.21729
-19	-0.502	0.20666
-18.5	-0.4923	0.2011
-18	-0.497	0.1969
-17.5	-0.4524	0.19043
-17	-0.4425	0.18472
-16.5	-0.4446	0.17949
-16	-0.4085	0.17421

Table 4: NACA 0024 Coefficients of Lift & Drag for Reynolds Number Reynolds 150 000		
AoA	CL	CD
-25	-0.7174	0.26558
-24.5	-0.6943	0.26133
-24	-0.6876	0.25519
-23.5	-0.6616	0.25086
-23	-0.6593	0.24453
-22.5	-0.6292	0.2401
-21.5	-0.5962	0.22932
-21	-0.5932	0.22276
-20.5	-0.5626	0.21858
-20	-0.5581	0.21168
-19.5	-0.531	0.20735
-19	-0.5208	0.2009
-18.5	-1.167	0.07638
-18	-1.1327	0.07467
-17.5	-1.2006	0.06282
-17	-1.1676	0.06093
-16.5	-1.2077	0.05331

-16.5	-0.3997	0.18985
-16	-0.3777	0.18397
-15.5	-0.3597	0.17874
-15	-0.3429	0.17363
-14.5	-0.3263	0.16859
-14	-0.31	0.16357
-13.5	-0.2929	0.15856
-13	-0.2765	0.15358
-12.5	-0.2594	0.14869
-12	-0.2439	0.14391
-11.5	-0.2322	0.13957
-11	-0.2305	0.13596
-10.5	-0.2208	0.13147
-10	-0.1961	0.12619
-9.5	-0.1789	0.12186
-9	-0.17	0.11825
-8.5	-0.1804	0.1158
-8	-0.181	0.11263
-7.5	-0.175	0.10957
-7	-0.1813	0.10749
-6.5	-0.2169	0.10643
-6	-0.4452	0.08554
-5.5	-0.5121	0.07967
-5	-0.7932	0.05863
-4.5	-0.7784	0.056

-15.5	-0.3931	0.16832
-14.5	-1.0866	0.05496
-14	-1.0589	0.05299
-13.5	-1.0916	0.04807
-13	-1.1357	0.04419
-12.5	-1.1187	0.04274
-12	-1.1322	0.0409
-11.5	-1.1836	0.03928
-11	-1.174	0.0383
-10.5	-1.1761	0.03716
-10	-1.1808	0.03597
-9.5	-1.1803	0.03486
-9	-1.1731	0.0339
-8.5	-1.1595	0.03308
-8	-1.1063	0.03265
-7.5	-1.0288	0.0321
-7	-0.9498	0.03167
-6.5	-0.8791	0.03109
-6	-0.7948	0.03064
-5.5	-0.733	0.02999
-5	-0.6569	0.02957
-4.5	-0.5834	0.02885
-4	-0.4954	0.02816
-3.5	-0.4348	0.02754
-3	-0.3631	0.02678

-16	-1.1773	0.05134
-15.5	-1.1717	0.04775
-15	-1.1857	0.04354
-14.5	-1.1569	0.04174
-14	-1.1464	0.03927
-13.5	-1.1502	0.03667
-13	-1.1391	0.03504
-12.5	-1.1272	0.03364
-12	-1.1293	0.03227
-11.5	-1.1522	0.03116
-11	-1.15	0.03045
-10.5	-1.168	0.02983
-10	-1.1878	0.02918
-9.5	-1.168	0.02848
-9	-1.0915	0.02768
-8.5	-1.0189	0.02687
-8	-0.951	0.02601
-7.5	-0.8729	0.0252
-7	-0.8111	0.02442
-6.5	-0.731	0.02359
-6	-0.6578	0.02271
-5.5	-0.584	0.02183
-5	-0.5307	0.02116
-4.5	-0.4689	0.02036
-4	-0.4165	0.01981

-4	-0.7023	0.05536
-3.5	-0.5897	0.05768
-3	-0.5053	0.05838
-2.5	-0.4663	0.05711
-2	-0.3764	0.05834
-1.5	-0.2776	0.05963
-1	-0.2377	0.0592
-0.5	-0.1983	0.05901
0	0	0.06118
0.5	0.1982	0.05901
1	0.2377	0.05919
1.5	0.2778	0.05962
2	0.377	0.05831
2.5	0.4662	0.0571
3	0.5053	0.05836
3.5	0.5903	0.05764
4	0.7025	0.05534
4.5	0.7787	0.05597
5	0.7941	0.05853
5.5	0.5127	0.07957
6	0.4457	0.08543
6.5	0.4161	0.0887
7	0.334	0.09544
7.5	0.2907	0.10063
9	0.1705	0.11817

-2.5	-0.2876	0.026
-2	-0.2407	0.02554
-1.5	-0.1658	0.02501
-1	-0.1191	0.02475
-0.5	-0.055	0.0246
0	0	0.02448
0.5	0.055	0.0246
1	0.1191	0.02475
1.5	0.1658	0.02501
2	0.2406	0.02554
2.5	0.2876	0.026
3	0.3631	0.02678
3.5	0.4347	0.02754
4	0.4954	0.02815
4.5	0.5833	0.02885
5	0.6567	0.02957
5.5	0.733	0.02998
6	0.7948	0.03063
6.5	0.8791	0.03108
7	0.9499	0.03166
7.5	1.0288	0.03209
8	1.1065	0.03263
8.5	1.1592	0.03308
9	1.1728	0.03389
9.5	1.1801	0.03485

-3.5	-0.3627	0.01921
-3	-0.3094	0.01879
-2.5	-0.2593	0.01845
-2	-0.2042	0.01812
-1.5	-0.1547	0.01793
-1	-0.1034	0.01779
-0.5	-0.0504	0.01768
0	0	0.01768
0.5	0.0504	0.01768
1	0.1034	0.01779
1.5	0.1547	0.01793
2	0.2042	0.01812
2.5	0.2593	0.01845
3	0.3094	0.01879
3.5	0.3627	0.01921
4	0.4165	0.01981
4.5	0.4689	0.02036
5	0.5307	0.02116
5.5	0.5841	0.02182
6	0.6578	0.02271
6.5	0.731	0.02359
7	0.8111	0.02441
7.5	0.873	0.0252
8	0.9511	0.026
8.5	1.0191	0.02686

9.5	0.1793	0.12178
11	0.2316	0.13595
11.5	0.2333	0.13957
12	0.245	0.14393
12.5	0.2606	0.14873
13	0.2779	0.15364
13.5	0.2944	0.15865
14	0.3115	0.16368
14.5	0.3278	0.16873
15	0.3445	0.17381
15.5	0.3613	0.17896
16	0.3793	0.18422
16.5	0.4011	0.19011
17	0.4279	0.1968
17.5	0.4422	0.20105
18.5	0.4683	0.20997
19	0.4885	0.21571
20	0.5253	0.22583
20.5	0.5407	0.23064
21	0.568	0.23831
21.5	0.5801	0.24142
22	0.5946	0.24597
22.5	0.6249	0.25495
23	0.6313	0.25624
23.5	0.6492	0.26163

10	1.1806	0.03596
10.5	1.1761	0.03715
11	1.1741	0.03829
11.5	1.1837	0.03926
12	1.1326	0.04088
12.5	1.119	0.04272
13	1.1359	0.04418
13.5	1.0936	0.04799
14	1.0601	0.05295
14.5	1.087	0.05498
16.5	0.4469	0.17974
17	0.4446	0.18501
17.5	0.4543	0.19077
18	0.4994	0.19733
18.5	0.4945	0.20156
19	0.5041	0.20719
19.5	0.5425	0.21371
20	0.5418	0.21797
20.5	0.5543	0.22364
21	0.5818	0.22904
21.5	0.5888	0.23429
22	0.6233	0.24084
22.5	0.6241	0.24483
23.5	0.6593	0.25527
24	0.6853	0.2619

9	1.0917	0.02767
9.5	1.1684	0.02847
10	1.1877	0.02917
10.5	1.1681	0.02981
11	1.1501	0.03044
11.5	1.1523	0.03115
12	1.1295	0.03225
12.5	1.1275	0.03362
13	1.1394	0.03502
13.5	1.1512	0.03664
14	1.1474	0.03923
14.5	1.158	0.04172
15	1.1864	0.04353
15.5	1.1737	0.04768
16	1.1789	0.05131
16.5	1.2121	0.0531
17	1.17	0.06084
17.5	1.2018	0.06286
18	1.1367	0.07444
18.5	1.1679	0.0765
19	0.5232	0.20136
19.5	0.5331	0.20792
20	0.5606	0.21228
20.5	0.5649	0.2193
21	0.5958	0.22353

24	0.6704	0.26731
24.5	0.6828	0.27124
25	0.708	0.27865

24.5	0.6922	0.26578
------	--------	---------

21.5	0.5987	0.23023
22.5	0.6318	0.24122
23	0.6621	0.24576
23.5	0.6642	0.25225
24	0.6905	0.25668
24.5	0.6971	0.26301
25	0.7204	0.26739

Table 5: NACA 0024 Coefficients of Lift & Drag for Reynolds Number Reynolds 200 000		
AoA	CL	CD
-25	-0.7161	0.26438
-24	-0.6871	0.25303
-23	-0.6572	0.24183
-22.5	-0.6351	0.23764
-22	-0.6277	0.23046
-21.5	-0.6033	0.22653
-21	-1.0996	0.11382
-20.5	-1.172	0.09717
-20	-1.1867	0.08923
-19.5	-1.1905	0.08289
-19	-1.2085	0.07499
-18.5	-1.1967	0.07084
-18	-1.2053	0.06452

Table 6: NACA 0024 Coefficients of Lift & Drag for Reynolds Number Reynolds 250 000		
AoA	CL	CD
-25	-0.7229	0.26199
-24.5	-0.7046	0.25744
-24	-0.6978	0.24966
-23.5	-0.6733	0.2463
-23	-1.1831	0.12728
-22.5	-1.1516	0.12588
-22	-1.1743	0.11598
-21.5	-1.2078	0.10486
-21	-1.1924	0.10089
-20.5	-1.2246	0.0903
-20	-1.2031	0.08733
-19.5	-1.2141	0.07991
-19	-1.2041	0.07545

Table 7: NACA 0024 Coefficients of Lift & Drag for Reynolds Number Reynolds 300 000		
AoA	CL	CD
-24.5	-1.1402	0.15502
-24	-1.1316	0.14974
-23.5	-1.2193	0.12899
-23	-1.1851	0.12806
-22.5	-1.1971	0.11978
-22	-1.2131	0.11117
-21.5	-1.2018	0.10657
-21	-1.221	0.09752
-20.5	-1.2069	0.09354
-20	-1.2093	0.0871
-19.5	-1.2056	0.08167
-19	-1.2028	0.0761
-18.5	-1.1991	0.0708

-17.5	-1.1954	0.06042
-17	-1.1893	0.05605
-16.5	-1.1873	0.05153
-16	-1.1697	0.04855
-15.5	-1.1655	0.04465
-15	-1.1515	0.04179
-14.5	-1.1356	0.03921
-14	-1.125	0.03654
-13.5	-1.1176	0.03414
-13	-1.1017	0.03242
-12.5	-1.0934	0.03076
-12	-1.0927	0.02932
-11.5	-1.0995	0.0282
-11	-1.1056	0.02735
-10.5	-1.1216	0.02663
-10	-1.1142	0.0259
-9.5	-1.0485	0.02491
-9	-0.9863	0.02398
-8.5	-0.9196	0.02303
-8	-0.8516	0.02207
-7.5	-0.779	0.0211
-7	-0.7098	0.02015
-6.5	-0.6442	0.01925
-6	-0.5948	0.01855
-5.5	-0.5431	0.01785
-5	-0.4938	0.01726

-18.5	-1.2052	0.06959
-18	-1.1949	0.0653
-17.5	-1.1944	0.05991
-17	-1.1804	0.05625
-16.5	-1.179	0.0513
-16	-1.161	0.04827
-15.5	-1.1498	0.04469
-15	-1.1406	0.04115
-14.5	-1.1237	0.03847
-14	-1.1099	0.03576
-13.5	-1.0986	0.03324
-13	-1.0864	0.03118
-12.5	-1.0773	0.02941
-12	-1.0736	0.02789
-11.5	-1.0799	0.02668
-11	-1.0893	0.02574
-10.5	-1.1058	0.02497
-10	-1.0422	0.0237
-9.5	-0.9785	0.02254
-9	-0.9117	0.02145
-8.5	-0.842	0.02037
-8	-0.7775	0.01937
-7.5	-0.7168	0.01842
-7	-0.6612	0.01752
-6.5	-0.616	0.01682
-6	-0.5732	0.01623

-18	-1.1925	0.06591
-17.5	-1.1859	0.06115
-17	-1.1792	0.05646
-16.5	-1.1689	0.05238
-16	-1.1611	0.04806
-15.5	-1.1476	0.04461
-15	-1.1354	0.04114
-14.5	-1.1226	0.03792
-14	-1.1083	0.03513
-13.5	-1.0946	0.03258
-13	-1.0823	0.03035
-12.5	-1.0743	0.02845
-12	-1.0713	0.02685
-11.5	-1.0759	0.0256
-11	-1.089	0.02466
-10.5	-1.0631	0.02347
-10	-0.9996	0.02215
-9.5	-0.9346	0.02087
-9	-0.8671	0.0197
-8.5	-0.797	0.0186
-8	-0.7379	0.01759
-7.5	-0.6834	0.01662
-7	-0.6423	0.01588
-6.5	-0.6055	0.0153
-6	-0.566	0.01482
-5.5	-0.5236	0.01438

-4.5	-0.4463	0.01678
-4	-0.3986	0.01636
-3.5	-0.3475	0.01597
-3	-0.2993	0.0157
-2.5	-0.2506	0.01547
-2	-0.1991	0.01528
-1.5	-0.151	0.01516
-1	-0.1002	0.01505
-0.5	-0.0499	0.015
0	0	0.01498
0.5	0.0499	0.015
1	0.1002	0.01505
1.5	0.151	0.01516
2	0.1991	0.01528
2.5	0.2506	0.01547
3	0.2993	0.0157
3.5	0.3475	0.01597
4	0.3987	0.01636
4.5	0.4463	0.01678
5	0.4938	0.01726
5.5	0.5431	0.01785
6	0.5948	0.01855
6.5	0.6443	0.01924
7	0.7099	0.02015
7.5	0.7791	0.0211
8	0.8518	0.02206

-5.5	-0.5295	0.01572
-5	-0.4828	0.01522
-4.5	-0.4369	0.01483
-4	-0.3908	0.01453
-3.5	-0.3433	0.01426
-3	-0.2945	0.01402
-2.5	-0.2459	0.01386
-2	-0.1975	0.01371
-1.5	-0.148	0.0136
-1	-0.099	0.01355
-0.5	-0.0494	0.01348
0	0	0.0135
0.5	0.0494	0.01348
1	0.099	0.01355
1.5	0.148	0.0136
2	0.1975	0.01371
2.5	0.2459	0.01386
3	0.2945	0.01402
3.5	0.3434	0.01426
4	0.3908	0.01453
4.5	0.4369	0.01483
5	0.4829	0.01522
5.5	0.5296	0.01572
6	0.5733	0.01623
6.5	0.6162	0.01682
7	0.6614	0.01752

-5	-0.4793	0.01397
-4.5	-0.4337	0.01364
-4	-0.3873	0.01339
-3.5	-0.3404	0.01316
-3	-0.2927	0.01296
-2.5	-0.2444	0.01282
-2	-0.1959	0.0127
-1.5	-0.1472	0.0126
-1	-0.0982	0.01257
-0.5	-0.0491	0.0125
0	0	0.01251
0.5	0.0491	0.0125
1	0.0982	0.01257
1.5	0.1472	0.0126
2	0.1959	0.0127
2.5	0.2445	0.01282
3	0.2927	0.01296
3.5	0.3405	0.01316
4	0.3874	0.01339
4.5	0.4337	0.01364
5	0.4793	0.01397
5.5	0.5237	0.01438
6	0.5662	0.01482
6.5	0.6057	0.0153
7	0.6425	0.01587
7.5	0.6836	0.01662

8.5	0.9194	0.02303
9	0.9867	0.02397
9.5	1.049	0.0249
10	1.1149	0.02589
10.5	1.1217	0.02661
11	1.1056	0.02733
11.5	1.0996	0.02818
12	1.0929	0.02929
12.5	1.0938	0.03074
13	1.1023	0.03239
13.5	1.1182	0.03412
14	1.1262	0.0365
14.5	1.1369	0.03918
15	1.1528	0.04176
15.5	1.1675	0.04458
16	1.1717	0.0485
16.5	1.1889	0.05151
17	1.1919	0.05595
17.5	1.1976	0.06037
18	1.2087	0.06436
18.5	1.1994	0.07077
19	1.2127	0.07475
19.5	1.1932	0.08285
20	1.1918	0.0889
20.5	1.1743	0.09724
21	1.1084	0.11297

7.5	0.7171	0.01842
8	0.7777	0.01937
8.5	0.8423	0.02036
9	0.9121	0.02145
9.5	0.9789	0.02254
10	1.0428	0.02369
10.5	1.1059	0.02495
11	1.0893	0.02571
11.5	1.08	0.02665
12	1.0739	0.02786
12.5	1.0777	0.02938
13	1.087	0.03115
13.5	1.0996	0.0332
14	1.1112	0.03572
14.5	1.1251	0.03842
15	1.1421	0.04111
15.5	1.1517	0.04463
16	1.163	0.04822
16.5	1.1818	0.05118
17	1.1829	0.05617
17.5	1.1966	0.05988
18	1.1979	0.06519
18.5	1.2078	0.06955
19	1.2075	0.07532
19.5	1.2167	0.07989
20	1.2069	0.08718

8	0.7382	0.01759
8.5	0.7973	0.0186
9	0.8675	0.01969
9.5	0.9351	0.02086
10	1.0002	0.02214
10.5	1.0638	0.02345
11	1.089	0.02464
11.5	1.0759	0.02557
12	1.0716	0.02682
12.5	1.0747	0.02842
13	1.083	0.03032
13.5	1.0956	0.03254
14	1.1096	0.03508
14.5	1.124	0.03788
15	1.1371	0.04108
15.5	1.1496	0.04455
16	1.1631	0.04801
16.5	1.1712	0.0523
17	1.1816	0.05639
17.5	1.1887	0.06105
18	1.1953	0.06582
18.5	1.2024	0.07067
19	1.2059	0.07602
19.5	1.2091	0.08154
20	1.2125	0.08704
20.5	1.2108	0.09341

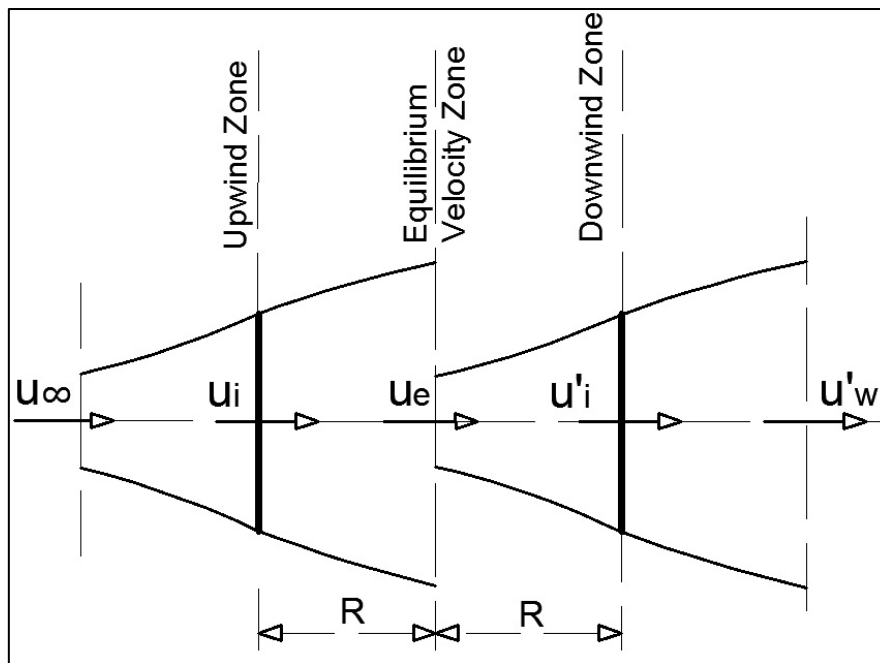
21.5	1.1549	0.11238
22	0.6304	0.23137
22.5	0.6376	0.23874
23	0.66	0.243
24	0.6899	0.25447
24.5	0.7191	0.25843
25	0.719	0.26616

20.5	1.2271	0.09035
21	1.1962	0.10077
21.5	1.2129	0.10458
22	1.1775	0.11601
22.5	1.1574	0.12555
23	1.1843	0.1277
25	0.7259	0.26369

21	1.224	0.09754
21.5	1.2057	0.10648
22	1.2178	0.11096
22.5	1.2006	0.1198
23	1.1897	0.12795
23.5	1.2253	0.12865
24	1.1364	0.14969
24.5	1.1463	0.1548

APPENDIX B – NUMERICAL FORMULATION FOR THE TUBRINE HYDRODYNAMICS

The following Appendix outlines the mathematical formulation of the governing equations used and highlighted in 7.4.1. The equations were derived by Strickland, et al. [73] initially whilst developing the double multiple streamtube model. The following derivations were obtained from Biadgo, et al. [16] as this was the most recent article found defining the equations.



Appendix B - 1: Double Streamtube Model, Biadgo, et al. [16]

The induced velocities for the upwind and downwind sections are illustrated in equations B.1 and B.2 respectively. It can be concluded that the induced velocity of the downwind actuator is dependent on the exit velocity of the upwind actuator. These equations provide the basis for calculation of the relative velocity of the fluid flow and the constantly changing attack angles of the turbine blades, by using the interference factors which are obtained via an iterative method, Biadgo, et al. [16].

$$u_i = (1 - a)U_\infty \quad (\text{B.1})$$

where:

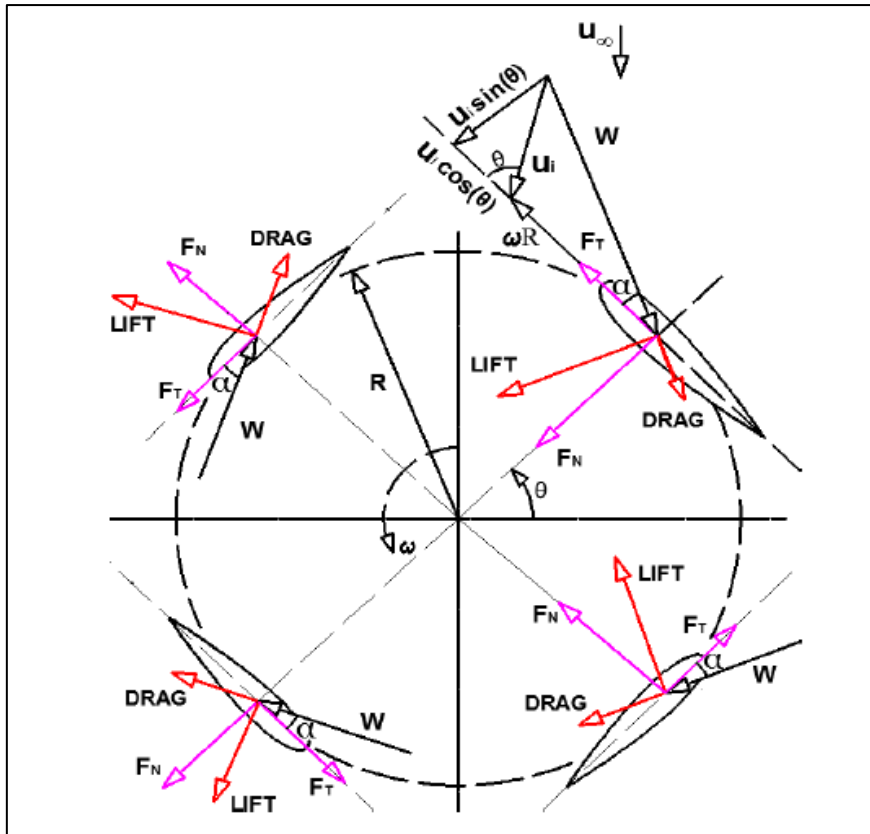
u_i	Induced velocity (Upwind)
a	Interference / Induction factor (Upwind)
U_∞	Incoming free-stream velocity

$$u_i' = (1 - a')(1 - 2a)U_\infty \quad (\text{B.2})$$

where:

u_i'	Induced velocity (Downwind)
a'	Interference / Induction factor (Downwind)
a	Interference / Induction factor (Upwind)
U_∞	Incoming free-stream velocity

To understand the vectors influencing a vertical axis turbine blade, the cross-sectional top view aids in the vector diagram construction as shown in Appendix B - 1, [16]. It can be seen that the relative velocity (w) can be obtained by means of Pythagoras.



Appendix B - 2: Vector diagram for VAWT systems, Biadgo, et al. [16]

This is done by obtaining the square root of the squared sums of the cordial and normal velocity components of the vector triangle. As a result of this the expression for the relative velocity (w or U_{Rel}) is given as follow:

$$U_{Rel} = \sqrt{(U_\infty + \omega R \cos \theta)^2 + (\omega R \sin \theta)^2} \quad (B.3)$$

Where:

- U_{Rel} Relative Velocity (m/s)
- U_∞ Free Stream Velocity (m/s)
- R Radius of the turbine (m)
- ω Rotational Speed (rad/s)
- θ Azimuthal Angle ($^\circ$)

From Appendix B - 1 and the geometry of the blade, the local angle of attack can be obtained. This angle of attack can be defined simply as follows in reference to Appendix B - 1, Biadgo, et al. [16]:

$$\alpha = \tan^{-1} \left(\frac{u_i \sin \theta}{u_i \cos \theta + \omega R} \right) \quad (\text{B.4})$$

The result of the geometric analysis is the following expression for the local angle of attack with regards to non-dimensional velocity components is represented in equation B.5, Biadgo, et al. [16]:

$$\alpha = \tan^{-1} \left(\frac{(1-a) \sin \theta}{(1-a) \cos \theta + \lambda} \right) \quad (\text{B.5})$$

where:

α	Attack Angle (Upwind)
a	Interference / Induction factor (Upwind)
λ	Tip Speed Ratio
θ	Azimuthal Angle

A similar relationship may be expressed for the lift and drag coefficients in terms of the turbine tangential force coefficient (C_T) and normal force coefficient (C_N) which are calculated as follows respectively, Biadgo, et al. [16]:

$$F_T = \frac{C_T}{0.5 \rho U_{rel}^2 cH} \quad (\text{B.6})$$

$$F_N = \frac{C_N}{0.5 \rho U_{rel}^2 cH} \quad (\text{B.7})$$

From the above equations the tangential and normal coefficients can be used to obtain the lift and drag coefficients of the blade profile. The lift and drag coefficients are represented in equations B.8 and B.9, Biadgo, et al. [16]:

$$C_N = C_L \cos(\alpha) + C_D \sin(\alpha) \quad (\text{B.8})$$

$$C_T = C_L \sin(\alpha) - C_D \cos(\alpha) \quad (\text{B.9})$$

Applying equations B.6 and B.7 to different azimuthal positions of the blade provide a very basic understanding of the forces generated by the flow but this does not give an accurate depiction of the flow behaviour within the vicinity of the turbine, Biadgo, et al. [16]:

$$T = F_T \cos \theta - F_N \sin \theta \quad (\text{B.10})$$

where:

T Torque (Nm)

F_T Tangential Force (N)

F_N Normal Force (N)

The resultant of these forces generates torque on the turbine shaft which is used to drive the coupled generator. This forms the basis for obtaining the torque coefficient (C_Q). It is noted that the tangential force is responsible for the rotation of the turbine which, in turn, results in the torque on the turbine shaft. Equation B.11 describes the instantaneous torque component on a blade of the turbine as follow:

$$T_i = F_T R \quad \text{B.11}$$

Where:

T_i Instantaneous Torque on blade (Nm)

F_T Tangential force on the blade (N)

R Radius of the turbine (m)

This can be expanded on taking into account the blade chord length (c) and height (h) as the area to obtain the torque as a function of the relative velocity of the flow and the tangential coefficient.

$$T_i = \frac{1}{2} \rho U_{Rel}^2 (hc) C_t R \quad \text{B.12}$$

Where:

T_i Instantaneous Torque on blade (Nm)

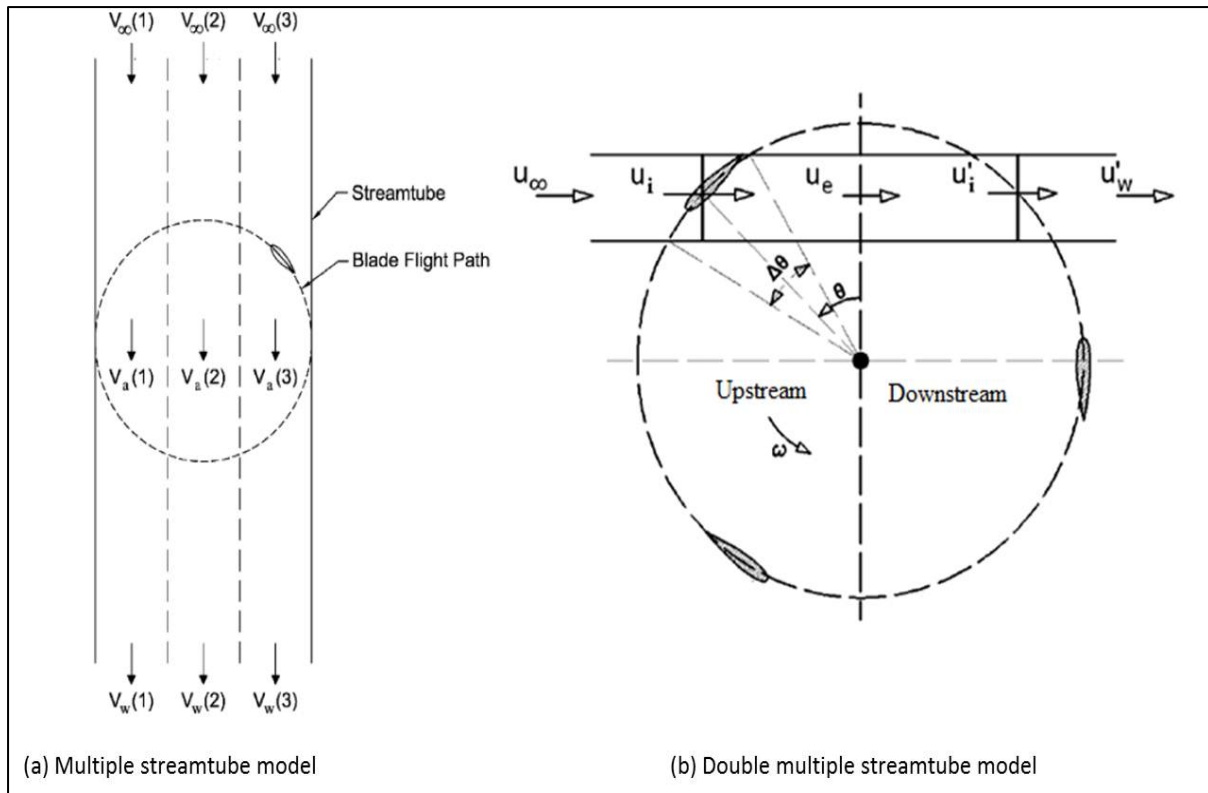
C_t Tangential coefficient (-)

U_{Rel} Relative velocity (m/s)

ρ Density (Kg/m³)

R Radius of the turbine (m)

Appendix B - 3 below indicates the multiple streamtube and double multiple streamtube models. This was the method which was chosen in the dissertation for the analysis of the vertical axis hydrokinetic turbine.



Appendix B - 3: Multiple & Double Multiple Streamtube Model, [16] & [77]

The common relating value was found between the analytical equations and the numerical models were found to be the thrust coefficient. The accuracy of the double multiple streamtube model is directly dependant on the total number of discrete streamtubes being used. The momentum balances for each of the streamtubes are calculated individually.

Understanding that the double multiple streamtube model effectively discretises the control volume into “N” amount of multiple streamtubes. The span of each blade spends within a control volume is depicted by equation B.13 as follows:

$$\Delta\theta = \frac{2\pi}{N_{\theta}} \quad \text{B.13}$$

Where:

$\Delta\theta$ Change in azimuth angle/ blade rotation (°)

N_θ Number of streamtubes (-)

The separate calculations results in the model having to acquire the “ N ” amount of induction factors for each streamtube. The induction factor for each streamtube will be different due to blade attack angle and resulting relative velocity being different in each streamtube. The average aerodynamic thrust on a turbine, with “ B ” number of blades can be expressed by Equation B.14. Equation B.14 was derived on the basis that each of the turbine blades spends $\Delta\theta/\pi$ percent of the rotational time in the streamtube, Biadgo, et al. [16].

$$T_{avg} = 2 \left(\frac{B\Delta\theta}{\pi} T_i \right) \quad (B.14)$$

where:

T_{avg} Average Torque
 B Number of turbine blades
 θ Azimuthal Angle
 T_i Instantaneous Torque on a single blade

It was found that the thrust coefficient was the common numerical value which can be utilised in the iterative solver model using the double multiple streamtube model. This can be calculated knowing the basic condition parameters of the turbine and correlated with the numerical formulation.

Taking into consideration that the streamtube has a wetted swept area of $A=hR\Delta\theta\sin\theta$, similarly to the torque coefficient of the entire turbine, the non-dimensional thrust coefficient of the turbine may be derived, as seen in equation B.16, Biadgo, et al. [16]:

$$C_{Thrust} = \left(\frac{T_{ave}}{0.5\rho\rho U_{Rel}^2(hR\Delta\theta\sin\theta)} \right) \quad B.15$$

$$= \left(\frac{Bc}{2R} \right) \left(\frac{w}{U_\infty} \right)^2 \frac{2}{\pi} C_t \left(\frac{\cos\theta}{\sin\theta} - C_n \right) \quad B.16$$

where:

C_{Thrust}	Thrust coefficient
B	Number of turbine blades
θ	Azimuthal Angle
w	Relative velocity
U_{∞}	Free stream velocity
C_t	Tangential Coefficient
C_n	Normal Coefficient

Within the computational model the average torque on a rotor with, “ B ” number of blades, in one complete turbine revolution and blade length “ h ” is given by equation B.17, Biadgo, et al. [16]:

$$Q_{avg} = B \sum_{i=1}^{N_{\theta}} \frac{Q_i}{N_{\theta}} \quad (\text{B.17})$$

where:

Q_{avg}	Average torque on turbine
N_{θ}	Number of streamtube
θ	Azimuthal Angle
Q_i	Instantaneous torque on a single turbine blade

The corresponding torque coefficient can be derived from the average torque and is shown in Equation B.18, Biadgo, et al. [16]:

$$C_Q = \left(\frac{Bc}{2R} \right) \sum_{i=1}^{N_{\theta}} \frac{\left(\frac{w}{U_{\infty}} \right)^2 C_t}{N_{\theta}} \quad (\text{B.18})$$

The numerical model uses the known relationship of tip speed ratio and torque coefficient to obtain the performance coefficient of the turbine and is given by Equation B.19:

$$C_P = \lambda C_Q \quad (\text{B.19})$$

The double multiple streamtube model solves the equations allocated for the upwind and downwind sections simultaneously. The equations are linked to the stream-wise force at each actuator disc. The following equations are obtained from the conservation of momentum and the aerodynamic coefficient characteristics of the turbine blade profiles being implemented. The equations for the upwind and downwind sections of the turbine, including the attack angle, are as follows, Biadgo, et al. [16]:

$$w = \sqrt{(u_i \sin \theta)^2 + (u_i \cos \theta + \omega R)^2} \quad (\text{B.20})$$

where:

w	Relative velocity (Upwind)
u_i	Induced velocity (Upwind)
ω	Rotational velocity of the turbine
θ	Azimuthal Angle
R	Radius of the turbine

$$\alpha = \tan^{-1} \left(\frac{(1-a)\sin\theta}{(1-a)\cos\theta + \lambda} \right) \quad (\text{B.21})$$

where:

α	Attack Angle (Upwind)
a	Interference / Induction factor (Upwind)
λ	Tip Speed Ratio
θ	Azimuthal Angle

$$w' = \sqrt{(u_i' \sin \theta)^2 + (u_i' \cos \theta + \omega R)^2} \quad (\text{B.22})$$

where:

w'	Relative velocity (Upwind)
u_i'	Induced velocity (Upwind)
ω	Rotational velocity of the turbine
θ	Azimuthal Angle
R	Radius of the turbine

$$\alpha' = \tan^{-1} \left(\frac{(1-a') \sin \theta}{(1-a') \cos \theta + \lambda} \right) \quad (\text{B.23})$$

where:

α'	Attack Angle (Downwind)
a'	Interference / Induction factor (Downwind)
λ	Tip Speed Ratio
θ	Azimuthal Angle